A Metallomic, Proteomic and Lipidomic Investigation of the Malaria Parasite's Digestive Vacuole and Insights into the Mediators of Haemozoin Formation

By

Roxanne Mohunlal

Thesis Presented for the Degree of

Doctor of Philosophy

In the Department of Chemistry

University of Cape Town

August 2019

Supervisor: Professor Timothy J. Egan

Declaration

A Metallomic, Proteomic and Lipidomic Investigation of the Malaria Parasite's Digestive Vacuole and Insights into the Mediators of Haemozoin Formation

I, Roxanne Mohunlal, declare the following:

1. That the above-titled report is my own work, both in concept and execution, apart from the normal guidance of my supervisor;
2. That in cases where others' work has been cited, this has been acknowledged and referenced;
3. That no part of this work has been, is being, or is to be submitted for another degree at this or any other university;
4. That I grant the University of Cape Town free license to reproduce this work, in whole or in part, for the purpose of research.

Taking the above-mentioned into account, I hereby present this report in fulfilment of the requirements for the degree of Doctor of Philosophy in the Department of Chemistry at the University of Cape Town.

Signed by candidate

Doctoral Candidate's Signature

Date: August 2019

Abstract

Novel and unambiguous mechanistic details of the biochemical processes that enable the most virulent form of the malaria pathogen, *Plasmodium falciparum,* to thrive within the human host are desperately required in order to find innovative strategies to counteract emerging parasite resistance that will inevitably render current malarial therapies obsolete. This study focused on exploring the *Plasmodium falciparum* metallome and investigated the mediators of haemozoin formation, an ingenious parasite-specific process critical to host immune evasion as well as parasite survival and one that is surprisingly rather contentious.

In order to obtain a comprehensive view of metal distribution, the trace metal content in parasites isolated at varying time-points over the 48 h intraerythrocytic cycle were measured by ICP-MS. The trace metals detected; namely, iron, magnesium, zinc, manganese and copper, were compared to control uninfected erythrocytes. With the malaria parasite being a haematophagous organism, iron was detected as the most abundant trace metal and found to exhibit a significant increase up to 32 h into the life cycle after which the measured iron content remained relatively constant and lower than the control. This was attributed to the maximum amount of haemoglobin having been ingested at this mature trophozoite stage and the active conversion of free haem (Fe(III)PPIX) into biocrystalline haemozoin. All other trace metals exhibited 2 to 4-fold increases in metal ion content as the parasite matured and were detected in amounts higher than those found in the erythrocyte control, demonstrating uptake of these ions from the external medium. These increases coincided with specific cellular events such as cell division and enhanced parasite metabolism. Qualitative proteomic analysis of parasite material identified several metalloproteins but most significant, was the discovery of magnesium and copper transporters. Together, these findings suggest that transition metal import is essential to promote important cellular events and parasite growth and are indicative of unique parasite-specific metal transport pathways.

The mediators of crystal formation were investigated by interrogating the haemozoin proteome and lipidome. Haemozoin was obtained from parasitised erythrocytes following a fractionation approach which culminated in their release from purified digestive vacuoles (DVs) following multiple freeze-thaw cycles. Isolated crystals were extensively washed with aqueous sodium acetate buffer (0.5 M, pH 5.2), detergent

(4% SDS) and organic solvents (acetone/methanol) prior to base dissolution (0.1 M NaOH). Mass spectrometry was used to investigate the biomolecules occluded by haemozoin by analysing extensively washed and dissolved crystals. Haem detoxification protein (HDP), a protein currently postulated to be potent in mediating haemozoin formation *in vivo*, was detected in high relative abundance in the dissolved haemozoin fraction by semi-quantitative label-free proteomics. Expression and purification of recombinant soluble HDP was optimised and both soluble and refolded protein were further investigated. Characterisation by circular dichroism and fluorescence spectroscopy revealed that soluble HDP differed in conformation to its refolded counterpart. In aqueous solution (pH 7.4), UV-vis spectrophotometric titrations showed soluble and refolded HDP to bind Fe(III)PPIX in a 1:1 ratio with a K_d of 1.2 ± 0.5 μM and 0.35 ± 0.04 μM respectively. Crucially, activity studies under biomimetic conditions (pH 5.2, 37°C) demonstrated that this protein was not competent to promote β-haematin (synthetic haemozoin) formation without the incorporation of detergent.

Mass spectrometry-based lipidomics identified and quantified over 400 lipids in dissolved haemozoin. Neutral lipids were found to be the dominant class comprising 90% cholesterol, 2% cholesterol esters and 0.6% acylglycerols. The detected lipids were used to prepare a model lipid blend which was found to efficiently promote β-haematin formation in yields greater than 90% in under 10 minutes and at concentrations as low as 18 μM. Crystals synthesised using the model lipid blend were found to exhibit similar morphological traits to haemozoin naturally produced by the parasite. Live-cell imaging by spinning disk confocal microscopy revealed that neutral lipid bodies localised externally from the DV or in close contact with the DV membrane but were not found in the immediate vicinity of haemozoin. β-Haematin was found to occlude labelled protein and lipid when synthesised in their presence. Furthermore, occluded biomolecules were not readily displaced from the crystal surface through simple washing with aqueous buffer (pH 5.2) but were only released upon base dissolution of crystals. Pre-formed β-haematin and haemozoin incubated with labelled biomolecules resulted in no further occlusion which demonstrated that these crystals occlude material in a manner non-exchangeable with the DV lumen, thus providing a window into the molecules present at the time and site of crystal formation.

Overall, this multidisciplinary *omics* approach has revealed that the malaria parasite has a unique metallome which may provide promising new drug targets. Significantly, this study has unequivocally demonstrated that haemozoin occludes proteins and lipids in detectable amounts in a non-exchangeable manner with the external milieu but, crucially, lipids occluded by haemozoin are present at the time and site of formation within the DV and are potent mediators of haemozoin formation in the malaria parasite.

Publications and Conference Proceedings

Publications:

(1) D. Kuter, R. Mohunlal, S. Fitzroy, C. Asher, P. J. Smith, T. J. Egan, and K. A. de Villiers, *CrystEngComm*., **2016**, 18, 5177-5187. "Insights into the initial stages of lipid-mediated haemozoin nucleation".

Conference Proceedings:

2013: 30th June-4th July, South African Chemical Institute Inorganic Conference, University of KwaZulu-Natal, Durban, South Africa.
Poster and Flash Talk: "Investigation of the *Plasmodium falciparum* Metallome"

2013: 10th October, Chemistry Research Day, Department of Chemistry, University of Cape Town, South Africa.
Poster: "Investigation of the *Plasmodium falciparum* Metallome"

2015: 20-24th July, 17th International Conference on Biological Inorganic Chemistry, Beijing, China. **[Awarded First Prize for Poster]**
Poster: "An *omics* Insight into the Mediators of Haemozoin Formation in the Malaria Parasite"

2015: 10th November, SACI Young Chemists' Symposium, University of the Western Cape, South Africa. **[Awarded First Prize for Poster]**
Poster: "An *omics* Insight into the Mediators of Haemozoin Formation in the Malaria Parasite"

2016: 15-18th November, H3-D Symposium on Malaria, Tuberculosis and Neglected Tropical Diseases: Progress in Drug Discovery and Development, Worcester, South Africa.
Poster: "A Lipidomics Insight into Haemozoin Formation in the Malaria Parasite"

2017: 25-29th June, South African Chemical Institute Inorganic Conference and Carman Physical Chemistry Symposium, Hermanus, South Africa.
[Awarded First Prize for Poster]
Poster: "An Investigation into the Biological Molecules Involved in Haemozoin Formation in the Malaria Parasite"

2017: 11-12th December, 3rd International Conference on Lipid Science and Technology, Rome, Italy.
Poster: "Haemozoin Formation in the Malaria Parasite: A Lipidomic Perspective"

2018: 26 July, Chemistry Research Day, Department of Chemistry, University of Cape Town, South Africa.
Poster: "A Lipidomics Insight into Haemozoin Formation in the Malaria Parasite"

Dedication

This thesis is dedicated to my dearest mother,

Jayshree Mohunlal

Your unconditional love, immense sacrifices, strength and perseverance has shaped me into the person I am today. Thank you for always believing that our future is not defined by our circumstances and for encouraging me to reach for the stars. I love you.

Acknowledgements

The most meaningful journeys are achieved through the influence of incredible people. Therefore, I would like to convey my deepest gratitude to the following people who have been instrumental and supportive throughout this work.

Professor Timothy Egan, thank you for nurturing me as a researcher, for constantly challenging my thought processes and helping me to build resilience I never thought was possible. Your extensive knowledge, rational approach, open-door policy as well as patience and guidance through this writing up process were invaluable. I am extremely thankful to you for allowing me the independence to try new ideas and for supporting me as these evolved. Thank you for gently reminding me that research is a marathon rather than a sprint especially when faced with adversity, I am sincerely grateful to you, Prof.

Dr Brandon Weber, thank you for taking me under your wing and exposing me to the discipline of protein expression and all the beauty (and chaos) that accompanies it. You have really been a guiding light and I am so grateful to have had the privilege to work alongside you. Thank you for being an absolutely incredible scientist and mentor, your input, intellectual discussions and insights in this project are immeasurable.

Past and present members of **The Haem Team**, particularly **Dr David Kuter**, for introducing me to haem chemistry in honours and being an excellent teacher. **Dr Fabrizio L'abbate**, we began this academic journey together and I have learnt a lot from you; thank you for being someone who I could count on, bounce ideas off and for your friendship. I am grateful to have shared this experience with you. **Dr Melvin Ambele** for being an amazing mentor and inspiring researcher. **Dr Jill Combrinck,** for teaching me to culture malaria parasites and overcome the challenges of life. **Dr Aneesa Omar**, your bubbly personality and strong character helped me break out of my shell, thank you for your guidance and confidence both professionally and personally, you are an absolute treasure. **Dr John Woodland**, from Jack Elsworth rehearsals to weekend-long experiments, you have been instrumental in helping me develop as a well-rounded scientist and have brought out the best in me. Thank you for all our incredible memories, for the lovely treats and spontaneous adventures. **Dr John Okombo,** my partner in crime, thank you for always being genuine and for inspiring me, helping me gain perspective, the long walks across campus and for the many laughs and antics over the years. **Nomakhwezi Mvumvu**, for your kindness, compassion and friendship. **Dr Kathryn Wicht** for your guidance and helpful discussions. **Dr Nicola Kuter** for your support and making sure our pipettes were well taken care of. I could not have asked for better group members who have really ignited the true spirit of ubuntu.

Professor David Fidock, for the opportunity to come to Columbia University for a research visit in your laboratory, for full access to available resources, sharing your passion and your constant motivation, support and encouragement throughout my stay. Thank you to all members of **The Fidock Lab** for welcoming me and sharing their laboratory space with me, especially **Dr Sachel Mok** for the many late nights shared doing experiments and for making my time in New York a memorable one.

Professor Peter Smith and the **Tissue Culture Team**, for allowing me full access to the tissue culture facilities at the Division of Pharmacology, UCT and for their support. Heartfelt thanks to **Mahomed Jaffer** for his extensive knowledge and experience with electron microscopy and always making time available to view my samples irrespective of how complex they were. To **Miranda Waldron**, for your guidance with SEM experiments as well as **Nasheeta Hanief** and **Sean Karriem** for all your assistance. Special thanks to **Christel Tinguely** for sharing your expertise and ICP-MS data collection. Many thanks to **Associate Professor Dirk Lang** and **Susan Cooper**, for sharing your knowledge regarding confocal imaging experiments. **Madhu Chauhan**, for always being willing to help.

Dr Estela Area-Gomez and **Yimeng Xu** for your contribution in lipidomic data collection and analysis at the Lipidomics Core Facility, Columbia University Medical Center. **Dr Laura Munteanu** for your expertise with spinning disk confocal microscopy and for going beyond the call of duty during my time at the imaging core. Images were collected, processed and analysed at the Confocal and Specialised Microscopy Shared

Resource facility of the Herbert Irving Comprehensive Cancer Center at Columbia University, supported by NIH grant #P30 CA013696 (National Cancer Institute). **Dr Maré Vlok,** for helpful discussions regarding experimental design and for performing proteomic data collection at the Central Analytical Facility at Stellenbosch University.

The **Department of Chemistry**, **UCT**, particularly **Professors Mino Caira**, **Roger Hunter** and **Susan Bourne** for your inspiration throughout my undergraduate studies which steered me towards research. I am immensely grateful to **Associate Professor Neil Ravenscroft** for being so passionate about research and changing the world and for sharing your enthusiasm, but most importantly for being my sounding board, knowing just what to say, for the needed reality checks and the endless supply of dark chocolate. **Professor Luigi Nassimbeni** for all your words of wisdom and thought provoking general knowledge questions, thank you for making Level 6 a pleasant work environment. **Professor Kelly Chibale**, for breaking through barriers and being a true and humble leader, your kind words of advice will always be with me. **Dr Eileen Murray**, for the gentle soul that you are, for being so understanding and for making first year demonstrating a pleasant experience and a place to grow. To the admin maestros and main postgraduate cheerleaders **Deidre Brooks**, **Karin Badenhorst**, **Elaine Rutherford-Jones**, thank you for your continuous encouragement, heartfelt chats and the occasional hugs, you ladies are such a blessing. Many thanks to past and present members of the **Central Admin Office** within the department for their assistance over the years. **Monique Muller**, for being an excellent health and safety officer and for the good energy that you bring.

To friends and colleagues with whom I have shared this PhD journey and walked alongside: **Kyle Fernandes**, **Matthew Golesworthy**, **Richard Payne**, **Dr Terrance Noonan, Dr Stephen Fienberg** and **Ibiye Dagogo,** thank you for being an integral part of this roller coaster ride. Special thanks to **Dr Shakeela Sayed** and **Dr Savannah Zacharias** for being the best tea buddies and for your constant support.

To the wonderful humans I get to do life with who always believed in me no matter what: **Dr Tameryn Stringer**, we are really kindred spirits, thank you for being a good listener, your advice and all the yoga dates and yummy food we have shared. You truly hold a special place in my heart. **Suvar Hariparsad**, thank you for being a superb best friend, for genuinely supporting me through all aspects of life, always encouraging me and for sharing the finer parts of life through your flair and fabulousness as well as the delicious red velvet cupcakes. **Pavit Ramnarain**, you are most certainly the *Meredith to my Christina*. Amongst the countless things I am grateful to you for, thank you for making life so pleasant and cheerful, for all the late-night trips to The Creamery during thesis writing, for being extremely dependable, patient, accommodating and open-hearted. You have brought such light into my life and always manage to make me laugh even through the toughest of days.

In loving memory of both my beloved **grandparents**, I am grateful for our humble beginnings, for your unconditional love, always spoiling me, protecting me and believing in me. I wish you were here.

To **my family** for your support especially my precious nephew **Shalen Mudaly**, and beautiful nieces **Emily Mudaly** and **Hannah Mudaly**, you are my rays of sunshine.

My superhero **mom**, thank you for all you have done to ensure that I have a chance at a better life, making sure that I am well fed, for the hills and valleys of life that have challenged us but also helped us to truly value every moment that we are blessed with. Thank you for always encouraging me to be my own person and not to conform to the ideas of the world. Your love and pureness have sustained me throughout this journey, I could not have done this without you. I thank **God** for the grace, fortitude and strength which have carried me through and for His many blessings that makes life so precious. *"Trust in the Lord with all your heart and lean not on your own understanding"- Proverbs 3 vs 5.*

Finally, I am incredibly grateful for the financial support provided by **The Council for Scientific and Industrial Research**, the **National Research Foundation**, the **University of Cape Town** and the **Postgraduate Funding Office** which made this project possible.

List of Abbreviations

ACT	Artemisinin-based combination therapy
CQR	Chloroquine resistant
CQS	Chloroquine sensitive
CHL	Cholesterol
CE	Cholesterol ester (cholesteryl oleate)
DV	Digestive vacuole
DVM	Digestive vacuole membrane
DLG	Dilineoylglycerol
DOG	Dioleoylglycerol
DPG	Dipalmitoylglycerol
Hz_{Dis}	Dissolved haemozoin
EELS	Electron energy loss spectroscopy
ESI	Electron spectroscopic imaging
FAMEs	Fatty acid methyl esters
Fe(III)PPIX	Ferriprotoporphyrin IX
FT-IR	Fourier transform-infrared spectroscopy
GPI	Glycosylphosphatidylinositol-anchored proteins
GFP	Green fluorescent protein
HDP	Haem detoxification protein
HCv	Haemoglobin-containing vesicles
Hz_{SL}	Haemozoin surface associated lipids
Hz_{SP}	Haemozoin surface associated proteins
HRP	Histidine-rich protein
HAP	Histo-aspartic protease
ICP-MS	Inductively coupled plasma-mass spectrometry
IPTG	Isopropyl β-D-1-thiogalactopyranoside
LC-MS	Liquid chromatography-mass spectrometry
MS	Mass spectrometry
MOG	Monooleoylglycerol
MPG	Monopalmitoylglycerol
MSG	Monostearoylglycerol
MDR	Multidrug resistant
NBD	7-Nitrobenz-2-oxa-1,3-diazole
PPM	Parasite plasma membrane
pRBC	Parasitised red blood cell
PV	Parasitophorous vacuole
PVM	Parasitophorous vacuole membrane
PfCRT	*P. falciparum* chloroquine resistance transporter
PBS	Phosphate-buffered saline
PC	Phosphatidylcholine
pXRD	Powder X-ray diffraction
rHDP	Recombinant haem detoxification protein
RBC	Red blood cell
SEM	Scanning electron microscopy
SEC	Size-exclusion chromatography
SDS	Sodium dodecyl sulfate
SDS-PAGE	Sodium dodecyl sulfate polyacrylamide gel electrophoresis
SOD	Superoxide dismutase
TLC	Thin layer chromatography
TEM	Transmission electron microscopy
TG	Triacylglycerol
T_{CYT}	Trophozoite cytoplasm

Table of Contents

Chapter 2: General Materials, Instrumentation and Experimental Methods

Chapter 3: Insights into the Trace Metal Distribution within the Malaria Parasite

Chapter 4: An Investigation of the Digestive Vacuole Metalloproteome

Chapter 5: Expression, Characterisation and Activity Studies of Haem Detoxification Protein

Chapter 6: The Investigation of Lipids Occluded by Haemozoin and their Role in Crystal Formation

Chapter 1

Introduction and Literature Review

1.1. Apicomplexa: master manipulators

The dynamic interplay and intrinsic properties pertaining to host-pathogen interactions influences disease progression. Intracellular pathogens actively sabotage host processes and cellular machinery to meet nutritional demands and evade host immune responses. Parasites comprising an apicoplast, a non-photosynthetic plastid, are members of the phylum Apicomplexa and are notorious for modifying their host cells to suit their needs. *Toxoplasma*, *Theileria*, *Cryptosporidium*, *Babesia* and *Plasmodium* represent the major apicomplexan pathogens that impact animals and humans globally. Even though morphologically similar, these obligate parasites differ in life cycle, host choice, modes of infection, invasion strategy, nutrient acquisition and replication.[1]

Some parasites require a dual-host system where sexual and asexual reproduction proceed independently, whereas others survive exclusively in a single host and transmission occurs through intermediaries. Following entry into host organisms of choice, Apicomplexa migrate to their respective target cells which range from erythrocytes to epithelial cells, macrophages or hepatocytes. During this transition the parasite has to overcome adverse conditions by interchanging between extracellular and intracellular environments coupled with several biological barriers such as the erythrocyte membrane, epithelial layer and blood-brain barrier. Successful invasion of target cells initiates the pathogen's remodelling processes where it transforms the host cell into a hospitable environment in which it thrives.

With development, the parasite induces several biochemical changes involving disruption of host cell signalling, development of intricate tubular networks and remodelling lipid trafficking pathways to obtain host-derived molecules. Each of these processes are pathogen specific and involve drastic manipulation of the host cell while sabotaging essential biochemical pathways to ensure survival. Indeed, each of these organisms trigger infectious diseases; however, *Plasmodium* has a severe impact on human health. *Plasmodium falciparum* is by far the most life-threatening aetiological agent of malaria worldwide and the complexities associated with this phylum makes eradication of this disease an onerous process.[2] Interrogating the pathophysiological properties of this pathogen and gaining novel mechanistic insights into its unique survival mechanisms are paramount to disease prevention and elimination.

1.2. Malaria, the Achilles heel of human health

Communicable diseases are caused by pathogenic microorganisms that are transmitted either directly from person to person or indirectly by means of a vector, with malaria being at the forefront of the latter. *Plasmodium* is transmitted to humans through the bite of an infected female *Anopheles* mosquito. The circular interplay between the invertebrate vector and vertebrate host contributes to the robust nature of this obligate pathogen. The five species of human malaria causing pathogens comprise *Plasmodium malariae*, *Plasmodium ovale*, *Plasmodium knowlesi*, *Plasmodium vivax* and *Plasmodium falciparum,* of which the latter is the most perilous. In 2017, *P. falciparum* accounted for 99.7% of malaria cases in World Health Organisation (WHO) regions of Africa as well as 60-72% of cases in South-East Asia, Eastern Mediterranean and the Western Pacific.[2] Inadequate health facilities, lack of resources, poor nutrition and the sub-tropical climate enhances the prevalence of malaria in these regions, which consequently debilitates health and socioeconomic status.

There were 219 million cases and 435 000 malaria deaths reported globally in 2017.[2] Even though malaria occurrences appeared to be 20 million fewer than figures reported in 2010, no significant reduction in global malaria was achieved over this period. Devastatingly, Sub-Saharan Africa carries most of the malaria burden globally with reported estimates of 92% and 93% of malaria cases and deaths respectively. Disease

progression in these areas are known for their aggressive attack on infants, children under the age of five and pregnant women. In response to the staggering statistics over the past decade, the WHO launched the E-2020 Initiative of 21 Malaria-Eliminating Countries which formed part of the Global Technical Strategy for Malaria 2016-2030. Thus far, significant progress has been made in response to this initiative as Paraguay became the first E-2020 country certified to be malaria-free in 2018 and, in May this year, Algeria and Argentina followed suit. Even though these are remarkable milestones, the global malaria burden seems to have reached a plateau; therefore, innovative strategies are urgently needed.

Rapid diagnosis and treatment are key components to effective malaria control. The intensity of malaria transmission is directly dependant on the environment, especially in tropical areas where the *Anopheles* species thrive. Current preventative measures employ insecticide-treated mosquito nets and indoor residual spraying with potent insecticides. In the 1990s, treatment of uncomplicated malaria as a result of *P. falciparum* infection was stringently controlled with antimalarial treatment comprising chloroquine and sulfadoxine-pyrimethamine. However, parasites from South-East Asia developed resistant mutants, thereby rendering these potent antimalarials obsolete, and the spread of resistance to Africa had devastating effects on the population.[3, 4] At the turn of the century, artemisinin-based compounds were found to exhibit the potency required to be regarded as a 'miracle drug' and now form the first line of defence in the form of artemisinin-based combination therapy (ACT) as regulated by the WHO and has been the main success in malaria treatment thus far. Potent artemisinin-based compounds are used in combination with partner drugs that belong to a different class of antimalarials, such as mefloquine, sulfadoxine/pyrimethamine or lumefantrine to name a few. This strategy was developed to circumvent or delay the development of resistance with the rapid action of the artemisinin to reduce the majority of the parasite load and the partner drugs to clear up remaining parasites.

The inevitable threat of emerging parasite resistance to artemisinin has been accelerated by recent reports of the ominous development of a multidrug resistant parasite strain in Cambodia and Vietnam deemed 'super malaria'.[5, 6] This has further been supported by the substantial failure rates observed in ACT therapies across varying regions, especially in South-East Asia where reduced sensitivity to artemisinin and the reappearance of

parasites 28-42 days following antimalarial treatment has been reported and it is only a matter of time before similar resistance patterns are observed in Sub-Saharan Africa.[7, 8]

1.3. Life cycle of *P. falciparum*

P. falciparum has a multifaceted life cycle in which it alternates between the invertebrate mosquito vector and warm-blooded vertebrate host. During its vagrant existence, the malaria parasite continuously evolves and modifies by strategically accessing its unique genome which encodes more than 5 000 genes thereby equipping this unicellular pathogen with the necessary machinery required to survive across diverse host-specific cellular environments.[9]

This pathogen undergoes tricyclic replication comprising the sexual cycle which occurs in the mid-gut of the mosquito and the asexual cycle comprising the hepatic and erythrocytic stages in the human host (Figure 1.1). The clinically silent hepatic stage has no known physiological symptoms associated with it even though a multitude of pathogenic merozoites are produced. By contrast, several physiological symptoms associated with malaria infection are expressed during the asexual intraerythrocytic stage thereby making this the pathologically distinct phase.

During a blood meal, an infected female anopheline mosquito deposits motile sporozoites into the dermal skin layer of the human host which then migrate to blood vessels thus initiating pathogenic infection.[10, 11] Sporozoites circulate within the bloodstream and are directed to the liver where they invade hepatocytes, mature and replicate, giving rise to thousands of new merozoites after approximately seven days' post-invasion. Interestingly, in some instances, sporozoites produced in *vivax* and *ovale* remain dormant during the hepatic stage in the form of hypnozoites and can go undetected for an extensive period until, inevitably, schizont development persists thereby giving rise to life-threatening relapses. Thousands of merozoites are released from infected hepatocytes into the circulatory system in membrane-bound vesicles which rupture thus liberating parasites.[12, 13] Merozoite invasion of surrounding host erythrocytes represents the initiation of the asexual intraerythrocytic cycle.

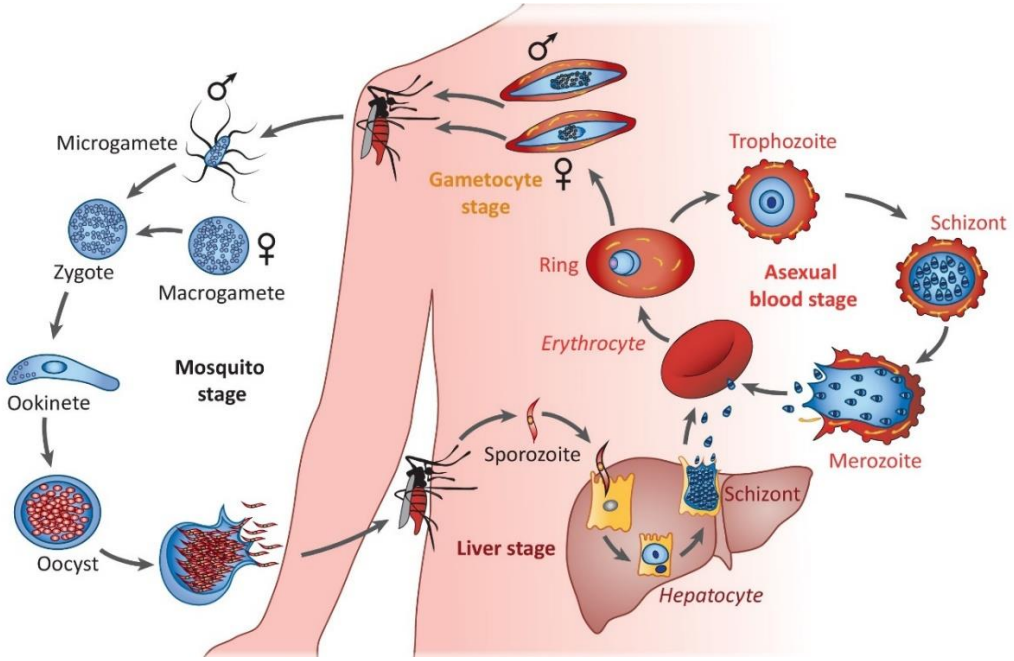

Figure 1.1. The complex life cycle of the malaria parasite illustrating pertinent processes from transmission to infection. Reprinted from Trends in Parasitology, 35, Maier *et al*, *Plasmodium falciparum*, 481-482, Copyright © 2019, with permission from Elsevier.[14]

Following invasion of mature erythrocytes, the merozoite finds itself enclosed within an exclusive parasitophorous vacuole (PV) which isolates it from the erythrocyte cytoplasm. Over the 48 h intraerythrocytic cycle of *P. falciparum*, the merozoite transitions across three morphologically-distinct stages; namely, the ring, trophozoite and schizont. During the first stage, immature parasites form a visually ring-like structure that persists for approximately 18-22 h post-invasion after which the parasite develops into the trophozoite, the most metabolically-active stage during the asexual cycle. Mature trophozoites, approximately 40 h post-invasion, undergo mitotic division producing approximately 20 merozoites thus signifying the start of the schizont stage. At this point the parasite prepares for egress from the host cell which ultimately results in host cell rupture and release of daughter merozoites back into the circulatory system, promoting further replication cycles. The symptomatic clinical symptoms associated with malaria infection are as a result of schizont rupture and the subsequent adherence of trophozoites to blood vessels, specific to *P. falciparum,* which otherwise would be subject to splenic clearance.[15, 16]

A small subset of liberated merozoites deviate from erythrocyte reinvasion and travel to the bone marrow or spleen where they develop into uninucleated male and female gametocytes thus forming precursors to the sexual stage. Gametocytes are morphologically different compared to their asexual counterparts as they transition over the five different replicative stages.[17, 18] Mature, distinguishable male and female gametocytes enter the circulatory system and, even though non-pathogenic, are competent in promoting transmission. Gametocytes are transmitted to the anopheline mosquito during a blood meal where they undergo sexual development.[19] Even though each stage of the parasite life cycle may provide novel pathways that could potentially be inhibited and exploited as potential drug targets, the current literature review and subsequent investigative studies are directly focused on the intraerythrocytic cycle of *P. falciparum* and the innate survival mechanisms thereof.

1.4. Morphological characteristics of the intraerythrocytic cycle

Each pathogen comprises distinctive permutations of genetic, physiological, molecular, chemical and physical traits responsible for host-pathogen interactions. Therefore, a comprehensive structural understanding reveals direct insights into their aetiological attributes. The establishment of continuous *in vitro* culturing of erythrocytic stage *P. falciparum* parasites allowed for detailed investigations into defining the ultrastructural characteristics contributing to the four morphologically-distinct stages (merozoite, ring, trophozoite and schizont) observed over the asexual cycle.

1.4.1. Merozoite

The specificity associated with the merozoite selectively invading host erythrocytes alludes to important ligand-receptor interactions which direct this crucial process. This form of the malaria pathogen briefly exists extracellularly between the period in which it egresses from one erythrocyte and invades another, making this is an important immunological target. Merozoites are approximately 1 µm wide making it the smallest form of *Plasmodium* organisms, very similar in size to a bacterium.[20] At the structural level, the merozoite comprises unique features which equip it to successfully promote cell adherence and invasion. One prominent feature is that of its thick, bristle-like surface coat

which allows the merozoite to capture an erythrocyte while moving through the circulatory system (Figure 1.2a). At its apical end, this lemon-shaped cell comprises three membranous vesicles, namely, micronemes, dense granules and rhoptries. These vesicles work together to secrete a specific blend of proteins and lipids which promote invasion and modify erythrocyte shape and composition. Following adherence, the merozoite re-orientates itself ensuring that its apical end is aligned with the erythrocyte membrane and, driven by microtubule activity, it enters the host cell by creating an invagination pit at the membrane surface. The parasite then localises within a membrane-bound PV, protecting it from the harsh intracellular surroundings.

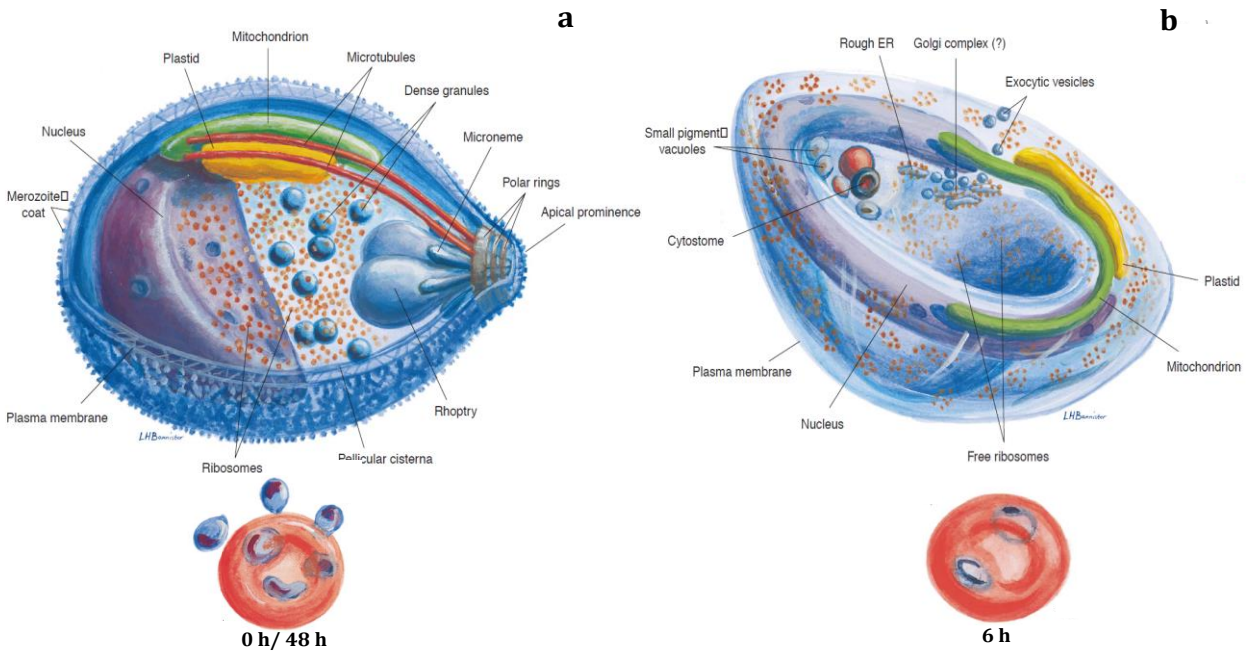

Figure 1.2. Three dimensional view of merozoite and ring stage parasites characteristic of *P. falciparum*. (a) Internal structures essential in promoting invasion and a coat of bristles can be observed in the ovoid merozoite. The inset represents merozoite invasion of a host erythrocyte following egress. **(b)** A cup-like form of an early ring stage parasite, the erythrocyte and PVM not included. Inset represents two rings at approximately 6 h post-invasion which appear to be morphologically different, one appears cup-shaped whereas the other more disk-shaped. Reprinted from Parasitology Today, 16, Bannister *et al*, A Brief Illustrated Guide to the Ultrastructure of *Plasmodium falciparum* Asexual Blood Stages, 427-433, Copyright © 2000, with permission from Elsevier.[20]

1.4.2. Ring

Following invasion, the ovoid merozoite flattens forming a thin cup-shaped structure within the erythrocyte, aptly termed a ‘‘ring’’ based on its appearance as a signet

structure observed through visualisation of Giemsa-stained parasites by light microscopy.[20, 21] The ring stage of the *P. falciparum* life cycle proceeds for approximately 18 to 22 hours post-invasion. At the structural level, ring-stage parasites appear to have a thick rimmed periphery comprising cytoplasmic content incorporating essential organelles such as ribosomes, endoplasmic reticulum, nucleus, mitochondrion and plastid, in contrast to its centre which appears markedly thinner and disc-like in shape (Figure 1.2b). This stage was initially thought to be metabolically nondescript; however, this hypothesis has evolved since with evidence supporting peak expression of parasite export proteins and the ingestion and catabolism of haemoglobin to actively occur in ring-stage parasites.[22-24] The parasite begins feeding on host cell cytoplasm through the cytostomes, endocytic structures present at the parasite periphery, by engulfing pockets of erythrocytes cytosol, parasitophorous vacuole membrane (PVM) and parasite plasma membrane (PPM).[25] These pockets are pinched off and digested within several small lysosomal vesicles within the parasite which eventually coalesce to form a single digestive vacuole (DV).[15, 26]

1.4.3. Trophozoite

The trophozoite is the most metabolically-active stage in the parasite life cycle. The distinguishing morphological features compared to ring-stage parasites are mainly attributed to cell shape and size rather than intracellular composition. Mid-trophozoites (Figure 1.3a), approximately 28 h post-invasion, appear to be irregularly shaped and tend to occupy more of the erythrocyte cytoplasmic space as they develop. Notably, drastic increases in the number of free ribosomes and size of the endoplasmic reticulum are observed, of which both structural features support enhanced protein biosynthesis during this stage.[20] Additionally, the nucleus, mitochondrion and apicoplast appear longer and more distinct along with an increase in organisation of membranous structures. There also exists a complex Golgi network comprising intricate tubular cisternae and vesicles located in close proximity to the nucleus. The trophozoite continues to actively ingest copious amounts of haemoglobin which is proteolytically degraded within the DV. As a result of heightened haemoglobin catabolism, the parasite copes with the consequential release of increasing amounts of toxic Fe(III)protoporphyrin IX (Fe(III)PPIX)) by activating the haem detoxification pathway which converts labile

Fe(III)PPIX to inert haemozoin. This is easily identified by the accumulation of electron dense haemozoin located within the acidic DV. Late-stage trophozoites experience the first phase of nuclear division giving rise to multiple nuclei in preparation for schizogony.

During this phase there is active import of nutrients and export of proteins which ensure the growth of the parasite and modification of the host cell membrane respectively. The host erythrocyte undergoes cellular remodelling driven by the parasite which alters its structural properties creating a more adhesive surface which ensures adherence of the parasitised cell to the vascular endothelium. These proteins are trafficked to the surface through the Maurer's clefts, which are compartments that concentrate virulent protein factors for export to the erythrocyte plasma membrane and protrusions at the host cell surface known as knobs which are responsible for adherence.[27-29]

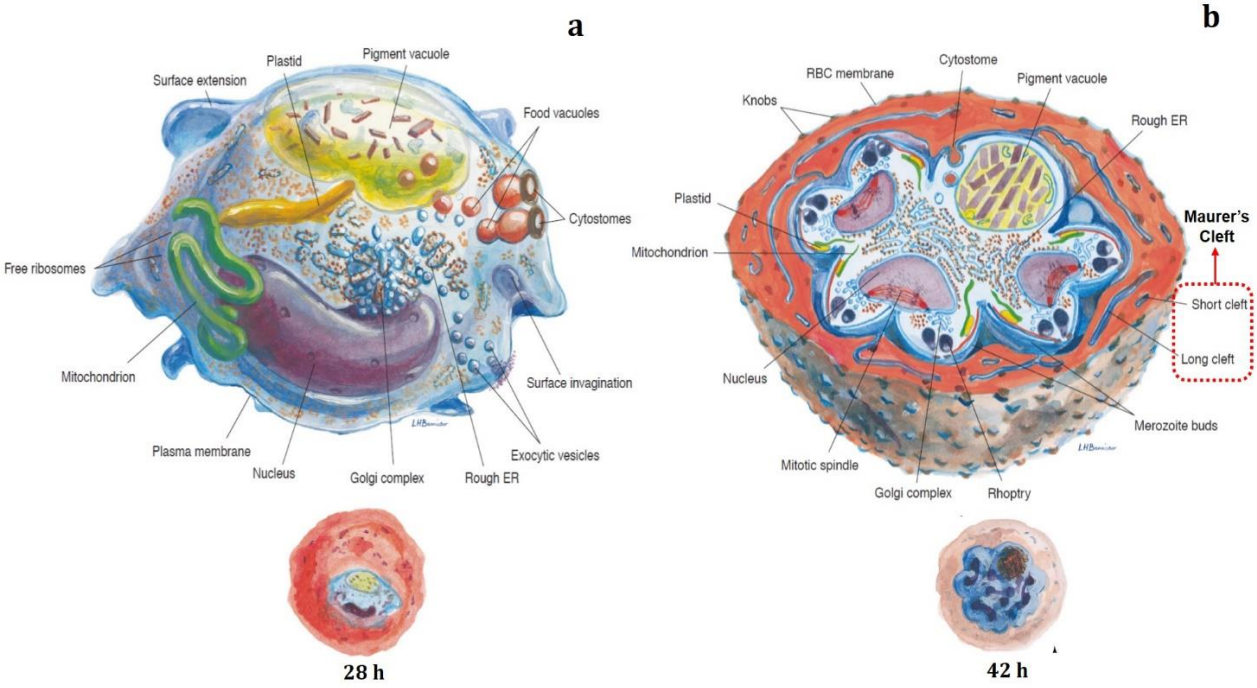

Figure 1.3. Three dimensional view of trophozoite and schizont stage parasites characteristic of *P. falciparum*. (a) Irregular shaped mid-trophozoite stage parasite containing increased number of ribosomes, defined Golgi complex and a prominent haemozoin-containing digestive vacuole. The inset represents a developing trophozoite within a deformed erythrocyte. **(b)** Transverse section of a schizont stage parasite illustrating parasite and erythrocyte content. Merozoites are seen budding from the parasite with the apex containing apical organelles. The inset represents a late-stage trophozoite that has undergone nuclear division to produce the schizont. Reprinted from Parasitology Today, 16, Bannister *et al*, A Brief Illustrated Guide to the Ultrastructure of Plasmodium falciparum Asexual Blood Stages, 427-433, Copyright © 2000, with permission from Elsevier.[20]

1.4.4. Schizont

A characteristic feature of the final stage of the intraerythrocytic cycle, 40-46 h post invasion, includes, but is not limited to, an increase in DNA and protein synthesis in preparation for schizogony. Notably, haemoglobin ingestion and catabolism continue during this stage and, as result of approximately 85% of the erythrocyte's cytoplasm having been engulfed, the parasite now occupies the majority of the host cell volume. As mentioned earlier, the first round of nuclear division begins at the late-trophozoite stage; thereafter mitotic division continues for four rounds producing a multinucleated schizont comprising 16-20 daughter merozoites per infected erythrocyte.[20] Individual merozoites are produced through invagination of the parasite membrane by an unconventional cytokinetically driven process known as budding (Figure 1.3b). As nuclear division proceeds and the parasite becomes larger, the erythrocyte appears distorted and irregularly shaped.

Fluorescence imaging studies reported by van Dooren *et al* illustrated that the mitochondrion adopts a highly ordered and branched structure and the apicoplast appeared to be more elongated during the schizont stage.[30] Following organelle metamorphosis, these structures were found to separate into each daughter cell prior to enclosure. Shortly prior to egress, the distorted parasitised erythrocyte abruptly transforms, appearing to be more circular and rigid and the new generation of merozoites are arranged in an orderly fashion around the mature DV in a 'flower conformation'.[31] The parasite appears to swell while the erythrocyte simultaneously shrinks in preparation for membrane rupture and release of merozoites. The exact molecular mechanisms related to egress are not well established but there have been a number of protein factors implicated to play important roles. A recent study by Hale *et al* using live-cell imaging and electron tomography reported the vacuolar membrane to increase in permeability at the start of egress and prior to cell rupture.[32] Interestingly, it was also demonstrated that the host erythrocyte cytoskeleton was actively dismantled prior to egress, causing the host cell to lose structural integrity- a process likely mediated by protease activity.

1.5. Haemoglobin ingestion and catabolism

1.5.1. The static metabolism of the erythrocyte

Human erythrocytes are well known for their biconcave disk shape and their distinct bright red appearance due to the spectroscopic properties associated with haem present in haemoglobin. These cells are approximately 8 μm in diameter and have an average volume of 90 femtolitres (fL). The erythrocyte is enclosed by a thin, semi-permeable membrane of highly-ordered structure comprising a complex mixture of proteins, carbohydrates and lipids. Unlike other cells which naturally migrate by chemotaxis, erythrocytic movement through the circulatory system is dependent on pressure differentials within blood vessels. Taken together, these attributes contribute to the specialised nature of erythrocytes in optimally performing their primary function in transporting oxygen to essential organs and regulating blood pH.

During erythropoiesis, developing reticulocytes undergo enucleation and lose cytoplasmic organelles thus forming mature erythrocytes devoid of nuclei, mitochondria, ribosomes and Golgi bodies.[33, 34] The lack of essential organelles results in erythrocytes being unable to actively synthesise proteins and enzymes in response to external stimuli or to promote energy production through the Krebs cycle, thus resulting in metabolically dormant cells. Additionally, erythrocytes are nutritionally deficient compared to the surrounding nutrient rich blood plasma which contains varying amounts of lipids, amino acids, trace elements, ions, hormones and glucose.

Haemoglobin accounts for approximately 95% of erythrocyte cytosolic content and is present at concentrations up to 5 mM making it a highly abundant iron reservoir within humans.[15] Since iron is an essential nutrient required for fundamental biological processes, haemoglobin serves as an attractive target as an iron-rich nutrient source for invading pathogens. Bacterial pathogens require substantial amounts of iron to promote function and survival. These organisms are equipped with modified uptake mechanisms which allow them to access iron from their surroundings. A general mechanism is that they utilise receptors to first capture haemoglobin molecules; thereafter, the haem porphyrin moiety is extracted and a toolkit containing haem oxygenase degrades the haem moiety releasing iron to the pathogen cell.[35] In most cases, globin undergoes disposal as metabolic waste. Alternatively, some bacteria are able to transfer haem iron

directly into their haemoproteins through a molecular process known as molecular-hijacking.[36] Strikingly, the malaria parasite's utilisation of haemoglobin contrasts to that of bacterial organisms in that globin undergoes degradation as a nutrient source and the release of free haem and accumulation thereof creates a potential toxin. Since *Plasmodium* actively and continuously ingests copious amounts of haemoglobin, the resulting release of free Fe(III)PPIX as a result of accumulation thereof has been shown to be detrimental to the parasite.[37] Overall, these attributes create an inhospitable environment for the malaria parasite and poses major metabolic challenges that need to be overcome in order for the parasite to survive.

Therefore, while residing within the erythrocyte, the parasite must impose a series of complex networks to endure the barren intracellular environment. Such Apicomplexan pathogens have varied metabolic and nutritional demands that are crucial to growth and development. Even though the erythrocyte lacks internal organelles, therefore providing a spacious environment for the parasite to develop, there are several inadequacies that accompany this host cell, posing questions such as how does this pathogen modify the host cell, what are the essential nutrients and ions required, how does the parasite fulfil these requirements, how does the parasite cope with the accumulation of free Fe(III)PPIX and what mechanisms are in place to circumvent potential toxicity? To date these vital questions have been addressed to some extent; however, there is ongoing contention regarding aspects of the mechanistic details of current hypotheses so that there remains a substantial portion of malaria parasite biology still to be elucidated.

1.5.2. Mechanism of haemoglobin uptake and trafficking

The malaria parasite ingests approximately 80% of host cell haemoglobin during the intraerythrocytic stage.[15] Since the erythrocyte can be considered a hostile host with the potential of cell lysis threatening the survival of this pathogen, copious haemoglobin ingestion is actually a critical survival mechanism required to create space within the cell to accommodate pathogen growth, produce osmolytes to circumvent premature cell lysis and utilise the by-products of digestion as a nutrient source.[38] The two key aspects to understanding this crucial process centre around the mechanistic details pertaining to

how the parasite ingests haemoglobin and which point over the 48 h cycle marks the initiation of this process.

Trafficking of haemoglobin from the erythrocyte cytosol into the parasite was originally thought to be most active during the trophozoite stage and was observed to occur through the cytostome as reported by Aikawa *et al*.[25] The cytostome is an endocytic invagination located at the parasite periphery comprising the PVM and PPM. It has been postulated that haemoglobin is trafficked into the parasite through pinching of the cytostome forming double-membrane bound lysosomal vesicles by endocytosis. Over the past decade, this process has been re-examined which has resulted in many conflicting hypotheses.

An investigation conducted by Elliot *et al* using serial thin-section electron microscopy has demonstrated four different haemoglobin uptake mechanisms in place.[39] This was the first study to propose that the first haemoglobin uptake event was observed during the early ring stage through macropinocytosis denoted as the 'big gulp' causing the parasite to adopt a cup-like fold. Small haemoglobin vesicles, cytostomal tubes and phagotrophs comprised the array of structures claimed to be involved in uptake at varying points over the intraerythrocytic cycle. Further studies reported by Bakar *et al* showed that haemoglobin uptake commenced in mid-ring to trophozoite stage parasites through the cytostomal invaginations which pinch off to form pre-DV compartments and not by macropinocytotic events.[24] As the parasite matures, the cytostome remains active and several of the haemoglobin-containing vesicles (HCv) coalesce to form a single mature DV to which newly formed vesicles are also trafficked.

Even though trafficking of haemoglobin from the erythrocyte to the DV has been established, the molecular mechanics driving this process are not well understood. Vesicle transport within eukaryotic cells are mediated either by a microtubule network comprising kinesin and dynein or an actin-myosin motor system.[40, 41] Recently, Milani *et al* investigated the potential role of such motor systems in haemoglobin trafficking.[42] Three dimensional models of parasites treated with various pharmacological agents responsible for perturbing or promoting function of actin, myosin and dynamin were imaged by serial thin-section electron microscopy (Figure 1.4).

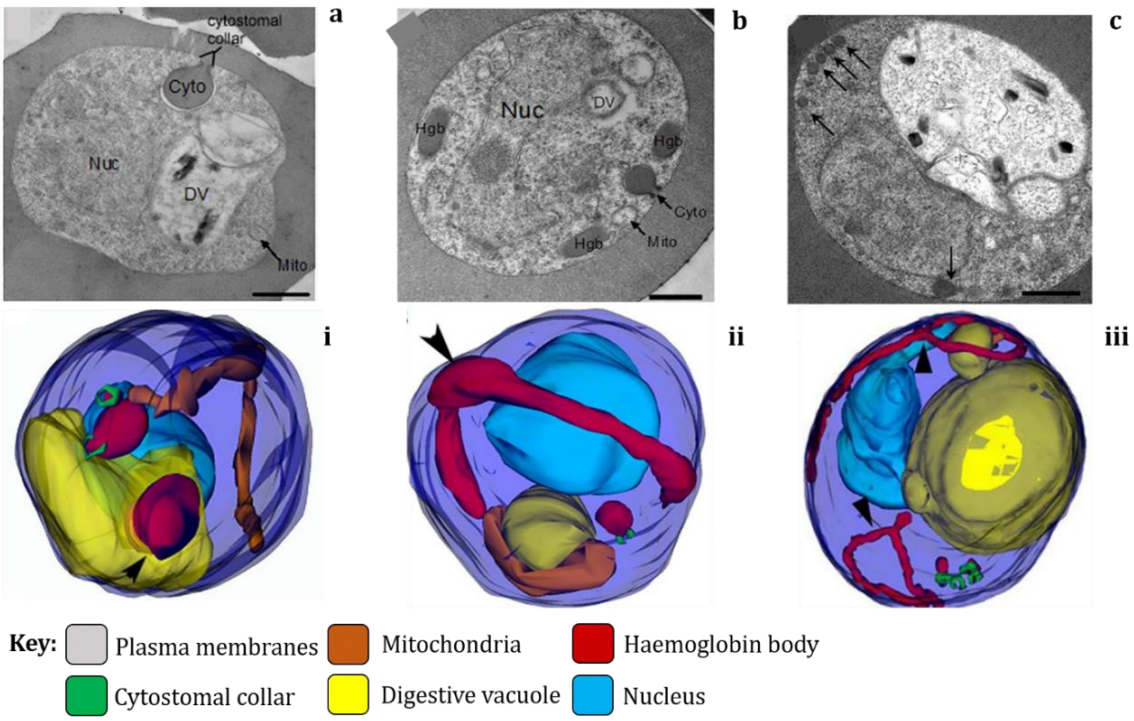

Figure 1.4. Investigation of haemoglobin transport in the malaria parasite by serial electron microscopy characterisation of control and pharmacologically-treated mid-trophozoite stage parasitised cells. (a-c) Electron micrographs and 3D reconstructions (i-iii) of control and treated parasitised erythrocytes. **(a, i)** Untreated control trophozoite containing two cytostomes and an HCv (black arrow). **(b, ii)** Trophozoite treated with jasplakinolide, an agent that promotes actin stabilisation and polymerisation, showing several haemoglobin vesicles at the parasite periphery which appear to be a long haemoglobin-containing tube lacking a cytostomal collar and open to the erythrocyte cytosol (black arrow) seen in the 3D model. **(c, iii)** Trophozoite treated with Dynasore, a dynamin inhibitor, showing several thin elongated haemoglobin-containing tubes at the parasite periphery. Key: nucleus (Nuc), digestive vacuole (DV), mitochondrion (Mito), cytostomal collar (Cyto), haemoglobin (Hgb) and haemoglobin-containing vesicle (HCv). Reprinted from Eukaryotic Cell, 14, Milani *et al*, Defining the Morphology and Mechanism of the Hemoglobin Transport Pathway in *Plasmodium falciparum* -Infected Erythrocytes, 415-426, Copyright © 2015, with permission from the American Society for Microbiology.[42]

Additionally, the mechanism relating to haemoglobin vesicle fusion with the DV was also investigated. This study proposed a refined model comprising three key points: (i) an electron dense cytostomal collar forms at the interface of the PVM and PPM providing structure to the developing cytostome, (ii) HCvs form at the distal end of the cytostome and are trafficked to the DV by an actin-myosin motor, actin and dynamin are involved in pinching off the cytostome and haemoglobin containing vesicle formation, (iii) HCv fusion to the DV may involve the *N*-ethylmaleimide sensitive factor attachment protein receptor dependant mechanism (SNARE).

1.5.3. Fate of haemoglobin

Following ingestion, haemoglobin catabolism culminates in the DV, an acidic organelle comprising two major protease families, namely plasmepsins and falcipains, responsible for the systematic degradation of haemoglobin (Figure 1.5).[43, 44] Treatment of *Plasmodium* with known cysteine protease inhibitors halted haemoglobin hydrolysis and resulted in the accumulation of haemoglobin and vacuolar swelling which subsequently caused parasite death thereby emphasising that these proteases are crucial to parasite survival.[45, 46] The four aspartic proteases, plasmepsin I, II, IV and histo-aspartic protease (HAP) initiate cleavage of haemoglobin.[47] Newly-generated peptides are then hydrolysed by the cysteine proteases falcipain II and III.[48] Following cysteine protease activity, falcilysin, a zinc metalloprotease belonging to the M16 family, utilises these peptides as substrates since it has a preference for smaller globin peptides approximately 20 amino acids in length and functions optimally in an acidic environment.[48, 49] Finally, amino acids are released following degradation of peptide fragments by aminopeptidases and exported to the parasite cytosol where they undergo further metabolism.[50] Later, a 200 kDa protein complex comprising plasmepsins II and IV, HAP, falcipain II and a protein named haem detoxification protein (HDP) has been reported to be present in the DV and claimed to direct haemoglobin hydrolysis and haem detoxification within the parasite.[51]

The active digestion of large amounts of haemoglobin by the parasite is known to be essential for survival. The recognised paradigm regarding the necessity of the haemoglobin degradation pathway centres around the need to provide a main source of amino acids for the parasite for protein synthesis and to meet metabolic requirements since *Plasmodium* is inadequately equipped for amino acid synthesis *de novo*.[52] Even though the parasite ingests over 65% of the host erythrocyte's cytoplasm, less than 25% of the generated amino acids are actually utilised by the parasite in protein synthesis with the remainder released into the external milieu.[53] Since the parasite produces far more hydrolysed amino acids than are required for general parasite metabolism, alternative theories suggest that this catabolic process is essential in maintaining osmotic balance and creating space within the host erythrocyte to ensure successful parasite growth.[38, 54, 55]

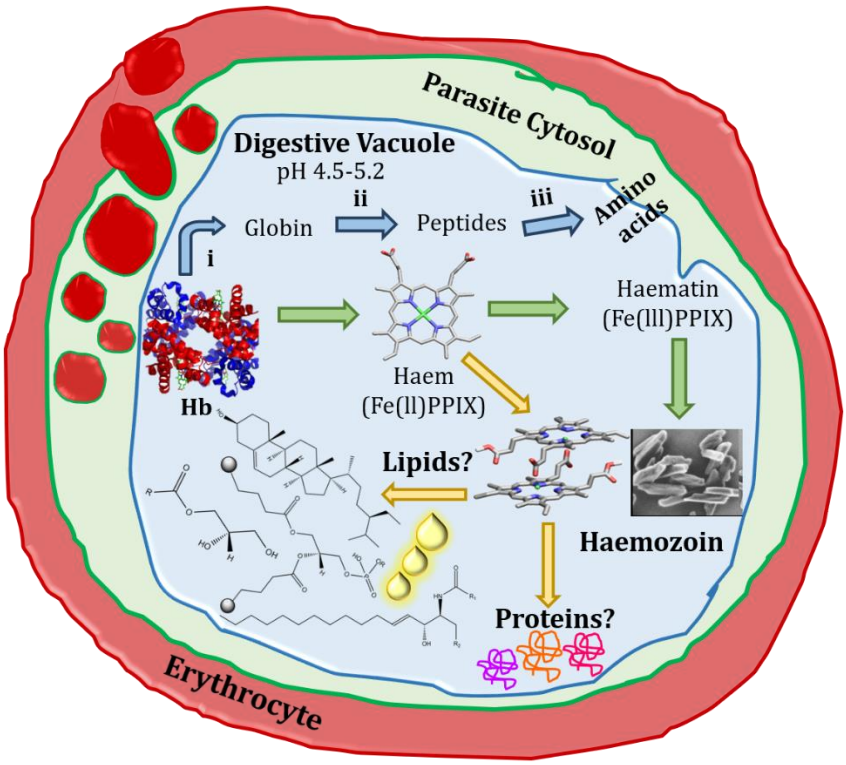

Figure 1.5. Schematic of haemoglobin catabolism and haemozoin formation within a parasitised erythrocyte. Ingested haemoglobin (Hb) undergoes a semi-ordered degradation process within the DV under the action of **(i)** plasmepsins, **(ii)** falcipain, falcilysin and **(iii)** aminopeptidases. The exact mediators and mechanism of haemozoin formation remain to be elucidated.

1.6. Detoxification of liberated haem

1.6.1. Haem detoxification in *P. falciparum*

Haemoglobin comprises an assembly of four subunits bonded non-covalently where each contains a prosthetic haem chromophore. Subsequent haemoglobin catabolism results in the liberation of four haem molecules per protein molecule that is hydrolysed. In contrast to the export of amino acids during haemoglobin degradation, free haem remains within the parasite's DV where intravacuolar haem concentrations of approximately 0.4 M can occur within this 4 fL organelle.[15] It is known that just micromolar quantities of liberated haem can perturb the normal functioning of cells by impeding protein activity, disrupting membrane bilayers and generating reactive oxygen species (ROS) through electron transfer reactions.[56, 57] The redox active iron core is responsible for the cytotoxicity of the haem moiety due to its ability to interchange between reduced ferrous (Fe^{2+}) and oxidised ferric states (Fe^{3+}); therefore, haemoglobin catabolism marks the

genesis of immense oxidative stress which is detrimental to the malaria parasite. In mammals, the liberation and circulation of free haem is counteracted with the efficient enzymatic cleavage of the porphyrin by the action of haem oxygenase I; however, *Plasmodium* lacks an active form of this enzyme during the blood stage and requires an alternate haem detoxification pathway.[58] As a result, the parasite has developed an ingenious mechanism in which it converts toxic free haem into inert haemozoin, thereby avoiding pro-oxidant toxic effects and promoting parasite survival. Released haem (Fe(II)PPIX) undergoes immediate oxidation to form haematin (Fe(III)PPIX) which is sequestered as haemozoin. During this redox reaction, free electrons are liberated which have the potential to react with surrounding free oxygen molecules thus producing several ROS such as hydrogen peroxide, superoxide anions and hydroxyl radicals of which the latter can additionally be produced by the Fenton reaction.[59, 60] Oxidative stress is circumvented through the parasite's antioxidant defence system comprising a complex network of thioredoxin oxidases and superoxide dismutases (SODs).[61] At the end of the intraerythrocytic cycle, following egress, the parasite releases a mature DV into the hosts' circulatory system where it undergoes phagocytosis by macrophages. Together, haemozoin formation, the rich antioxidant network and disposal of haemozoin-containing DVs form the intricate yet efficient haem detoxification pathway unique to *Plasmodium*.

1.6.2. Structural properties of haemozoin and β-haematin

Early in the 17th century, G. Lancisi, an Italian physician observed brownish-black blemishes in the brain, spleen and liver of victims experiencing intermittent fevers which are characteristic of malaria symptoms.[62] More than a century later, a German physician, J. H. Meckel, observed similar black pigmented granules in the liver and spleen of a psychiatric patient. However, it was only two years later in 1849 that a German pathologist, R. Virchow, conclusively discovered the link between these dense pigmented granules and malaria.[63] What was originally proposed to be merely melanin contributed to the discovery of the parasitic malaria causing protozoan by a French surgeon, C. L. A Laveran, who observed various stages of the malaria parasite life cycle in blood films prepared from infected patients in North Africa.[64] In 1911, W. H Brown disproved the idea of melanin by demonstrating that this contained haematin and postulated the link

between haemoglobin degradation and haematin formation.[65] For several decades the importance of haemozoin in the overall context of malaria was greatly overlooked. In the late 1980s, studies by Fitch *et al* demonstrated that isolated haemozoin can be stripped of contaminating lipids and proteins through washing with detergent and a non-specific protease followed by extraction with chloroform/methanol.[66] The residual black precipitate was found to be highly insoluble and exhibited the characteristic spectral properties of Fe(III)PPIX.

Shortly after, Slater *et al* used a combination of chemical synthesis, infrared spectroscopy and X-ray absorption spectroscopy to provide structural insights of haemozoin and β-haematin in one of the earliest studies that pioneered subsequent research.[67] This study demonstrated that synthetically-prepared β-haematin under acidic conditions was identical in structure to its natural haemozoin counterpart as supported by infrared spectroscopy, powder X-ray diffraction (pXRD) pattern as well as solubility studies. Furthermore, Slater *et al* postulated that haemozoin was a polymer comprising haem subunits linked through coordination from the propionate group of one haem moiety to the iron centre of another. Synchrotron pXRD patterns obtained for dried trophozoite lysate and synthetically prepared β-haematin in a study by Bohle *et al* revealed that both samples corresponded to a crystalline triclinic lattice comprising the same parameters thereby further supporting that these were identical molecules.[68] The crystallographic symmetry suggested that the haem moieties were arranged as two anti-parallel polymer chains which were linked by hydrogen bonding since haemozoin was found to belong to the centrosymmetric space group P-1. Electron paramagnetic resonance and Mössbauer spectroscopy studies unequivocally clarified previous misconceptions regarding the spin state of the ferric centre showing that haemozoin comprises exclusively the high-spin Fe^{3+} species.[69] Finally, the crystal structure of β-haematin (Figure 1.6) was elucidated by Pagola *et al* using high resolution pXRD with Rietveld refinement.[70] Solving the crystal structure consisted of positioning the molecule within the unit cell in order to find the torsion angles that were optimum between the calculated and experimental pXRD patterns. A haem dimer subunit was found per unit cell where porphyrins were linked through reciprocal iron-carboxylate bonding of one moiety to the propionate side chain of the other. Resulting dimers were arranged through hydrogen bonding and π-π stacking interactions forming a chain-like three-dimensional crystal structure, thus rendering previous hypotheses regarding β-haematin and haemozoin as polymers obsolete. These

findings were further corroborated in a study by Gildenhuys *et al* which reported the first single crystal Fe(III)PPIX model of haemozoin by forming the β-haematin DMSO solvate with correspondingly more accurate atomic positions.[71]

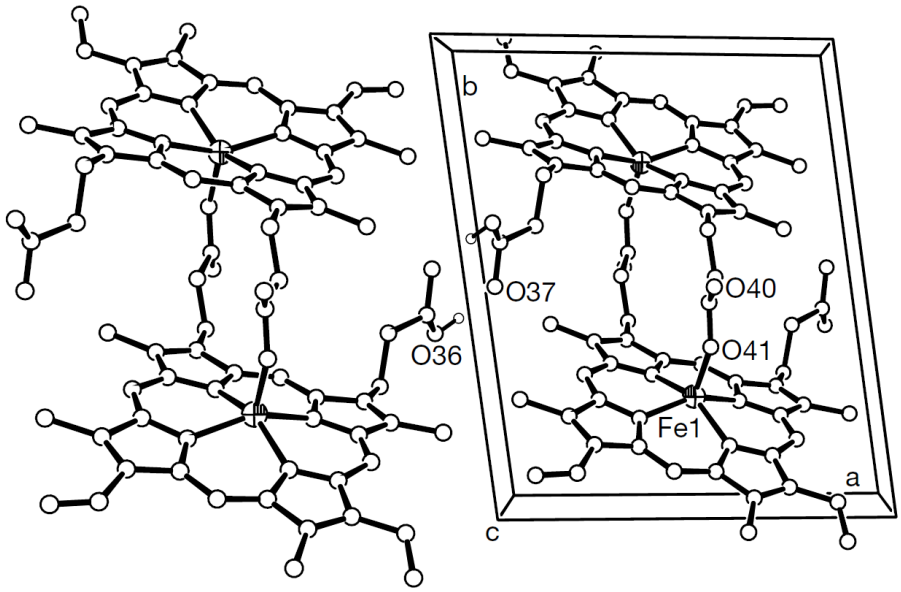

Figure 1.6. Crystal structure of β-haematin representing cyclic dimers in two unit cells as viewed along the (001) axis. Reprinted by permission from Springer: MacMillan Magazine Ltd, Letters to Nature, Pagola *et al*, Copyright (2000).[70]

1.6.3. Biomineralisation in diverse non-related organisms

1.6.3.1. Haemozoin-forming organisms

Haematophagous organisms are defined by their blood-enriched diet and represent a group of genetically diverse organisms ranging from single-celled organisms to arthropods and even small mammals. These organisms consume large amounts of blood in a single meal which, in some cases, exceeds the body weight of that organism.[72] Subsequent haemoglobin degradation results in a drastic insult of free haem which has deleterious effects if not appropriately disposed of. As discussed earlier, *Plasmodium* suffers a similar challenge regarding haem toxicity and the ingenious survival mechanism pertaining to haemozoin formation was originally thought to be novel to the malaria parasite. However, it has been established that other haematophagous organisms such as *Rhodnius prolixus,* the triatomine vector responsible for Chagas disease, *Schistosoma mansoni,* a trematode causing schistosomiasis and *Haemoproteus columbae*, a relative of

Plasmodium, form haemozoin as part of their haem detoxification strategies.[73-75] When compared to haemozoin produced *in vivo* by *Plasmodium*, crystals obtained from the above-mentioned organisms exhibited characteristic signals and patterns by FT-IR and pXRD which unequivocally identified this material as haemozoin.[75, 76]

The phospholipid bilayers comprising the mid-gut of *Rhodnius prolixus* have been reported to be the mediator of haemozoin formation, initially postulated by Oliveira *et al*.[73, 77] Silva *et al* demonstrated the association between free haem and the perimicrovillar membranes lining the insect's acidic mid-gut lumen by successfully synthesising β-haematin in the presence membrane extracts, thereby suggesting that the phospholipid-rich membrane provides the adequate environment in terms of hydrophobicity and acidity required to promote solubilisation of haem and consequential haemozoin nucleation. This was further supported in recent studies by Stiebler *et al* where lipids extracted from the mid-gut and commercially-available unsaturated glycerophospholipids were found to efficiently and rapidly promote β-haematin formation *in vitro*.[78] In earlier studies, Oliveira *et al* reported that lipid extracts obtained from the gut of mature *Schistosoma mansoni* was efficient at promoting crystallisation of β-haematin *in vitro*.[79] Lipids were further implicated as mediators of haemozoin formation by Soares *et al*, where it was demonstrated that crystal formation occurred at the surface of extracellular lipid droplets present within the gut of this helminth as visualised by electron microscopy.[80] These data suggest that the specific lipid composition of these droplets provided the catalytic effect to initiate nucleation and created a lipid-water interface at which crystal formation occurs.

Until very recently, the intracellular accumulation of free haem has not been observed in mammals since these represent higher-order creatures with alternative mechanisms in place to efficiently promote detoxification. One such process is that of erythrophagocytosis, which eliminates damaged erythrocytes following engulfment by macrophages.[81] In mammals, the haem responsive gene (HRG-I) transports haem to the cytosol where it is degraded by haem oxygenase I, thus liberating iron.[82, 83] Earlier this year, in what represents a seminal study, Pek *et al* reported the formation of haemozoin in genetically-modified (GM) mice which lacked HRG-I.[84]

In that study, macrophages in HRG-I deficient mice were observed to contain higher levels of cellular iron where the abundance corresponded to regions of interest which contained

dark pigmented granules when compared to the wild type. These dense granules were characterised by high resolution pXRD which confirmed this to be haemozoin. This phenomenon was visualised by confocal microscopy as seen in Figure 1.7 by using antibodies against lysosomal-associated membrane protein-I (LAMP-I), a well-known erythrophagosomal marker.[85] These imaging studies demonstrated that haemozoin localised within LAMP-I containing vesicles, with an approximate pH of 4-6, which appeared enlarged compared to standard lysosomes. Taken together, the results in this study demonstrated that the lack of HRG-I in a mammalian model results in the accumulation of free haem and resulting haemozoin formation in lysosomes. The common theme between this and the above-mentioned haemozoin forming organisms is the exploitation of an acidic environment by macrophages which indicates the essential nature of a low pH environment in promoting haemozoin formation both *in vitro* and *in vivo*.

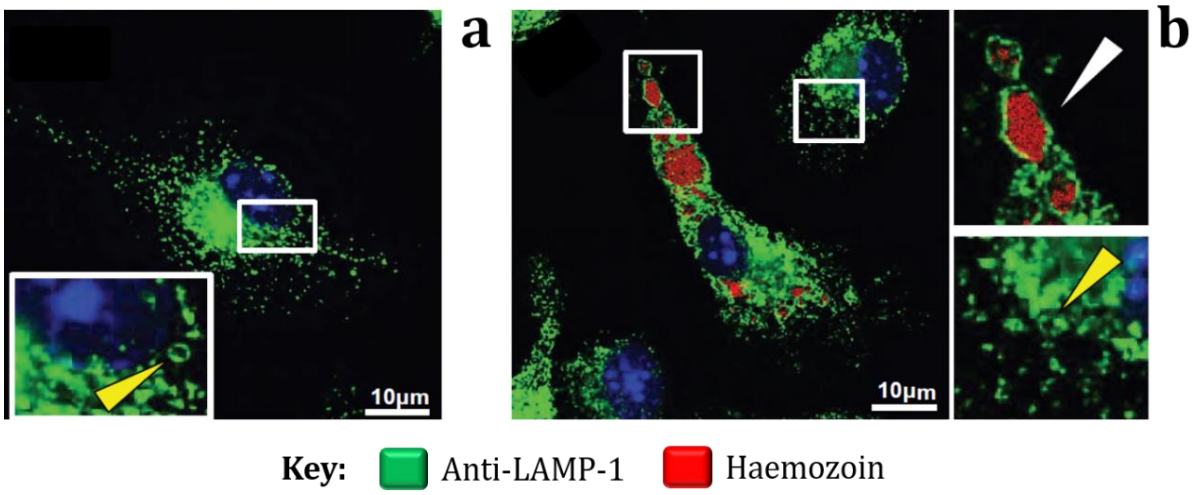

Figure 1.7. **Immunofluorescence confocal microscopy of macrophages treated with anti-LAMP-1 and Alexa-488 antibodies.** Macrophages obtained from bone marrow from (a) wild type mice and (b) HRG-I deficient mice. Insets represent acidic vesicles devoid of haemozoin and the white arrow indicates vesicles loaded with haemozoin. Reprinted with permission from author, bioRxiv, Pek *et al*, Copyright (2019).[84]

1.6.3.2. Biomineralisation in non-haemozoin forming organisms

Biomineralisation refers to the amalgamation of organic and inorganic molecules that give rise to three-dimensional structured assemblies such as teeth, bone and shells within living organisms.[86] The subsequent formation of inorganic biocrystals provides mechanical support and structure as is the case for the coral skeleton, transmit signals

from the surrounding milieu as with teeth and provides protection which is characteristic of crustacean cuticles and mollusc shells, as well as offering the embryonic protection provided by the egg shell.[87-90] This complex process is tailor-made for each organism resulting in intricate mechanisms that culminate in crystal formation. Biocrystal formation occurs as a result of a variety of factors which can be grouped into four main stages: (i) the pre-assembly of organic material prior to inorganic molecular deposits which determine the location and function of nucleated material, (ii) molecular recognition of the bioinorganic interfaces determining crystal growth, (iii) regulation of crystal development and (iv) the synergistic biochemical composition and regulation of biological macromolecules including environmental factors not limited to pH and temperature that are optimal for biocrystal formation.[91]

Various biomolecules comprise the organic matrix which promotes biomineralisation across various organisms. Studies into the molecules that promote calcification in dentin, cartilage and bone have implicated lipids and proteins in this process. Small spherical bodies bound by a lipid bilayer were often observed to be associated with calcium phosphate crystals. These are commonly known as matrix vesicles (MVs) and were thought to be the initial sites of calcium phosphate biocrystal formation.[92, 93] MVs were found to be phospholipid-rich with a smaller composition of neutral lipids and fatty acids.[94] The interaction of acidic phospholipids with calcium and phosphate ions, complemented by a minor protein component, are thought to form the precise molecular mixture that promotes nucleation and crystallisation of hydroxyapatite.[95-97] Similarly, coccolith formation in marine algae *Emiliana huxleyi* has been known to be promoted by the cytoskeletal contents of phospholipid-rich MVs.[98] Thus, it is evident that lipids create the ideal hydrophobic environment conducive to biocrystal nucleation and growth.

A range of proteins have been implicated in biomineralisation processes across a diverse range of unrelated organisms. At the microorganism level, freshwater magnetotactic bacteria produce iron-rich magnetite crystals named magnetosomes which enable the organism to navigate in accordance with the earth's magnetic field.[99] Investigations into the protein composition of the bacterial membrane surface identified a small acidic protein, Mms6, strongly associated with magnetite.[100] Characterisation and functional analysis of Mms6 demonstrated the protein's ability to bind iron, promote crystallisation of magnetite as well as regulate shape and size of crystals.[101-103] Recent genomic analysis

identified two genes encoding trypsin-like proteases to be essential in magnetite formation.[104] Disruption of these genes eliminated magnetite formation in the bacterial cell line thereby signifying the essential nature of these proteases in promoting biomineralisation within the *Magentospirillum* species.[104, 105]

Proteomic analysis by one-dimensional gel electrophoresis and mass spectrometry of the test and shell of the sea urchin, *Strongylocentrotus purpuratus*, identified more than one hundred proteins forming the organic matrix component.[106] The skeletal components analysed were thoroughly cleaned with sodium hypochlorite with the intention of destroying all surface associated organic material thereby leaving behind intra-crystalline material. A host of proteins were identified comprising those with C-type lectin-like domains, carbonic anhydrase, collagen, proteases, membrane associated glycoproteins as well as hypothetical proteins. Since this formed a diverse cohort of proteins each equipped with novel functions that may contribute to different aspects of biomineralisation, the identified proteins emphasised the complexity associated with the process. Similar proteomic-based methods were employed in a study which profiled the proteome of the limpet shell, *Lottia gigantea*.[107] Utilising liquid chromatography-tandem mass spectrometry (LC-MS/MS), Drake *et al* reported the skeletal biomineral proteome for the stony coral, *Stylophora pistillata*.[108] The proteins identified in this study comprised cadherins, integrins and other similar adhesion related proteins which form a part of the extracellular matrix and enable adhesion. Several collagens which provide support, as well as actins and tubulins which are responsible for regulating shape and growth of the calicoblastic space during aragonite crystallisation, were found.

Turning to biomineralisation in higher-order organisms, kidney stone formation resulting in urolithiasis impedes human health. Calcium oxalate and calcium phosphate are the major constituents of kidney stones dependant on the type of stone. Over the past decade, extensive efforts have been made to determine the constituents of the organic matrix. Through various technological advancements, the proteome of kidney stones has been explored, where proteins appear to form an intimate association with the calcium salt crystals.[109, 110] However, even though proteins have been identified, their actual role in mediating crystal formation and determining whether these are promoters or inhibitors of crystal formation has not yet been extensively investigated. The mineralised extracellular matrix is a characteristic feature of bone compared to other tissues. A

large-scale study reported by Alves *et al* profiled the bone proteome using SDS-PAGE and nano-LC-MS/MS as complementary techniques.[111] Thousands of proteins were identified and quantified and the resulting dataset differentiated proteins grouped by family and functionality using gene ontology terms. Of particular interest was the identification of several members of the annexin family, known to promote bone mineralisation. Annexin 2, 5 and 6 were found to be amongst the high abundant proteins and were previously reported to function as calcium channels and localise in MVs that promote biomineralisation.[112] Therefore, this study successfully demonstrated an array of proteins specific to the bone matrix and discovered those with functional capabilities directly linked to biomineralisation. Thus, it is evident that proteins contribute to biomineralisation processes and constitute an integral component of the organic phase of the biocrystal matrix. Given parallels between haemozoin and biomineralisation, analogous approaches might shed light on its mechanism of formation.

1.6.4. Mechanistic insights of haemozoin formation to date

Haemozoin formation within *Plasmodium* is a parasite-specific mechanism therefore making this an attractive target for antimalarial therapy. Studies by Egan *et al* have demonstrated that approximately 95% of liberated haem undergoes conversion to inert haemozoin within the DV. Even though only a small portion of unsequestered haem remains this could be adequate to cause damage to the parasite.[113] The impact and potency of various antimalarials, specifically the 4-aminoquinolines, as inhibitors of β-haematin formation and the consequent build-up of free haem in the parasite has been extensively investigated.[37, 114, 115] Additionally, haemozoin is thought to play a critical role in the host immunological response to malaria, involving cytokine dysregulation, immunosuppression and severe malaria anaemia.[116-118] There has also been a concerted effort to exploit the optical properties of these biocrystals as potential diagnostic tools in the fight against malaria.[119-121] Apart from haemozoin formation enabling parasite survival, these crystals play a prominent role in clinical symptoms associated with malaria as well as ongoing efforts focusing on diagnosis and treatment. Given the critical significance of haemozoin in this infectious disease, there has been substantial effort dedicated to haemozoin research over the past three decades. Regardless of this, the mechanistic aspects pertaining to crystal formation remain poorly understood; more

specifically, the biomolecules involved in promoting crystal formation *in vivo* remain highly contentious. Currently there are two main theories that focus on the mediators of haemozoin formation and these will be discussed further.

1.6.4.1. Proteins

Slater and Cerami demonstrated that extracts from trophozoite lysate promoted the successful conversion of Fe(III)PPIX to β-haematin (synthetic haemozoin) under acidic conditions, mimicking those similar to the DV.[114] This reaction was postulated to proceed under the influence of an enzyme classified as 'haem polymerase', of which activity was inhibited following treatment with known aminoquinolines. On the other hand, Dorn *et al* showed that β-haematin activity was not impeded upon heating trophozoite lysate or haemozoin thereby dismissing the theory that this was an enzymatically-driven process.[122] This study hypothesised that haemozoin formation was likely to be an auto-catalytic chemical process that proceeded in the presence of pre-formed haemozoin.

Histidine-rich protein II (HRP II), a 30 kDa protein with a 34% *His* amino acid content, initially thought to be present in large quantities in the parasite DV, was implicated as being the key mediator of haemozoin formation based on its ability to successfully bind Fe(III)PPIX and promote formation of β-haematin as reported by Sullivan *et al* thereby implying a direct role in haemozoin nucleation *in vivo*.[123, 124] Despite HRP II being able to bind Fe(III)PPIX and promote β-haematin formation, subsequent genetic and biochemical studies have questioned the actual function of this protein.[125, 126] Immunofluorescence studies by Papalexis *et al* showed that majority of HRP II is localised in the erythrocyte cytoplasm with a small overlapping sub-population present in the DV.[127] A subsequent study by Akompong *et al* further validated this finding by reporting that 97% of HRP II was secreted at the periphery of the erythrocyte and avoided endocytosis with only 3% present in the DV, the location of haemozoin formation.[128] Furthermore, haemozoin obtained from *Plasmodium* strains incorporating deletions for HRP II and/or its homologue HRP III were investigated.[129, 130] The 3D7 strain of *P. falciparum* includes both HRP II and III genes, HB3 comprises HRP II only, Dd2 comprises HRP III only, genetic crosses of HB3 and Dd2 producing 3B-D5 lacked both HRPs and *Plasmodium vivax* does not possess any of these genes. All of these parasites were found to continue with

haemoglobin degradation and produced haemozoin that was morphologically indistinct from each other (Figure 1.8), thereby strongly arguing against HRP II as the key mediator in haemozoin formation.[130]

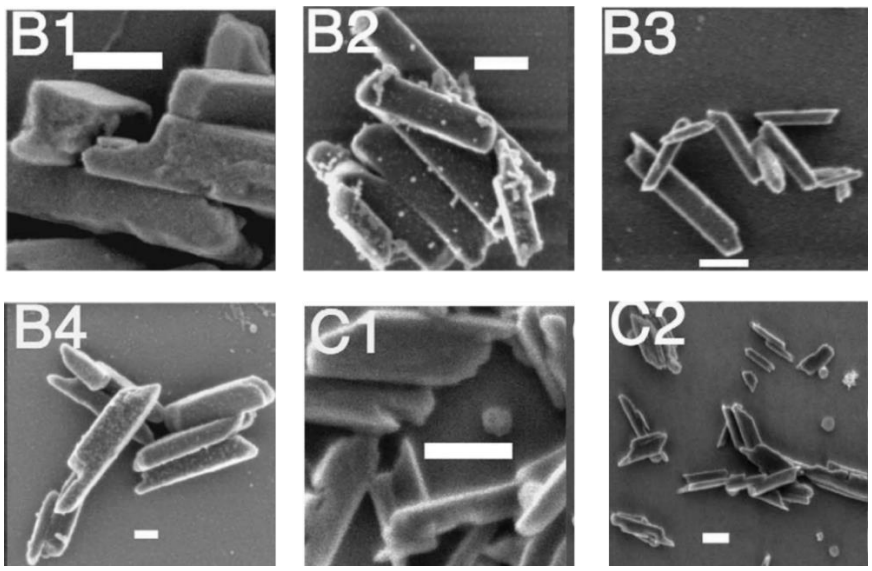

Figure 1.8. Scanning electron micrographs of haemozoin isolated from various *Plasmodium* clones showing morphological homogeneity. *Plasmodium* strains **(B1)** 3D7, **(B2)** HB3, **(B3)** Dd2, **(B4)** 3B-D5 and **(C1,2)** *Plasmodium vivax*. Scale bar represents 200 nm. Reprinted from Molecular and Biochemical Parasitology, 130, Noland *et al*. The shape and size of haemozoin crystals distinguishes diverse *Plasmodium* species, 91-99, Copyright © 2003, with permission from Elsevier.[130]

Over the past decade, HDP has been implicated as a potent mediator in the conversion of Fe(III)PPIX to haemozoin. HDP was first identified, characterised and recombinantly expressed by Jani *et al* and was reported to be responsible for haemozoin formation within the malaria parasite.[131] Immunoelectron microscopy studies of parasitised erythrocytes treated with gold-conjugated antibodies illustrated that early ring stage parasites first exported HDP to the host cytosol after which this protein was detected in close proximity with haemozoin within the DV and also localised in transport vesicles containing haemoglobin, thereby marking a novel trafficking route to the potential site of activity (Figure 1.9 a-c). Isothermal titration calorimetric investigations demonstrated that recombinant HDP has a high binding affinity to haem with a reported K_d of 80 nM which was at least four times higher than that reported for HRP II and bound 2.7 haem molecules.[132]

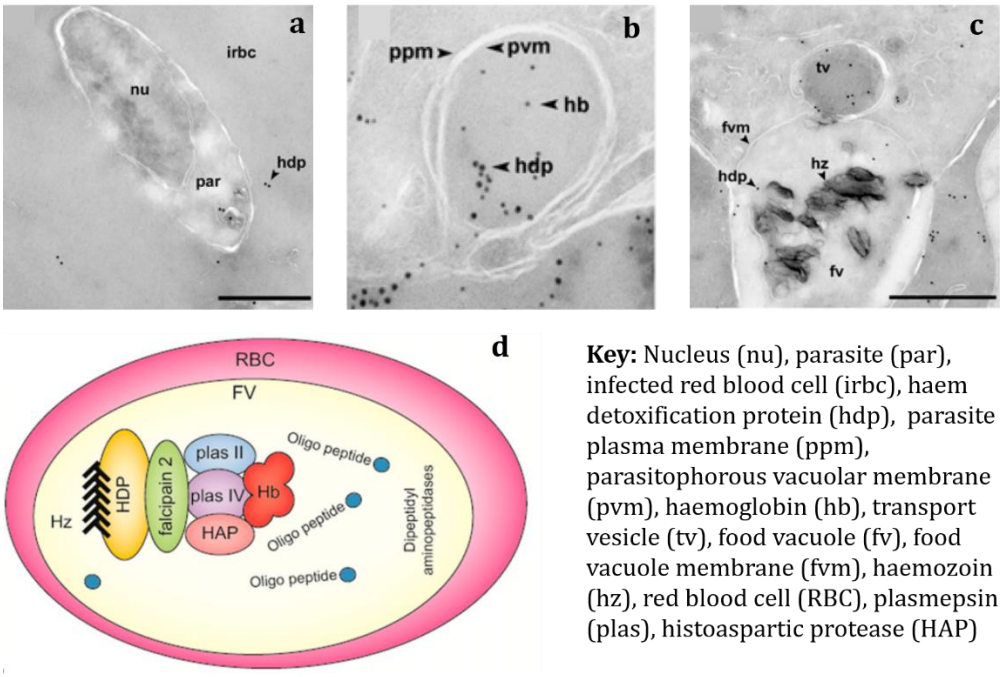

Figure 1.9. Trafficking and proposed enzymatic association of HDP in *P. falciparum*. Immunoelectron micrographs showing **(a)** HDP released into the erythrocyte cytosol in an early ring stage infected cell, **(b)** HDP is being engulfed along with haemoglobin through the cytostome and **(c)** transport vesicles appear to traffic HDP to the DV where it appears to be in close proximity to haemozoin. Reprinted by permission from Creative Commons: PLoS Pathogens, Jani *et al*, Copyright (2008).[131] **(d)** Schematic of the proposed multienzyme complex responsible for haemoglobin degradation and haemozoin formation within the DV of the malaria parasite. Reprinted from PNAS, Chugh *et al,* Copyright (2013).[51]

Furthermore, it was reported that, in an assay using enzymatic-like concentrations of protein in combination with a molar excess of haem, β-haematin formation rapidly progressed in a concentration-dependant manner where at least 75% of β-haematin was produced within the first 20 min and the reaction reached completion within an hour.[131] HDP-mediated crystals were characterised by pXRD and were reported to exhibit similar dimensions to those of haemozoin, indicating that both of these crystals belong to the same unit cell and have the same structure. Indeed, native HDP obtained by immunoprecipitation was also reported to successfully promote β-haematin formation under the same conditions used for recombinant protein, suggesting that this protein could play a similar role *in vivo*.

As mentioned earlier, a 200 kDa multienzyme complex was proposed to be responsible for catalysing the process from haemoglobin degradation to haemozoin formation in the DV. Coimmunoprecipitation studies by Chugh *et al* identified this complex to comprise a

range of cysteine and aspartic proteases as well as HDP which appeared to be in association with haemozoin in the DV as illustrated in Figure 1.9d. This model proposes that haemoglobin binds to the protein complex and undergoes digestion by the endopeptidases and consequentially released haem is converted to haemozoin through the action of associated HDP. Additionally, Chugh *et al* reported the strong association of HDP and falcipain II which were efficient in haemoglobin to haemozoin formation. Notably, each individual component was itself unsuccessful in haemoglobin to haemozoin formation and showed that the association of each with the other was a necessity in this process.[51]

Recently, studies by Kapishnikov *et al* reported an *in vivo* rate of haem crystallisation using a combination of correlative cryo X-ray fluorescence microscopy and cryo soft X-ray tomography.[133] Together, these advanced complementary techniques enabled quantitative measurements of haem at various locations within the malaria parasite through the generation of iron X-ray fluorescence maps which were visualised at the ultrastructural level by three dimensional tomography images whilst imaging parasites in their native state. They reported an estimated *in vivo* rate of ≈ 6 900 haem units/s which appeared to be in agreement with reported *in vitro* rates of haem crystallisation catalysed by HDP in acetate buffer (pH 5.2) of 10 000 haem units/s while that produced in octanol-saturated citrate buffer (OSCB) (pH 4.8) is only > 3200 haem units/s.[131, 134] Given that if the rate of haemoglobin degradation exceeded that of haemozoin formation the resultant spontaneous accumulation of free haem would be destructive to the parasite, there would need to be a certain degree of congruity between these two rates. Considering that Chugh *et al* reported the rate of haemoglobin digestion by falcipain II to exceed that of crystal formation and the strong association of this protease with HDP, is has been suggested that such homeostatic balance may be realised through this mechanism. Taken together, Kapishnikov *et al* have postulated that non-crystalline haem remains in the DV in the form of haemoglobin and, upon degradation, undergoes haemozoin formation catalysed by HDP. Even though HDP has been reported to produce β-haematin at the above-mentioned rate, it should be noted that OSCB does not mimic biological membranes that constitute the DV and octanol is not a lipid; therefore, this system does not represent an accurate model thereby making this argument inconclusive.

Transcriptomics studies have shown that HDP is actively transcribed through all stages of the parasite life cycle indicating that this protein is both crucial to survival and has different functions.[135] Several HDP orthologues are present across other *Plasmodium* species; however, these exist with only a 60% similarity in sequence identity. HDP is a 25 kDa polypeptide comprising 205 amino acids with high *Asn* and *Leu* content of approximately 11% and a *His* content of 4%. Notably, this protein exhibits no similar homology to any known haem-binding proteins. The carboxyl terminus represented by amino acid positions 88 to 205 contains a conserved fasciclin 1 domain (FAS 1). The FAS 1 domain is known as an ancient extracellular structural domain which is implicated in various functions such as cell adhesion, intracellular trafficking and endocytosis and extends to all kingdoms of life.[136]

Building on the premise of HDP as a potent mediator of haemozoin formation, Nakatani *et al* investigated the amino acid residues that could potentially be responsible for this activity in an attempt to elucidate the reaction mechanism of HDP.[137] Since *His* residues have been previously found to have a high affinity for haem binding and native HDP comprises nine *His* residues, the role of each *His* was explored by single point mutation studies. Each *His* was replaced with *Ala* thus generating nine different mutants including a variation in which all nine *His* residues were replaced forming the 9HA mutant. The role of each of the generated mutants was investigated by measuring the activity using a β-haematin formation assay as well as by spectroscopy.

Notably, the most influential changes reported were for the H122A mutant which exhibited a 50% decrease in β-haematin formation activity when compared to that of the wild-type (Figure 1.10a) and was observed to display a very broad Soret band representing a 15 nm shift in the electronic spectrum when compared to wild-type HDP. This broad shift was indicative of His122 likely being an axial ligand to the haem moiety in HDP. Significant decreases in β-haematin activity were reported for H172A, H175A and H197A mutants with the largest decrease observed for H172A and distinguishable spectral changes recorded for H175A, whereas activity for all five other mutants remained similar to that of the wild-type. Therefore, Nakatani *et al* reported that these four *His* residues are at the active site of the protein and that their main role was to properly align haem moieties in the active site of HDP which encourages β-haematin formation. Earlier work by the same group reported that recombinant HDP binds two haem molecules per

protein unit, indicating the presence of two binding sites.[138] Therefore, Nakatani *et al* proposed that His122 and 175 were essential for anchoring haem whereas His172 and 197 were important in ensuring proper alignment of the haem groups to maximise interaction to encourage dimer formation within the hydrophobic core and initiate seed nucleation as detailed in Figure 1.10b. However, it is important to note that the 9HA mutant exhibited only a 50% decrease, an astonishing result which appears to be rather problematic because the mutant protein was still able to synthesise β-haematin even though it contained no *His* residues that were thought to be essential, thus creating doubt around this proposed mechanism.

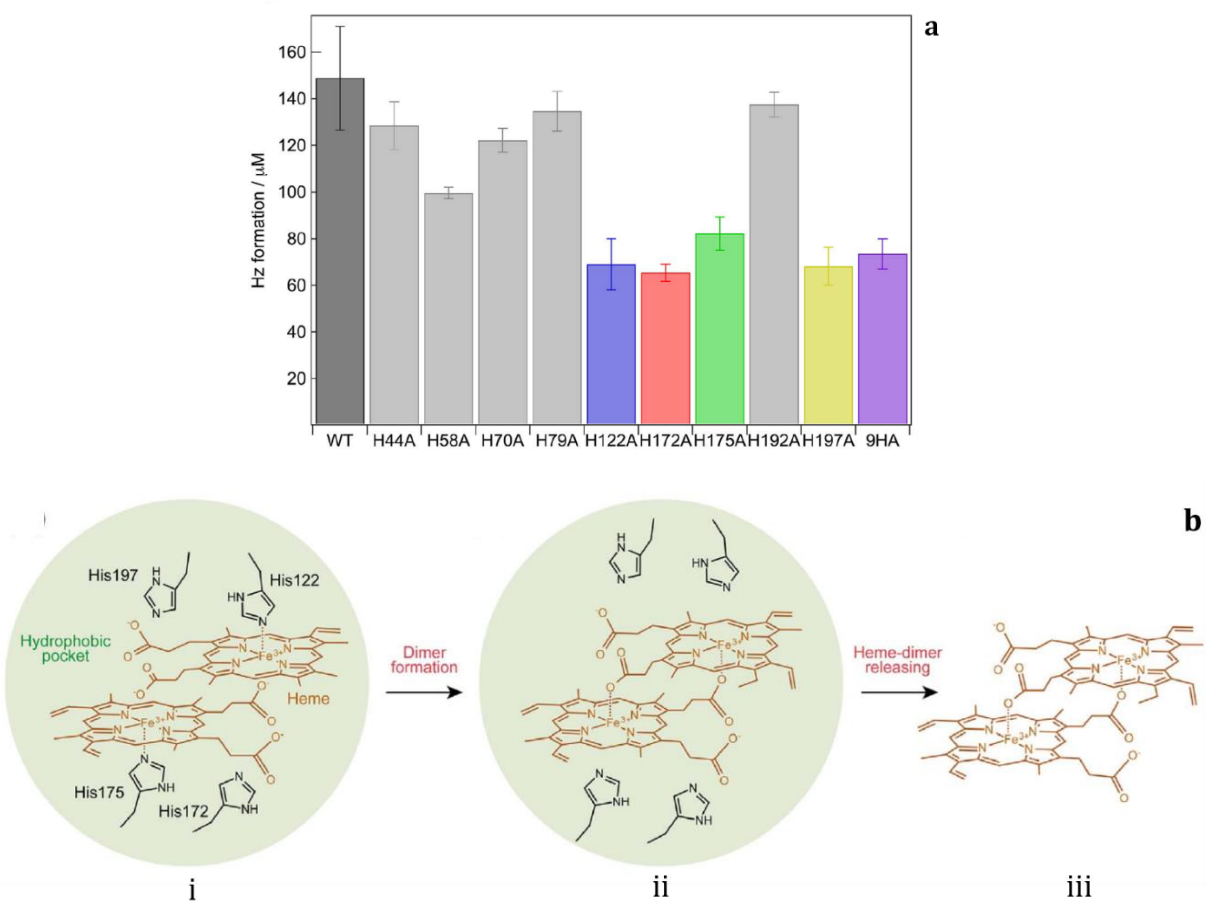

Figure 1.10. Proposed role of *His* residues in haemozoin formation. (a) β-haematin formation activity of recombinant HDP wild-type (WT) and mutant proteins. **(b)** Proposed reaction mechanism for HDP mediated haemozoin formation through essential *His* residues. (i) His122 and His175 anchor each haem molecule into the hydrophobic pocket of HDP, while His197 and His172 bring about correct alignment; (ii) once properly aligned, the coordination bonds between haem moieties form and finally (iii) newly formed dimer is released serving as seed to initiate crystal growth. Reprinted by permission from Creative Commons: Nature Scientific Reports, Nakatani *et al*, Copyright (2014).[137]

1.6.4.2. Lipids

The influence of lipids on haemozoin formation in *P. falciparum* has evolved as a promising potential mediator or catalyst of crystal formation. The hypothesis proposing the involvement of lipids began in 1995 with a study by Dorn *et al* where parasite lysate that was boiled and treated with protease was still successful in promoting β-haematin *in vitro*.[122] Additionally, this study also demonstrated that haemozoin and pre-formed β-haematin encouraged crystal formation. Taken together, Dorn *et al* proposed that haemozoin formation could be viewed as an auto-catalytic chemically driven process. Thereafter, Bendrat *et al* argued that this process was actually initiated by lipids present in the parasite lysate and pre-formed haemozoin which provided a site for crystal nucleation thereby calling into question the autocatalytic theory and sparked further comprehensive investigations into lipids as the driving force behind haemozoin formation *in vivo*.[139] Subsequently, Dorn *et al* demonstrated that acetonitrile extracts of trophozoite as well as uninfected erythrocyte lysate in a protein-free medium promoted rapid β-haematin formation *in vitro* thereby supporting the idea of lipid involvement in crystal formation.[140] Notably, a comprehensive study reported by Fitch *et al* identified at least 70% of the molecules responsible for β-haematin formation were concentrated in chloroform extracts of lysate obtained from infected erythrocytes.[141] Interestingly, the remaining residue exhibited no activity towards crystal formation. Fitch *et al* identified monooleoylglycerol as the model lipid which co-precipitated with Fe(III)PPIX in an acidic buffer system and successfully formed β-haematin. Additionally, dioleoylglycerol and certain detergents were found to be active whereas saturated fatty acids, trioleoylglycerol and cholesterol were found to be inactive.

In 2004, Palacpac *et al* demonstrated that mature trophozoite stage parasites displayed enhanced synthesis and accumulation of triacyglycerols (TAG).[142] Using immunofluorescence microscopy, they reported the stage-dependant development of lipid bodies in close proximity to the nucleus and the PVM. In contrast, studies by Jackson *et al* showed that parasites treated with Nile red dye and imaged by fluorescence and electron microscopy were observed to contain prominent spherical lipid rich bodies a few nanometres in diameter and localised in close association with the DV.[143] Lipid analysis indicated that these bodies consisted of neutral lipids, comprising mainly di- and triacylglycerols. Thereafter, a combination of mono-, di- and triacylglycerols were

reported to be effective mediators of β-haematin formation suggesting that neutral lipid bodies or their precursors could be involved in the haem detoxification pathway. The intimate association of neutral lipid bodies with haemozoin in the DV and the formation of its synthetic counterpart through various glycerolipids suggested that the lipid bodies may play a prominent role in haemozoin formation within the parasite. Subsequently, Coppens and Vielemeyer visualised electron dense lipid bodies within mature parasites stained with Malachite green.[144, 145] Remarkably, haemozoin crystals were found apparently enveloped by neutral lipid bodies as illustrated in Figure 1.11 alluding to the idea that lipid bodies are key in haem detoxification within the malaria parasite. This study, for the first time, illustrated the direct localisation of haemozoin and lipid bodies within the parasite which led to a comprehensive study by Pisciotta *et al* into the role of neutral lipid bodies in haem crystallisation which transformed the mechanistic understanding of haemozoin formation.[146]

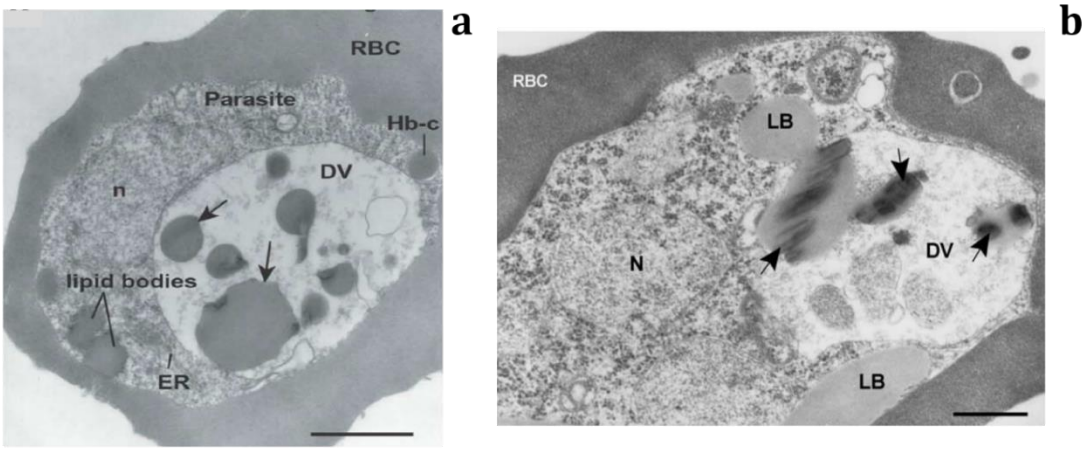

Key: Endoplasmic reticulum (ER), mitochondrion (m), nucleus (n), red blood cell (RBC), digestive vacuole (DV), haemoglobin containing vesicle (Hb-c) and lipid body (LB).
Scale bars represents 0.25 μm and 0.5 μm for a and b respectively.

Figure 1.11. Transmission electron micrographs of parasitised erythrocytes treated with Malachite green. (a) Lipid bodies appear electron dense and located within the DV and at the parasite periphery. Reprinted from Molecular and Biochemical Parasitology, 135, Vielemeyer *et al*, 195-207, Copyright (2004), with permission from Elsevier.[144] **(b)** Haemozoin appears encapsulated by lipid bodies within the DV as indicated by the black arrows. Reprinted from International Journal for Parasitology, 35, Coppens and Vielemeyer, 597-615, Copyright (2005), with permission from Elsevier.[145]

Trophozoite-stage parasitised erythrocytes were stained with Malachite green and fixed with glutaraldehyde prior to ethanol washes and imaged by TEM. Electron dense lipid

spheres devoid of any membrane bilayer were observed to envelop haemozoin crystals within the DV (Figure 1.12a, b), similar to that reported by Coppens and Vielemeyer, and were termed lipid nanospheres.[145, 146] Previously, these lipid structures were not easily visualised because of chemical processing during fixation; therefore, the inclusion of Malachite green was to preserve any potential lipids present in the parasite and maintain their structure. Lipid extracts obtained through sucrose cushion centrifugation of haemozoin were analysed by thin layer chromatography (TLC) and mass spectrometry (MS). Purified haemozoin was analysed for protein content by gel electrophoresis. There appeared to be no detectable proteins in this fraction (Figure 1.12c) which called into question the postulated role of proteins discussed earlier.

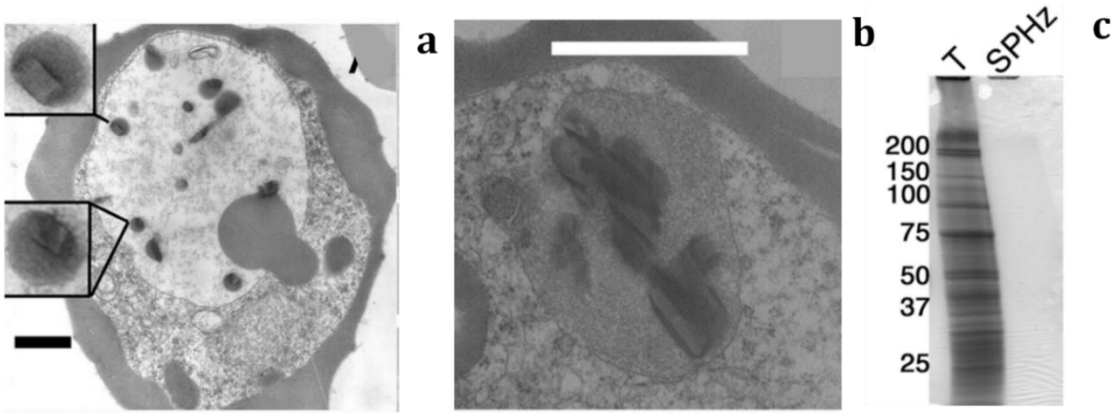

Key: Saponin-purified trophozoites (T) and sucrose-purified haemozoin (SPHz).
Scale bars represents 1 µm.

Figure 1.12. Distribution of lipid nanospheres and protein with respect to haemozoin. (a) Early stage trophozoite with several small haemozoin crystals each surrounded by what appears to be a lipid nanosphere. The inset shows no distinct membrane surrounding the lipid nanospheres. **(b)** Mature trophozoite containing bigger crystals surrounded by a thinner lipid sphere. **(c)** Parasite lysate and haemozoin corresponding to approximately 10×10^6 parasites separated by SDS-PAGE and stained with Coomassie Blue shows no trace of proteins associated with haemozoin in contrast to the abundance seen in trophozoites. Reprinted from Biochemical Journal, 402, Pisciotta *et al*, 197-204, Copyright (2007), with permission from Portland Press.[146]

TLC analysis of lipid content following a two-phase separation indicated that haemozoin-associated lipids comprised predominantly monoacylglycerols with substantial amounts of triacylglycerols and phosphatidylethanolamine and smaller amounts of diacylglycerols. MS analysis following the derivatisation of lipids into fatty acid methyl esters (FAMEs)

identified mono-stearic (MSG) and mono-palmitic glycerol (MPG) to be the principle components of haemozoin associated lipids and surprisingly neither mono-oleic glycerol (MOG) nor mono-linoleic glycerol (MLG) were identified. Pisciotta *et al* reported a neutral lipid blend comprising MPG/MSG/DPG/DOG/DLG in a 2:4:1:1:1 volume ratio which represented the various lipids found associated with haemozoin.[146] The synthetic neutral lipid blend was reported to effectively catalyse the formation of β-haematin with the monoacylglycerols being the most potent catalyst from the neutral lipids found.

Studies by Egan *et al* investigating β-haematin formation under biomimetic conditions demonstrated that crystal formation proceeds rapidly at the lipid/water interface providing mechanistic insights into β-haematin formation thereby corroborating the lipid theory.[147] Octanol/water and pentanol/water aqueous buffered systems (pH 4.8) were shown to produce β-haematin within 30 min at 37°C. A range of lipids were explored for their efficiency at promoting crystal formation which unequivocally demonstrated that, under physiologically-relevant conditions, these lipids are able to mediate formation at rates that are probable *in vivo*. Further insights into crystal nucleation at the lipid/water interface was provided by Hoang *et al* where synthetically produced lipid particles mimicking neutral lipid bodies in the DV of the malaria parasite demonstrated that β-haematin crystals localise at the interface of these lipid particles and water.[148] This study suggested that β-haematin crystallisation proceeds via epitaxial nucleation at the lipid water interface which directs nucleation, orientation and size of crystals formed.

Furthermore, Hoang *et al* demonstrated that Fe(III)PPIX rapidly accumulated within these synthetically produced lipid particles and that the neutral lipid blend reported by Pisciotta *et al* lowered the activation energy of β-haematin formation thereby supporting the role of lipids in haemozoin formation *in vivo*.[149] This was further supported in an independent study reported by Ambele *et al* where the neutral lipids specifically associated with haemozoin were more than adequate at mediating β-haematin formation and various biologically-relevant ions that are likely present within the parasite DV are unlikely to impact the rate at which haemozoin formation proceeds.[150]

An investigation into the orientation and location of haemozoin within the DV was carried out by Kapishnikov *et al* using a combination of cryogenic soft X-ray tomography (SXRT) and three-dimensional electron microscopy.[151] Small, developing crystals were observed to align side by side along the inner membrane of the DV in early stage trophozoites

(Figure 1.13a). As the parasite matured it metamorphosed from a flat disk-like shape into a more spherical shape with larger, more prominent crystals found clustered in the centre of the DV while younger crystals remained along the inner membrane (Figure 1.13b). Since the crystals appeared to perfectly align in a specific orientation and no lipid bodies or nanospheres were detected in this study, Kapishnikov *et al* argued against the hypothesis that haemozoin localises within lipid bodies stating that if this were the case then no order or alignment would be possible within this organelle. Kapishnikov *et al* also suggested that haemozoin nucleation occurred within the aqueous rather that the lipid phase.

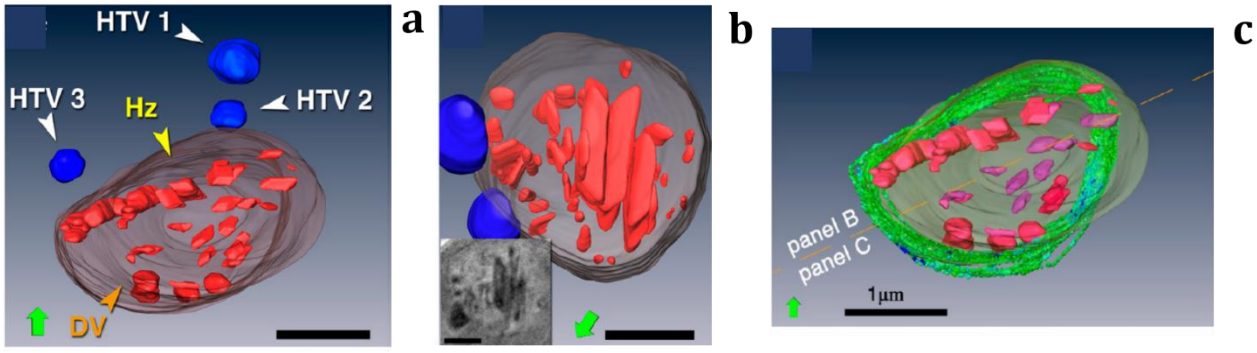

Key: (a and b) Haemoglobin transport vesicle (HTV, blue), haemozoin (Hz, red), digestive vacuole (DV, maroon). **(c)** Haemozoin close to the membrane (red), central haemozoin (purple) and lipid bilayer comprising thicker (blue) and thinner (green) areas. All scale bars represents 1 µm.

Figure 1.13. Orientation of haemozoin at the DV membrane represented by 3D reconstructions and surface renderings. (a) DV of an early trophozoite stage parasite showing alignment of haemozoin with the inner membrane. **(b)** DV of a mature trophozoite stage parasite with larger haemozoin in the centre and smaller crystals at the periphery. Reprinted from PNAS, 109, Kapishnikov *et al*, 11188-11193, Copyright (2012), with permission from National Academy of Sciences.[151] **(c)** 3D colour coded view showing the variation in thickness of the DV membrane. Reprinted from Langmuir, 29, Kapishnikov *et al*, 14595-14602, Copyright (2013), with permission from ACS.[152]

Quantitative analysis of the SXRT images allowed for the measurement of the thickness of the DVM.[152] Kapishnikov *et al* reported that the DVM was predominantly a bilayer 4.2 nm and the remaining membrane comprised patches ≈ 8 nm thick indicating a double bilayer (Figure 1.13c). It was therefore suggested that the observed change in membrane thickness may comprise mono- and diacylglycerols which expose appropriate hydroxyl or amide head groups which allow for the correct stereochemical interaction with the

crystal face thus catalysing haemozoin nucleation. More recently, Ambele *et al* showed that, even though parasitised erythrocytes were stained with Malachite green and imaged by TEM (Figure 1.14 a, b), no distinguishable lipid droplets were observed within the DV or in association with haemozoin, however, crystals appeared to align parallel.[153] Haemozoin appeared to lack any defects in crystal structure as well-ordered lattice fringes were observed (Figure 1.14c).

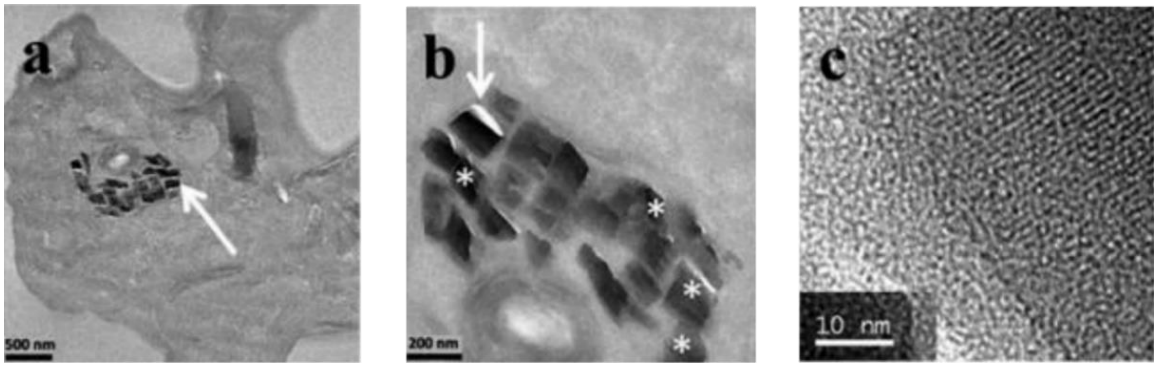

Figure 1.14. Transmission electron micrographs of mature parasitised erythrocyte stained with Malachite green. (a) Haemozoin crystals appear to be aligned within the DV. **(b)** Enlargement of a shows crystals in close association with the inner membrane and at an angle (*). No lipid bodies present. **(c)** Ordered lattice fringe corresponding to crystal indicated by white arrow in b. Reprinted from Crystal Growth and Design, 13, Ambele *et al*, 4442-4452, Copyright (2013), with permission from ACS.[153]

In addition to proteins and lipids, β-haematin formation can readily proceed in the presence of an array of diverse mediators which include pre-formed β-haematin crystals, DMSO, polyethylene glycols, detergents and high concentrations of acetate.[154-156] Crystal formation influenced by diverse non-physiological and physiological mediators raises questions regarding the evidence supporting the above-mentioned protein and lipid theories. The approaches employed thus far encompass substantial limitations which include but are not limited to the high probability of contamination of haemozoin from other cellular compartments and the lack of specificity in the exact role these biomolecules exhibit in biomineralisation. The presence and role of biomolecules in biomineralisation processes in other non-related organism is well established and recent studies have shown the occlusion of various biomolecules and incorporation of chemical additives into biominerals.[157-159] Gaining insights into the biomolecules intimately associated with haemozoin would considerably reduce the list of potential mediators and

point to the actual mechanism of formation. In this regard, there are very limited studies that have focused on investigating the surface of haemozoin, most of which have explored the effect of crystal size and morphology. Very recently, using X-ray photoelectron spectroscopy (XPS) and MALDI-TOF mass spectrometry, Guerra *et al* reported the surface of haemozoin and β-haematin to strongly adsorb various molecules.[160] The exact identity of the adhering molecules remains unknown but evidence of an excess of nitrogen atoms suggested the presence of peptide fragments. Bearing in mind that haemozoin is quite adhesive, following protease treatment during washing of the crystals, the association of such fragments may not be surprising. Identifying the biomolecules associated with haemozoin would be indicative of the role these play in crystal formation. To date, there have been no studies that have explored the occlusion capabilities of haemozoin or unequivocally demonstrated the biomolecules associated with haemozoin and promotion of crystal formation at physiological amounts within the DV.

1.7. The *omics* revolution

1.7.1. Overview

All forms of life comprise an intricate network of molecular interactions which ultimately determines existence. Irrespective of whether these are dependant on large molecules such as genes and proteins or small molecules such as sugars, lipids or amino acids, the dynamic flow and balance between these regulate functioning from the basic cellular level to tissues, organs and inevitably the organism as a whole. The investigation of molecular networks that link to diverse biochemical pathways provides a deeper understanding of the biological mechanisms and functions of various organisms. This in turn directly impacts health and disease. Unravelling the pathophysiological factors that are detrimental to human health are key driving forces to biological and clinical research; however, it has been argued that the historically-used reductionist approach has resulted in gaps in thinking and sometimes inadequate, contentious hypotheses relating to important processes that impact health.[161]

By contrast, the rapidly evolving *omics* fields offers a holistic perspective of the molecules that form the foundation of various cells, tissues and organs since it considers complex systems as a whole. The *omics* field focuses on the comprehensive characterisation and

quantification of the collection of biological molecules that contribute towards the structure and dynamic functioning of an organism. There are four major branches of the *omics* cascade comprising genomics, transcriptomics, proteomics and metabolomics where each respectively represents the possibility of what can occur, what appears to occur, the molecules that actually drive action and finally what has occurred within a biological system (Figure 1.15), therefore making this a discovery-science based approach.

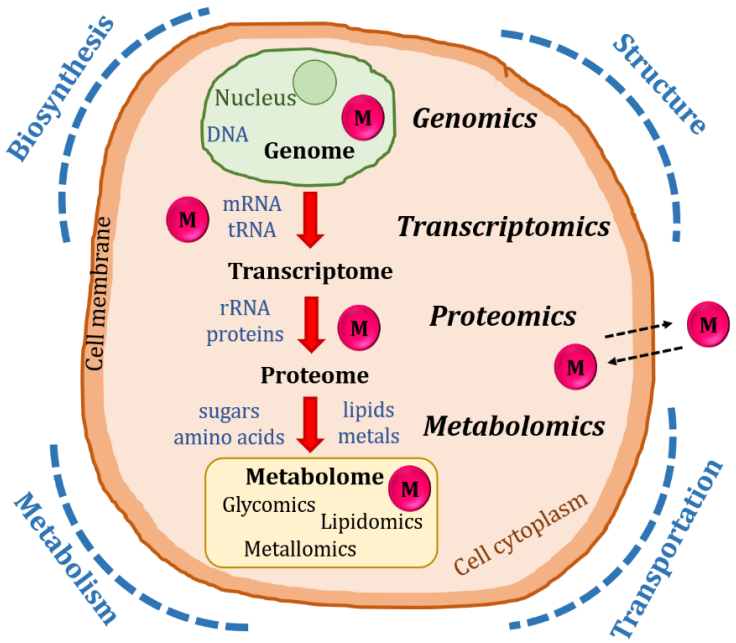

Figure 1.15. Schematic representing the evolution of *omics* disciplines from the genome to gain a global profile of an entire cell or biological system. Key: Metal ions (M).

The genome, forming the core of all biology, was a termed coined by a German botanist, H. Winkler, in 1920 and was the first *omics* discipline to emerge.[162] Genomics focuses on the study of the entire contents of the nucleus as well as all nucleotides and genes and their function as opposed to genetics which investigates single genes in isolation. The transcriptome, a term first introduced in the 1990s, builds on from the genome as it focuses on the array of messenger RNA molecules produced from the genome based on expression and circumstances.[163] The proteome, a term coined by M. Wilkins in 1994, describes the entire set of proteins that are expressed within an organism at a specific time in response to environmental exposure.[164] Proteomics focuses on the study of proteomes and their functions and is a discipline that holds a very central role in that it

addresses the phenotype complement of any organism since proteins are macromolecules that directly impact the structure and function of cells which is constantly changing. Finally, the metabolome, a term first used in 1998 during a functional study on the yeast genome, focuses on the array of small molecules present within a biological system.[165] These small molecules are representative of those endogenously-produced building blocks involved in cellular metabolism and are not limited to lipids, sugars, nucleotides and vitamins but also exogenous molecules not naturally synthesised by the organism such as toxins, food preservatives and drugs.

Omics encompasses multidisciplinary techniques and advanced technologies that span various fields used to complement each other in order to gain a holistic view of the system under investigation. In infectious diseases such as malaria, there is a need to better understand the intricate host-pathogen interactions in order to obtain mechanistic insights. The combination of omics with advanced technology enables health-related research to proceed using a comprehensive, integrative approach at unprecedented rates. Since macromolecules are complex and information-rich, these advances have occurred hand-in-hand with the rise of information technology. Using traditional biochemical approaches and techniques are very time consuming compared to omics approaches and do not offer the efficiency, accuracy and throughput. The field has therefore evolved considerably since the initial theories leading to the current omics discipline were first proposed in the 1950s (Figure 1.16).

Technologies that enable this approach in the field of genomics have developed in a revolutionary way since the discovery of the structure of DNA, ranging from Sanger sequencing, DNA microarrays to next-generation sequencing (NGS) which also leads into transcriptomics.[166-168] Proteomics has evolved and is now on par in terms of sensitivity and experimental pipelines with that of genomics. Since proteins bridge the gap between genetic information and the structural capacities which govern cellular processes, proteomics-based research is essential in gaining insights into the potential biomarkers involved in diseases. Proteomic-based technology has evolved from hyphenated mass spectrometry-based techniques with the initial soft ionisation technologies to the present array of technologies encompassing label-free vs isotopic labelling and qualitative vs quantitative approaches.[169, 170] Even though various types of MS form the core of metabolomics, the accompaniment of bioinformatics tools is an essential aid in data

analysis and interpretation. The major omics techniques are now quite mature. On the other hand, the various sub-domains such as lipidomics, metallomics and glycomics are still at their infancy in comparison, and further development and refinement are needed.

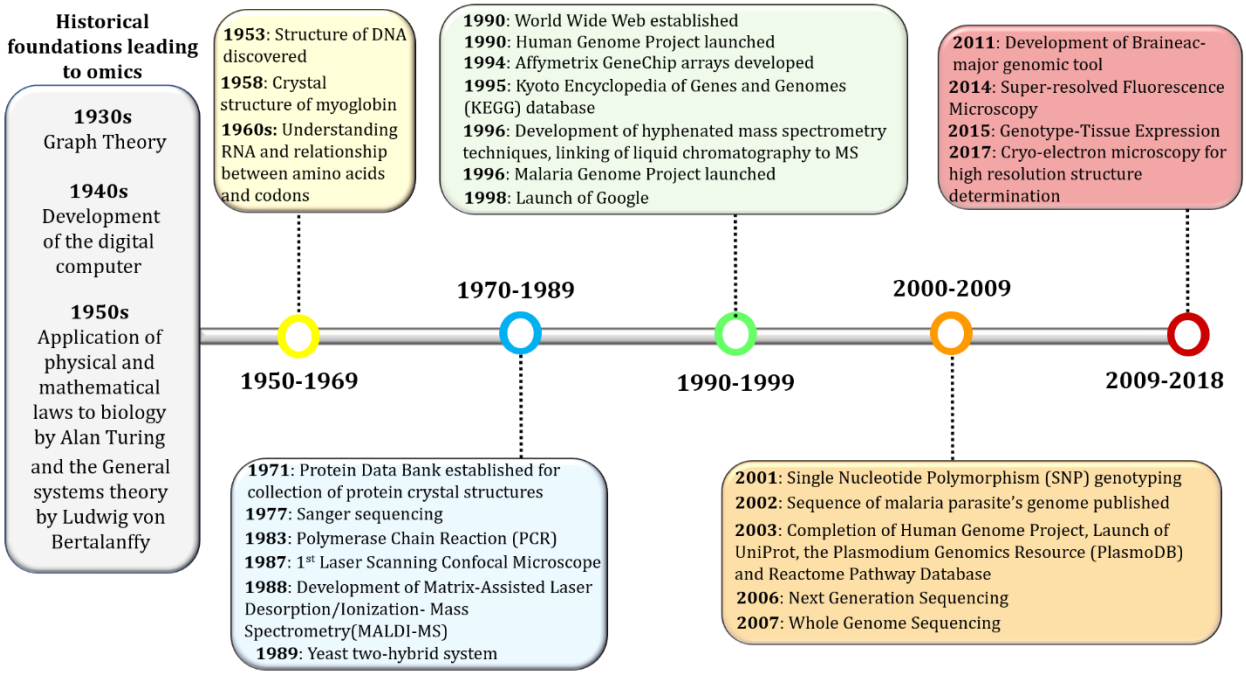

Figure 1.16. Timeline illustrating the progression of technological advancements and key discoveries. The grey block (far left) represents the ideas and roots that laid the foundation for development of the omics field prior to 1950**.** Time periods denoted by coloured circles represents the integration of several disciplines and advances in bioinformatics.

Overall, the main aims of establishing and employing omics centres around employing an integrative and iterative approach to generate multidimensional data that can be used to identify key molecules and process unique to biological processes and chemical pathways. Thus far, integrative omics has established a prominent role in human-related research pertaining to Mendelian diseases, diabetes, cancer as well as bacterial- and viral-related infectious diseases.[171-174] Since mapping of the *P. falciparum* genome sequence in 2002, genomic and proteomic based research on the malaria parasite has gained considerable momentum.[135] Due to the parasite's ability to evolve rapidly with consequent emerging resistance to current antimalarial therapy, a more holistic approach is beneficial to gain greater insights into the survival mechanisms of this pathogen. A broad discussion relating to three omics domains and their application to malaria will be discussed further.

1.7.2. Proteome of intraerythrocytic *P. falciparum*

The genome can be regarded as the blueprint of life as each unique sequence provides information about the genetic potential of an organism. Translating genetic information into cellular characteristics and function is key to elucidating essential physiological processes. Proteins are complex organic molecules that comprise chains of polypeptides of varying lengths where each peptide contains unique permutations of amino acids. These large molecules are regarded as the workhorses of the cell and are responsible for vital life processes in their dynamic roles as transporters, enzymes, messengers and structural components. The large-scale identification, quantitation and characterisation of the set of proteins within a biological system with the aid of various omic technologies has led to the field of proteomics developed in the mid-1990s.[175]

Following the completion of whole genome sequencing of *P. falciparum*, proteomic and transcriptomic investigations into the malaria parasite has developed along with technological advances of the field.[135] Attempts to better understand malaria parasite biology began with a study which used two-dimensional gel electrophoresis to investigate the changes in the parasite protein profile in response to treatment with mefloquine.[176, 177] However, data generation was restricted with these earlier techniques as target protein identification was not easily achieved and has evolved remarkably over the past decade. The past limitations strongly influenced the foundational basis of current proteomic-based methods. Even though *Plasmodium* is a unicellular pathogen, it undergoes a range of morphological and biochemical changes as it alternates between various hosts and intra- vs extracellular environments, therefore indicating the complexity of the protein expression profile that accompanies such changes.

Soon after completion of the genome sequence, two groups reported the first proteomic analyses of *P. falciparum* propelling further in-depth proteomic research efforts. By employing multidimensional protein identification technology (MudPIT), Florens *et al* identified more than 2 400 proteins across four stages of the parasites lifecycle demonstrating marked differences in the respective proteomic components following characterisation into ten functional categories (Figure 1.17).[178] The majority of the proteome corresponded to hypothetical proteins indicating that more than 60% were uncharacterised. Complementary studies by Lasonder *et al* used a high-accuracy mass spectrometry proteomic approach to independently map the proteome of sexual and

asexual stage parasites.[179] Lasonder *et al* reported the identification of a total of 1 289 proteins of which 714 were unique to asexual stage parasites. Despite the limited technology and rudimentary approach to data analysis, these two seminal studies provided the first insights into variable antigenic protein expression and gene clustering events.

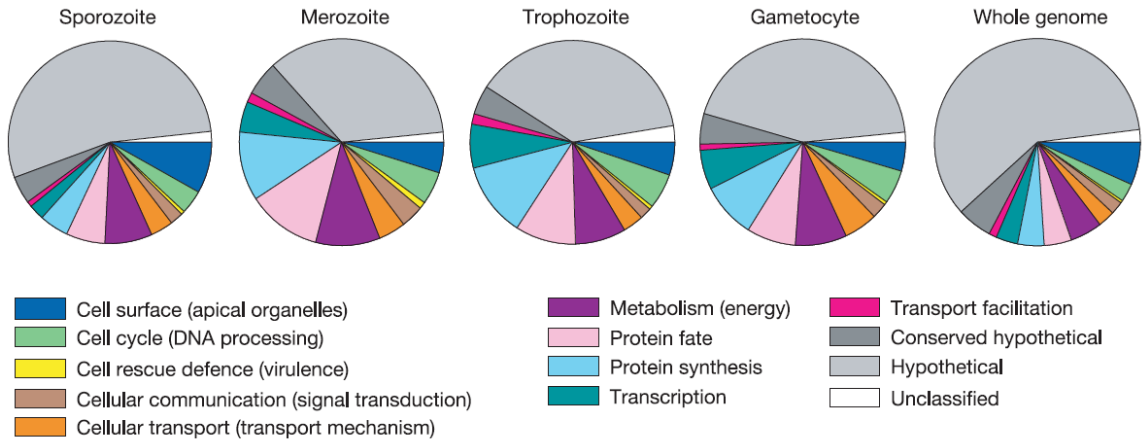

Figure 1.17. Graphical overview of proteins identified by MudPIT across four stages of the parasite's life cycle. Functional profiles of expressed proteins compared to the whole genome. Reprinted from Nature, 419, Florens *et al*, 520-526, Copyright (2002), with permission from Nature Publishing Group.[178]

Ultimately, proteomics provides detailed information of the specific proteins expressed within an organism at a particular point in time. It can give an idea of how the expression profile changes in response to various pharmacological effects which can lead to the identification of new therapeutic targets. For a dual-host pathogen like *Plasmodium*, the ideal strategy would be to find a solution that simultaneously targets multiple phases of the life cycle. Therefore, numerous proteomic investigations have been carried out to date as illustrated in Figure 1.18; however, most studies thus far have focused on the asexual stage with very little carried out on the liver and mosquito stages. Since the asexual stage is responsible for clinical symptoms associated with malaria and since there are well-established protocols to culture this stage *in vitro*, it is feasible to produce large sample sizes for analysis.

Proteomic studies associated with the whole organism have become unpopular due to the complexities involved at this large-scale level. A major concern is the loss of information

with this kind of experiment; low abundance proteins can be easily left undetected and, even if this does not occur, there still remain immense data processing challenges even though one may not have detected the complete protein data set. Therefore, exploring the sub-proteome of an organism is thought to provide a more useful and comprehensive profile of the proteins present.

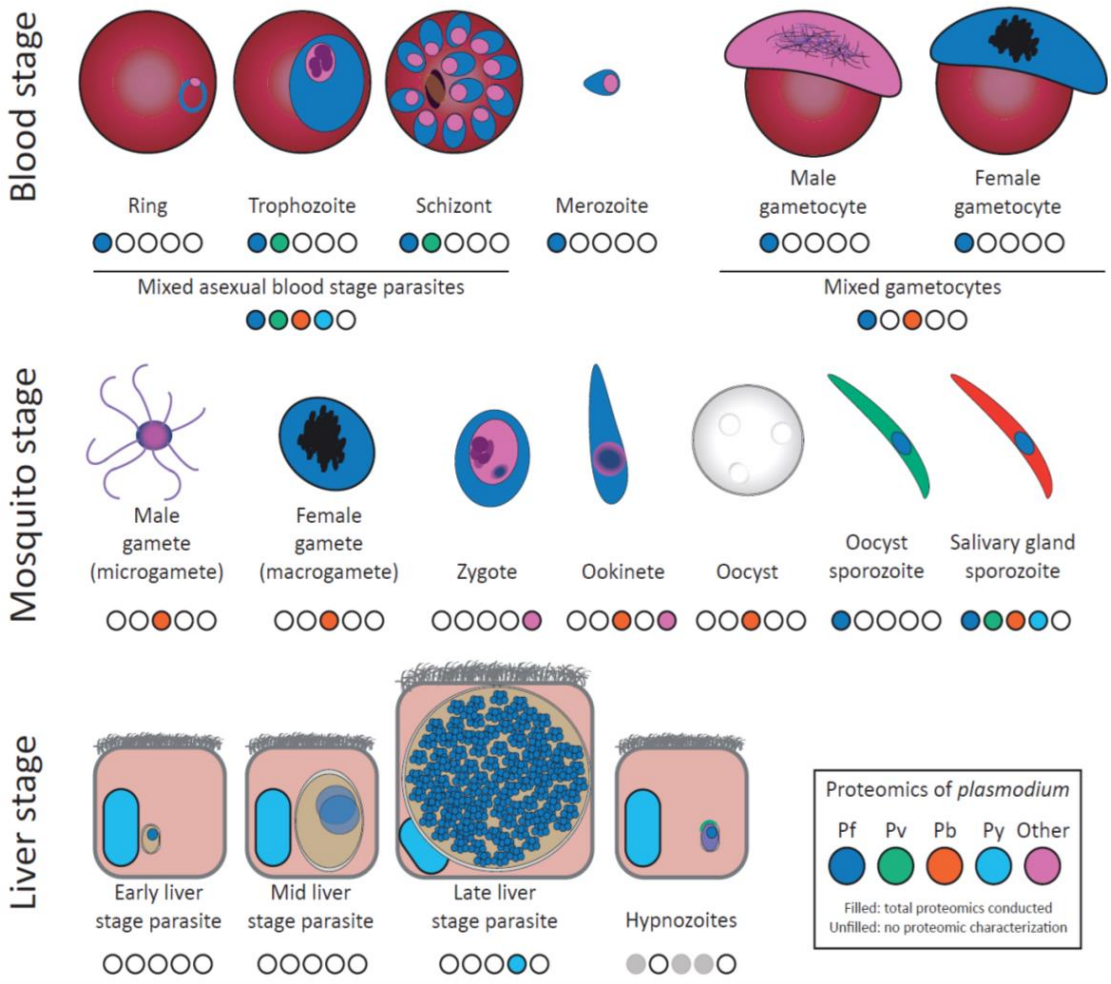

Key: *Plasmodium falciparum* (Pf), *Plasmodium vivax* (Pv), *Plasmodium berghei* and *Plasmodium yoelli*

Figure 1.18. Proteomic studies reported on major lifecycle stages across the various species of *Plasmodium*. In some cases, proteomic data representing a particular stage in the pathogen life cycle may have been obtained from a single study on a particular species. Coloured circles represent reports of global proteomics and empty circles represent no proteomic reports. Reprinted from Trends in Parasitology, 34, Swearingen and Lindner, 945-960, Copyright (2018), with permission from Cell Press.[180]

To date, there have been several studies focusing on the various sub-proteomes of the asexual stage of *P. falciparum* with leading efforts into proteomes corresponding to surface proteins, apicoplast, PV, nuclear material and phosphoproteomics to name a few.[180] Interestingly, there has only been a single study exploring the proteome of the DV reported by Lamarque *et al* in 2008.[181] Since proteins have been implicated in biomineralisation in other organisms as highlighted in Section 1.6.3. and haemozoin formation proceeds in the DV, any potential proteins involved in this process would ideally form part of the DV protein cohort. Therefore, current understanding of the DV proteome will be reviewed further.

The DV is an acidic organelle that plays a fundamental role in the pathophysiology of the malaria parasite. Not only is this the site of haemoglobin digestion but the consequent formation of haemozoin makes this organelle an ideal site for therapeutic action. Therefore, Lamarque *et al* undertook a study using SDS-PAGE and tandem mass spectrometry to profile the DV proteome by analysing a DV-enriched fraction of parasite material in which 116 proteins were identified. Since haemoglobin is the major component of erythrocytes and the DV is the final site of haemoglobin trafficking, it was not surprising that several known proteins and enzymes (plasmepsins I, II and IV, HAP, falcipain 2, M1-family aminopeptidase) unique to this process were identified. Additionally, a putative peptidase and aminopeptidase were also identified. Interestingly, expected proteins falcilysin, DPAP-1 and falcipain 3 were not detected in this study regardless of the fact that the gene expression levels reported to be as high as that of plasmepsin I.[182]

Several proteins, including Sar1, p24, Rab1, Rab2 and the ADP-ribosylation factor, were identified to be involved in vesicle biogenesis and vesicle-mediated trafficking processes. Three transporters unique to the PVM and PPM were reported to be in this enriched DV fraction, which probably formed part of the cytostome, emphasises the idea of cystotome-formed vesicles and their role in DV fusion and haemoglobin trafficking. Various metabolic enzymes as well as chaperone, surface and hypothetical proteins were identified in this study. The comprehensive protein list can be found in the original publication by Lamarque *et al*. These proteins suggest a continuous interplay between the DV and the surrounding parasite cytosol.

The multidrug resistance transporter, chloroquine resistance transporter, V-type H^+-ATPase, H^+-pyrophosphatase and three ATP synthases which were previously regarded as putative proteins in PlasmoDB database were identified in this study. The V-type H^+-ATPase and H^+-pyrophosphatase are of significant interest as these comprise two major proton pumps which function synchronously and that are responsible for maintaining the low pH of the DV.[183] However, two essential DV marker proteins, *N*-ethylmaleimide-sensitive factor, reported to be involved in vesicle trafficking, and CG2, shown to be located in the PVM, cytostome and DV, were not found in this proteomic analysis. Since haemozoin formation is an attractive target and proteins have been implicated in its formation, it is reasonable to assume that any protein exclusive to this process would unequivocally be present in the immediate site of haemozoin formation; namely, the DV. Notably, independent protease components comprising the hypothesised protein complex by Chugh *et al* was definitively detected within the DV. However, neither HRP II nor HDP was detected in the DV proteome or within the cohort of hypothetical proteins reported here. It has been suggested than less than 5% of HRP II content present within a parasitised erythrocyte actually makes its way to the DV, therefore suggesting that this may be below the detection limit of the techniques used.[128] If this were the case, a similar argument could be applied to the detection of HDP and that if either protein had a direct association with haemozoin, a concentrated form would allow for detection.

1.7.3. Lipidome of intraerythrocytic *P. falciparum*

Lipids, in contrast to genes, tend to fluctuate in their nature due to their intrinsic link to an organism's metabolism. In humans, these molecules are not only influenced by one's diet but also by the state of health as alterations in expression of genes related to their synthesis, structure and function have the ability to induce metabolic diseases such as cardiovascular disease, obesity and diabetes. The lipidome describes the complete set of lipids within a cell, tissue or organism and lipidomics, a new addition to the omics cohort, refers to the broad study of cellular lipid related pathways and interactions within a biological system.[184, 185] In 2003, Han and Gross introduced the field of lipidomics by interrogating the cellular lipidome using ESI/MS.[186] The complex and extensively diverse nature of lipids, due to their hydrophobicity and almost infinite permutations of fatty acid side chains, makes the unequivocal identification and quantitation of these biomolecules

quite challenging. One strategy in addressing these challenges is to first decide between whether the investigation at hand requires targeted or global lipidomic analysis where the former focuses on specific cell-signalling events as well as optimising known lipids and the latter provides a broad overview of molecular mechanisms, lipid pathways and has the potential for biomarker discovery by detecting every lipid species in a particular sample.[187] The experimental workflow that ensues is critical to a successful experiment and focuses on utilising a combination of different techniques to optimise output and ensure the highest level of precision and accuracy. Lipidomics workflow encompasses four main branches comprising (i) extraction, which is dependant on the lipid classes of interest, (ii) chromatographic separation by thin layer chromatography (TLC) or high-performance liquid chromatography (HPLC), (iii) detection and profiling using various ionisation techniques coupled to mass spectrometry and, finally, (iv) bioinformatic and statistical analysis of large data sets. With rapid technological advances in chromatographic separation and MS, methods have evolved that provide the high sensitivity needed to detect trace amounts of material. Nonetheless, as with proteomics-based data, accurate processing, analysis and in-depth understanding of immensely large datasets remains the Achilles heel of lipidomics.

In multicellular organisms, lipids are building blocks that serve as sources of energy storage and are involved in membrane biogenesis, cell-signalling pathways and play roles in the absorption of fat-soluble vitamins. However, lipids exhibit unique roles in the context of host-pathogen interactions. In malaria, invasion of the host erythrocyte results in the cell undergoing remodelling and structural organisation to accommodate the new entity present. The invasion process, recognition events, intracellular trafficking and egress all encompass major structural and metabolic changes across the malaria parasite and the host cell which are all likely lipid-driven processes.[188] Furthermore, the malaria parasite does not synthesise lipids *de novo* and thus places a greater metabolic burden on the host erythrocyte. In comparison to the invasive strategies of bacteria and viruses, the malaria parasite's invasion of host erythrocytes adopts a relatively passive role. However, following invasion, the parasite extensively remodels the host cell cytoskeleton and membrane to strategically prepare for sequestration and nutrient uptake.[14] Consequently, the parasite activates an array of lipid-driven processes which include membrane biogenesis, intracellular signalling and protein trafficking. Investigations thus

far have demonstrated that lipid production, uptake and transport are vital for intraerythrocytic development.[189]

The role of lipids in merozoite invasion and virulence has been substantially investigated suggesting that (i) invasion and PVM formation involves the incorporation of parasite lipids into the host membrane and that (ii) lipid rafts regulate parasitophorous vacuole formation thereby playing an important role in the infection and invasion process.[190, 191] Lipid rafts are characterised as heterogenous transient, cholesterol and sphingolipid-rich microdomains approximately 300 nm in size which are formed through protein-lipid and lipid-lipid interactions (Figure 1.19).[192] *P. falciparum* has no known ability to produce cholesterol by *de novo* synthesis; nonetheless, cholesterol is an essential component of parasite cell machinery.[193, 194] Regions enriched with cholesterol, sphingolipids and glycosylphosphatidylinositol-anchored proteins (GPIs) are classified as detergent resistant membranes (DRMs).[195-197] Since disruption of lipid raft structure by cholesterol depletion resulted in arrest of merozoite invasion, DRMs are thought to be crucial in the invasion process of *P. falciparum*.[198]

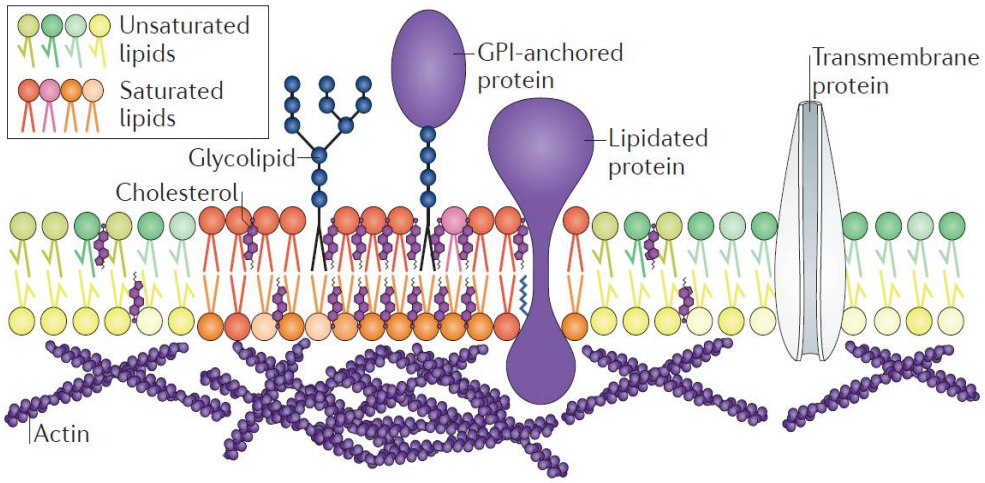

Figure 1.19. Model of a lipid raft domain. Lipid rafts represent a portion of the plasma membrane composed of the asymmetric distribution of cholesterol, glycolipids, glycosylphosphatidylinositol (GPI)-anchored proteins, saturated phospholipids and sphingolipids. This combination of proteins and lipids equip the domains with unique physical properties. Reprinted from Nature Reviews Molecular Cell Biology, 18, Sezgin *et al*, 361-374, Copyright (2017), with permission from MacMillan Publishers.[192]

In 2010, studies by Küzler *et al* reported novel mobile structures that are cholesterol rich and comprised the J-domain of heat shock proteins.[199] These were termed J-dots and

were suggested to be responsible for the intracellular trafficking of parasite virulence factors accounting for the pathophysiology of infected erythrocytes.[199, 200] Most recently, a study by Behl *et al* further implicated the role of cholesterol in parasite virulence by exploring the interaction between a co-chaperone, PFA0060w, parasite virulence factor PfEMP1 and the chaperone, PfHsp70-x.[201] Through recombinant expression and biochemical studies Behl *et al* reported that PFA0060w plays a dual role in both lipid binding through its active sites for cholesterol and as a chaperone protein and that PFA0060w complexes with PfHsp70-x and behaves as a vehicle to assist PfEMP1 across the erythrocyte through cholesterol bound J-dots.

A study by Tokumasu *et al* using confocal and fluorescence lifetime microscopy (FLIM) demonstrated the variations in membrane lipid content between parasitised erythrocytes and their host cells.[202] This study suggested that an inward cholesterol gradient exists which is diluted by non-sterol lipids as the parasite develops within the erythrocyte. FLIM studies using various cholesterol-sensitive fluorophores demonstrated that the PVM of ring-stage parasites constitute a similar cholesterol concentration to that of the host cell. As the parasite matures, large amounts of synthesised phospholipids are supplied to the PVM thereby decreasing its overall cholesterol content. They also reported that it is likely that, through cytostome formation, cholesterol may be trafficked into the parasite along with haemoglobin thereby enhancing the intracellular cholesterol content of the parasite. Additionally, the trafficking of serum cholesterol through exosomes into the parasite can contribute to cholesterol content.

Recently, Gulati *et al* reported the global lipid profile of intraerythrocytic stage parasites over the 48 h cycle by liquid chromatography-mass spectrometry.[203] Analysed lipids were categorised into three separate classes, viz. phospholipids, neutral lipids and sphingolipids. Since phospholipids play an integral role structurally, this was found to be the major lipid class comprising predominantly phosphatidylcholine and phosphatidylethanolamine.[189, 203] However, total phospholipid content remained relatively constant as the parasite developed over the life cycle. Total sphingolipid content was observed to exhibit a decrease as the parasite developed but constituted the second major lipid class as these lipids play a vital role in signalling and membrane structure with sphingomyelin measured as the most abundant in the class and third most abundant

overall.[204, 205] Lipids that were higher in the host cells could potentially act as reservoirs for the parasites to scavenge from.

In contrast, neutral lipids exhibited an overall increase over the 48 h cycle with the two most abundant lipids in this class, diacylglycerols (DAG) and triacylglycerols (TAG), observed to drastically increase in abundance in mid-trophozoite to schizont stage parasites.[203] DAG are important secondary messengers which trigger protein kinase C and also act as precursors to TAG and phospholipids.[206] TAG accumulate in cytoplasmic vesicles commonly known as lipid bodies as a form of energy storage for metabolic processes.[207] Lipid droplets have an array of functions in eukaryotes but most significant are their role in supplying fatty acids to the cell to ensure the metabolic demands are met during periods of nutrient deprivation. In *P. falciparum*, lipid bodies have been reported to be in close association with the DV and in some cases enveloped haemozoin crystals as highlighted earlier in Section 1.6.4.2.[142, 143, 146] The only study to date that profiled the lipids associated with haemozoin was that reported by Pisciotta *et al* where the lipids associated with the surface of the crystals were analysed by gas chromatography-MS to reveal the proposed potent neutral lipid blend comprising a mixture of mono- and diacylglycerols as detailed in Section 1.6.4.2.

1.7.4. Metallome of intraerythrocytic *P. falciparum*

Metal ions are essential components of living organisms and their homeostatic balance is of utmost importance to ensure proper functioning of dynamic biological processes. Physiological processes that require metal ions range from gene expression and catalysis to cell signalling. Depletion, absence or drastic changes in essential metal content can lead to severe health problems owing to deficiency or result in toxicity within the cell. Significantly, transition metals, iron, magnesium, copper and zinc for example, appear to be a double-edged sword in that these are essential as cofactors but also have the ability to catalyse cytotoxic reactions.[208] Cells are able to avidly acquire transition metals which are exploited for their catalytic properties at the active sites of proteins. Regulation of intracellular metal ions is guided by diverse groups of proteins which adopt various roles based on cellular signalling and recognition events, ranging from proliferation,

detoxification, protection and apoptosis. The mechanisms involving metal directed protein interactions are not fully understood.

In 2001, bioinorganic chemist R. J. P. Williams, noted that individual elements follow a defined path within an organism giving it its unique character and that these paths create a specific elemental distribution which he defined as the metallome.[209] Therefore, the metallome represents the distribution, identity, quantity and localisation of metals across various subcellular components of an organism. A third of all proteins require a transition metal cofactor to promote activity within a cell.[210] Therefore, the ensemble of metal complexes with proteins are defined as metalloproteins and biomolecules involved in trafficking of metal ions across membranes or within the surrounding milieu are termed metallochaperones.[211] Building on this premise, in 2004, Haraguchi introduced the field of metallomics as the study of the metallome and the interactions of metal ions with various biomolecules within a cell or organism.[212] Therefore, unravelling the metallome of any organism will provide vital information regarding (i) quantitative and qualitative metal distribution within a specific cell type, (ii) insights into the coordination environment unique to each metal, (iii) metabolism of metal related biomolecules, (iv) chemical evolution of biological organisms and systems over time and (v) potential medical diagnosis and metallodrug design and therapy.[213, 214]

As highlighted at the beginning of this chapter, Apicomplexan parasites are notorious for exploiting the host cell to ensure that nutrient and metabolic demands are adequately met to ensure survival. One way in which *Plasmodium* exhibits this characteristic trait is through haemoglobin ingestion and catabolism. Since this process continues through to late stage trophozoites, it is not surprising that iron becomes the most abundant transition metal within the parasite. Early studies by Egan *et al* were the first to investigate elemental iron content within the malaria parasite.[113] By using a combination of a parasite fractionation assay with UV-visible determination of total iron content, Mössbauer spectroscopy of whole parasites and electron spectroscopic imaging (ESI) with TEM, the amount and distribution of iron was obtained. Egan *et al* showed that the majority of iron present in the parasite localised within the DV in the form of haemozoin. Even though this study preceded the metallomics regime, this was a landmark study which prompted further investigations regarding the effect of antimalarials on the various iron species and parasite growth inhibition.[37, 215]

The most recent contribution towards metallomic insights of *P. falciparum* was an investigation into elemental zinc content within intraerythrocytic stage parasites by Marvin *et al*.[216] Using inductively coupled plasma-mass spectrometry (ICP-MS), single-cell quantitative imaging and small-molecule treatment, these authors reported that the parasite exhibits massive zinc influxes which are essential for intraerythrocytic growth. The parasite also appeared to accumulate labile zinc in compartments external to the DV and compartmentalisation paralleled Fe distribution and haemozoin formation. X-ray fluorescence maps illustrated that Fe concentrated in the DV therefore corroborating the earlier studied by Egan *et al* while the host erythrocyte was devoid of iron. Zinc appeared to concentrate in close proximity to the DV but in separate compartments (Figure 1.20a). Additionally, ICP-MS measurements of cellular Fe, Ca, Zn, Cu and Mg detected in control compared to parasitised erythrocytes were reported to remain unchanged for Fe but exhibited a 6-fold increase for Ca and 2-fold increases for Zn, Cu and Mg. Asynchronous parasites were dual stained with a DNA specific fluorophore, Syto24 and a labile zinc fluorophore, Zinbo5 (Figure 1.20b). This study illustrated that, as the parasite develops, it accumulates pools of labile zinc in sub-compartments surrounding formed merozoites and independent of haemozoin. The authors proposed that the *P. falciparum* gene PF07_0065 (PF3D7_0715900) could be a potential candidate as a zinc transporter due to its 29% transcriptomic similarity with the mouse Znt2 transporter. This study demonstrated that zinc was essential for parasite survival; however, the mechanistic details regarding how the parasite acquires and distributes the transition metals it needs remains to be elucidated.

Even though there has been limited research into the transition metal composition and distribution and the impact over the intraerythrocytic cycle, there have been substantial efforts at understanding independent metal pathways using the more traditional, biochemical approach. Calcium has been classified for its importance in its role as a secondary messenger in signal transduction due to its unique coordination chemistry.[217] Malaria parasites require Ca for normal cell function; however, the host erythrocytes lack the required amount needed and therefore the parasite needs to extract it from extracellular sources and it has been proposed that Ca homeostasis is regulated by Ca-dependent protein kinases (CDPK) and P-type Ca-ATPases.[218]

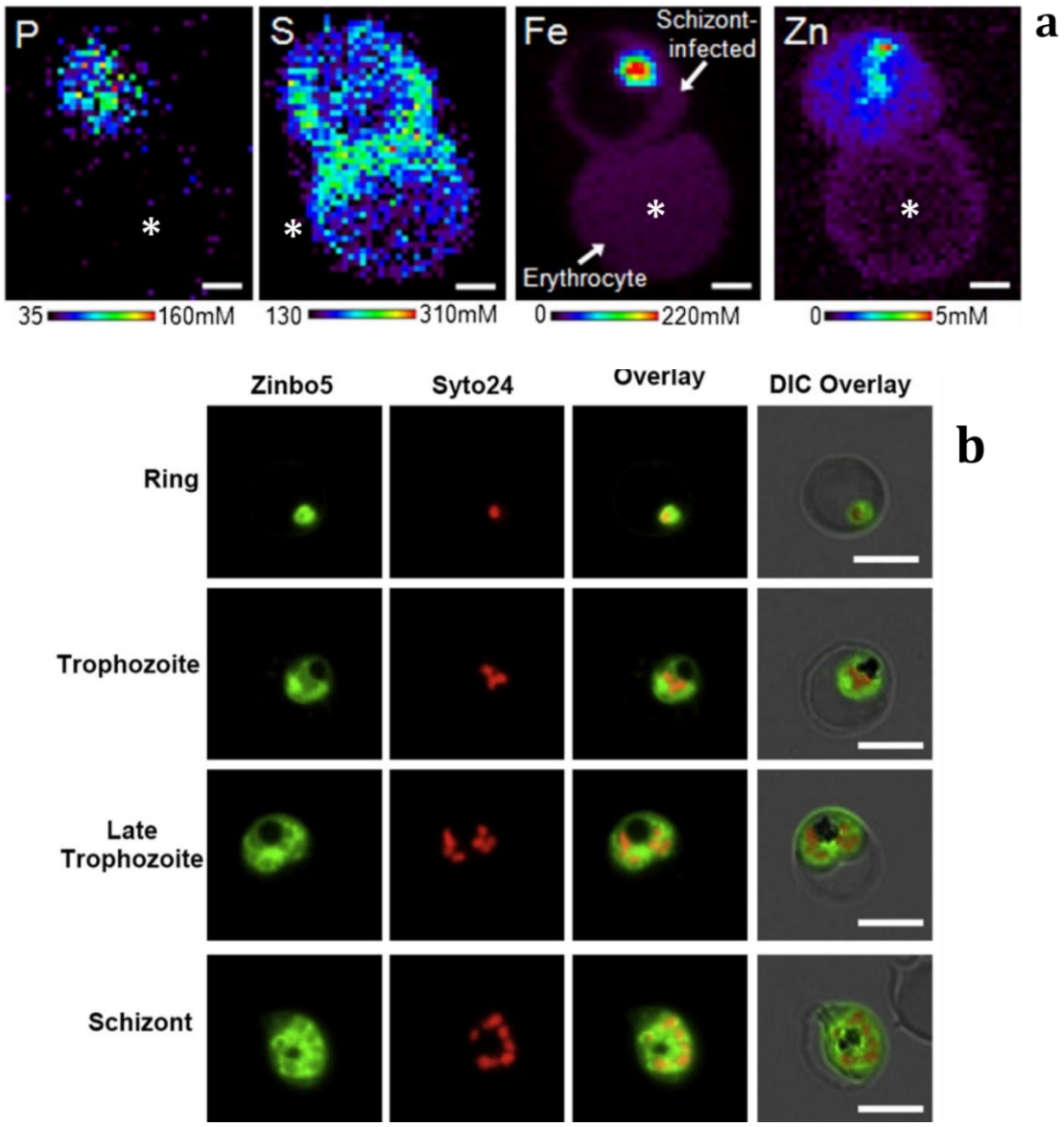

Figure 1.20. Single-cell metal distribution within parasitised erythrocytes. (a) Two-dimensional X-ray fluorescence elemental maps of phosphorous (P), sulphur (S), iron (Fe) and zinc (Zn) in schizont stage parasites compared to host erythrocyte (*). P and S highlight nuclear material and the cell. Rainbow scale represents linear fluorescent intensities with black and red representing lowest to highest signal respectively. Scale bars represent 2 μm. **(b)** Epifluorescence microscope images of mixed stage parasitised erythrocytes treated with Zinbo5 (green) and Syto24 (red) representing labile zinc and nuclear material respectively. Overlaid images (yellow) shows no colocalisation. Scale bars represent 5 μm. Reprinted from Chemistry and Biology, 19, Marvin *et al*, 731-741, Copyright (2012), with permission from Cell Press.[216]

The role of Ca and calmodulin, a calcium binding messenger protein which regulates activity of other enzymes and ion channels, has been extensively investigated with the general consensus that Ca is vital for growth, calmodulin is essential for intraerythrocytic cycle parasite growth and the accumulation of calmodulin in the merozoite plays essential roles in invasion and egress from host cell.[219, 220] Furthermore, even though *P. falciparum*

encodes seven different CDPKs, this protein family is poorly characterised. Most recently, Andresen *et al* reported the structural characterisation of the calmodulin-like domain of CDPK-3.[221] Additionally, CDPK-5 has been reported to localise in the microneme and is vital for parasite egress.[222]

Iron and copper share several similarities in terms of their chemical reactivity; however, the most significant is their ability to generate free oxyradicals through the Fenton reaction.[223] Initial studies reported by Rasoloson *et al* demonstrated that parasitised erythrocytes treated with neocuproine, a copper chelator, stagnated the progression of ring to trophozoite stage parasite and caused a decrease in the intracellular levels of parasite Cu/Zn SOD as well as catalase.[224] Measurements of copper content by AAS indicated that parasites have a lower copper level than that of the host erythrocyte and they therefore proposed that the parasite comprises an efflux pathway to prevent the accumulation of this transition metal in an attempt to circumvent potential toxicity. Since eukaryotic cells acquire and distribute copper through copper transporters and metallochaperones, follow up studies identified potential *Plasmodium*-specific copper transporters; however, even though the recombinant forms of these proteins appear to bind copper *in vitro* there has not been substantial evidence to support this *in vivo*.[225, 226] Very little is known about magnesium, manganese and other transition metals that may be present in trace amounts.

Parasites are known to lack the ability to synthesise nutrients de novo and are entirely dependent on host acquisition which is directed by membrane transporters. Remarkably, the number of transporter families (≈50) in free living organisms such as yeast appears to be higher than those of parasitic protists (20-38).[227] There has been extensive researchers into nutrient transporters in *Plasmodium* focusing on influx and efflux of sugars, nucleotides and small molecules such as inorganic phosphate ions; there is only knowledge of abundant metal ion transporters pertaining to Ca, Fe, Mg and Zn but those for the remaining metal ions remain to be elucidated.[228-230] Several metal ion transporters have been identified but have been assigned a putative function of being a divalent metal cation channels.[231] Most recently, Slavic *et al* reported a vacuolar iron transporter homologue (PFVIT) in playing a role in Fe homeostasis and as a potential detoxifier in both *P. falciparum* and *P. berghei*.[232] Thus overall, metallomic investigations of *P. falciparum* remain in their infancy.

1.8. Aims and objectives

1.8.1. Aims

The general aims of this study were as follows: (1) To explore the metallome of *P. falciparum*; (2) to systematically investigate the proteome and lipidome associated with haemozoin; and (3) to identify and characterise the biomolecules responsible for mediating haemozoin formation in the malaria parasite.

1.8.2. Specific objectives

To achieve these aims, the envisioned objectives for this work were as follows:

i. To profile the distribution of trace metals in the malaria parasite as it develops over the intraerythrocytic cycle using ICP-MS.

ii. To identify metal-associated and possible haemozoin-forming proteins by using qualitative and semi-quantitative proteomics-based mass spectrometry.

iii. To probe whether haemozoin and β-haematin crystals occlude material and whether this material is exchanged with the surrounding environment using labelled biomolecules and monitoring this phenomenon by SDS-PAGE and TLC.

iv. To interrogate the current hypothesis of HDP as a haemozoin mediator by synthesising and characterising soluble recombinant HDP and to investigate its ability to form β-haematin.

v. To identify and quantify the specific lipids associated with haemozoin by lipidomics-based mass spectrometry. If appropriate, develop and investigate a synthetic lipid blend model based on the specific lipids associated with haemozoin and to establish the potential of these lipids as mediators of β-haematin formation.

vi. To investigate the disposition of neutral lipid bodies in relation to haemozoin and the DV by imaging parasites treated with lipid- and organelle-specific fluorescent probes by confocal microscopy.

Chapter 2

General Materials, Instrumentation and Experimental Methods

2.1. Materials and reagents

All solvents and reagents were purchased from Sigma-Aldrich, Sigma Life Sciences or Kimix Chemicals and were of analytical grade or higher and used without further purification. Reagents specific to certain aspects of this study that were acquired from alternative sources are mentioned under the relevant sections. General laboratory consumables were obtained from Millipore, Merck South Africa and Lasec. Double distilled deionised Millipore® Direct-Q water was used throughout this study and is further referred to as MilliQ water. Due to the photosensitivity of fluorescent probes as well as haematin, prepared solutions were stored in the dark and working solutions freshly prepared prior to use. All buffers, biological samples and lipid solutions were maintained on ice through the course of experiments and stock solutions stored at 4°C until further required. The instrumentation, techniques and methods described below focus on those that were of general use in this study while those specific to each experiment are described under the relevant experimental section pertaining to each chapter.

2.2. General instrumentation and techniques

2.2.1. Incubator

A Labcon 508IU thermo-controlled incubator was used to maintain parasite cell cultures at 37°C.

2.2.2. Light Microscope

A Laborlux 12 Leitz Light microscope was used to visualise Giemsa-stained thin films of malaria parasites prepared on glass microscope slides to monitor parasite growth. A Bright-Line™ Haemocytometer was used to count red blood cells (RBCs), isolated trophozoites, DVs and haemozoin under the light microscope.

2.2.3. Centrifuges

Parasite cultures were centrifuged using an Eppendorf Centrifuge 5804 in sterile, plastic 15 or 50 mL Greiner tubes. β-Haematin was centrifuged in Naglene™ 3115 Oak Ridge polypropylene tubes using an Eppendorf Centrifuge 5810R. Material less than 2 mL was centrifuged using a Microspin12 Eppendorf Centrifuge 5415 D (Boeco, Germany). Samples containing proteins or lipids were centrifuged at low temperature using a Labnet Prism™ R Refrigerated Microcentrifuge (Labnet International). Bacterial cells were pelleted, and cell suspensions fractionated at high speed with the Allegra X-30R, Beckman Coulter, Life Sciences benchtop centrifuge.

2.2.4. pH Measurements

A Crison MicropH 2000 pH meter equipped with a Crison 52 03 glass electrode was used to adjust the pH of all aqueous solutions to the required working pH. The pH meter was calibrated using buffer reference standard solutions of pH 4.00 ± 0.01 and pH 7.00 ± 0.01 (Sigma-Aldrich) at room temperature prior to use. The electrode was immersed in a 3 M KCl solution for storage.

2.2.5. Water Baths

A GRANT digital Y6 water bath was used for β-haematin formation in acetate buffer (60°C) and heat shock treatment of plasmids as well as fast digest enzymes (80°C) which required a temperature-controlled environment. A thermometer was used to measure the temperature of the vessels and water bath as a confirmatory measure before the start of any experiments.

2.2.6. Dry Bath

An AccuBlock™ Digital Dry bath was used to boil all protein samples at 95-100°C in preparation for gel electrophoresis.

2.2.7 Weighing Balances

All gram quantities of solid reagents were weighed using a 4-decimal place Adventurer™ OHAUS weighing balance. Milligram quantities were measured using a Sartorius 2006 MP balance with accuracy to 5 decimal places. All balances were calibrated with mass standards on a regular basis.

2.2.8 Sonicator

The Bandelin Sonorex RK100H sonicator was used to ensure complete dissolution of samples.

2.2.9. Nucleic Acid and Protein Quantification

DNA was quantified using a NanoDrop™ 2000 (Thermo Fisher Scientific) by measuring the absorbance at 260 nm. Protein was quantified using the Multiskan™ GO Microplate Spectrophotometer (Thermo Fisher Scientific) equipped with a µDrop plate by measuring the absorbance at 280 nm.

2.2.10. Fourier-Transform Infrared Spectroscopy

Dried β-haematin was mounted on a Perkin Elmer 100 spectrophotometer equipped with and ATR attachment. The background was run in air, spectra were recorded at room temperature and data collected from 4000-400 cm^{-1}.

2.2.11. pXRD

Synthesised β-haematin crystals, dried over P_2O_5, were gently crushed into fine powder. Commercially available haematin (Sigma-Aldrich) was used as a control and treated in the same manner. The powder X-ray diffraction patterns were recorded on a Bruker D8 Advance diffractometer equipped with a Lynxeye detector using CuKα-radiation (λ = 1.5406 Å) at 25°C. Samples were placed on a zero-background sample holder. The samples were scanned over the 2θ range of 4 to 40° and step size of 0.012° to give a total of 3 000 steps. The X-rays were generated by a current flow of 40 mA and accelerating voltage of 30 kV. A receiving slit of 0.6 mm and primary and secondary slits of 2.5 mm were used. Generated data were saved as text files and replotted using GraphPad Prism to obtain the pXRD traces.

2.2.12. SEM

SEM was employed to visualise crystals and gain an idea of the morphological and topographical characteristics of synthesised β-haematin. In general, dry crystals were sputter-coated with carbon prior to surface analysis to establish conductivity. Electron micrographs were obtained using the FEI Nova NanoSEM 230 where an operating voltage of 5 keV, a high vacuum detector and a working distance of 3.5 mm were used. β-Haematin prepared using the acetate method was coated with a thin layer of gold to induce conductivity. Surface morphology images were obtained using a Zeiss MERLIN FEG® scanning electron microscope equipped with a GEMINI II® column. High resolution images were generated using an operating voltage of 5 keV, a working distance of 3.6 mm and an I-Probe of 200 pA.

2.2.13. TEM

TEM was used to visualise parasitised cells with and without treatment with Malachite green, haemozoin isolated from mature trophozoites and β-haematin crystals prepared by different methods. Isolated haemozoin crystals stored in PBS and solutions containing lipid mediated β-haematin crystals in acetone/methanol (1:9 *v/v*) were dispensed onto glow-discharged carbon coated grids. Excess solvents were blotted using Whatman® qualitative filter paper, grade 1 and dried at room temperature. Haemozoin crystals were stained using 1% (*w/v*) uranyl acetate for 10 min followed by five washes with MilliQ water. Ultrathin sections of parasitised cells embedded in resin (Section 2.5.9) were transferred onto copper grids and stained with 1% (*w/v*) uranyl acetate followed by 1% (*w/v*) lead citrate in a closed vessel containing sodium hydroxide for 10 min with five washes with MilliQ water between each stain. Samples were dried at room temperature after which image acquisition proceeded using a TECNAI TF20 transmission electron microscope operating at 200 kV.

2.3. Software

GraphPad Prism Version 4 (GraphPad Software Inc, USA) for Windows was used to plot, analyse and calculate statistical significance for all data. Image Lab™ Software (Bio-Rad) for windows was used to process and analyse images of SDS-PAGE gels. Open source imaging software, GIMP version 2.8 (The GIMP Developing Team, USA) was downloaded and used to outline parasite compartments and organelles in electron microscopy images.

Chemical structures were generated using ChemDraw Ultra 12.0 (Perkin Elmer). The bibliography was prepared using Endnote X9 (Thomson Reuters).

2.4. Preparation of Solutions

2.4.1. Tissue culturing of *P. falciparum*

5% Sodium bicarbonate

A 5 % solution of sodium bicarbonate ($NaHCO_3$) was prepared by dissolving 50 g sodium bicarbonate in 1 L MilliQ water. This solution was stirred until solute was completely dissolved then filtered using a 0.22 µm membrane and stored in autoclaved Schott bottles.

5% D-Sorbitol

A 5 % solution of D-sorbitol was prepared by dissolving 50 g D-sorbitol in 1 L MilliQ water. This solution was filtered through a 0.22 µm sterile filter into autoclaved Schott bottles.

Incomplete culture medium

Incomplete culture medium was prepared by dissolving 52 g RPMI-1640 medium (supplemented with glutamine but without $NaHCO_3$), 30 g HEPES, 0.44 g hypoxanthine, 20 g D-(+)-glucose, 25 g Albumax II and 5 mL (0.05 g/L) gentamycin in 5 L MilliQ water. The medium was pressure filtered through a 0.45 µm filter then sterile filtered through a 0.22 µm membrane filter into autoclaved Schott bottles and stored at 4˚C until further use.

Complete culture medium

Complete culture medium was prepared by adding 17 mL of the 5% (*w/v*) bicarbonate solution to 400 mL incomplete culture medium prior to use.

Culture Medium supplemented with human serum

O^+ human serum was obtained from the Western Province Blood Transfusion Services, Cape Town, South Africa. Complete culture medium was supplemented with 10% (*v/v*) human serum as required and stored at 4˚C. Serum supplemented medium was used within 3 days of preparation.

Wash medium

Wash medium was prepared as described above for complete culture medium but did not contain Albumax II.

Washed RBCs

Human blood cells were obtained from the Western Province Blood Transfusion Services, South Africa and the Interstate Blood Bank Inc., Memphis, Tennessee, U.S.A, for *in vitro* culturing of *P. falciparum* performed at the Division of Pharmacology, UCT, and Department of Microbiology and Immunology, CUMC respectively. RBCs were decanted in 20 mL fractions from blood transfusion bags lined with anticoagulants into sterile 50 mL centrifuge tubes. Wash medium was added to decanted blood in a 1:1 (*v/v*) ratio and centrifuged at 1 200 *rcf* for 5 min. The supernatant was aspirated off and the washing procedure repeated after which RBCs were stored at 4˚C until further use.

Reaction Buffer, pH 7.5

Reaction buffer was prepared by dissolving 0.5 g magnesium sulphate heptahydrate ($MgSO_4.7H_2O$), 7.4 g potassium chloride (KCl), 0.58 g sodium chloride (NaCl) and 2 g HEPES in 800 ml MilliQ water. The pH of this solution was adjusted to 7.5 using 1 M NaOH. The reaction buffer was then made up to 1 L and filtered through a 0.22 µm sterile filter.

Phosphate buffered saline (PBS) solution, pH 7.4

A solution of PBS comprising 0.01 M phosphate buffer, 0.0027 M KCl and 0.14 M NaCl was prepared by dissolving five PBS tablets in 1 L MilliQ water to afford a solution of pH 7.4 at 25°C. The solution was stirred until tablets completely dissolved then filtered through a 0.45 µm syringe filter.

1% Saponin

A 1% saponin solution was prepared by dissolving 0.5 g saponin in 50 mL reaction buffer. This solution was filtered through a 0.22 µm membrane into a sterilised falcon tube and stored at 4°C until further required.

10% Giemsa stain

A 10% Giemsa solution was freshly prepared prior to use by diluting Giemsa's azur eosin methylene blue solution 1:10 (*v/v*) in 0.01 M PBS.

5× RPMI-1640/25% D-Sorbitol

A stock solution of 5× RPMI-1640/25% D-sorbitol was prepared by dissolving 2.63 g of RPMI-1640 (supplemented with glutamine but without $NaHCO_3$) and 12.5 g of D-sorbitol in 40 mL MilliQ water. The pH was adjusted to 7.4 using 1 M NaOH and diluted to 50 mL with MilliQ water. The solution was sterile-filtered through a 0.22 µm membrane and stored.

Percoll® solutions

A 60% (*v/v*) Percoll® solution was prepared by mixing 4 mL of 5× RPMI-1640/25% D-Sorbitol solution with 6 mL Percoll®. A 90% (*v/v*) solution was prepared by mixing 1 mL of 5× RPMI-1640/25% D-Sorbitol with 9 mL Percoll®.

2.4.2. Fractionation of parasite components for *omics* experiments

Acidified water

The pH of MilliQ water was adjusted to 5.4 using 0.1 M HCl and stored at room temperature until further use.

Protease Inhibitors

A 10× stock solution of protease inhibitors was prepared by dissolving one SigmaFAST™ EDTA-free Protease Inhibitor Cocktail tablet in 10 mL acidified water (pH 4.8-5.4). This solution was kept on ice and diluted to a 1× working concentration prior to use.

4% Sodium Dodecyl Sulphate (SDS) Solution

A 4% solution of was prepared by dissolving 4 g SDS in 100 mL MilliQ water.

Acetone/Methanol Solution

A 1:9 (*v/v*) acetone/methanol solution was prepared by mixing 10 mL acetone with 90 mL methanol using a measuring cylinder. The mixture was stored in an air-tight bottle.

2.4.3. Synthesis of β-haematin

0.1 M Sodium Hydroxide

A 0.1 M solution of NaOH was prepared by dissolving 0.20 g NaOH in 50 mL MilliQ water.

Haemin stock solution

Haemin solutions were freshly prepared prior to use by dissolving 30 mg of porcine haemin in 3.5 mL of 0.1M NaOH. This solution was sonicated for 2 min until haemin was completely dissolved and then topped up to 5 mL with 0.1 M NaOH to afford a concentration of 9.2 mM.

Sodium Acetate Buffers

Sodium acetate buffer was prepared by dissolving 53.98 g sodium acetate trihydrate and 32.9 mL of acetic acid in 100 mL MilliQ water to obtain a 9.7 M buffer at pH 4.8. A 0.5 M sodium acetate buffer was prepared by dissolving 6.81 g sodium acetate trihydrate in 100 mL MilliQ water and the pH adjusted to 5.2 using glacial acetic acid.

0.2 M HEPES Buffer, pH 7.4

A solution of 0.2 M HEPES buffer was prepared by dissolving 4.77 g HEPES in 80 mL MilliQ water. The pH was adjusted to 7.4 using 1 M NaOH before diluting to a final volume of 100 mL with MilliQ water.

5% Pyridine Solution

A 5% solution of buffered pyridine was prepared by mixing 5 mL pyridine, 5 mL 0.2 M HEPES, pH 7.5 and 40 mL MilliQ water.

2.4.4. TEM

Wash Buffer

This was prepared by dissolving 2.14 g sodium cacodylate trihydrate, 3.42 g sucrose, 0.022 g calcium chloride and 0.019 g magnesium chloride in 80 mL MilliQ water. The pH was adjusted to 7.4 and the buffer made up to 100 mL with MilliQ water.

1% Malachite green

A 1% stock solution of Malachite green was prepared by dissolving 0.1 g Malachite green in 10 mL MilliQ water. The solution was filtered using a 0.45 μm syringe filter and stored at room temperature in a dark cupboard.

Fixing Buffer

This buffer was prepared by dissolving 1.07 g sodium cacodylate trihydrate and 5 mL of a 25% (*v/v*) stock solution of glutaraldehyde in 40 mL MilliQ water. The pH was adjusted to 7.4 and the buffer made up to 50 mL with MilliQ water.

Fixing Buffer containing 0.1% Malachite green

This was prepared by dissolving 1.07 g sodium cacodylate trihydrate in 35 mL MilliQ water and the pH adjusted to 7.4. The buffered solution was dosed with 5 mL of a 25% (*v/v*) stock solution of glutaraldehyde and 5 mL of 1% (*w/v*) Malachite green and made up to a final volume of 50 mL with MilliQ water.

4% Agarose

This solution was prepared by dissolving 0.4 g low-melting agarose in 10 mL MilliQ water with gentle heating.

2.4.5. SDS-PAGE

Resolving Gel Buffer

The resolving gel buffer (lower gel buffer) was prepared by dissolving 18.2 g of Tris and 0.4 g of SDS in 100 mL MilliQ water and the pH was adjusted to 8.8.

Stacking Gel Buffer

The stacking gel buffer (upper gel buffer) was prepared by dissolving 6.05 g of Tris and 0.4 g SDS in 100 mL MilliQ water and the pH was adjusted to 6.8.

15% Separating and 5% Stacking Gels

The quantity of reagents used to prepare the separating and stacking gels at 15% and 5% (*w/v*) acrylamide concentrations respectively, are summarised in Table 2.1. Ammonium persulfate (APS) was prepared by dissolving 0.2 g APS in 2 mL MilliQ water and stored at

-20°C until further use. Since *N*,*N*,*N*′,*N*′-tetramethylethane-1,2-diamine (TEMED) was used as the polymerising agent causing the acrylamide to solidify, this was added last.

Table 2.1: Proportion of reagents required to prepare 15% separating and 5% stacking gels for SDS-PAGE

	15% Separating Gel (20 ml)	**5% Stacking Gel (6 ml)**
40% Acrylamide/Bis Solution	7.5 mL	750 µL
MilliQ Water	7.1 mL	4.44 mL
Buffer	5.2 mL Resolving Buffer	810 µL Stacking Buffer
10% Ammonium persulfate	200 µL	60 µL
TEMED	12 µL	12 µL

Sample Application Buffer

A 4× stock solution of sample application buffer was prepared by mixing 10 mL of stacking buffer, 8 mL glycerol, 0.8 g SDS, 0.8 mL β-mercaptoethanol, 0.4 mg bromophenol blue and 1.2 mL MilliQ water. The solution was stored in an air tight bottle at room temperature in the fume hood.

Running Buffer

This buffer was prepared at a 5× concentration by dissolving 15.1 g Tris, 72 g glycine and 5 g SDS in 1 L MilliQ water. This solution was not pH adjusted.

Coomassie Brilliant Blue Stain

A 0.25% Coomassie Brilliant Blue stain was prepared by first dissolving 2.5 g Coomassie Brilliant Blue R250 in 450 mL methanol. Upon complete dissolution, 450 mL water and 100 mL acetic acid was added to this staining solution which was stirred and stored at room temperature.

Destaining Solution for Coomassie Brilliant Blue

This solution was prepared by mixing 500 mL MilliQ water, 400 mL methanol and 100 mL acetic acid together and stored at room temperature until required.

2.5. General experimental methods

2.5.1. Tissue culturing of *P. falciparum*

The *P. falciparum* strains NF54, D10, Dd2 and K1 obtained from the Malaria Resource and Reference Centre (MR4) were used in this study. Dd2 PfCRT-GFP mutant parasites were created by Pedro A. Moura and kindly donated by Professor David A. Fidock, Columbia University, U.S.A. NF54 is a chloroquine-sensitive (CQS) strain that was originally isolated from a patient living near Schipol Airport, Amsterdam, who had never left the Netherlands.[233] The second CQS strain, D10, was cloned from FQC-27 isolated in Papua New Guinea.[234] Chloroquine-resistant (CQR) Dd2 parasites were cloned from the parent W2-Mef strain in Indochina and the multi-drug resistant (MDR) K1, was isolated from a patient in Thailand.[235, 236]

Parasites were maintained in continuous culture at 2-5% haematocrit following the methods of Trager and Jensen with modifications and expanded to 8-10% parasitaemia prior to harvesting.[237] Cultures were maintained under sterile conditions in complete medium containing freshly washed O^+ RBCs. Daily, parasite cultures were transferred into a sterile 50 mL falcon tube, centrifuged at 750 *rcf* for 5 min and the supernatant aspirated. The percentage parasitaemia and the dominant phase of the parasite life cycle were determined by preparing a blood smear of the cell pellet. Briefly, a droplet of the parasitised RBC pellet was smeared across a glass microscope slide creating a thin film. Pure methanol was used to fix these cells onto the glass surface after which cells were stained with freshly prepared 10% (*v/v*) Giemsa stain for 10 min. Giemsa binds to DNA thus enabling one to visualise and differentiate parasitised from unparasitised RBCs using light microscopy.[238] Following incubation at room temperature, the stain was gently washed off with cold tap water and the slide air dried. The fixed cell preparation was viewed under a light microscope using an oil immersion lens at 100× magnification. Percentage parasitaemia was determined by counting the number of pRBCs and dividing that number by the total cell count (pRBCs + RBCs) within the field of view.

To maintain parasite synchrony, cultures were treated with 5% (*w/v*) D-sorbitol at the ring stage of their life cycle. In a mixed culture containing both rings and trophozoites, the addition of sorbitol caused lysis of pRBCs containing trophozoites but maintained the integrity of ring stage parasites. This is due to the increased membrane permeability in

host RBCs during the metabolically-active trophozoite stage that makes these cells more amenable to sorbitol induced osmotic-lysis.[239] A 20 mL sorbitol solution was added to the pRBC pellet and the solution incubated in a water bath at 37˚C for 10 min. Thereafter the solution was centrifuged at 750 *rcf* for 5 min, the supernatant containing cell debris was aspirated off and the synchronised pellet placed back into culture.

At the trophozoite stage, cultures were diluted to maintain 5% parasitaemia using washed RBCs. Parasites were cultured in 200 mL flat-bottom culture flasks where 45 mL complete medium was added to 1 mL pRBC pellet. Prior to harvesting, 400 mL flat-bottom culture flasks were used instead as these provided an increased surface area thus promoting efficient and increased parasite growth as needed. Culture flasks were gassed with a mixture comprising 3% O_2, 4% CO_2 and 93% N_2 for 2 min and were then incubated at 37˚C. Parasites used in lipidomic studies and spinning disk microscopy were maintained in RPMI-1640 culture medium supplemented with 10% (*v/v*) O^+ human serum or 0.5% (*w/v*) Albumax II.

2.5.2. Harvesting trophozoites

Trophozoites were harvested by treating 1 mL pelleted parasitised red blood cells (pRBCs) with 47.5 mL reaction buffer and 2.5 mL 1% (*w/v*) saponin. Saponin causes haemolysis of RBCs releasing the contents of the cell into the surrounding environment, in this case, the intact parasite was liberated.[240] This solution was gently vortexed and incubated at room temperature for 10 min. Thereafter the solution was centrifuged at 1 500 *rcf* for 10 min and the supernatant containing RBC debris was aspirated off and the resultant pellet (1 mL on average) was washed multiple times with 25 mL PBS (0.01 M, pH 7.4) until the supernatant was clear. An aliquot of the washed pellet was used to determine the cell count and the remaining pellet stored at -20˚C until further use.

2.5.3. Isolation of DVs

DVs were isolated from trophozoites by trituration. The stored trophozoite pellet (≈ 200 µL) was washed with 1 mL cold reaction buffer. This solution was vortexed thoroughly and centrifuged at 10 900 *rpm* for 1 min, thereafter the supernatant was discarded, and the process repeated twice more. The washed trophozoite pellet was resuspended in 1 mL acidified water containing 100 µL of the 10× protease inhibitor stock

solution and triturated 10-15 times using a 27.5 gauge needle. This sheared the parasite cell wall thereby releasing DVs and parasite cytosol into solution. The triturated cells were centrifuged at 10 900 *rpm* for 5 min and the supernatant representing the trophozoite cytoplasm was pooled and stored. The pellet was resuspended in acidified water containing protease inhibitors and trituration repeated until all trophozoites had successfully lysed.

Cells were monitored by examining wet mounts of isolated samples using the 100× oil objective lens on a light microscope to confirm successful lysis. The pellet was then resuspended in 1 mL cold reaction buffer containing 10 µL DNase l, thoroughly vortexed and incubated in a water bath at 37˚C for 10 min. DNase l was used to eliminate free DNA in the sample as a result of trituration ensuring cleaner sample preparation. Following incubation, the solution was centrifuged at 10 900 *rpm* for 3 min and the supernatant discarded. The resulting DV pellet was then washed 5 times using 300 µL reaction buffer followed by a further three washes with 300 µL PBS (0.01 M, pH 7.4) and the resulting pellet was stored at -20˚C until further use.

2.5.4. Isolation of haemozoin

Haemozoin crystals were liberated from isolated DVs by multiple freeze/thaw cycles as previously described by Ambele *et al.* with modifications.[153] Briefly, isolated DVs were suspended in acidified water (pH 4.8-5.4) in at least 3× the pellet volume. This solution was vigorously vortexed and frozen at -80 ˚C. After an hour, the pellet was thawed at 37˚C for 30 min after which it was immediately frozen at -80˚C. This freeze-thaw cycle was repeated over several days until all DVs had successfully lysed through hypotonic lysis thereby releasing haemozoin crystals. The resulting solution was centrifuged at 12 000 *rpm* for 5 min and the supernatant containing DV lumen was pooled and stored separately for further processing. The resulting haemozoin pellet was washed with 1 mL PBS (0.01 M, pH 7.4) and stored at -20˚C. Crystallinity and quality of haemozoin crystals were verified using a Nikon AFX-II light microscope coupled with a polariser.

2.5.5. Enrichment of pRBCs by Percoll® density gradient centrifugation

A *P. falciparum* culture was tightly synchronised using D-sorbitol and allowed to develop over the 48 h life cycle where growth was monitored by Giemsa staining. Mature trophozoite stage parasitised cells were isolated 32 h into the life cycle by centrifuging

parasite cultures at 750 *rcf* for 10 min. The resulting pellet was enriched using a Percoll® density gradient as previously described by Ginsburg *et al*. with modifications.[241] The Percoll® gradient was created by carefully layering 300 µL of 60% Percoll® over 300 µL of 90% Percoll® in a 2 mL Eppendorf tube. A 150 µL aliquot of the pRBC pellet was very slowly layered over the 60% Percoll® layer. The sample was centrifuged at 12 000 *rpm* for 20 min. After centrifugation the parasites had separated into different layers with mature trophozoites forming a distinct band within the 60-90% layer. Mature trophozoites were extracted using a micropipette and transferred into a 15 mL falcon tube. The pRBCs were washed in 10 mL complete medium at 37˚C for 10 min, centrifuged at 1 200 *rpm* for 5 min and the supernatant discarded. The pellet was washed twice more with 5 mL medium and a Giemsa slide was prepared to evaluate the enriched pellet. Enriched pellets were either processed immediately for electron microscopy or stored at -20˚C until further use. This process was repeated to isolate pRBCs at varying time intervals over the 48 h life cycle.

2.5.6. Determining cell count

Control RBCs, isolated pRBCs, trophozoites, DVs and haemozoin crystals were counted using a bright-line haemocytometer. Following the final wash of the respective cell samples, the pellet was diluted to a final volume of 1 mL in PBS and thoroughly mixed using a vortex. The cell suspension was used to prepare a 1:50 or 1:25 dilution for counting on the haemocytometer in order to obtain a cell/mL count. A 10 µL aliquot of the respective diluted solution was dispensed onto the centre of the haemocytometer stage and incubated at room temperature for 30 min to allow cells to adhere. The number of cells/mL was determined by counting the number of cells or crystals present in each of 10 blocks across the 5 × 5 grid of the haemocytometer. The cell count was calculated as follows:

$$\text{Cell count/mL} = N \times B \times Df \times 10\,000$$

where N = Number of cells (or crystals) counted across 10 blocks, B = Number of blocks counted and Df = dilution factor.

2.5.7. Preparation of haemozoin crystals for *omics* studies

Isolated haemozoin crystals were extensively washed to provide unique material that was weakly associated with and strongly occluded by haemozoin for proteomic and lipidomic investigations. For proteomic studies, crystals were first washed with 100 µL sodium acetate buffer (0.5 M, pH 5.2), thoroughly vortexed and centrifuged at 12 000 *rpm* for 10 min. The supernatant was discarded and the pellet was sequentially washed using 100 µL aliquots of 4% (*w/v*) SDS solution. In each of the SDS washes, the supernatant represented the proteins weakly associated with the crystals and were stored separately. Detergent washes proceeded until there was no longer any trace of proteins present as monitored by gel electrophoresis after which the haemozoin pellet was washed 5 times with PBS buffer (0.01 M, pH 7.4). Extensively washed haemozoin was resuspended in a minimum volume 0.1 M NaOH and the suspension was sonicated for 15 min to ensure complete dissolution. Haemozoin crystals isolated for lipidomic analysis were processed as described above with the incorporation of three 100 µL acetone/methanol (1:9 *v/v*) washes following the first SDS wash to ensure that all weakly-associated lipids were successfully removed prior to base dissolution of haemozoin.

2.5.8. Synthesis of β-haematin using 4.5 M acetate

β-Haematin was synthesised using previously reported methods with modifications.[154] A 6 mg/mL stock solution of haemin was prepared in NaOH (0.1 M). Once dissolved, 2.5 mL of the haemin solution was transferred to a glass reaction vessel. The solution was neutralised by adding 0.25 mL HCl (1 M). To this, 2.31 mL of sodium acetate buffer was added to give a final solution of 4.5 M, pH 4.8. The solution was incubated at 60 °C for an hour whilst stirring after which, the reaction was quenched with water and immediately placed on ice to cool. The product was collected by filtration using a 0.22 µm nitrocellulose membrane and washed with copious amounts of water. The resulting black precipitate was pooled into a 15 mL falcon tube together with 2 mL freshly prepared 5% (*v/v*) pyridine solution to remove unreacted Fe(III)PPIX. This mixture was vigorously vortexed and diluted to 10 mL with water, centrifuged for 15 min and the supernatant discarded. The resulting pellet was washed with water until the supernatant was clear. The precipitate was collected by filtration and allowed to dry over P_2O_5 for 72 h. The identity of synthesised material was confirmed by FT-IR and further characterised by pXRD and SEM.

2.5.9. Preparation of pRBCs for TEM

Parasitised RBCs were prepared following methods previously described by Egan *et al*. with modifications.[113] Following enrichment using Percoll® gradient, the pRBC pellet containing mature trophozoites was washed twice with wash buffer (Section 2.4.4). Briefly, an equal volume of wash buffer was added to the cell pellet and the cell suspension incubated at room temperature for 5 min. Following incubation, samples were centrifuged at 3 000 *rpm* for 1 min after which the supernatant was discarded. Fixation proceeded by resuspending the washed pellet in equal volumes of fixing buffer containing 2.5% (*v/v*) glutaraldehyde which was incubated at room temperature for 60 min. In the case of visualising lipid bodies, cells were resuspended in fixing buffer containing 2.5% (*v/v*) glutaraldehyde and 0.1% (*w/v*) Malachite green and processed in the same way as the control. Following fixation, cell pellets were washed twice with 1 mL wash buffer after which the cell pellets were resuspended in 1 mL fixing buffer supplemented with 1% (*v/v*) tannic acid and incubated for 30 min at room temperature.

Following three washes with 1 mL wash buffer, cells were incubated in 1 mL fixing buffer containing 1% (*w/v*) osmium tetroxide and 0.1% (*w/v*) Malachite green in the case of samples specific to visualising lipid bodies, at room temperature for 60 min. Samples were washed twice with wash buffer and MilliQ water and stained with 1% (*w/v*) uranyl acetate. After washing twice with MilliQ water, samples were suspended in a 1:1 (*v/v*) ratio of 4% (*w/v*) agarose and allowed to solidify. Embedded samples were sliced into 1 mm cubes under water and sequentially dehydrated using aqueous ethanol at concentrations of 30%, 50%, 60%, 70%, 80%, 90%, 95% (*v/v*) for 5 min each, followed twice by 100% ethanol for 10 min and twice with acetone for 10 min. Acetone was gradually replaced with Spurr's epoxy resin over 2 days. The blocks were transferred into fresh resin and allowed to harden for 16 h at 60°C. Samples were cut into ultrathin sections with a diamond knife using a Reichert Ultracut S ultratome. Slices were picked up on 200 mesh square copper grids and processed for staining as described in Section 2.2.13.

2.5.10. Gel electrophoresis

2.5.10.1. Casting denaturing gels for SDS-PAGE

All casting and spacer plates as were cleaned with 70% (*v/v*) ethanol prior to use. SDS-PAGE gels of either 0.75 mm or 1 mm thickness were hand-cast as required. The resolving gel buffer (Section 2.4.5) was carefully poured into a Bio-Rad Mini-PROTEAN 3 casting chamber to avoid the formation of air bubbles. The lower gel layer was allowed to solidify at room temperature; thereafter, the stacking gel was carefully poured over the solidified gel and a 10-lane comb was immediately inserted into the gel and set aside to solidify at room temperature. Once polymerisation was complete, the comb was very carefully removed forming wells in the gel.

Protein samples for SDS-PAGE were prepared by mixing 10 µL of 4× sample application buffer and 30 µL of the respective protein sample in a sterile tube. The solution was vortexed and boiled at 95°C for 5 min using a digital dry bath. Prepared 15% SDS-PAGE gels were secured using a Bio-Rad Mini-PROTEAN Tetra System where 5 µL of the molecular weight marker and 15 µL of each protein sample was loaded into appropriate wells. The protein molecular weight markers used were either the PageRuler™ Plus, Prestained Protein Ladder (Fermentas) or the Colour Prestained Protein Standard, Broad Range, 11-245 kDa (New England BioLabs) and are specified in the respective experiments. Single gels were run at constant current of 20 mA for 60 min and double gels were run at 30 mA for 85 min using the Bio-Rad PowerPac Basic.

2.5.10.2. Staining and destaining SDS-PAGE gels

Following a gel run, protein separating gels were gently rinsed with MilliQ water and placed in a staining dish. Gels were immersed in Coomassie Brilliant Blue R250 stain and incubated overnight at room temperature whilst gently shaking on an orbital shaker (FINEPCR Orbital Shaker SH30). Following incubation, gels were rinsed with MilliQ water and immersed in destaining solution. The gel was allowed to destain while gently shaking for 30 min after which the destaining solution was discarded and replaced with fresh solution. The gel was allowed to destain for 5 h until the appearance of distinct protein bands. Destaining solution was replenished with new solution until a clear background was obtained.

Alternatively, after electrophoresis, gels were incubated in Acqua Stain for 15 min at room temperature whilst gently shaking. This is a water-based stain which is a rapid and sensitive alternative to Coomassie blue allowing immediate visualisation of protein bands with no destaining required. Stained gels were visualised using a Bio-Rad ChemiDoc XRS+ equipped with ImageLab software, version 5.2.1, Bio-Rad Laboratories Inc.

2.5.11. Mass spectrometry for qualitative proteomics

i. Preparation of Gel Samples

Protein bands of interest were carefully excised using a surgical steel blade and cut into 1 mm x 1 mm pieces. Each band was transferred into individually labelled Eppendorf tubes where 100 µL HPLC grade acetonitrile was added to cover gel pieces for an hour to help desiccate the gel. This was removed using a SpeedyVac® leaving behind desiccated protein-containing gel pieces and stored at -20°C. Coomassie stained gel pieces were destained with 0.2 M NH_4HCO_3/acetonitrile (50:50 *v/v*) until transparent. Acqua stained samples were destained with 30% (*v/v*) ethanol followed by 30% (*v/v*) acetone.

ii. In-Gel Digest

In-gel trypsin digestion and peptide extraction for mass spectrometry followed a modified version of methods established by Shevchenko *et al.*[242] Desiccated gel samples were reduced with 0.002 M triscarboxyethyl phosphine (TCEP) in 0.1 M NH_4HCO_3 for 15 min at room temperature with agitation. Excess TCEP was removed and the gel pieces again dehydrated. Cysteine residues were thiomethylated with 0.02 M *S*-methyl methanethiosulfonate in 0.1 M NH_4HCO_3 for 30 min at room temperature. After thiomethylation, the gel pieces were dehydrated and washed with 0.05 M NH_4HCO_3 followed by further dehydration. Proteins were then digested by rehydrating the gel pieces in a solution comprising 20 ng/µL trypsin (Promega) in 0.05 M NH_4HCO_3 which was then incubated at 37°C overnight. Peptides were extracted from the gel pieces once with 50 µL water followed by extraction with 50% acetonitrile. The samples were dried down and resuspended in 30 µL of a solution comprising 2% acetonitrile/water and 0.05% trifluoracetic acid (TFA).

iii. Desalting

Residual digest reagents were removed using an in-house manufactured C_{18} stage tip (Empore Octadecyl C_{18} extraction discs; Supelco). First, the C_{18} membrane was activated with 30 µL methanol followed by equilibration with 30 µL 2% acetonitrile/water containing 0.05 % TFA. The sample was loaded onto the stage tip following equilibration, the bound sample was washed with 30 µL 2% acetonitrile/water containing 0.05% TFA. The bound peptides were then eluted with 30 µL 50% acetonitrile/water and 0.05% TFA. The eluent was evaporated to complete dryness. The dried peptides were then dissolved in 2% acetonitrile/water and 0.1% formic acid (FA) in preparation for LC-MS analysis.

iv. Liquid Chromatography

Liquid chromatography was performed using a Thermo Scientific Ultimate 3000 RSLC equipped with a 2 cm × 100 µm C_{18} trap column and a 25 cm × 75 µm Pepmap analytical column (Thermo Scientific). The solvent systems employed were:

Loading: 2% acetonitrile/water; 0.1% FA
Solvent A: 2% acetonitrile/water; 0.1% FA
Solvent B: 80% acetonitrile/water

The samples were loaded onto the trap column using loading solvent at a flow rate of 5 µL/min from a temperature controlled autosampler set at 7°C. Loading was performed for 10 min before the sample was eluted onto the analytical column. Flow rate was set to 250 nL/min and the gradient generated as follows: 2.5% A constant over 10 min; 2.5-5% A from 10-15 min; 5-35% A from 15-130 min using Chromeleon non-linear gradient 6 and 35-50% A from 130-150 min. Chromatography was performed at 50°C and the outflow delivered to the mass spectrometer through a stainless steel nano-bore emitter.

v. Mass Spectrometry

Mass spectrometry was performed using a Thermo Scientific Fusion mass spectrometer equipped with a Nanospray Flex ionization source. The sample was introduced through a stainless-steel emitter. Data were collected in positive mode with spray voltage set to 2.35 kV and ion transfer capillary set to 300°C. Spectra were internally calibrated using polysiloxane ions at m/z = 445.12003 and 371.10024. MS1 scans were performed with

the orbitrap detector set at 120 000 resolutions over the *m/z* scan range 380-1500 with a fill time of 50 ms or until an adaptive gain control (AGC) target at 4×10^5 was reached. MS2 acquisitions were performed using monoisotopic precursor selection for ions with charges +2 to +6 and dynamic exclusion of 1 over 140 s with the error tolerance set to ± 10 ppm. Precursor selection was performed in Top Speed data dependent mode with the most intense precursor selected first with a cut off intensity higher than 50 000. Precursor selection was performed using the quadrupole mass analyser with an isolation window of *m/z* 1.5 prior to HCD fragmentation. Precursor ions were excluded from fragmentation once for a period of 30 s and were selected for fragmentation in HCD mode using the quadrupole mass analyser with HCD energy set to 35%. The AGC target was set to 1×10^4 and the maximum injection time to 40 ms.

vi. Data Analysis

The raw files generated by the mass spectrometer were imported into Proteome Discoverer version 1.3 (Thermo Scientific) and processed using the Mascot 2.3.1 algorithm (Matrix Science). Database interrogation was performed against the *P. falciparum* PlasmoDB and *Homo sapiens* Uniprot (v 1.3) databases with trypsin cleavage allowing for 2 missed cleavages. Precursor mass tolerance was set to 10 ppm and fragment mass tolerance set to 0.8 Da. Protein *N*-terminal acetylation, deamidation (NQ) and oxidation (M) was allowed as dynamic modifications and carbamidomethylation of C as static modification. Peptide validation was performed using the peptide validator node set to search against a decoy database with strict FDR 1%.

Chapter 3

Insights into the Trace Metal Distribution within the Malaria Parasite

3.1. Introduction

Various naturally-occurring elements bridging both the organic and inorganic spheres of life form the cohort of molecules essential to living organisms. Amidst these are trace metals, which are present in minute quantities that are essential to overall physiological function and cellular stability.[243] The continuous interplay between maintaining homeostasis and sudden influxes or effluxes of trace metals ultimately governs whether organisms remain healthy or are susceptible to disease. For example, Menkes disease was discovered to occur within humans through mutations of a copper polypeptide, Cu(I) ATP7A.[244] Understanding the metal complement adds a new dimension to the already well-established building blocks (nucleotides, lipids, carbohydrates and proteins), thus making metallomics a vital addition to the omics fields of study.

The metal cations calcium, potassium and sodium as well as the anionic non-metals chlorine, sulphur and phosphorus are known to be present in larger quantities thus contributing to the macronutrient constituent of an organism. However, trace metals iron, magnesium, zinc, manganese, cobalt, copper, nickel and the non-metals selenium, bromine and iodine are found at micromolar concentrations thus making up the trace element component. In any living organism, a range of biological mechanisms are regulated by trace metal ions. The reactivity of such ions is determined by metal oxidation and coordination states thus making these elements, specifically transition metals,

unique in their ability to participate in life-dependant processes.[245] Such metal ions are usually found bound to proteins giving rise to metalloproteins and when acting as a catalytic centre of such molecules these are better known as metalloenzymes.

Metal ions play biologically important roles in redox reactions, cellular metabolism and growth, amongst others; therefore, maintenance of intracellular concentrations is of utmost importance. In addition, divalent metals are known to be actively involved in host-pathogen interactions where any metal imbalance directly influences pathogenesis which in turn impacts health and disease. In some cases, upon infection, the host cell triggers a series of events which restricts the amount of bioavailable metals that a pathogen requires; however, in other cases pathogens have evolved and developed mechanisms to overcome this limitation and access host metals thereby enabling them to meet their nutritional demands.

In this continuous host-pathogen battle for metal ions, metals are obtained by either scavenging the host, direct import or by expropriating host metalloproteins. For example, pathogens such as *Pseudomonas aeruginosa* and *Mycobacterium tuberculosis* employ siderophores to obtain iron from the host by competing with transferrin.[246, 247] On the other hand, copper may be essential to a number of eukaryotes; however, this trace metal is deleterious to yeast and fungi which actively export into the host whatever is taken up to reduce toxicity, thus maintaining survival.[248]

In the case of malaria, the intracellular protozoan *P. falciparum* actively ingests host haemoglobin throughout the asexual intraerythrocytic cycle. As discussed in Chapter 1, the toxicity of free iron as a result of haemoglobin catabolism was circumvented through the formation of haemozoin, therefore studies thus far have been devoted to detecting and measuring iron content within the parasite. Since trace elements are essential and little is known about other trace metals that may be present within the malaria parasite and their potential importance during the asexual cycle, this chapter explores a portion of the *P. falciparum* metallome. Analytical techniques were employed to investigate the distribution of trace metals over the 48 h intraerythrocytic stage of the parasite life cycle as well as to explore the trace metal content across different strains.

3.2. Experimental Methods

Experimental methods pertaining to this chapter regarding parasite culturing, isolation of components and preparation of cells for electron microscopy are described in detail in Chapter 2.

3.2.1. Preparation of parasite samples for trace metal measurement

Intact mature trophozoites from CQS strains NF54 and D10, CQR strain Dd2 and MDR strain K1 were isolated from pRBCs. In addition, DVs were isolated separately from trophozoites obtained from NF54 strain parasites. All cells and isolated parasite components were counted using a haemocytometer which afforded a cell/mL count. Thereafter, samples were centrifuged, and the supernatant discarded. Resulting cell pellets were resuspended in 400 µL concentrated trace metal grade nitric acid (HNO_3). Solutions were then transferred qualitatively into volumetric flasks and made up to 1 mL with HNO_3. Dissolved samples were allowed to completely digest overnight at room temperature.

3.2.2. ICP-MS

Unparasitised erythrocytes, isolated parasites and culture medium were analysed for their metal content using ICP-MS. Internal standards rhenium, bismuth, indium and rhodium were added to a 5% (*v/v*) HNO_3 standard solution which was used to prepare a calibration curve prior to analysis. Digested biological samples were further diluted 1:100 with 5% (*v/v*) HNO_3 solution prior to instrument injection. ICP-MS was performed on a Thermo-Fisher X-Series 2 Quadrupole instrument. Samples were analysed for iron, magnesium, zinc, copper and manganese. Data were processed using Thermo Plasma Lab and metal content was reported in ppb (parts per billion). Trace metal content data were converted from ppb to femtogram/cell by incorporating the respective cell/mL counts corresponding to each sample. All ICP-MS measurements were carried out on at least three different samples and averaged to obtain a single representative concentration corresponding to each trace element.

3.2.3. TEM coupled Electron Energy Loss Spectroscopy (EELS)

Parasitised mature trophozoite stage NF54 RBCs were fixed, embedded in resin and prepared for TEM as described in Chapter 2. The distribution of Fe, Zn, Mg and Cu were determined by ESI/EELS in conjunction with TEM following a similar method to that reported by Egan *et al*.[113] All spectra were recorded using a FEI TECNAI 20 with GIF 863 Tridiem transmission electron microscope where images were collected at a slit width of 18 eV equipped with a charge-coupled-device camera and processed using Digital Micrograph Software (Gatan). Two images were recorded at energies slightly before the L_3 absorption edge for Fe, Zn and Cu and just before the K absorption edge in the case of Mg as noted in Table 3.1. The third image was centred at around the L_3 and K edges for the respective metals. Background images were then extrapolated from the data obtained at the two lower energies and subtracted from that obtained at the L_3/K edge affording an elemental map representing areas of the parasite corresponding to a specific metal. A high signal to noise ratio for Cu was observed due to the likely low concentration within the pRBC; therefore, this trace element was excluded from the discussion that follows.

Table 3.1. Energy values corresponding to major edges used in ESI/EELS measurements

Element	Major Absorption Edge (eV)	Low energies (eV)
Fe	708 (L_3)	650, 693
Zn	1020 (L_3)	960, 990
Mg	1305 (K)	1245, 1275
Cu	931 (L_3)	871, 916

3.3. Results and Discussion

3.3.1. Trace metal detection in *P. falciparum* by ICP-MS

Quantifying trace metal content as well as gaining an idea of the subcellular distribution are key factors to better understanding the metallome of any organism. However, one of the challenges faced with achieving the first of the above-mentioned two goals is that many elements tend to naturally occur in very low amounts. This necessitates technologies that offer high sensitivity whilst maintaining experimental accuracy. Thus far various techniques such as potentiometric sensors, stripping voltammetry, flame atomic absorption spectroscopy (FAAS) and graphite furnace atomic absorption

spectroscopy (GF-AAS) have been used to detect trace metals across an array of samples from biological material to soil.[249]

Even though each of these techniques have their unique traits giving each certain advantages over the other; overall, there still remain a number of limitations. In some cases, certain techniques are biased towards the type of analytes measured; for example, potentiometry can only detect free metal ions in solution and not elements that form part of complexes or total metal concentration, whereas X-ray techniques can only measure total elemental distribution. Other limitations are in the form of spectral interferences, being able to detect only a single trace metal of interest per sample, poor selectivity of metal ions due to competing ions in solution and poor detection limit rendering many elements undetectable.

In order to address these deficiencies, analytical spectrometry using inductively coupled plasmas (ICPs) have become quite favoured as they are highly selective and sensitive.[250] More specifically, ICP-MS offers simultaneous multi-element detection and quantification at trace and ultra-trace levels. In addition to rapid multi-elemental detection, ICP-MS allows for isotopic identification, minimal inter-element interference, analysis on a picogram scale, is applicable across all phases of matter, offers excellent precision and accuracy and requires small sample volumes per run.

Digested samples were individually delivered into the sample introduction system consisting of a nebuliser, spray chamber and ICP torch (Figure 3.1 b-d). Liquid was injected into the sample valve after which it was transported to the nebuliser through the action of a peristaltic pump where it was mixed with argon gas to produce an aerosol. Larger droplets were separated from aerosol droplets in the spray chamber which then entered the plasma torch. Here, aerosol droplets reacted with the plasma source at high temperatures of 6000-8000 K where ion generation occurred. Aerosol droplets were dried, decomposed and ionised whilst in the plasma source, producing an abundance of positively charged ions (e). The plasma torch was used to selectively generate positive ions thereby making this step characteristic of the sensitivity that this technique offers.

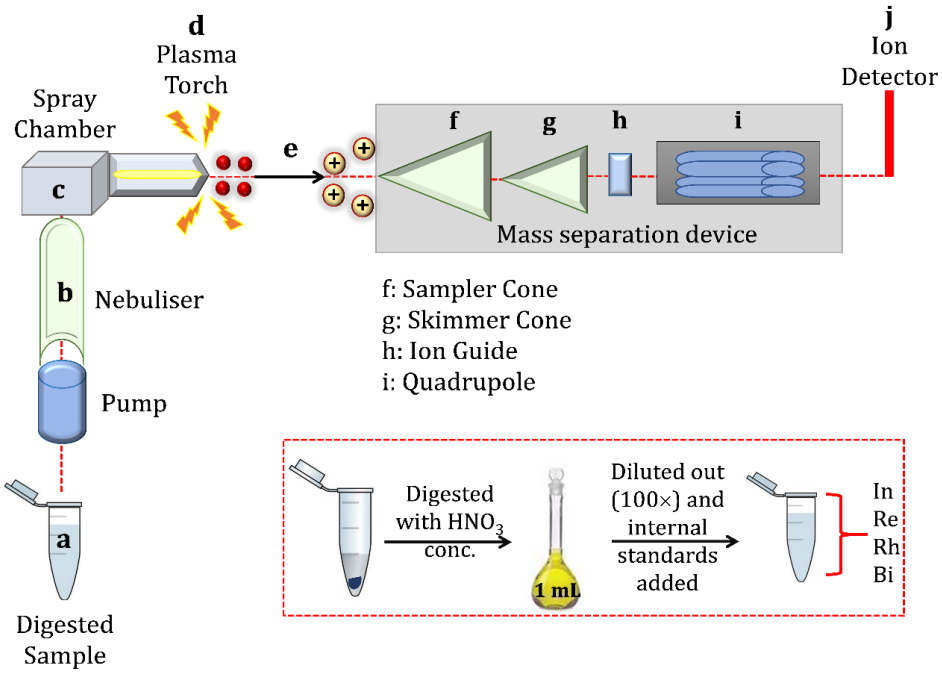

Figure 3.1. Schematic illustrating the experimental workflow of an ICP-MS run from sample injection to ion detection. The inset depicts sample preparation by acid digest prior to measurement. Indium, rhenium, rhodium and bismuth were used as internal standards.

Positive ions were extracted from the plasma through the sampler cone (f) where these enter a high vacuum region through a skimmer cone (g). The ion guide (h), operated in collision mode, accesses helium gas which reduces the kinetic energy of bigger unwanted neutral atoms and selectively filters smaller positively charged ions, thus reducing polyatomic interferences. These ions then entered the quadrupole mass filter (i) where they were separated by their mass-to-charge ratios. The resultant analytes, or rather, target ions were converted into an electric signal using a dynode detector (j) generating a mass spectrum where the intensity is directly proportional to the concentration of the isotope at a specific mass.

ICP-MS has a wide range of applications across many fields such as petrochemical, environmental, food, geochemical fields as well as from toxicology analysis to nutritional studies. Therefore, this technique was employed to detect and monitor changes in trace metal distribution in the malaria parasite and RBCs, making this a suitable approach as a preliminary step in elucidating the *P. falciparum* metallome.

3.3.2. Total metal distribution over the 48 h intraerythrocytic cycle

Due to the unique ability of ICP-MS to simultaneously detect multiple elements, this technique was employed to measure several trace metals in the malaria parasite. CQS NF54 parasites were used in a time point study where trace metal distribution was determined over the intraerythrocytic stage of the parasite's life cycle.

In this study, trophozoites were isolated from pRBCs at 8 h time intervals starting from the early trophozoite stage at 24 h until the schizont stage between 46-48 h post invasion (Figure 3.2). In addition, DVs were isolated from trophozoites corresponding to each of these time points with the exception of the 24 h trophozoite which was still fairly immature, in order to determine the distribution of metals between parasite compartments. Unparasitised erythrocytes were also analysed for trace metal content and used as a control in this study.

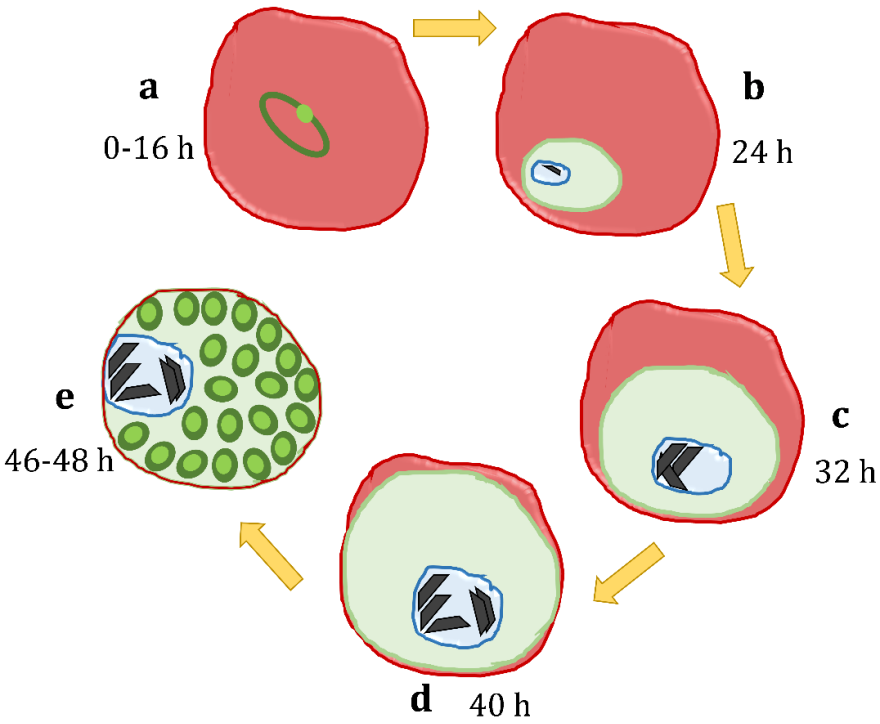

Figure 3.2. Schematic representing maturation of *P. falciparum* during the intraerythrocytic stage of its life cycle. Parasite growth illustrating progression from **(a)** ring-stage, **(b)** early trophozoites, **(c)** mature trophozoites and **(d)** late-stage trophozoites to **(e)** the schizont.

Elements of potential interest were Ca, Se, Fe, Mg, Zn, Cu and Mn. Calcium has been reported as an essential element involved in various processes in the malaria parasite ranging from merozoite invasion and parasite growth to egress from pRBCs. Even though it may be a fairly abundant element, Ca was not pursued further in the current study due to spectroscopic interferences.[219, 251] As sensitive and accurate as ICP-MS may be, there are inevitable disadvantages as with any other technique with spectral interference being the main challenge in this case. Such interferences are categorised as isobaric and polyatomic interferences associated with the generation of polyatomic species.[252] Isobaric interferences encompass different elements which have isotopes that correspond to the same mass ratio. Current ICP-MS software is able to account and correct for this type of interference thereby minimising its effect on the overall spectra and measurements. By contrast, polyatomic interferences are slightly more complex.

Polyatomic interferences arise from the combination of matrix and sample ions reacting with elements constituting the solvents used in sample preparation as well as the plasma source consisting of oxygen, carbon, nitrogen and argon. Certain elements, for example, the first-row transition metals of the periodic table and selenium are more susceptible to form polyatomic ions due to the multiple combinations that are possible. These can influence the reaction of Ar at high temperatures with matrix components. In addition, since the noble gas Ar is exploited at high temperatures (>6 000 K) to produce the plasma, it is responsible for a number of interferences and can also combine with itself to form Ar_2. The isotopes of Ar_2 tend to overlap with those of Se which likely explains why Se was either below the detection limit or undetermined in the biological samples investigated in this study. Ca exhibits dominant interference by combining with O, N and Ar specifically. This phenomenon is heightened in samples comprising a high Fe content due to the isotopic relation between Fe and potential Ca adducts thereby restricting the accurate measurement of both Ca and Fe.[253]

Trace metals Fe, Mg, Zn, Cu and Mn were successfully measured by ICP-MS across these samples and contributed to the total metal content measured in RBCs and intact trophozoites as depicted in Figure 3.3. Total trace metal content of RBCs was found to be 133 ± 13 fg/cell of which approximately 89% consisted of Fe. Mg and Zn accounted for 6.4 and 4.5% of the RBC metal content respectively with Mn and Cu comprising the remaining 0.3%.

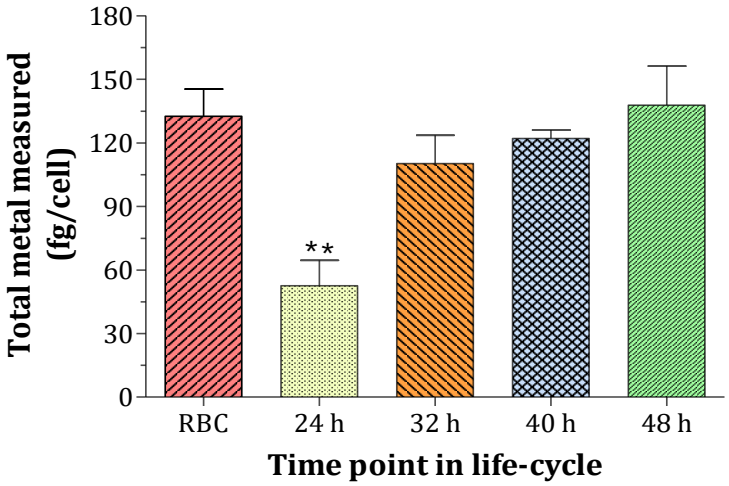

Figure 3.3. Total metal content measured in isolated trophozoites at 8 h time intervals post-invasion over the intraerythrocytic cycle compared to the RBC control. Metal content is reported in femtogram/cell (fg/cell), *N*=3, error bars represent SEM. Asterisks displayed on the graph indicates statistical significance in comparison to the control at specified confidence intervals using the Student's two-tailed *t*-test (** denotes $p < 0.01$).

As the parasite matures within the host RBC, a number of important processes occur as it transitions from ring to trophozoite and eventually into the schizont. These processes include high cellular energy demands, nuclear division and preparation of the parasite to commence egress from the host cell, all of which are integral in promoting growth and pathogenesis within the human host. Most notable, as discussed in Chapter 1, is haemoglobin uptake and haemozoin formation within the parasitised cell as these processes govern survival within the host in terms of meeting nutritional requirements and evading the host immune system. A number of these key processes are in fact reliant on the interplay between host and parasite metal ions where, in some cases, certain trace metals are responsible for catalytic activity and replication.

Total trace metal content was found to almost double as the parasite developed from young to mature-stage trophozoites (24 to 32 h) after which a steady increase was observed as the parasite further matured (Figure 3.3). At 24 h post-invasion, a significant difference was found between young trophozoites and control RBCs suggesting that, as the parasite transitions from ring to early trophozoite, it is largely dependent on the host RBC for most nutritional requirements including trace metals needed for development.

Throughout the intraerythrocytic cycle total trace metal content in the parasite remained lower than or similar to that of the host cell. This may be attributed to the abundance of Fe which is restricted by the amount of haemoglobin consumed and also indicates regulation of metal homeostasis in this specific host-pathogen system. Trophozoites isolated at each of the time points indicted above can be thought of as representatives of key processes which occur specifically at these points post-invasion. Early to mature-stage trophozoites (24 to 32 h) represent rapid ingestion and catabolism of haemoglobin which in turn leads to the activation of the haem detoxification pathway. At 40 h, the parasite's metabolic demands are drastically enhanced as the parent cell prepares for and undergoes cell division forming daughter cells. Finally, following cell division the schizont forms (46 to 48 h) where the parasite now prepares for egress from the host cell.

3.3.3. Distribution profile of trace metals across parasite compartments

Each of the above-mentioned processes are likely to have specific trace metals associated with them which in turn provide insight into possible metalloproteins or metalloenzymes responsible for such cellular events. Since ICP-MS is a non-discriminatory technique and measures metal content irrespective of the complex ion species or whether free or bound, this allowed for the determination of total metal content. Of the six trace metals measured, Fe was found to be the most abundant element followed by moderate amounts of Mg and Zn with trace amounts of Cu and Mn.

3.3.3.1. Total Iron

The measured mass content of Fe in RBCs was found to be 117 ± 12 fg/cell which agreed with previously reported ranges of 95 ± 26 fg/cell by Combrinck *et al* as well as 90-111 fg/cell by Greendyke *et al*.[37, 254] A significant difference ($p = 0.0063$) was observed in Fe content measured in 24 h trophozoites compared to the RBC control. Early stage trophozoites were found to contain 38 ± 9 fg Fe/cell representing approximately 33% of RBC Fe (Figure 3.4). This supports the premise that the parasite gradually transitions from ring to trophozoite stage whilst actively ingesting haemoglobin.

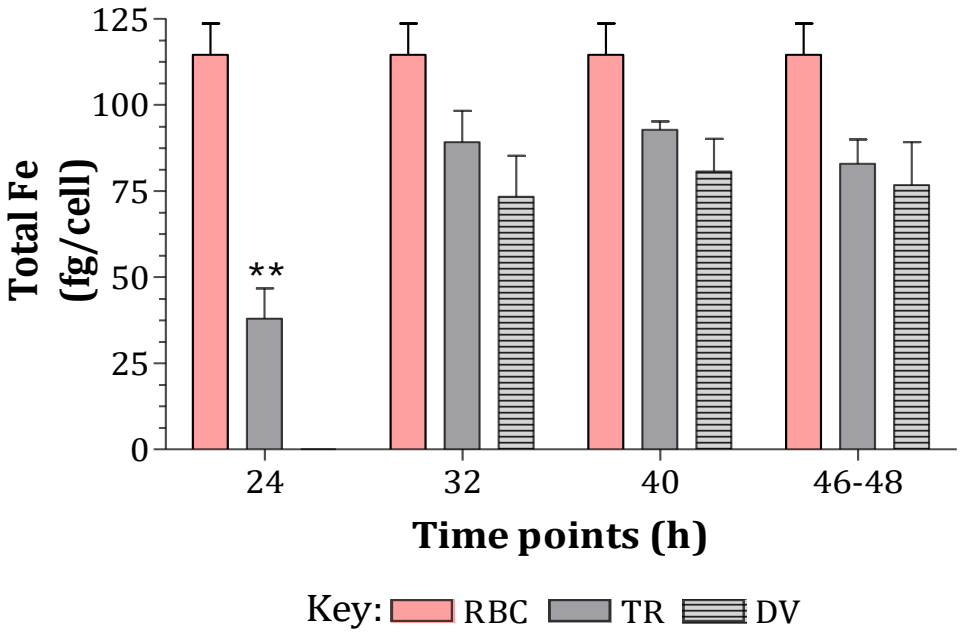

Figure 3.4. Distribution of total Fe in NF54 parasites as measured by ICP-MS, *N* = 3, error bars represent SEM. Asterisk displayed on the graph indicates statistical significance in comparison to the RBC control at specified confidence intervals using Student's two-tailed *t*-test (** denotes $p < 0.01$). Key: Red blood cells (RBC), trophozoites (TR) and digestive vacuoles (DV).

A 2-fold increase in Fe content was observed in 32 h trophozoites. The mass of Fe found was 89 ± 9 fg/cell and 73 ± 1 fg/cell for trophozoites and DVs respectively. This is consistent with the large amounts of haemoglobin ingested as the parasite progressed to the most metabolically-active stage of its life cycle. Previous studies carried out by Egan *et al* reported CQS D10 trophozoites at 32 h to contain 58 ± 2 fg Fe/cell showing that approximately 60% of host haemoglobin had been digested by the parasite using a haem fractionation based assay.[113] The values obtained in the current study were found to be slightly higher than those previously reported but this may be attributed to different strains of *P. falciparum* used (D10 vs NF54) or the implementation of a more sensitive analytical technique. At 32 h the parasite was found to have digested approximately 76% of host haemoglobin with 82% of measured Fe found concentrated in the DV. This was not surprising since haemoglobin, an iron-containing human protein, comprising more than 90% of RBC content and hence was expected to be the major contributing source of Fe in the parasite.

As the parasite developed from 32 to 48 h there was no significant increase observed in Fe content in isolated trophozoites between the respective stage parasites or the RBC. This demonstrates that the majority of host haemoglobin was ingested by 32 h into the life cycle and that no drastic change in total Fe content of RBC upon infection was seen, thus supporting the observation previously demonstrated by Egan *et al*.[113] At 40 h into the life cycle, close to 80% of haemoglobin was digested with the DV maturing along with the parasite containing approximately 92% of Fe content. This high percentage of Fe which was found to concentrate in the DV in the form of haemozoin crystals was supported by the Fe map obtained through electron microscopy coupled with EELS as shown in Figure 3.5. ESI/EELS was used to map Fe within pRBCs which illustrated that the high Fe content localises within the DV and found almost exclusively in the form of biocrystalline haemozoin.

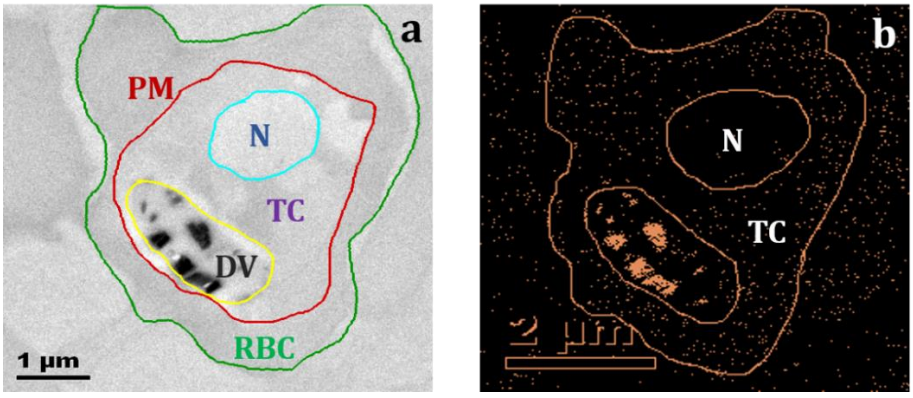

Figure 3.5. Transmission electron micrograph and corresponding Fe map of mature NF54 pRBC. (a) Section of TEM micrograph representing the parasitised cell used for elemental mapping. Dense black regions within the DV represent haemozoin crystals. **(b)** ESI/EELS analysis illustrating the distribution of Fe within a pRBC. Orange regions specifically represent Fe signal detected by EELS. Solid orange lines were used to outline cellular regions and does not represent elemental distribution. Fe is seen to concentrate within the DV, with a lower amount distributed in the RBC and no localisation within the nucleus (N). Key: Red blood cell (RBC), parasite membrane (PM), trophozoite cytoplasm (TC) and digestive vacuole (DV).

3.3.3.2. Total Magnesium

Mg is known to be the second most abundant divalent cation found in living cells and has been well characterised to be involved in hundreds of essential physiological processes

within organisms ranging from bacteria to humans. The total Mg content found in control RBCs was found to be 8.6 ± 7 fg/cell (Figure 3.6) which translates to approximately 3.5 mM Mg using an approximate volume of an average mature RBC of 100 fL. Taking into account the error associated with counting cells, the measured Mg concentration appeared to be in reasonable agreement with previously estimated concentration of 2.5 mM.[255, 256]

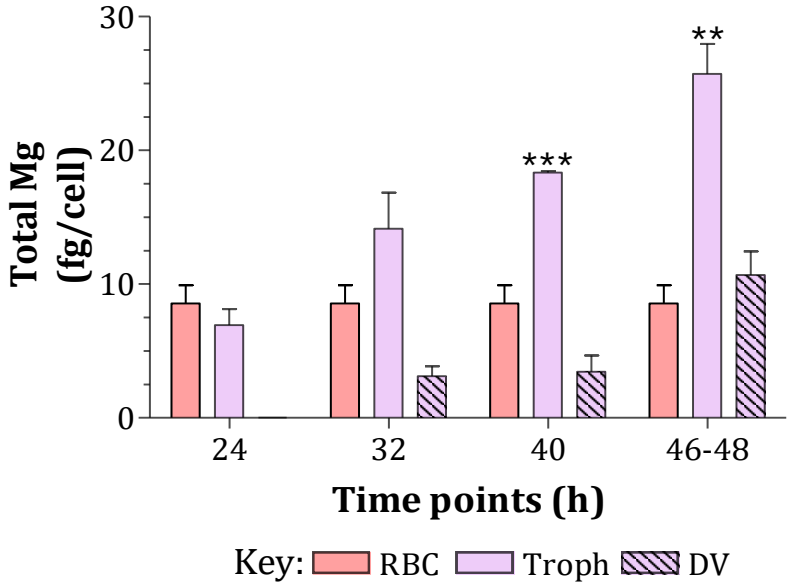

Figure 3.6. Distribution of total Mg in NF54 parasites as measured by ICP-MS, *N* = 3, error bars represent SEM. Asterisks displayed on the graphs indicates statistical significance in comparison to the RBC control at specified confidence intervals using Student's two-tailed *t*-test (** denotes $p < 0.01$ and *** denotes $p < 0.001$). Key: Red blood cells (RBC), trophozoites (Troph) and digestive vacuoles (DV).

Significant increases were observed at both the 40 and 48 h time points where the total Mg measured in trophozoites was found to be more than double than that of RBCs (Figure 3.4b). Progression from early to late-stage trophozoites showed a steady increase in Mg content as the cell reached the most metabolically-active stage with an initial 2-fold increase observed between 24 to 32 h and ultimately a 4-fold increase towards the schizont stage. Mg content of 18 ± 0.1 and 26 ± 2 fg/cell was measured at the 40 and 48 h time points respectively. Only 20-40% Mg was found to be in the DV as the parasite matured thereby indicating that this trace metal concentrates and distributes itself within the TC, an observation further supported by elemental mapping of Mg illustrated

in Figure 3.7. These findings indicate that uptake of additional Mg is essential for growth and the parasite likely imports Mg^{2+} from the external milieu to satisfy its nutritional demands. It is known that RPMI 1640 culture medium is enriched with various amino acids and inorganic ions of which Mg comprises a significant component. Therefore, it is highly probable that the parasites import required Mg from the culture medium in *in vitro* systems and from blood serum when within the human host. RBCs have lower Mg content than most cells; therefore, it is not surprising that the parasite promotes uptake of this specific divalent ion.

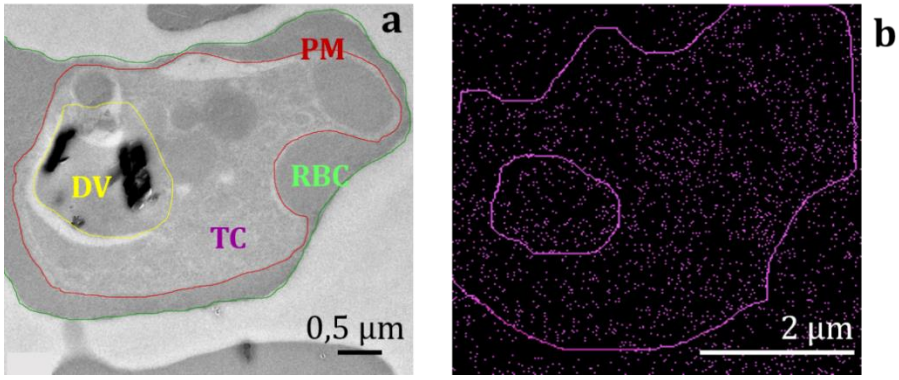

Figure 3.7. Transmission electron micrograph and corresponding Mg map of mature NF54 pRBC. (a) Section of a TEM micrograph representing the parasitised cell used for Mg mapping outlining the parasite and DV. **(b)** ESI/EELS analysis showing the distribution of Mg throughout the trophozoite cytoplasm (TC) within a portion present in the DV. Key: Red blood cell (RBC), digestive vacuole (DV) and parasite membrane (PM).

The observed increases in Mg content pertaining to specific time points during the intraerythrocytic stage and localisation thereof was not surprising since late-stage parasites represent a period of intense growth and development. Given that, as the parasite develops and a number of different processes are simultaneously occurring the energy demand of the parasite is proportionally enhanced, it is likely that the amount of Mg measured correlates to the need for ATP production which occurs through anaerobic glycolysis, an energy production process favoured by rapidly growing cells thereby meeting the unique energy demands of *Plasmodium*.[257] Intraerythrocytic stage *Plasmodium* parasites accumulate glucose from the host RBC using a glucose transporter

thus providing the substrate required to trigger and promote the glycolytic pathway.[258, 259] Many of the glycolytic enzymes such as aldolase, hexokinase and phosphoglycerate kinase are regulated by Mg^{2+} due to activity promoted by chelation to this divalent metal making it the foundation of glycolysis and ATP production within *P. falciparum*. Especially since mitochondrial ATP synthase was reported by Sturm *et al* not to be essential for blood-stage energy production this emphasises the importance of glycolysis to generate substantial energy for the parasite.[260] In addition, Mg is involved in protein biosynthesis, generation of essential building blocks, cell production, assists in transport across the cell membrane as well as plays as role in cellular redox homeostasis, all of which contribute to the survival and functioning of the parasite thereby emphasising the need for Mg during the intraerythrocytic cycle.

3.3.3.3. Total Zinc

Zn has been shown to play prominent roles in various cellular processes ranging from enzyme regulation to gene expression and translation but is still not a well understood transition metal in the protozoan pathogen relation with humans.[261] Approximately 10% of the human proteome was reported to contain Zn-binding proteins of which the most abundant class were Zn-fingers.[262] Additionally, the *Plasmodium* genome encodes for over 200 transcription factors and proteins that require Zn to promote activity thus indicating that Zn has a potential role in malaria pathogenesis and disease progression.[135]

Total Zn was found to be 6 ± 0.7 fg/cell in RBCs which roughly translates to a concentration of 0.9 mM, a concentration in agreement with the accepted range of 0.9 to 1.5 mM intracellular erythrocytic Zn. The amount of total Zn remained fairly similar to that of the control cells as the parasite developed from early (24 h) to mature (32 h) trophozoites (Figure 3.8). However, a gradual increase was detected as the parasite progressed from mature (32 h) to late-stage trophozoites (40 h) with a significant increase in Zn content (p = 0.0331) observed at the schizont stage (46-48 h). A 2 and 4-fold increase was observed in trophozoites isolated at the latter two time points respectively.

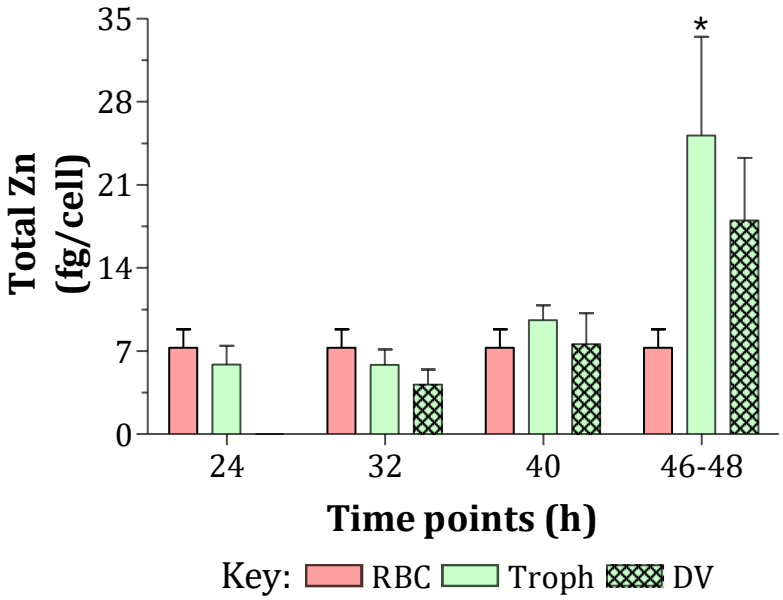

Figure 3.8. Distribution of total Zn in NF54 parasites as measured by ICP-MS, *N* = 3, error bars represent SEM. Asterisk displayed on the graph indicates statistical significance in comparison to the RBC control at specified confidence intervals using Student's two-tailed *t*-test (* denotes $p < 0.05$). Key: Red blood cells (RBC), trophozoites (Troph) and digestive vacuoles (DV).

Since the amount of measured Zn was higher than that present in RBCs, this indicates that this trace metal was obtained from external sources in addition to the host cell. The distribution of intracellular Zn can be seen in the Zn distribution map in Figure 3.9. At this stage the parasite occupies ≈60% of the RBC, this implies that the concentration of Zn would be higher in the parasite than in the host RBC. The measurements indicate that more than half of detected Zn is within the DV but with a fairly large standard deviation. Given that the DV occupies 50% of the parasite, it was not surprising that there was no discernible difference between parasite components in the Zn map but a distinct difference in Zn content between the parasite and RBC. This in turn suggests possible redistribution of this metal and a potential membrane transporter. Similar fold increases in Zn content was observed in a study carried out by Marvin *et al* where the amount of Zn increased with parasite stage.[216]

It is noteworthy to mention that discrepancies in absolute values would be expected since mixed stage pRBCs where used by Marvin *et al* to determine trace metal content whereas in the current study synchrony of stage-specific isolated parasitised cells were further ensured by enrichment using a Percoll gradient prior to isolation of parasite components.

Based on ICP-MS measurements, Zn content in the DVs isolated at each time point appeared to account for approximately 70% of that measured in the trophozoite.

Bearing in mind the role that the metalloprotease falcilysin plays in haemoglobin catabolism within the DV, this likely accounts for the detected Zn content as well as its role in cellular redox homeostasis. The observed increase of Zn in late-stage parasites coincides with cell division and proliferation which directly links with DNA replication. Zn is known to contribute to the stability of DNA therefore making it vital in DNA synthesis.[263] The specificity of Zn for this stage of the life cycle suggests that a major role is likely to be in transcription and nuclear processes involved in cell proliferation.

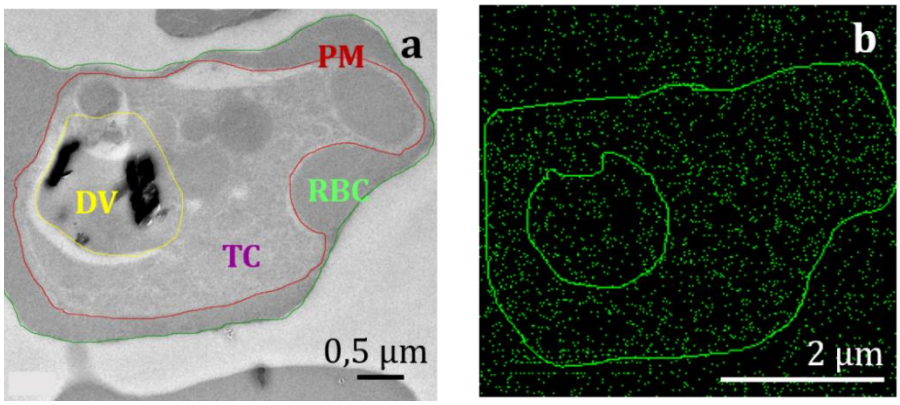

Figure 3.9. Transmission electron micrograph and corresponding Zn map of mature NF54 parasitised RBC. Section of a TEM micrograph representing the parasitised cell used for Zn mapping (a). ESI/EELS analysis showing the distribution of Zn throughout the parasite. Key: red blood cell (RBC), parasite membrane (PM), trophozoite cytoplasm (TC) and digestive vacuole (DV).

In a study reported by Marvin *et al*, parasite cultures were treated with *N,N,N',N'*-tetrakis(2-pyridylmethyl)-ethylenediamine (TPEN), a zinc chelator, which restricted the level of bioavailable Zn in the parasite. This showed that parasite growth was inhibited upon Zn depletion which in turn suppressed the mitochondrial membrane potential of the parasite.[216] Imaging studies carried out by Dooren *et a*l using fluorescent reporter proteins have illustrated that the mitochondrion undergoes a number of morphological changes over the asexual cycle.[30] The mitochondrion transforms from a simple tubular to ordered, branched structures and divides as the parasite matures in proportion to schizogony. Therefore, the observed increases in Zn at 48 h also correlates with enhanced

mitochondrial content and, since it has been shown that Zn depletion suppresses mitochondrial membrane potential, this further supports the importance of Zn in promoting successful parasite growth and replication.

3.3.3.4. Total Copper

Copper exhibits similar redox behaviour to that of Fe in that it is able to produce hydroxyl radicals under aerobic conditions by the Fenton reaction.[223] The formation of free radicals within an organism has deleterious effects in that these free radicals are able to induce oxidative damage at the molecular level by impairing lipids, proteins and DNA thereby making Cu homeostasis and the tight regulation thereof exceptionally important.[264]

Previously reported studies by Asahi *et al* explored the role of Cu ions in intraerythrocytic development of *P. falciparum*. These experiments illustrated that blood-stage parasites treated with a tetrathiomolybdate used to inhibit Cu binding proteins or neocuproine, a compound that selectively removes Cu^{+} ions, arrested and inhibited the progression of *Plasmodium* within RBCs indicating that Cu is essential for malaria parasite development and survival even if present in trace amounts.[224, 265, 266]

In the current study, isolated parasites were found to contain at least 3-fold more Cu than the RBC control (Figure 3.10). Total Cu measured in RBCs was found to be 0.4 ± 0.1 fg/cell. Total Cu gradually increased as the parasite developed over the intraerythrocytic cycle exhibiting a significant increase compared to the control cells suggesting that a portion of total Cu was likely taken up through additional sources and potentially redistributed within the parasite. A 2-fold increase in total Cu was observed in late stage trophozoites to schizonts making this finding similar to the trends observed in Cu content detected by Marvin *et al*. These findings are in contrast to studies indicating an expected decrease in total Cu in parasitised cells due to the Cu efflux pathway present in *P. falciparum.* However, the increase observed as the parasite matures from ring to trophozoite was in agreement with that observed in a study carried out by Rasoloson *et al* who measured Cu using AAS.[224] It is probable that a portion of detected parasite Cu was as a result of human Cu/Zn SOD which was delivered to the DV through the cytostome along with haemoglobin.

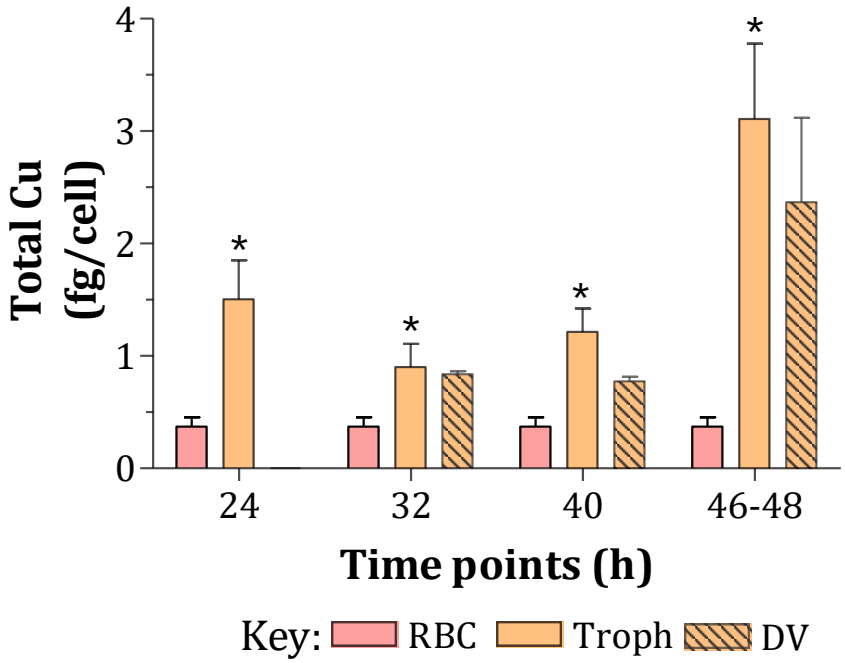

Figure 3.10. Distribution of total Cu in NF54 parasites as measured by ICP-MS, *N* = 3, error bars represent SEM. Asterisks displayed on the graph indicates statistical significance in comparison to the RBC control at specified confidence intervals using Student's two-tailed *t*-test (* denotes $p < 0.05$). Key: red blood cells (RBC), trophozoites (Troph) and digestive vacuoles (DV).

The known cytotoxicity of Cu suggests that the remaining Cu was in fact present at levels biochemically safe for the parasite and required for physiological functions. Bioavailable Cu is known for its importance as a cofactor and to activate certain mitochondrial enzymes. The significant increase in Cu content was detected during the rapid cell division period of the intraerythrocytic cycle whereby increased mitochondrial content is known to coincide with this phase, thereby requiring the increase in Cu. DVs appear to concentrate Cu with over 60% of detected Cu residing in the DV as the parasite develops. The acquisition and distribution of Cu is not comprehensively understood, but these findings provide a preliminary step towards understanding the role this trace metal plays.

3.3.3.5. Total Manganese

Mn is the 25th most abundant element found on earth located next to Fe in the periodic table with the ability to access a variety of oxidation states thereby making it an exceptional redox-active metal. At the cellular level, Mn is required in minute amounts to

maintain homeostasis which in turn promotes proper cell functioning. The role of Mn is understood to a certain degree in bacterial cells ranging from being a cofactor in mitochondrial SOD in *Streptococcus pneumoniae* to regulating Fe homeostasis in *Bradyrhizobium japonicum,* but little is known about the presence or even fate of Mn in the malaria parasite.[267, 268]

Control RBCs were found to contain 0.08 ± 0.03 fg Mn/cell (Figure 3.11). Mn content in from early to mid-stage trophozoites (0.09 ± 0.006 to 0.1 ± 0.02 fg Mn/cell respectively) were similar to that of the RBC with an increase observed in 40 h trophozoites; however, no significant changes were observed between these time points as well as in comparisons to the control. A significant increase (p = 0.013) was found at the schizont stage where Mn content was found to be 0.5 ± 0.1 fg/cell, exhibiting a 5-fold increase compared to the control and early trophozoites. Approximately 45-60% of Mn was found to be represented by the trophozoite as the parasite matured. Since the trophozoite represents intact parasites inclusive of the DV, significant differences were observed between parasite components and Mn was found to concentrate within the DV (Figure 3.11).

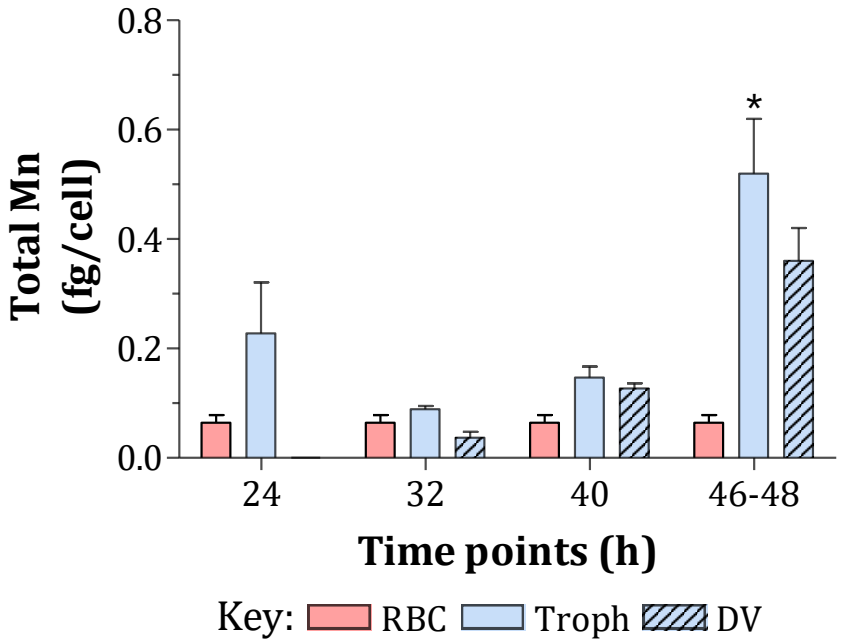

Figure 3.11. Distribution of total Mn in NF54 parasites as measured by ICP-MS, *N* = 3, error bars represent SEM. Asterisk displayed on the graph indicates statistical significance in comparison to the RBC control at specified confidence intervals using Student's two-tailed *t*-test (* denotes $p < 0.05$). Key: red blood cells (RBC), trophozoites (Troph) and digestive vacuoles (DV).

Even though Mn was found to be one of the least abundant trace metals investigated in this study (total Mn remaining below 0.7 fg/cell), the significant increase observed at the schizont stage coincides with schizogony. At this point there would be intense cellular energy demands in order to prepare the parasite for egress. It is possible that Mn is required in higher amounts during this period for energy production and protein synthesis to enhance cellular machinery; therefore, the parasite obtains excess amounts from an external source.

Additionally, due to the parasite living in two different hosts, rapid cell proliferation, short lived life cycle as well as rapid haemoglobin degradation produces a variety of free radicals or reactive oxygen species (ROS) within the parasite.[60] The parasite has an extensive network of redox proteins and enzymes located at specific points within the cell from thioredoxins to SODs.[269] Since only a percentage of the *Plasmodium* genome has been functionally annotated, it may be speculated that there exists a Mn-SOD within the DV to aid in combatting the ROS and free electrons formed during haemoglobin degradation as a result of haem oxidation thereby accounting for the DV containing most of the measured Mn content. Also, the increase as seen with Zn corresponds to an increase in mitochondria which contain Mn-SOD thereby suggesting the role Mn plays at this specific time point in the parasite life cycle.

3.3.4. Metal distribution across parasite strains

Having observed changes in trace metal content over the intraerythrocytic stage which suggest that these are appropriately orchestrated by the parasite itself in order to meet its needs to allow for survival and growth, a similar study was carried out looking at the trace metal content across different strains of *P. falciparum*. Trophozoites were isolated from three different strains in addition to CQS NF54 at 32 h post invasion. This specific time point was chosen as it is the most metabolically-active stage of the intraerythrocytic cycle and represents mature trophozoites. The CQS D10, CQR Dd2 and MDR K1 strains of *P. falciparum* were cultured and processed in the same manner as done in the NF54 study discussed above.

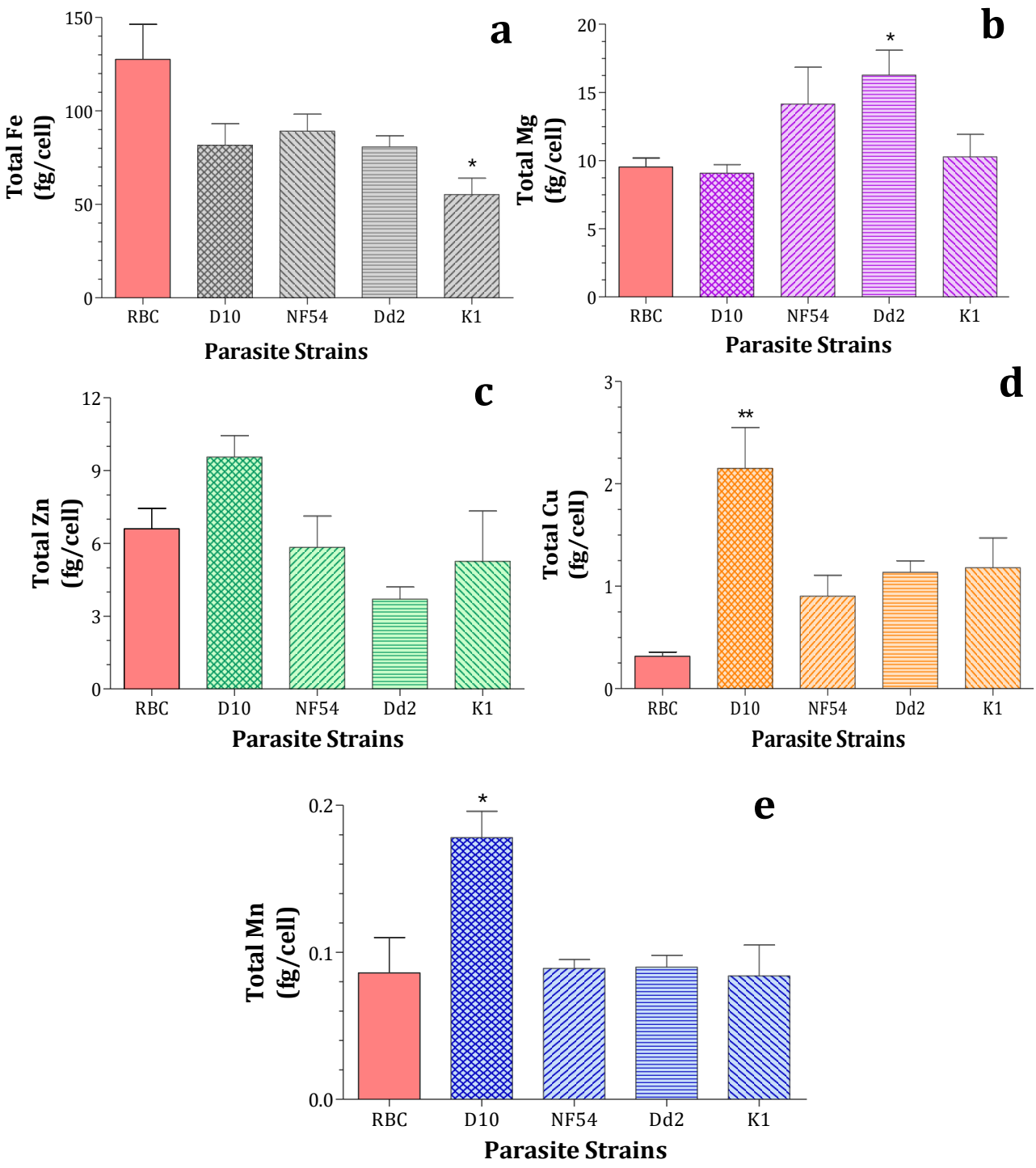

Figure 3.12. Distribution of trace metals measured across different parasite strains at 32 h post-invasion, *N*=3, error bars represent SEM. Distribution profiles of **(a)** Fe, **(b)** Mg, **(c)** Zn, **(d)** Cu and **(e)** Mn detected in isolated trophozoites compared to control RBCs. Asterisks displayed on graphs indicate statistical significance at specified confidence intervals using one-way ANOVA analysis (*denotes $p < 0.05$, ** denotes $p < 0.01$).

Trace metal content measured in control RBCs shows Fe to be the most abundant with similar much lower levels of Mg and Zn and trace amounts of Mn (Figure 3.12). The Fe distribution profile represented by Figure 3.12a illustrated that total Fe detected in isolated trophozoites across different strains exhibited no significant differences compared to that of the control RBCs with the exception of K1 (p = 0.018). This MDR strain had a low Fe content of 55 ± 9 fg/cell representing only 40% of that of the RBC whereas the other stains averaged approximately 66% of the control cell at the same time point. This could be representative of slower growth of the K1 strain, or inherently reduced digestion of haemoglobin in this strain. However, comparison of total Fe content across the other four strains showed these to be similar with no significant differences observed and extrapolating from the NF54 study it was expected that majority of Fe localised in the DV.

With respect to Mg, D10 was the only strain with a similar amount of total Mg when compared to the RBC whereas the other three strains had Mg present higher than that of the control as illustrated in Figure 3.12b. Interestingly Dd2 parasites exhibited the most significant difference. At this 32 h time point, the amount of total Zn detected in isolated trophozoites did not differ significantly from the control cell; however, the CQS D10 was found to have the higher Zn content whereas CQR Dd2 had the lowest (Figure 3.12c).

Turning to Cu (Figure 3.12d), in all cases total Cu measured was higher in the parasite than the RBC with a significant difference observed in D10 parasites (p = 0.005). Overall, D10 appears to accumulate the most Cu compared to other strains which all contain approximately half of the total content found in D10. A similar trend was observed for Mn content between RBC and D10 parasites (p = 0.01) whereas the other strains were found to have a similar content to the control (Figure 3.12e). Total Mn content in D10 trophozoites was found to be significantly different (p = 0.005) to that observed in NF54, Dd2 and K1 trophozoites, indicating that D10 may have a different metal uptake system or trace metal requirements.

3.4. Chapter Summary

Trace metals were measured across parasite compartments as well as uninfected RBCs by ICP-MS. This technique provided the required sensitivity and allowed for simultaneous multi-element detection. Five trace metals were successfully measured of which, as expected, Fe was found to be the most abundant with smaller amounts of Mg, Zn, Cu and Mn constituting the remaining portion. Elemental mapping by ESI/EELS illustrated that Fe localised in the DV of the parasite in the form of haemozoin crystals. Trace metals monitored over the intraerythrocytic stage of the parasite's life cycle showed that the amount of Fe remained limited by the RBC, whereas levels of Mg, Zn, Cu and Mn all increased as the parasite developed from late trophozoite to schizont stage. This suggests that these trace metals are essential in influencing the growth stages specific to cell proliferation and preparation of the parasite for egress.

Comparison of trace metal content across various strains of *P. falciparum* revealed that the CQS D10 contained a different metal profile in terms of amount and distribution compared to the other three strains. Lower trace metal content was observed in the CQR and MDR strains. Overall, these studies explored the trace metal content and differences between strains thus providing a preliminary view into the metal distribution of *P. falciparum.* The noted differences could reveal possible novel pathways that could be potential parasite strain or stage-specific drug targets. The accumulation of free metals would be toxic to the cell; therefore, it is unlikely that the total trace metal content exists in free form within the parasite. The next chapter will focus on identifying potential metal containing proteins and enzymes to gain further insights into the *Plasmodium* metallome.

Chapter 4

An Investigation of the Digestive Vacuole Metalloproteome

4.1. Introduction

Proteins are complex macromolecules responsible for crucial cellular activity and a variety of chemical reactions across living systems. Changes in gene expression levels make the proteome intricate and dynamic as it undergoes temporal modifications based on the environment as well as in response to cellular demand. The variation in polypeptide side chains making each protein unique in structure and function is brought about by the amino acid composition. The unique sequence of amino acids constituting a protein partially governs its potential chemical reactivity. Furthermore, functional diversity is enhanced by the natural ability of proteins to incorporate cofactors into their active sites. These cofactors exist as small organic molecules such as haem or flavin or as inorganic ions or molecules in the form of metal ions or metal clusters. Metalloprotein refers to the sub-set of proteins where metal ions are essential for correct protein folding or activity whereby sulfur, oxygen or nitrogen atoms of amino acid residues coordinate to specific metal ions.[270]

Approximately a quarter to a third of all proteins require at least one transition metal cofactor for structural stability or function.[271, 272] Metal ions promote structural integrity, play an imperative role in detoxification processes and act as redox centres. Well known metalloproteins such as haemoglobin and metalloenzymes such as superoxide dismutase are responsible for a variety of essential functions from oxygen transport to antioxidant defence.[273, 274] In living organisms, the intracellular metal content exists in a steady state; however, pathogenic infection by organisms such as bacteria or fungi perturbs this steady

state resulting in continuous competition for metalloproteins at the host-pathogen interface.

Maintaining metal homeostasis upon infection prevents the host from experiencing the metabolic disadvantages of metal deficiency or accumulation, thus reducing toxicity whilst activating the innate immune response.[275] Studies have illustrated the importance of divalent metals such as Zn^{2+}, Fe^{2+}, Cu^{2+} and Se^{2-} in infectious diseases where non-related organisms such as *Staphylococcus aureus* and *Neisseria spp* scavenge host metalloproteins as a nutrient source.[276, 277] Similarly, in *Escherichia coli*, the siderophore yersiniabactin chelates host Cu^{2+} thus preventing reduction to the toxic Cu^{+} species enabling survival within the host.[278]

Thus far, little is known about the metalloproteome of *P. falciparum*, specifically with relation to the DV, as the main focus has been on understanding iron distribution within the parasite since this aligns with the haem detoxification pathway and haemozoin formation, both of which are ingenious parasite survival mechanisms that are still not fully understood.[279] Having observed trends in metal distribution over the intraerythrocytic life cycle of *P. falciparum* (Chapter 3), this chapter focuses on using a proteomic-based approach to investigate the proteome and metalloproteome associated with the DV. Understanding both the proteome and its inorganic complement are essential steps in attempting to elucidate the survival mechanisms unique to the malaria parasite. Tandem mass spectrometry was employed to gain insight into the proteins specifically associated with the surface of, and those found in, dissolved haemozoin crystals as a sample of DV content. The qualitative and semi-quantitative proteomic profiles pertaining to specific parasite fractions will be discussed.

4.2. Experimental Methods: Label-Free Quantitative Proteomics

All experimental methods used in this chapter with the exception of label-free quantitative proteomics are described in detail in Chapter 2.

4.2.1. Preparation of In-Solution Samples

In-solution samples (trophozoite cytosol, DV lumen, haemozoin wash and dissolved haemozoin) were precipitated overnight with ice cold acetone in a ratio of sample to acetone of 1:5 (*v/v*). The resulting solution was centrifuged at 12 000 g for 10 min pelleting out protein, the supernatant discarded, and the pellets allowed to air dry at room temperature. All pellets except for dissolved haemozoin sample were dissolved in 0.1 M triethylammonium bicarbonate (TEAB) containing 4 M guanidine-HCl and 1% octylgluco-mano-pyranoside. The dissolved haemozoin pellet was solubilized in 0.1 M TEAB containing 4 M guanidine-HCl, 1% octylgluco-mano-pyranoside supplemented with 0.02 M EDTA. Protein concentration was determined using a NanoDrop™ UV Spectrophotometer (Thermo Fisher Scientific) measuring absorbance at 280 nm. Samples were adjusted to the lowest measured concentration prior to digest.

4.2.2. In-solution digest

Protein samples were reduced using 0.05 M triscarboxyethyl phosphine (TCEP) in 0.1 M TEAB for 30 min at 37 °C. Following reduction, the cysteine residues were modified to methylthio derivatives using 0.2 M methane methylthiosulphonate (MMTS) in 0.1 M TEAB for 30 min. After modification, the samples were diluted to 98 µl with 0.1 M TEAB. Proteins were digested by adding 10 µL trypsin solution (1 µg/µL, Promega) and were incubated at 37 °C overnight. The samples were then dried down and resuspended in 30 µL of a solution comprising 2% acetonitrile: water and 0.1% formic acid. Desalting was performed as previously described in Section 2.5.11 to remove residual digest reagents.

4.2.3. Liquid Chromatography

Liquid chromatography was performed on a Thermo Scientific Ultimate 3000 RSLC equipped with a 2 cm × 100 µm C_{18} trap column and a 35 cm × 75 µm in-house manufactured C_{18} (Luna C_{18}, 5 µm; Phenomenex) analytical column. The solvent systems employed were:

Loading: 2% acetonitrile:water; 0.1% formic acid

Solvent A: 2% acetonitrile:water; 0.1% formic acid

Solvent B: 100% acetonitrile:water

The samples were loaded onto the trap column using loading solvent at a flow rate of 5 µL/min from a temperature controlled autosampler set at 7°C. Loading was performed for 10 minutes before the sample was eluted onto the analytical column. Flow rate was set to 350 nL/min and the gradient generated as follows: 2.0% A for 6 min; 2-35% B from 6-140 min using Chromeleon non-linear gradient 7, 140-150 minutes 35-50% B and 50-80% B from 150-160 min. Thereafter the column was washed for 10 min with 80% B followed by equilibration. Chromatography was performed at 50°C and the outflow delivered to the mass spectrometer through a stainless steel nano-bore emitter.

4.2.4. Mass Spectrometry

Mass spectrometry was performed using a Thermo Scientific Fusion mass spectrometer equipped with a Nanospray Flex ionization source. The sample was introduced through a stainless-steel emitter. Data were collected in positive mode with spray voltage set to 1.9 kV and ion transfer capillary set to 275°C. Spectra were internally calibrated using polysiloxane ions at m/z = 445.12003 and 371.10024. MS1 scans were performed using the orbitrap detector set at 12 000 resolution over the scan range 350-1650 with AGC target at 2×10^5 and maximum injection time of 50 ms and data acquired in profile mode. MS2 acquisitions were performed using monoisotopic precursor selection for ions with charges +2 to +7 with error tolerance set to ± 10 ppm. Precursor ions were excluded from fragmentation once for a period of 45 s. Precursor ions were selected for fragmentation in HCD mode using the quadrupole mass analyser with HCD energy set to 35%. Fragment ions were detected in the ion trap mass analyser using rapid scan rate. The AGC target was set to 5×10^4 and the maximum injection time to 50 ms. These data were acquired in centroid mode.

4.2.5. Data Analysis

The raw files generated by the mass spectrometer were imported into Proteome Discoverer (Version 1.4, Thermo Scientific) and processed using the Mascot algorithm (Matrix Science), as well as the SequestHT algorithm included in Proteome Discoverer. Data analysis was structured to allow for methylthio as fixed modification as well as NQ deamidation (NQ), oxidation (M), N-terminal acetylation. Peptide validation was

performed using the percolator node set to search against a decoy database with strict FDR 1%. An additional analysis was performed using X!Tandem Sledgehammer (2013.09.01.1) algorithms. For quantitative analysis, Mascot and Sequest were used with settings as before. Database interrogation was performed against both the Uniprot *H. sapiens* database (2014 edition) and *P. falciparum* (2015) with trypsin cleavage allowing for 2 missed cleavages. The output files generated were combined for statistical analysis and quantitation using Scaffold (Version 4.4.1.1 Proteome Software Inc.). Quantitation were set to spectral counting with normalization and regulation reported as fold change per category (fold change times $p \leq 0.0002$) and Holm-Bonferroni correction. Protein filter settings were FDR at 5% with minimum of 3 peptides per protein.

4.3. Results and Discussion

4.3.1. Probable origin of proteins associated with the DV

Various parasite components were isolated from NF54 strain *P. falciparum* following a fractionation approach in an attempt to reduce the complexity of parasite material. This was also done to minimise contamination by cellular debris in order to identify proteins specifically associated with the respective compartments. Following saponin lysis and trituration, respectively, trophozoites and DVs were monitored by TEM during the isolation process. Electron micrographs of isolated trophozoites (Figure 4.1a) revealed a double membrane present which likely represents the outer PVM and the inner PPM. In certain cases, a third membrane was observed external to, but in close contact with the PVM which likely represents the RBC membrane indicating the presence of RBC ghosts which was expected following saponin lysis. Incubation of RBCs with saponin in an isotonic buffer solution is known to permeabilise the RBC membrane and stimulate haemolysis and in some cases, this results in remnants of RBC membranes that may be present, commonly referred to as RBC ghosts.[280]

DVs obtained by trituration were dispensed onto a glow-discharged copper grid and imaged by TEM. Spherical bodies approximately 1 μm in diameter containing black crystals were observed (Figure 4.1b).[281] These spherical bodies represented intact DVs that appeared to be free of contaminating organelles and membranes. The purified DV preparation was then used to isolate haemozoin crystals following multiple freeze-thaw

processes as described in Section 2.5.7. Isolated haemozoin, approximately 300-500 nm in length, was extensively washed with solutions of SDS and PBS to liberate proteins associated with the surface of the crystals prior to base dissolution. During washing, isolated crystals were monitored by TEM (Figure 4.1 c and d) to ensure that they were free from cellular matter.

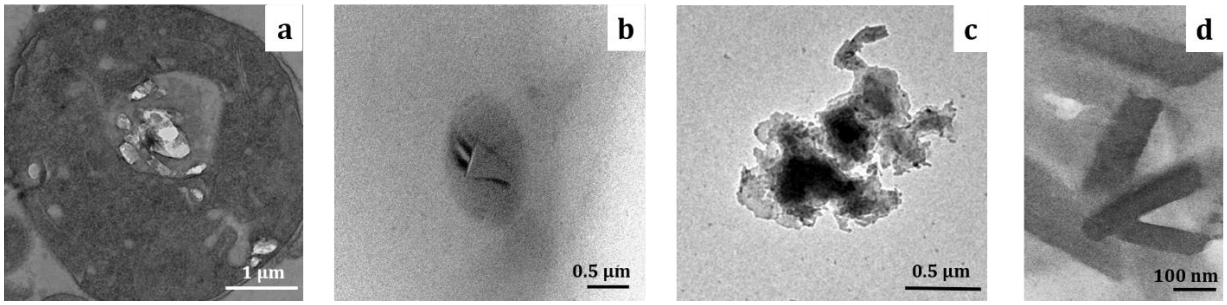

Figure 4.1. Transmission electron micrographs of parasite isolates from NF54 *P. falciparum.* (a) Representative image of a section of isolated trophozoites following saponin lysis of pRBCs embedded in Spurr's epoxy resin. **(b)** Purified DVs after trituration, **(c)** haemozoin crystals liberated from purified DVs following freeze-thaw cycles and **(d)** after extensive washing.

The asexual intraerythrocytic life cycle begins with invasion of RBCs by *P. falciparum.* Upon schizont rupture, merozoites are released into the blood stream and seek to re-invade new RBCs within minutes. The complex surface of the merozoite comprising an array of proteins including ligands and antigens are key components in promoting invasion.[282] Invasion begins when the merozoite attaches to the RBC using its surface proteins and orientates into optimum position to allow the apical end to be in direct contact with the cell surface (Figure 4.2a). The RBC surface undergoes various modifications upon interaction and attachment of the merozoite brought about by a unique sequence of recognition events.[283] Once the merozoite is in the correct position, rhoptries secrete its contents into the cell forming tight junctions leading to the development of the growing parasitophorous vacuole. Invasion proceeds via the merozoite actin-myosin motor which allows the merozoite to burrow into the RBC cytoplasm (Figure 4.2b).[284]

The merozoite continues to make its way into the RBC cytoplasm whilst shedding off its surface proteins with the process culminating in resealing of the RBC membrane (Figure 4.2c).[285] Since merozoite invasion leads to formation of the parasitophorous vacuole, one would expect a combination of merozoite and RBC membrane proteins to ultimately be

trafficked to the DV which are likely to be identified as part of protein milieu directly associated with haemozoin.

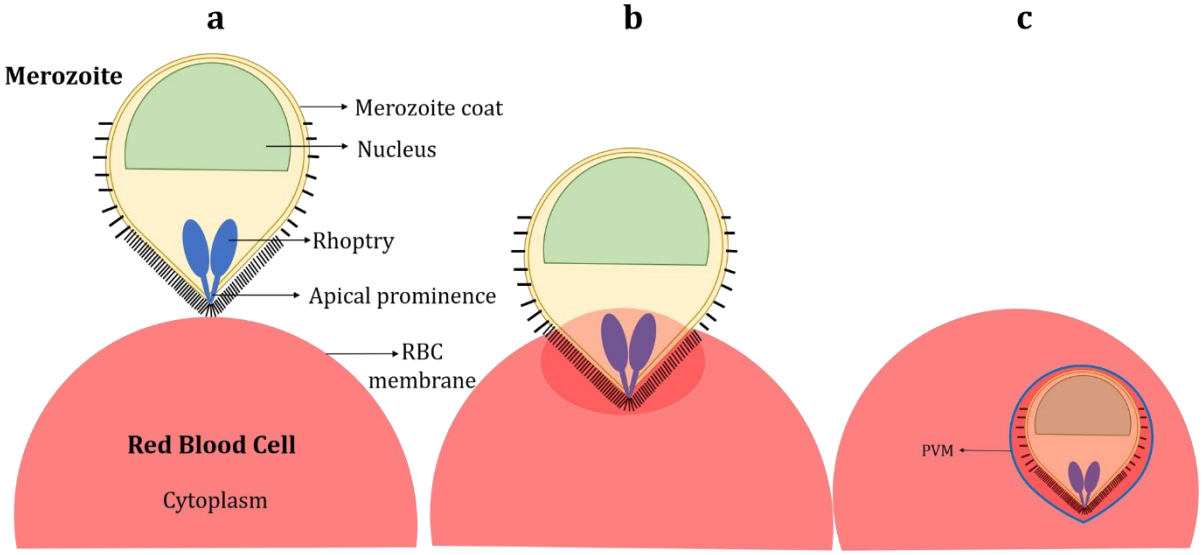

Figure 4.2. Schematic representing merozoite invasion of the host red blood cell. **(a)** Merozoite orientates itself with respect to the RBC in preparation for attachment to the host cell surface. **(b)** Using its own cell machinery, the merozoite burrows into the red blood cell until it enters the cytoplasmic space. **(c)** Merozoite located within the RBC following successful invasion and enclosed within the newly formed parasitophorous vacuole membrane (PVM).

RBCs containing haemoglobin, the major metalloprotein component accounting for approximately 95% of dry cell weight, are enclosed by a plasma membrane. Following invasion, the parasite begins to feed on the host cytoplasm by taking up pockets of haemoglobin thereby triggering the haemoglobin trafficking and degradation pathway which is essential for parasite development and survival as highlighted in Chapter 1. Haemoglobin is trafficked (Figure 4.3) into the parasite through the formation of the cytostome, which is an invagination of the PVM and PPM. As the parasite develops from ring to trophozoite stage, several of these acidic, double-membraned HCvs coalesce to form a single-membrane DV where haemoglobin digestion and haemozoin formation occur.[24, 42] As the parasite matures and engulfs more haemoglobin, these HCvs continue to be trafficked to the DV which fuse with the DVM thereby releasing their contents into this lysosomal organelle.

Due to the way in which haemoglobin trafficking within the parasite occurs, it is noteworthy to mention that RBC membrane and cytoplasmic proteins, parasite-specific

proteins present in the PVM, PPM and cytoplasm as well as excreted parasite proteins are likely to constitute the protein component delivered to the DV and subsequently be identified in the current proteomic study. During isolation of parasite components and cell lysis, a number of organelle-derived proteins such as those from the nucleus, mitochondrion, ribosomes and ER, are also to be expected to be detected as these would likely be carried through as contaminants. The haemozoin samples would not be expected to be enriched in RBC and parasite proteins not related to its formation, however, since these crystals were washed only using detergent and not organic solvents, they may contain remnants of DVM material.

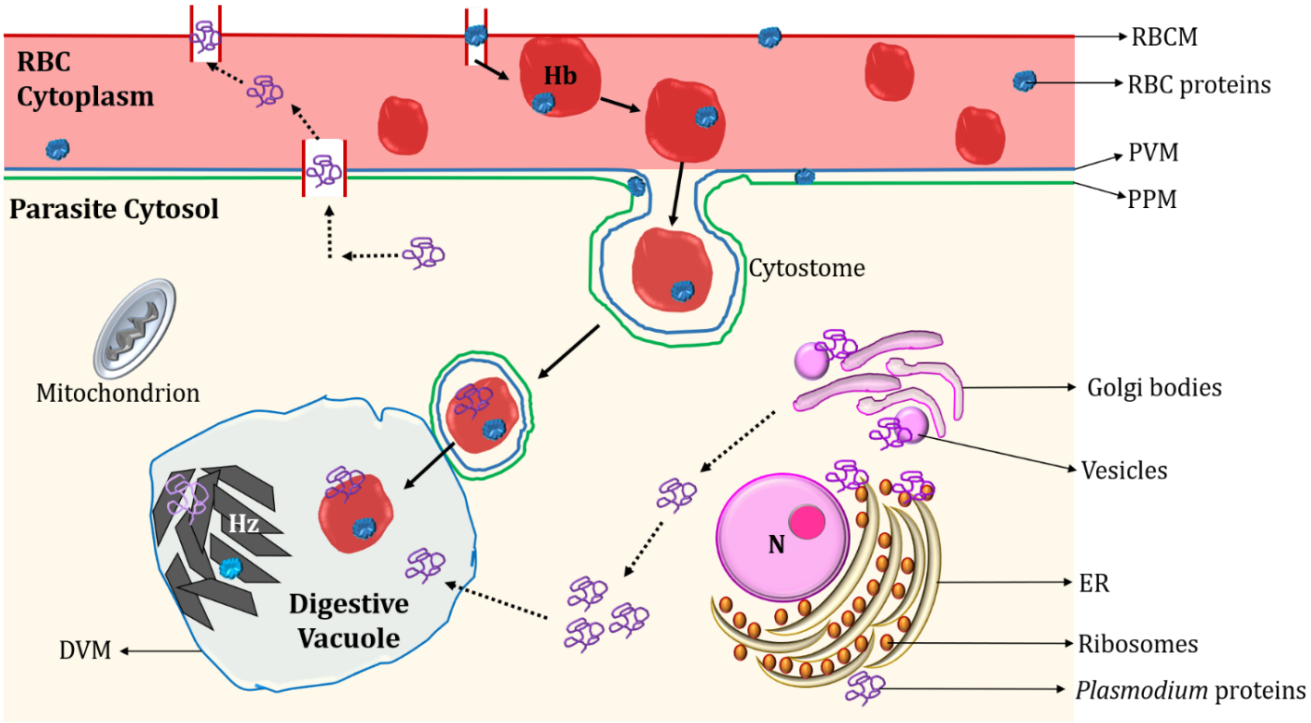

Figure 4.3. Schematic representing protein trafficking in a parasitised red blood cell. Haemoglobin is engulfed by the parasite through cytostome formation and trafficked to the DV where haemozoin formation occurs. There is constant import of host proteins into the parasite and export of parasite proteins to modify the RBC as the parasite develops over the asexual cycle. The main focus of this study was to identify the proteins associated with haemozoin crystals highlighted in the DV. Key: Red blood cell (RBC), haemoglobin (Hb), red blood cell membrane (RBCM), parasitophorous vacuole membrane (PVM), parasite plasma membrane (PPM), haemozoin (Hz), digestive vacuole membrane (DVM), nucleus (N), endoplasmic reticulum (ER), solid arrows represents protein trafficking of host proteins, dashed arrows represent trafficking of parasite proteins.

4.3.2. A Label-Free Quantitative Proteomic Approach

Identifying and characterising proteins by their individual amino acid sequence following proteolytic digestion prior to mass spectrometry is classically termed as 'bottom-up' proteomics.[286] This approach offers better sensitivity with respect to upfront separation of peptides in complex biological samples. As mass spectrometry methods gained more popularity and began to greatly influence the field of proteomics, the evolution of quantitative proteomics resulted in the need for technological advancements to determine protein abundance across various organisms and protein isolates. In response to this need, stable isotope labelling methods were developed, some of which include Stable Isotope Labelling in Cell Culture (SILAC), Isotope-Coded Affinity Tag (ICAT), Isobaric Tags for Relative and Absolute Quantification (iTRAQ) amongst many other chemical labelling approaches. However, the high costs associated with isotope labelling, increased complexity and time spent on sample preparation, variation and, in some cases, incomplete labelling, as well as the challenges associate with detecting low abundant peptides, resulted in labelled proteomics being a suboptimal approach.

In contrast to labelled proteomics, label-free quantification is a mass spectrometry method that is focused on determining relative protein abundance in two or more biological samples without the incorporation of chemical tags that bind to proteins. Quantitative label-free protein approaches have gained popularity in attempting to overcome and improve the drawbacks associated with labelling methods as mentioned earlier. All label-free proteomic methods consist of a fundamental work flow incorporating sample preparation (consisting of protein extraction, reduction and alkylation), enzymatic sample digestion, separation of peptides by liquid chromatography, mass spectrometry analysis and lastly, data analysis incorporating peptide identification, quantification and statistical analysis as described earlier in Section 4.2. Samples were prepared independently and subjected to individual LC-MS/MS runs after which quantification proceeded by employing one of two methods, viz. measuring the peak ion intensity or spectral counting.[287] For the purpose of the current study, the latter will be discussed further.

Spectral counting infers the quantity of proteins based on the number of spectra that correspond to that specific protein. In other words, spectral counting estimates the relative protein abundance by counting the number of unique MS/MS spectra that

confidently represent peptides used to identify a protein. Studies carried out by Liu *et al* demonstrated a positive linear correlation between protein abundance and spectral counts thereby suggesting that the more abundant a protein is, the higher the number of proteolytic peptides there are in a specific sample.[288] Normalisation of relative protein abundance focuses on the summation of total spectral counts which accounts for potential variation across multiple mass spectrometry runs.

Turning to the current study, samples were derived from *Plasmodium*-infected erythrocytes and a fractionation approach was used to isolate various parasite components for proteomic analysis. The aim was to investigate what metalloproteins and metalloenzymes may be associated with the elements measured in the previous chapter in terms of identity and abundance. A mixed culture of mature trophozoites and early schizonts were fractionated as described earlier in Sections 2.5.2-2.5.4. T_{CYT} represents the trophozoite cytoplasm following DV isolation which includes associated cellular content like the apicoplast, mitochondrion and ribosomes and could possibly contain intact as well as lysed DVs in trace amounts.

Owing to the ongoing debate as to which biomolecules are responsible for haemozoin formation, the ideal approach would be to obtain pure haemozoin and release any material entrapped by the crystal matrix to reveal what was incorporated at the time of haemozoin formation. Guerra *et al* have recently reported that even after treatment of isolated crystals with detergent washes and proteases, biomaterial appeared to be strongly adsorbed to the crystal surface suggesting that it is unlikely that the surface of haemozoin could ever be completely free of contaminants.[160] Complementary techniques were then used in an attempt to identify this biological composition; however, the methods used were only capable of confirming that the biomaterial consisted of carbon rich molecules but not whether these were lipids or proteins. It is important to note that the organic material that strongly adhered to the crystal surface may have been present at the time and site of nucleation and were possibly incorporated into the crystal matrix as is commonly seen to occur in other unrelated organisms where biomineralisation processes occur as discussed in Chapter 1.

In this study, haemozoin crystals were washed extensively with a 4% SDS solution and then dissolved in 0.1 M NaOH. The SDS wash released proteins presumed to be associated with the surface (Hz_{SP}) while proteins present in the dissolved haemozoin fraction were

presumed to represent proteins that strongly adhere to the surface of haemozoin, those incorporated in the crystal matrix or both (Hz_{Dis}). The DV excluding haemozoin represents the DV lumen and DVM (DV_{LM}). Post analysis, proteins belonging to DV_{LM}, Hz_{SP} and Hz_{Dis} were grouped together for simplicity and represented the DV unless otherwise stated. Parasite fractions were maintained in-solution and subjected to trypsin digest following the estimation of protein concentration across samples. Sample digest was deemed satisfactory as supported by the total ion chromatogram. Peptide sequences were processed, identified and quantified using Scaffold Proteome Discoverer where the spectral counting approach was employed for analysis of all in-solution samples and the data were normalised using total spectrum count. Target proteins were also analysed and validated against a decoy concatenated database which was constructed by reversing the protein sequences to account for false positive results. These predicted false positives also lead to the false discovery rate (FDR) which provides confidence in generated data.

4.3.3. Global overview of proteins identified by label-free proteomics across all parasite fractions

The *Plasmodium* genome encodes for over 5 000 proteins; therefore, any proteomic analysis of parasite isolates would result in lists amounting to thousands of identified proteins. In an attempt to restrict and obtain a more focused protein data set, the current data was analysed by applying protein filters which considered the minimum number of peptides as well as protein and peptide thresholds. At first, stringent settings incorporating 4 peptides at a 99% minimum protein threshold and a 9.9% FDR afforded a list of 177 *Plasmodium* proteins. However, most of the proteins identified were of ribosomal or nuclear origin and could be classified as expected contaminants carried through the isolation process.

By relaxing the search filters to 2 peptides at a 95% minimum protein threshold and a 49.7% FDR, a list of 1 102 *Plasmodium* proteins were generated. Due to the high FDR, 371 proteins were identified as decoy sequences and were discarded, thereby resulting in 731 unique proteins forming the parasite specific dataset. In the case of human proteins, stringent filtering criteria were maintained throughout which identified erythrocyte-specific proteins. Settings employed were 5 peptides at a 99% minimum protein threshold and a 95% peptide threshold which afforded a list of 175 human proteins.

Overall, a total of 906 proteins were identified across samples of which 731 (80.68%) and 175 (19.32%) represented *P. falciparum* and *H. sapiens* respectively.

Plasmodium proteins were interrogated against protein databases (PlasmoDB, UniProt) in order to obtain characteristic protein information. As mentioned above, a total of 731 parasite proteins were found; however, only 227 were characterised proteins and the remaining 504 constituted the putative uncharacterised group. This large number of uncharacterised proteins was not surprising since only about 40% of the *Plasmodium* genome has been fully functionally annotated resulting in the remaining set yet to be supported by experimental evidence. The uncharacterised proteins were classified by subcellular location and function based on similarity and predictions reliant on gene sequences and, in some cases, a single protein was assigned more than one function.

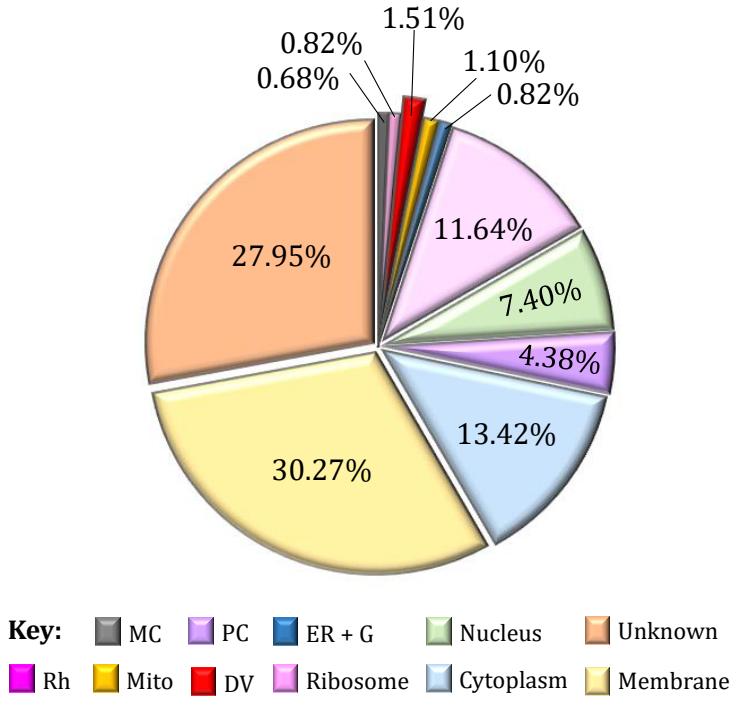

Figure 4.4. Pie chart illustrating the percentage distribution of detected *Plasmodium* proteins by subcellular location. Key: Maurer's cleft (MC), protein complexes (PC), endoplasmic reticulum and Golgi (ER + G), rhoptry (Rh), mitochondria (Mito) and digestive vacuole (DV).

Analysis of all identified proteins revealed the putative subcellular location and compartmentalisation of 526 (72.05%) proteins whereas 204 (27.95%) remained unknown. Of the categorised proteins, approximately 70% were found to be membrane associated or located in organelles such as the mitochondria, endoplasmic reticulum,

Golgi bodies, nucleus or ribosomes as illustrated in Figure 4.4. Of the remaining proteins, approximately 7% were DV specific, 7% were rhoptry- and Maurer's cleft-associated, 20% represented protein complexes and the remaining 65% were found to be cytoplasmic proteins. Due to limited information available regarding hypothetical proteins, only 65% of the identified proteins were characterised by their respective biological functions or processes in which they are involved while the remaining 35% were unknown. Of the characterisable subset, approximately 15% were assigned to each of the functions related to pathogenesis, metabolic processes and enzymatic activity (Figure 4.5). About a third of proteins were involved in translation, transport including chaperone activity as well as binding of molecular subunits and cofactors; namely, DNA, GTP and ATP. Approximately 10% were found to be metal-associated proteins and 4% were involved in cellular redox homeostasis with the remaining proteins constituting smaller fractions representing structure, protein folding and catalytic activity.

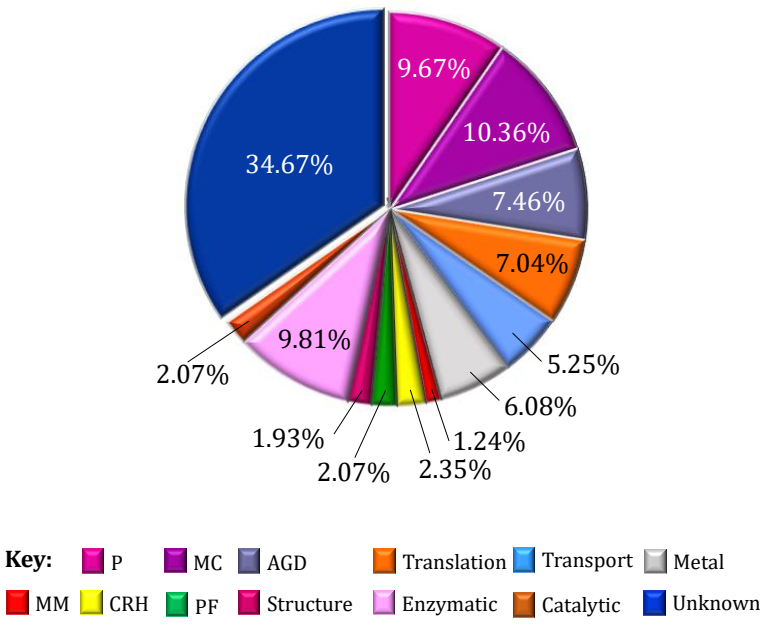

Figure 4.5. Pie chart illustrating percentage distribution of detected *Plasmodium* proteins by function or process. Key: Pathogenesis (P), metabolic pathways and cellular processes (MC), ATP, GTP and DNA binding (AGD), metal ion binding (Metal), microtubule motor (MM), cell redox homeostasis (CRH) and protein folding (PF).

4.3.4. Semi-Quantitative Protein Profile

4.3.4.1. Insights into the proteins profiled by abundance

Of the 731 *Plasmodium* and 175 human proteins identified across T_{CYT} and DV fractions, semi-quantitative profiles were obtained for 171 and 112 proteins for each organism respectively. It is well known that analysis of complex biological samples is often accompanied by an array of challenges irrespective of the proteomic approach applied. Therefore, it was not surprising that when a label-free quantitative proteomic approach was applied to investigate the various parasite fractions, only a subset of proteins was successfully profiled in terms of relative abundance.

It is important to note that individual peptides in such a complex system as mentioned above are likely to exhibit diverse behaviour patterns when analysed by mass spectrometry; therefore, it is highly improbable that every single peptide will be identified in every fraction and injection.[289]A specific sample may contain thousands of peptides, yet only the most abundant of these are chosen during each MS experiment resulting in variation across injections. If a peptide is not 'quantified' in a specific injection corresponding to a sample replicate, it does not imply that the protein does not occur in the cell. There are a number of factors that affect the identity and quantification of proteins; in certain cases, proteins may not have digested optimally, there may be incomplete or poor fragmentation of peptides, hydrophilicity and size may cause loss of peptides during on-column fractionation thereby distorting mass spectrometry data to name just a few.[290] At times, peptides fragment in ways that result in complicated spectra that cannot be analysed; this is mainly influenced by lysine, arginine, proline and histidine amino acid residues which are problematic and often give incomplete fragmentation. Due to the AT-rich *P. falciparum* genome giving rise to the disproportionately high lysine content, it was expected that not all proteins would be identified.[181]

When using spectral counting, abundance profiles are determined after considering the applied normalisation factor during data analysis. Abundance data are reported as either high or low which is relative when comparing one sample to another. In some cases, one is unable to assign abundance as the specific peptides may be present just below the detection limit of the low-abundance peptides, a factor which is influenced by uneven protein loading per injection.[291] Several peptides are usually used to identify and quantify a specific protein; this process can be further influenced by peptides which tend to have

multiple elution patterns even though the same chromatographic conditions were employed as well as posttranslational modifications (PTMs) which affect the abundance of unmodified peptides.[290] Even though most of these factors have been accounted for by applying various filters during data analysis, these points need to be borne in mind when interpreting the abundance of proteins discussed below.

The semi-quantitative subset of *Plasmodium* and human proteins for which abundance profiles were assigned represent the relatively more abundant proteins present in T_{CYT} and DV fractions. Analysis of the 171 *P. falciparum* proteins in terms of subcellular location showed that approximately 35% of proteins were ribosomal and nuclear in origin as illustrated in Figure 4.6a. This distribution consisted mainly of the 40S and 60S ribosomal subunits and histones H2B, H4 and H2A which are core nucleosome components. This data was interrogated against PaxDb, a comprehensive absolute protein abundance database based on whole genome sequences from various organisms to gain insight into the abundance of specific proteins.[292] Eight of the most abundant *P. falciparum* proteins can be found listed in Table 4.1.

The information reported on PaxDb was obtained from five different datasets and represents a proteome consisting of 5 429 proteins. Histone H4, 2B and 60S ribosomal protein were found to be three of the highest abundance proteins in *P. falciparum,* with the other ribosomal subunits being almost as abundant and found present within a range of 400-5 000 ppm. The high abundance of these proteins makes it easy for carry through as contaminants during cell fractionation and sample preparation, making it almost impossible to completely free sample preparations of these proteins. Due to their overwhelming presence, the associated spectra may have overwhelmed the peptide signals of other proteins present, therefore resulting in potential loss of information regarding the identity of various other proteins present in the sample due to signal suppression which was unfortunately unavoidable.

Table 4.1. The most abundant *P. falciparum* proteins [a]

No.	Gene code	Protein Name	Abundance (ppm)
1	PFB0100c	Knob-associated histidine-rich protein	30 385
2	PfSBP1	Skeleton-binding protein 1	21 509
3	GAPDH	Glyceraldehyde-3-phosphate dehydrogenase	16 194
4	PF10_0084	Tubulin beta chain	13 200
5	PF11_0061	Histone H4	12 154
6	PF11_0062	Histone H2B	10 831
7	PF13_0346	60S ribosomal protein L40/UBI, putative	9 542
8	PFD0310w	Sexual stage-specific protein	8 150

[a] *Data obtained from PaxDb. Abundance values obtained from the whole organism (integrated) and reported in parts per million (ppm).*

Approximately 40% of parasite proteins were membrane- and cytoplasm-related with the remaining proteins associated with other organelles as illustrated in Figure 4.6a. Turning to the erythrocyte proteins profiled, approximately 60% were found to be cytoplasmic and the remaining 40% represented membrane-associated proteins as illustrated in Figure 4.6b. Interestingly, knob-associated histidine-rich protein, the most abundant in the parasite (Table 4.1) was found to be present in high abundance in the DV fraction compared to T_{CYT}. This transmembrane protein is well known to play a role in pathogenesis by altering the membrane properties of the host erythrocyte.[293] In addition to this finding, the identification of rhoptry-associated protein 1 [D7NSU9_PLAFA], merozoite surface protein 2 [I6M1H2_PLAFA], high molecular weight rhoptry protein-2 [Q8I060_PLAFA], and Maurer's cleft two transmembrane protein [B9ZSJ3_PLAF7] highlights the likely cohort of proteins trafficked in with haemoglobin that is delivered to the DV as discussed earlier in Section 4.3.1.

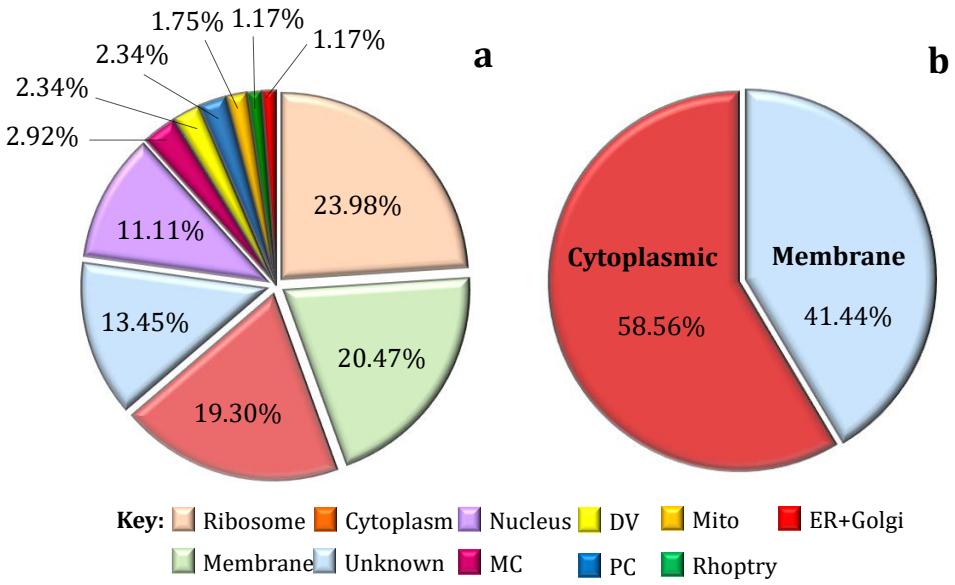

Figure 4.6. Pie charts illustrating the percentage distribution of abundant proteins by subcellular location. Distribution of abundant **(a)** *Plasmodium* and **(b)** human proteins as profiled by label-free proteomics using spectral counting. Key: Digestive vacuole (DV), mitochondria (Mito), endoplasmic reticulum (ER), Maurer's cleft (MC), protein complexes (PC).

4.3.4.2. Identification of metalloproteins across parasite fractions

Proteins identified through label-free quantitative proteomics were further investigated using a bioinformatics approach to establish which of these were metalloproteins or metalloenzymes. Of the *Plasmodium* proteins, 13 were found to be metal-associated and their relative abundance determined are listed in Table 4.2. In addition, 30 proteins were identified as metal-associated but were below the detection limit of the instrument; therefore, it was not possible to determine which of these were present in high or low abundance relative to other proteins present in the samples. These proteins are listed in Table 4.3. Out of the 30 proteins, 22 were identified as uncharacterised proteins where their potential metal association was either predicted or inferred from homology. Turning to human proteins, 30 were found to be metal-associated with their corresponding relative abundance profiles found listed in Table 4.4 and 16 which were below the detection limit can be found in Table 4.5.

Table 4.2. List of semi-quantitative profile of metal related *P. falciparum* proteins

No.	Accession No.	Protein Name	Relative Abundance		Associated Metal
			DV	T_{CYT}	
1	Q8IIR7_PLAF7	Endoplasmic reticulum-resident calcium binding protein	High	High	Ca
2	A0A024VGU2_PLAFA	S-adenosylmethionine synthase	High	High	Mg
3	AMP1_PLAFQ	M1 family aminopeptidase	Low	High	Zn
4	A0A024WGY1_PLAFA	Uncharacterised protein	Low	High	Mn, Zn
5	AMP1_PLAFQ	M1 family aminopeptidase	Low	High	Zn
6	A0A024WGY1_PLAFA	Uncharacterised protein	Low	High	Mn, Zn
7	W4IFN3_PLAFA	Adenosine deaminase	Low	High	Zn
8	Q8I272_PLAF7	Centrin-1	High	Low	Ca
9	Q8IJC7_PLAF7	Centrin-3	High	Low	Ca
10	W4I7W1_PLAFA	Uncharacterised protein	High	Low	Ca
11	HDP_PLAF7	Haem Detoxification Protein	High	Low	Fe
12	W7K445_PLAFA	Uncharacterised protein	High	Low	Fe
13	ENO_PLAFG	Enolase	Low	High	Mg

Table 4.3. List of metal related *P. falciparum* proteins identified in quantitative study that were below the detection limit

No.	Accession No.	Protein Name	Associated Metal
1	SET1_PLAF7	Putative histone-lysine N-methyltransferase	Zn
2	Q8IJP9_PLAF7	ADA2-like protein	Zn
3	CALM_PLAF7	Calmodulin	Ca
4	RAD50_PLAF7	Probable DNA repair protein RAD50	Zn
5	A0A024WHN2_PLAFA	CAMK protein kinase (Fragment)	Ca
6	E1CCC2_PLAFA	P-type Ca^{2+} transporting ATPase	Ca
7	A0A024VHB7_PLAFA	Alanine tRNA ligase	Zn
8	W4J2N1_PLAFP	Hypoxanthine-guanine-xanthine phosphoribosyl transferase	Mg
9	W7JFD0_PLAFA	Uncharacterised protein	Zn
10	A0A024X754_PLAFC	Uncharacterised protein	Zn
11	A0A024X9M7_PLAFC	Uncharacterised protein	Mg
12	A0A024VT95_PLAFA	Uncharacterised protein	Metal
13	A0A024WZM8_PLAFC	Uncharacterised protein	Zn
14	A0A024VJ16_PLAFA	Uncharacterised protein	Zn
15	W4IV38_PLAFP	Uncharacterised protein	Mg, Fe, Zn
16	Q8I3P9_PLAF7	Uncharacterised protein	Zn
17	W7FEM7_PLAF8	Uncharacterised protein	Zn
18	W4IAN0_PLAFA	Uncharacterised protein	Zn
19	A0A024WH04_PLAFA	Uncharacterised protein	Zn
20	W7F173_PLAF8	Uncharacterised protein	Mn
21	W7JWM2_PLAFA	Uncharacterised protein	Zn
22	W4IEU5_PLAFA	Uncharacterised protein	Metal
23	A0A024VMK0_PLAFA	Uncharacterised protein	Cu

24	Q8I4T2_PLAF7	Uncharacterised protein	Ca
25	A0A024X9R4_PLAFC	Uncharacterised protein	Metal
26	A0A024WNC9_PLAFA	Uncharacterised protein	Zn
27	W4IBE5_PLAFA	Uncharacterised protein	Metal
28	A0A024WFW4_PLAFA	Uncharacterised protein	Mg
29	A0A024VV51_PLAFA	Uncharacterised protein	Zn
30	Q8II44_PLAF7	Uncharacterised protein	Zn

Table 4.4. List of semi-quantitative profile of metal related *H. sapiens* proteins

No.	Accession No.	Protein Name	Relative Abundance		Associated Metal
			DV	T_{CYT}	
1	SPTA1_HUMAN	Spectrin alpha chain, erythrocytic 1	High	Low	Ca
2	HBB_HUMAN	Haemoglobin subunit beta	High	Low	Fe
3	HBA_HUMAN	Haemoglobin subunit alpha	High	Low	Fe
4	EPB42_HUMAN	Erythrocyte membrane protein band 4.2	High	Low	Fe
5	CAH1_HUMAN	Carbonic anhydrase 1	High	High	Zn
6	PRDX2_HUMAN	Peroxiredoxin-2	High	High	Cu
7	ANXA7_HUMAN	Annexin A7	High	Low	Ca
8	HBD_HUMAN	Haemoglobin subunit delta	High	Low	Fe
9	CATA_HUMAN	Catalase	High	High	Fe
10	BLVRB_HUMAN	Flavin reductase (NADPH)	High	High	Fe
11	CALM_HUMAN	Calmodulin	High	Low	Ca
12	C9J0K6_HUMAN	Sorcin	High	Low	Ca
13	CAN1_HUMAN	Calpain-1 catalytic subunit	High	Low	Ca
14	AT2B4_HUMAN	Plasma membrane calcium-transporting ATPase 4	High	Low	Ca, Mg
15	A6PVW9_HUMAN	Selenium-binding protein 1	High	Low	Se
16	ANXA5_HUMAN	Annexin A5	High	Low	Ca
17	CPNS1_HUMAN	Calpain small subunit 1	Low	Low	Ca
18	HBG2_HUMAN	Haemoglobin subunit gamma-2	High	High	Fe
19	ABCB6_HUMAN	ATP-binding cassette sub-family B member 6, mitochondrial	High	Low	Fe
20	S10A6_HUMAN	Protein S100-A6	High	High	Ca
21	OXSR1_HUMAN	Serine/threonine-protein kinase OSR1	Low	High	Mg
22	ANXA1_HUMAN	Annexin A1	High	Low	Ca
23	KELL_HUMAN	Kell blood group glycoprotein	High	Low	Mg, Ca
24	B4DIT7_HUMAN	Protein-glutamine gamma-glutamyl transferase 2	High	Low	Ca
25	ANK2_HUMAN	Ankyrin-2	High	Low	Ca
26	AGO2_HUMAN	Protein argonaute-2	High	Low	Metal
27	UBR4_HUMAN	E3 ubiquitin-protein ligase UBR4	High	Low	Zn
28	AT1A1_HUMAN	Sodium/potassium-transporting ATPase subunit alpha-1	High	Low	Mg
29	CPNE3_HUMAN	Copine-3	High	Low	Ca
30	K6PF_HUMAN	6-phosphofructokinase	High	Low	Mg

Table 4.5. List of metal related *H. sapiens* proteins identified in quantitative study that were below the detection limit

No.	Accession No.	Protein Name	Associated Metal
1	CAH2_HUMAN	Carbonic anhydrase 2	Zn
2	S10A4_HUMAN	Protein S100-A4	Ca
3	LRP1_HUMAN	Prolow-density lipoprotein receptor-related protein 1	Ca
4	LRP2_HUMAN	Low-density lipoprotein receptor-related protein 2	Ca
5	LRP1B_HUMAN	Low-density lipoprotein receptor-related protein 1B	Ca
6	CAND1_HUMAN	Cullin-associated NEDD8-dissociated protein 1	Fe
7	J3QRS3_HUMAN	Myosin regulatory light chain 12A	Ca
8	KMT2A_HUMAN	Histone-lysine N-methyltransferase 2A	Zn
9	ASH1L_HUMAN	Histone-lysine N-methyltransferase ASH1L	Zn
10	BSN_HUMAN	Protein bassoon	Metal
11	FA8_HUMAN	Coagulation factor VIII	Cu
12	CAPS1_HUMAN	Calcium-dependent secretion activator 1	Ca
13	ADCY1_HUMAN	Adenylate cyclase type 1	Mg
14	CP4AB_HUMAN	Cytochrome P450 4A11	Fe
15	CBPD_HUMAN	Carboxypeptidase D	Zn
16	STAB2_HUMAN	Stabilin-2	Ca

Seven trace metals were found to be prominent amongst the identified metalloproteins thus emphasising their importance to this specific host-pathogen system; namely, Ca, Fe, Zn, Mg, Mn, Cu and Se. The metal-specific elemental distribution relating to this finding is depicted in Figure 4.7. A subset of these proteins in which potential metal association and activity were predicted and no specific metal was identified were termed as unknown metals for the purpose of this study. This subset mainly applied to uncharacterised proteins which, upon closer inspection, did not appear to exhibit a high degree of similarity to known proteins and were involved in functions pertaining mainly to metabolic processes. As discussed in Chapter 3, calcium was not measured by ICP-MS due to polyatomic interferences of different isotopes produced by calcium and argon on the iron signal, which was an important metal of interest as this was found to be the most abundant trace metal specifically concentrating in the DV. However, in the current proteomic study Ca-related proteins comprised a substantial portion of the metallome of *P. falciparum*, accounting for approximately 30% of the metalloproteome with Zn being equally prominent (Figure 4.7a). Fe and Mg were the next most abundant metalloproteins with much smaller numbers of Mn-, Cu- and Se-containing proteins identified.

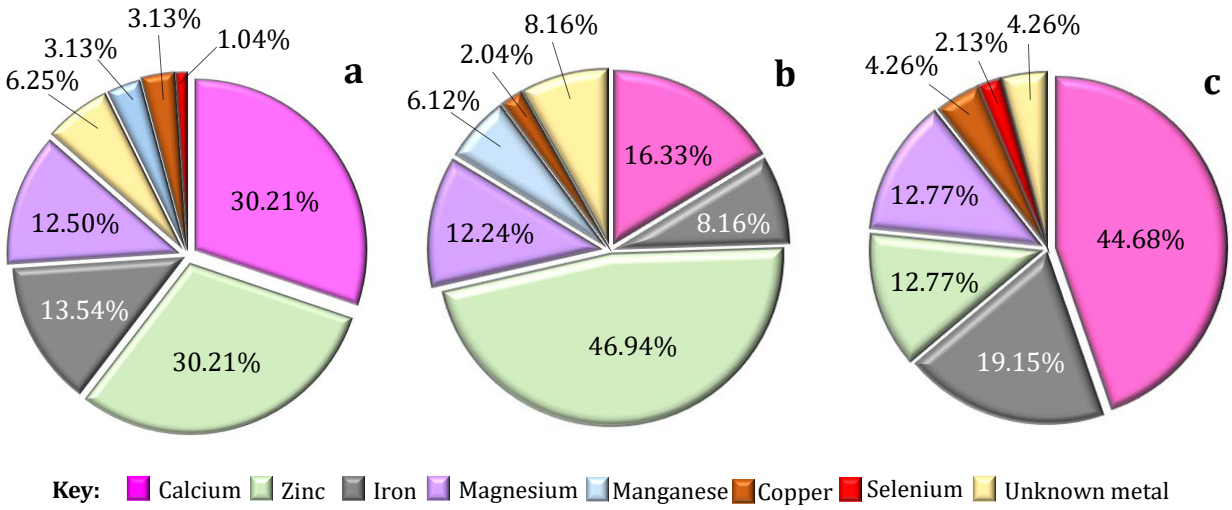

Figure 4.7. Pie charts illustrating the percentage distribution of metalloproteins based on the number of proteins detected. (a) General distribution of all proteins contributing to the metallome of *P. falciparum*. Identified metal-associated **(b)** *Plasmodium* and **(c)** human contributing proteins as profiled by label-free proteomics based on the number of proteins detected.

A closer look at parasite- and erythrocyte-specific proteins showed differences in the metalloprotein profiles. In the case of *Plasmodium,* Zn and Ca were the major contributors while Fe accounted for only 8.16% of the metalloproteome (Figure 4.7b). However, erythrocyte proteins were dominated by Ca accounting for approximately 45% (Figure 4.7c). Interestingly, haemoglobin subunit gamma-2 (Table 4.4) was detected in high abundance within the DV fraction which was surprising since this gamma subunit is an exceptionally strong binder of oxygen and characteristic of foetal haemoglobin. However, it does appear that adults contain very low levels of this subunit, usually less than 1% of total haemoglobin.[294] The parasite is known to engulf massive amounts of haemoglobin which is the highest abundant protein in erythrocytes which in turn allows for the detection of this low abundant subunit. Indeed, this finding alludes to the actual amount trafficked to the DV for degradation. The 90 proteins identified to be metal-associated represented approximately 10% of the proteins found. The list generated appeared to be a limited representation of the metalloproteins that were present, this could be due to the complexity of the samples in addition to previously mentioned difficulties in identifying proteins. A second proteomic study using a qualitative approach was therefore used to gain a snapshot of the metalloproteins present in the DV.

4.3.5. Global overview of proteins associated with haemozoin: A qualitative proteomic approach

4.3.5.1. Determination of the number of proteins associated with haemozoin

Following on from the report by Guerra *et al* where it has been suggested that washed haemozoin could potentially have proteins associated with the crystals as discussed in Chapter 1, the current study attempted to decipher the identity of such proteins.[160] Haemozoin crystals isolated from *P. falciparum* were used to gain insights into the array of metalloproteins associated with the crystals. Approximately 6.15×10^9 crystals extracted from isolated DVs were washed with detergent and all of the crystals were dissolved in base. Aliquots of equal volume, each representing Hz_{SP} and Hz_{Dis}, were analysed by one-dimensional gel electrophoresis. In the case of dissolved haemozoin, the material separated corresponded to approximately 1.86×10^9 crystals per lane; however, the protein content corresponding to this number of crystals was too low to detect by SDS-PAGE.

Given the failure to detect proteins in dissolved haemozoin crystals by SDS-PAGE, it was decided to turn to mass spectrometry. In a study investigating the size of β-haematin crystals, Buller *et al* reported the dimensions of haemozoin crystals which was used to determine the approximate average length to be 400 nm and width of 133 nm. The width to thickness ratio of 1.3 was used to obtain a thickness of 103 nm.[295] Based on these measurements, haemozoin crystals on average have a volume of 5.47×10^6 nm^3 (400 nm × 133 nm × 103 nm). Considering the unit cell dimension of haemozoin as reported by Bohle *et al* of 1.416 nm^3, this implies that there were approximately 3.86×10^6 unit cells that constitute a single crystal.[70] Given that there are two haem molecules per unit cell, this affords 7.73×10^6 haem molecules per crystal. Approximately 1.85×10^9 haemozoin crystals were used per lane therefore correlating to 1.42×10^{16} haem molecules per lane thereby translating to approximately 24 nmol haem per lane run on the 1D gel. Bovine serum albumin was used as a protein standard to ascertain the detection limit of the LC-MS/MS instrument used.[296] Considering the 5 to 10 fmol detection limit of the instrument, this translates to 2.4 to 4.8 $\times10^6$ haem molecules per protein molecule which in turn corresponds to 3 to 6 proteins per haemozoin crystal per lane. This amounts to a detection limit of 30 to 60 proteins on average per haemozoin crystal based on the total number of crystals used in this study.

4.3.5.2. Proteins identified in the haemozoin washings

The first detergent wash, Hz_{SP}, can be viewed as a putative representation of the DV as this sample depicts the material in which haemozoin was in close contact with when it formed within this acidic organelle. Contaminants picked up during isolation are also possible, although isolation from purified DVs was aimed at reducing such contamination. A total of 1 593 proteins where identified by LC-MS/MS of which 1 417 (88.95%) and 176 (11.05%) were *P. falciparum*- and *H. sapiens*-specific, respectively. Of the human protein subset, obvious protein contaminants such as various isoforms of keratin were found and excluded as these were expected as a result of sample handling. Using a bioinformatic approach, approximately 10% of the *Plasmodium* and 25% of the human proteins were found to be metalloproteins or proteins that require a metal cofactor to be functional. Metalloproteins found associated with the haemozoin wash are listed in Tables 4.6 and 4.7.

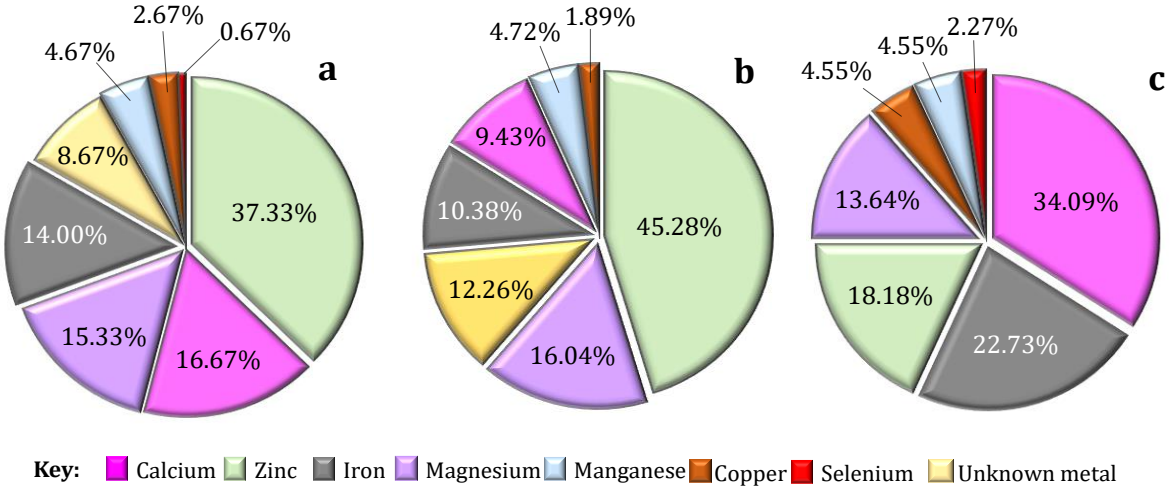

Figure 4.8. Percentage distribution of metal associated proteins found associated with the haemozoin wash. (a) General distribution of all metalloproteins found associated with the haemozoin wash based on total number of proteins. Identified metal associated **(b)** *Plasmodium* and **(c)** human contributing proteins as profiled by qualitative proteomics.

The overall metalloprotein distribution, taking into account both human and parasite origin, showed Zn metalloproteins to represent a significant number in comparison to the other metalloproteins, accounting for approximately 38% of total distribution (Figure 4.8a). Ca, Mg and Fe were the sources of the next three most abundant

metalloproteins with the remaining constituting smaller amounts of Cu, Mn, Se and unknown divalent metals. Focusing on *Plasmodium* proteins, 102 were found to be metal associated where this can be categorised into those which are in fact metalloproteins, a portion which have a metal-binding domain and some which require a metal cofactor. Of these, 42 were characterised proteins were the function was certain; however, 60 were uncharacterised proteins and found by using gene ontology to predict potential metal binding ability.

Parasite metalloproteins exhibited a different profile from that of the erythrocyte as can be seen in Figure 4.8 b vs c. Zinc- and magnesium-related proteins accounted for just over 60% (Figure 4.8b). A significant portion of the proteins, 12.26%, were predicted to be associated with metals as metal binders; however, the exact identity of the transition metal involved remained undefined. Approximately 10% were Fe-related with smaller portions represented by Mn and trace amounts of Cu. Erythrocyte contributing proteins were dominated by Ca- and Fe-associated proteins which accounted for more than half of the proteins identified, making this a likely origin of these specific proteins trafficked into the parasite during the intraerythrocytic stage (Figure 4.8c). Interestingly, only one Se-containing protein was identified in Hz_{SP} which was of human origin.

Table 4.6. List of metal-related *P. falciparum* proteins identified by qualitative proteomics study found in the haemozoin wash

No.	Accession No.	Protein Name	Associated Metal
1	Q9U445_PLAFA	P-type ATPase4	Metal
2	A0A024WKT2_PLAFA	Carbamoyl-phosphate synthase, large subunit	Metal
3	A0A024WSP0_PLAFA	Diphosphate-fructose-6-phosphate 1-phosphotransferase	Mg
4	E1CC99_PLAFA	P-type Ca2+-transporting ATPase	Ca
5	A0A024VGU2_PLAFA	S-adenosylmethionine synthase	Mg
6	A0A024W498_PLAFA	M1 family aminopeptidase	Zn
7	W4J2N1_PLAFP	Hypoxanthine-guanine-xanthine phosphoribosyl transferase	Metal
8	Q8I586_PLAF7	Asparagine/aspartate rich protein, putative	Zn
9	W4IA64_PLAFA	Isocitrate dehydrogenase [NADP]	Mg, Mn
10	Q8IIR7_PLAF7	Endoplasmic reticulum-resident calcium binding protein	Ca
11	A0A024V8S0_PLAFA	Mannose-6-phosphate isomerase, class I	Zn
12	Q8IKZ6_PLAF7	Multidrug resistance protein 2	Fe
13	Q8IB60_PLAF7	PfSec23 protein	Zn
14	Q8IIW2_PLAF7	Phenylalanine--tRNA ligase, putative	Mg
15	Q8IJ37_PLAF7	Pyruvate kinase	Mg

16	ENO_PLAF7	Enolase	Mg
17	A0A024V5V4_PLAFA	4-hydroxy-3-methylbut-2-en-1-yl diphosphate synthase	Fe
18	O96387_PLAFA	Inosine-5'-monophosphate dehydrogenase	Metal
19	Q8IE40_PLAF7	Ribose-phosphate pyrophosphokinase, putative	Mg
20	W4I9T7_PLAFA	Acetyl coenzyme A synthetase (ADP forming), alpha domain-containing protein	Metal
21	W4IA10_PLAFA	Ubiquinol-cytochrome c reductase, iron-sulfur subunit	Fe
22	Q8IL67_PLAF7	Stromal-processing peptidase, putative	Zn
23	W7FN36_PLAF8	4-hydroxy-3-methylbut-2-enyl diphosphate reductase	Metal
24	A0A024XD54_PLAFC	DNA-directed RNA polymerase	Zn
25	RTCB_PLAF7	tRNA-splicing ligase RtcB homolog	Mn
26	A0A024VD99_PLAFA	CAMK/CDPK protein kinase	Ca
27	PRI1_PLAF7	DNA primase small subunit	Zn
28	A0A024WFS7_PLAFA	Chaperone DnaJ	Zn
29	A0A024VPL9_PLAFA	Serine/threonine-protein phosphatase	Ca
30	ZNRF2_PLAF7	RING finger protein PFE0100w	Zn
31	A0A024WKA7_PLAFA	Alanine--tRNA ligase	Zn
32	Q8IID2_PLAF7	Calcium-dependent protein kinase, putative	Ca
33	Q8IEA0_PLAF7	Palmitoyltransferase	Zn
34	A0A024WJP7_PLAFA	Aconitate hydratase 1	Fe
35	Q8IBH9_PLAF7	Cation transporting ATPase, cation transporter	Ca
36	DPOD1_PLAFK	DNA polymerase delta catalytic subunit	Fe, Zn
37	RIR2_PLAFG	Ribonucleoside-diphosphate reductase small subunit	Fe
38	O15798_PLAFA	CG3	Cu
39	A0A024V7Z4_PLAFA	Methionine aminopeptidase 1	Zn, Mn, Fe
40	A0A024VHS5_PLAFA	DNA-directed RNA polymerase	Zn
41	B3XYA7_PLAMA	Cytochrome b (Fragment)	Metal
42	A0A024X0J4_PLAFC	Serine/threonine-protein phosphatase	Ca
43	A0A024W3H9_PLAFA	Uncharacterised protein	Mg
44	A0A024VT57_PLAFA	Uncharacterised protein	Metal
45	W4I910_PLAFA	Uncharacterised protein	Zn
46	W4IAN0_PLAFA	Uncharacterised protein	Metal
47	A0A024VI00_PLAFA	Uncharacterised protein	Metal
48	W7FXF2_PLAFA	Uncharacterised protein	Zn
49	W4I7B6_PLAFA	Uncharacterised protein	Zn
50	A0A024X9R4_PLAFC	Uncharacterised protein	Metal
51	W7JGC0_PLAFA	Uncharacterised protein	Zn
52	W4ID13_PLAFA	Uncharacterised protein	Mg
53	A0A024VMK0_PLAFA	Uncharacterised protein	Cu
54	W4IIJ9_PLAFA	Uncharacterised protein	Zn
55	A0A024VG17_PLAFA	Uncharacterised protein	Fe
56	W7K8I9_PLAFO	Uncharacterised protein	Zn
57	W7FM76_PLAFA	Uncharacterised protein	Zn
58	Q8IKJ8_PLAF7	Uncharacterised protein	Ca
59	A0A024VTC0_PLAFA	Uncharacterised protein	Zn
60	A0A024VMB8_PLAFA	Uncharacterised protein	Zn
61	W7F7L5_PLAF8	Uncharacterised protein	Zn
62	A0A024WL86_PLAFA	Uncharacterised protein	Zn

63	A0A024W2A1_PLAFA	Uncharacterised protein	Mg
64	A0A024V9F8_PLAFA	Uncharacterised protein	Mg
65	W4IHP5_PLAFA	Uncharacterised protein	Fe
66	A0A024VZW9_PLAFA	Uncharacterised protein	Zn
67	A0A024VQK6_PLAFA	Uncharacterised protein	Mg
68	A0A024UY30_PLAFA	Uncharacterised protein	Zn
69	A0A024VHF1_PLAFA	Uncharacterised protein	Zn
70	A0A024W296_PLAFA	Uncharacterised protein	Zn
71	A0A024VKE5_PLAFA	Uncharacterised protein	Zn
72	W4IET7_PLAFA	Uncharacterised protein	Mg
73	A0A024WG81_PLAFA	Uncharacterised protein	Fe
74	W7JNC8_PLAFA	Uncharacterised protein	Zn
75	W7JTE4_PLAFO	Uncharacterised protein	Zn
76	A0A024VMG0_PLAFA	Uncharacterised protein	Mn
77	A0A024VQZ6_PLAFA	Uncharacterised protein	Zn
78	W7FIN9_PLAF8	Uncharacterised protein	Zn
79	A0A024V5D8_PLAFA	Uncharacterised protein	Ca
80	W7K086_PLAFO	Uncharacterised protein	Zn
81	A0A024WI54_PLAFA	Uncharacterised protein	Zn
82	W4IBF3_PLAFA	Uncharacterised protein	Metal
83	Q8I5K3_PLAF7	Uncharacterised protein	Zn
84	W4IA54_PLAFA	Uncharacterised protein	Mg
85	W4I7W1_PLAFA	Uncharacterised protein	Ca
86	A0A024VV51_PLAFA	Uncharacterised protein	Zn
87	A0A024VV08_PLAFA	Uncharacterised protein	Zn
88	A0A024VVG1_PLAFA	Uncharacterised protein	Mg
89	A0A024VFU2_PLAFA	Uncharacterised protein	Mn
90	A0A024UXJ5_PLAFA	Uncharacterised protein	Mg
91	A0A024WWW0_PLAFA	Uncharacterised protein	Zn
92	A0A024VA55_PLAFA	Uncharacterised protein	Zn
93	A0A024VGS2_PLAFA	Uncharacterised protein	Zn
94	A0A024VV81_PLAFA	Uncharacterised protein	Mg
95	A0A024V588_PLAFA	Uncharacterised protein	Metal
96	W7K5K6_PLAFO	Uncharacterised protein	Zn
97	A0A024VDD9_PLAFA	Uncharacterised protein	Zn
98	A0A024WQR6_PLAFA	Uncharacterised protein	Fe
99	W4IBL0_PLAFA	Uncharacterised protein	Zn

Table 4.7. List of metal-related *H. sapiens* proteins identified by qualitative proteomics study found associated in the haemozoin wash

No.	Accession No.	Protein Name	Associated Metal
1	HBB_HUMAN	Haemoglobin subunit beta	Fe
2	EPB42_HUMAN	Erythrocyte membrane protein band 4.2	Fe
3	HBA_HUMAN	Haemoglobin subunit alpha	Fe
4	CAN1_HUMAN	Calpain-1 catalytic subunit	Ca
5	CAH1_HUMAN	Carbonic anhydrase 1	Zn
6	A6PVW9_HUMAN	Selenium-binding protein 1	Se
7	AT2B4_HUMAN	Plasma membrane calcium-transporting ATPase 4	Ca
8	ABCB6_HUMAN	ATP-binding cassette sub-family B member 6, mitochondrial	Fe
9	KELL_HUMAN	Kell blood group glycoprotein	Zn
10	ALBU_HUMAN	Serum albumin	Zn, Cu
11	CATA_HUMAN	Catalase	Fe
12	KPYR_HUMAN	Pyruvate kinase	Mg
13	ANXA7_HUMAN	Annexin A7	Ca
14	B4DIT7_HUMAN	Protein-glutamine gamma-glutamyltransferase 2	Ca
15	ANXA1_HUMAN	Annexin A1	Ca
16	PERE_HUMAN	Eosinophil peroxidase	Ca, Fe
17	CPNE3_HUMAN	Copine-3	Ca
18	RINI_HUMAN	Ribonuclease inhibitor	Ca
19	NB5R3_HUMAN	NADH-cytochrome b5 reductase 3	Fe
20	K6PL_HUMAN	6-phosphofructokinase	Mg
21	RN123_HUMAN	E3 ubiquitin-protein ligase RNF123	Zn
22	UGGG1_HUMAN	UDP-glucose: glycoprotein glucosyltransferase 1	Ca, Mn
23	PRPS1_HUMAN	Ribose-phosphate pyrophosphokinase 1	Mg
24	ARF1_HUMAN	ADP-ribosylation factor 1	Mg
25	CAH2_HUMAN	Carbonic anhydrase 2	Zn
26	BLVRB_HUMAN	Flavin reductase (NADPH)	Fe
27	ACSL6_HUMAN	Long-chain-fatty-acid--CoA ligase 6	Mg
28	UBP5_HUMAN	Ubiquitin carboxyl-terminal hydrolase 5	Zn
29	ANXA5_HUMAN	Annexin A5	Ca
30	HBD_HUMAN	Haemoglobin subunit delta	Fe
31	CPNS1_HUMAN	Calpain small subunit 1	Ca
32	CAN5_HUMAN	Calpain-5	Ca
33	GNAI2_HUMAN	Guanine nucleotide-binding protein G(i) subunit alpha-2	Mg
34	PP2AA_HUMAN	Serine/threonine-protein phosphatase 2A catalytic subunit alpha isoform	Mn
35	BIEA_HUMAN	Biliverdin reductase A	Zn
36	B4DGP8_HUMAN	Calnexin	Ca
37	ANXA4_HUMAN	Annexin A4	Ca
38	CALR_HUMAN	Calreticulin	Ca
39	S40A1_HUMAN	Solute carrier family 40 member 1	Fe
40	MBLC2_HUMAN	Metallo-beta-lactamase domain-containing protein 2	Zn
41	ATP7A_HUMAN	Copper-transporting ATPase 1	Cu

4.3.5.2. Proteins identified in the dissolved haemozoin fraction

Dissolved haemozoin material was representative of proteins that either remained strongly associated with the surface of the crystals following extensive washing or those that form part of the biocrystal matrix that were incorporated during haemozoin formation or both. Study of this material likely provides a unique snapshot into the potential proteins that were present at the time of crystal formation since these proteins are less likely to be contaminants. A total of 1 470 proteins were identified in Hz_{Dis}, of which 250 (17.01%) were of human origin and 1 220 (82.99%) were *Plasmodium* specific proteins. Screening for potential metalloproteins revealed approximately 8% were specific to *Plasmodium* and 18% were of human origin (Tables 4.8 and 4.9).

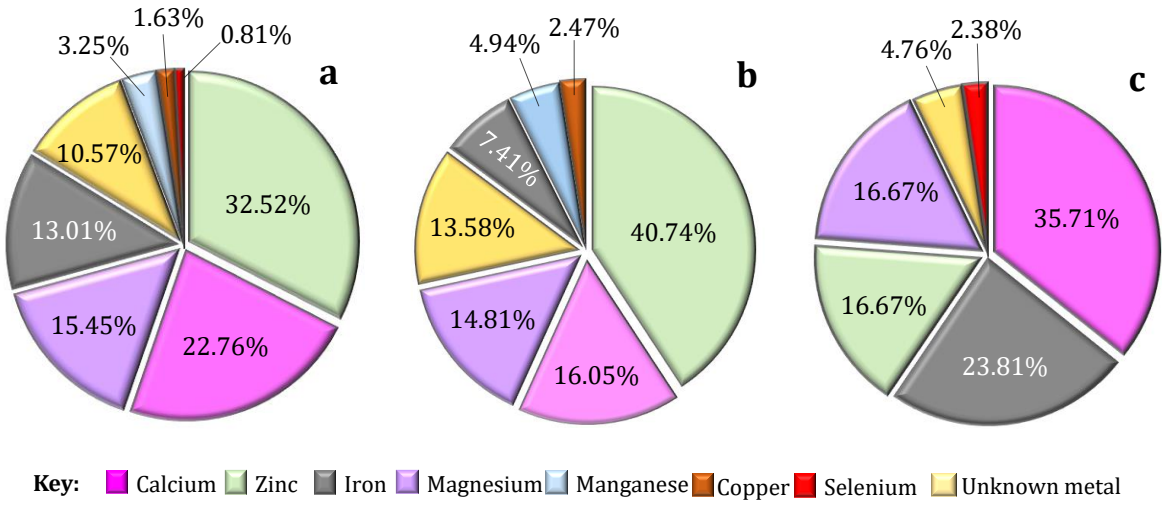

Figure 4.9. Percentage distribution of metal-associated proteins found in the dissolved haemozoin fraction. (a) General distribution of all metalloproteins found in dissolved haemozoin. Identified metal associated **(b)** *Plasmodium* and **(c)** human contributing proteins as profiled by qualitative proteomics.

Approximately 18% of the identified human proteins screened were found to be metalloproteins and about 8% were specific to *Plasmodium*. Turning to the Hz_{Dis} metalloproteome, 77 and 41 metalloproteins were identified to be of parasite and human origin respectively. Of the parasite cohort, 64 proteins were characterised, and metal-related information was found for the remaining 13 uncharacterised proteins by database interrogation. The overall metalloprotein distribution as well as parasite- and host-specific contributors (Figure 4.9) followed similar trends as observed in Section 4.3.5.2.

Table 4.8. List of metal-related *P. falciparum* proteins identified by qualitative proteomics study found in the dissolved haemozoin fraction

No.	Accession No.	Protein Name	Associated Metal
1	PFF1185w	SNF2 helicase, putative (Smarca-related protein)	Zn
2	PFF0285c	DNA repair-like protein, putative	Zn
3	PF10_0143	Transcriptional coactivator ADA2	Zn
4	PFE0465c	RNA polymerase I	Zn
5	PF13_0150	DNA-directed RNA polymerase 3 largest subunit	Zn
6	PF07_0115	Cation transporting ATPase, putative	Metal
7	PFI0240c	Cu2+ -transporting ATPase, putative	Cu
8	PFC0840w	P-type ATPase, putative	Mg
9	PFL0950c	Aminophospholipid-transporting P-ATPase	Mg
10	PFA0310c	Calcium-transporting ATPase	Ca
11	PF11_0189	Insulinase, putative	Metal
12	PFL0590c	Non-SERCA-type Ca2 -transporting P-ATPase	Ca
13	PF13_0322	Falcilysin	Zn
14	MAL13P1.56	M1-family alanyl aminopeptidase	Zn
15	PF13_0048	NUDIX hydrolase, putative	Mn
16	MAL13P1.405	Erythrocyte membrane protein pfemp3	Zn
17	PF11_0203	Peptidase, putative	Zn
18	PFB0815w	Calcium Dependent Protein Kinase 1	Ca
19	PFL1345c	Histone S-adenosyl methyltransferase, putative	Fe
20	MAL13P1.22	DNA ligase I	Ca, Mn, Mg
21	PF10_0186	Zinc finger C-x8-C-x5-C-x3-H type, putative	Zn
22	PF14_0630	Protein serine/threonine phosphatase	Fe, Mn
23	PF10_0244	Formin 2, putative	Ca
24	PF07_0085	Ferrodoxin reductase-like protein	Fe
25	PFF1300w	Pyruvate kinase	Mg
26	PF10_0155	Enolase	Mg
27	PF14_0517	Aminopeptidase P	Zn
28	PF07_0072	Calcium dependent protein kinase 4	Ca
29	PFL1890c	HD superfamily phosphohydrolase protein	Metal
30	PF11_0210	Mitochondrial Mg Ion transporter	Mg
31	PFD0462w	Heat shock protein 40	Metal
32	PFI1090w	S-adenosylmethionine synthetase	Metal
33	PFD0250c	Sec24 subunit b	Zn
34	PF14_0439	M17 leucyl aminopeptidase	Mn, Zn
35	PF13_0242	Isocitrate dehydrogenase (NADP), mitochondrial precursor	Mg
36	PFE1155c	Mitochondrial processing peptidase alpha subunit, putative	Zn
37	PFF1070c	Radical SAM protein, putative	Fe
38	PF11_0051	Phenylalanyl-tRNA synthetase beta chain, putative	Mg
39	PFI1215w	Splicing factor 3A	Zn
40	PF14_0255	CorA-like Mg2 transporter protein, putative	Mg
41	PFI1020c	Inosine-5'-monophosphate dehydrogenase	Metal
42	PFI0380c	Peptidyl deformylase	Fe
43	PFI1625c	Organelle processing peptidase, putative	Zn

44	PF11_0098	Endoplasmic reticulum-resident calcium binding protein	Ca
45	PF10_0150	Methionine aminopeptidase 1b, putative	Zn
46	PF14_0261	Proliferation-associated protein 2g4, putative	Zn
47	PFI1570c	M18 aspartyl aminopeptidase	Zn
48	PF10_0122	Phosphoglucomutase, putative	Mg
49	MAL7P1.73	Calcium/calmodulin-dependent protein kinase, putative	Ca
50	PF14_0570	Pyridoxal 5'-phosphate synthase, putative	Metal
51	PF14_0443	Centrin-2	Ca
52	MAL13P1.76	TFIIH basal transcription factor subunit	Zn
53	MAL7P1.26	O-sialoglycoprotein endopeptidase, putative	Zn
54	PF13_0349	Nucleoside diphosphate kinase	Mg
55	PFE0660c	Purine nucleoside phosphorylase	Metal
56	PF11_0066	Centrin-4	Ca
57	PF14_0369	Copper transporter putative	Cu
58	PF13_0028	Membrane integral peptidase, M50 family, putative	Zn
59	PF07_0027	DNA-directed RNA polymerase 2 8.2 kDa polypeptide, putative	Zn
60	PF07_0065	Zinc transporter, putative	Zn
61	PFL2225w	Myosin A tail domain interacting protein	Ca
62	PF14_0492	Protein phosphatase 2b regulatory subunit, putative	Ca
63	PF08_0071	Fe-superoxide dismutase	Metal
64	PFF0485c	Palmitoyltransferase	Zn
65	PF14_0315	Conserved Plasmodium membrane protein	Zn
66	PFF0755c	Conserved Plasmodium protein	Zn
67	PFI0805w	Conserved Plasmodium protein	Zn
68	PFL1010c	Conserved Plasmodium protein	Zn
69	PFL0360c	Conserved Plasmodium protein	Metal
70	PF14_0479	Conserved Plasmodium protein	Zn
71	PF11_0389	Conserved Plasmodium protein	Ca
72	PF14_0657	Conserved Plasmodium protein	Metal
73	PFL0275w	Conserved Plasmodium protein	Zn
74	PFE1130w	Conserved Plasmodium protein	Mg
75	MAL13P1.79	Conserved Plasmodium protein	Metal
76	PF14_0054	Conserved Plasmodium protein	Zn
77	PF13_0099	Conserved Plasmodium protein	Zn

Table 4.9. List of metal-related *H. sapiens* proteins identified by qualitative proteomics study found in the dissolved haemozoin fraction

No.	Accession No.	Protein Name	Associated Metal
1	HBB_HUMAN	Haemoglobin subunit beta	Fe
2	HBA_HUMAN	Haemoglobin subunit alpha	Fe
3	CAH2_HUMAN	Carbonic anhydrase 2	Zn
4	ASNA_HUMAN	ATPase ASNA1	Metal
5	CAND1_HUMAN	Isoform 1 of Cullin-associated NEDD8-dissociated protein 1	Fe
6	DRG1_HUMAN	Developmentally-regulated GTP-binding protein 1	Mg
7	HBD_HUMAN	Haemoglobin subunit delta	Fe
8	HBG_HUMAN	Haemoglobin subunit gamma-2	Fe
9	ENPL_HUMAN	Endoplasmin	Ca
10	RN123_HUMAN	Isoform 1 of E3 ubiquitin-protein ligase RNF123	Zn
11	VATA_HUMAN	V-type proton ATPase catalytic subunit A	Fe
12	ENOA_HUMAN	Isoform alpha-enolase of Alpha-enolase	Mg
13	CATA_HUMAN	Catalase	Fe
14	PERE_HUMAN	Eosinophil peroxidase	Fe
15	ABCB6_HUMAN	Isoform 1 of ATP-binding cassette sub-family B member 6, mitochondrial	Fe
16	ABCG2_HUMAN	Isoform 1 of ATP-binding cassette sub-family G member 2	Fe
17	ANXA1_HUMAN	Annexin A1	Ca
18	BIEA_HUMAN	Biliverdin reductase A	Zn
19	CAH1_HUMAN	Carbonic anhydrase 1	Zn
20	CAN1_HUMAN	Calpain-1 catalytic subunit	Ca
21	CPNE1_HUMAN	Copine-1	Ca
22	CPNS1_HUMAN	Calpain small subunit 1	Ca
23	KCNN4_HUMAN	Intermediate conductance calcium-activated potassium channel protein 4	Ca
24	KELL_HUMAN	Kell blood group glycoprotein	Zn binding
25	OXSR1_HUMAN	Serine/threonine-protein kinase OSR1	Mg
26	PRPS3_HUMAN	Ribose-phosphate pyrophosphokinase 1	Mg
27	S10A4_HUMAN)	Protein S100-A4	Ca
28	S10A6_HUMAN	Protein S100-A6	Ca
29	SBP1_HUMAN	Isoform 1 of Selenium-binding protein 1	Se
30	TGM1_HUMAN	Isoform 1 of Protein-glutamine gamma-glutamyltransferase 2	Ca
31	TGM3_HUMAN	Protein-glutamine gamma-glutamyltransferase E	Ca
32	ZN512_HUMAN	Zinc finger protein 512	Zn
33	DSG1_HUMAN	Desmoglein-1	Ca
34	ACSL6_HUMAN	Isoform 7 of Long-chain-fatty-acid--CoA ligase 6	Mg
35	ZN384_HUMAN	zinc finger protein 384 isoform c	Zn
36	ICAM4_HUMAN	cDNA FLJ56442, highly similar to ATP-citrate synthase	Mg
37	ITAM_HUMAN	integrin alpha-M isoform 1 precursor	Ca
38	ESYT1_HUMAN	Isoform 2 of Extended synaptotagmin-1	Ca
39	PDCD6_HUMAN	Programmed cell death 6	Ca, Mg
40	ANXA7_HUMAN	cDNA FLJ55060, highly similar to Annexin A7	Ca
41	PDE6A_HUMAN	Rod cGMP-specific 3',5'-cyclic phosphodiesterase subunit alpha	Metal

4.3.6. Metalloproteins identified in *P. falciparum*

Considering the overall metal-associated proteins identified, it is likely that the human-related proteins are mere contaminants or taken up by the parasite through its feeding mechanism and may bear no functional role within the parasite. On the other hand, identified parasite proteins are likely to exhibit more specificity to functions within the DV and will be discussed further.

4.3.6.1. Calcium

Calcium, in its ionised form (Ca^{2+}) is an essential second-messenger molecule involved in intracellular signalling in eukaryotic cells.[297] Ionised calcium cannot be metabolised, therefore cells promote tight regulation of intracellular Ca^{2+} and homeostasis through various binding and transport proteins. *P. falciparum* has a complex life cycle. Within the human host the parasite has adapted to survive in environments where there exists a Ca^{2+} concentration gradient, from high extracellular Ca^{2+} in blood plasma of approximately 2.5 mM to 30-60 nM within the erythrocyte and over a millimolar range within the parasite itself.[298-300] Eukaryotic cells require ATPase-type pumps or transporters to maintain equilibrium by transporting Ca^{2+} into the cellular Ca^{2+} stores or out of the cell through membrane-type channels. Such Ca^{2+} channels are represented by the identified parasite P-type Ca^{2+} transporting ATPase [E1CC99_PLAFA] found associated in the Hz_{SP} fraction, non-SERCA-type Ca^{2+} transporting ATPase [PFL0590c] detected in Hz_{Dis} and the plasma membrane calcium-transporting ATPase 4 [AT2B4_HUMAN] found in higher abundance in DV compared to T_{CYT} probably trafficked directly to the DV with haemoglobin.

Ca^{2+} has been implicated in a number of essential host-pathogen interactions that enable the malaria parasite to progress from one phase of its life cycle to the next. One crucial process is erythrocyte invasion, where an influx of Ca^{2+} has been shown to be essential which in turn triggers additional molecular events such as phosphorylation of cytoskeletal proteins.[301] Following invasion, the Ca^{2+} cellular content of the parasitised cell drastically increases over the asexual life cycle.[302] Mid- to late-stage trophozoites were used in this study, with some cells potentially in the early schizont stage, thus marking the commencement of nuclear division. This supports the presence of Centrin 1

[Q8I272_PLAF7], 2 [PF14_0443] and 3 [Q8IJC7_PLAF7] in high abundance in both DV and T_{CYT} fractions (Table 4.2). The qualitative study identified Centrin 4 [PF11_0066] in addition to these. Centrins are cytoskeletal proteins that possess four Ca^{2+} binding EF hand domains and play an intrinsic role in cell division. Electron microscopy images reported by Mahajan *et al* illustrated that centrin was expressed in close proximity to the nucleus; therefore, the high abundance across all parasite fractions was expected as this could have possibly carried through with nuclear material during sample preparation.[303]

Plasmodium endoplasmic reticulum-resident calcium binding protein [Q8IIR7_PLAF7] expressed mainly during the intraerythrocytic stage was found in high abundance in the DV cytosol and T_{CYT} but in lower abundance across haemozoin fractions (Table 4.2). This protein which is conserved across *P. falciparum* and *Toxoplasma gondii*, has recently been reported to play an essential role in controlling the proteolytic egress cascade within the malaria parasite by promoting Ca^{2+} signalling with respect to the endoplasmic reticulum.[304]

P. falciparum contain calcium-dependent protein kinases (CDPK), a family of kinases responsible for calcium sensing within the parasite. Activity is stimulated upon calcium or calmodulin binding.[221] In general, kinases are responsible for catalysing the phosphorylation of proteins, lipids or carbohydrates and are critical to metabolic functions, protein transport and cell signalling to name a few. Five proteins belonging to the CDPK family, A0A024VD99_PLAFA, Q8IID2_PLAF7, PFB0815w, PF07_0072 and MAL7P1.73, were identified to be associated with the haemozoin fractions (Table 4.2). Typically, the kinase domain constitutes Ser/Thr kinase, but activity of the activation loop is regulated by conserved acidic residues.[305] The CDPK family has been shown to be responsible for cell adhesion, invasion, gliding motility and egress of parasites out of the host erythrocyte.[306] All other identified Ca^{2+} related proteins or enzymes were mainly those originating in the endoplasmic reticulum and involved in Ca^{2+} regulation and various metabolic processes within the cell.

Human-related Ca^{2+} proteins also likely contributed to the levels of calcium present within parasitised erythrocytes. A number of these were detected, some in relative abundance, by the label-free quantitative approach (Table 4.4). In cases where the abundance was high in the DV fraction, this supports trafficking to the DV following digestion of host cytoplasm. A subset of these proteins [SPTA1_HUMAN, ANXA7_HUMAN,

CALM_HUMAN, C9J0K6_HUMAN, AT2B4_HUMAN, CPNS1_HUMAN] are known to be mainly involved in Ca^{2+} binding, act as ion channels or in cytoskeletal remodelling whereas others are involved in ion transport [AT2B4_HUMAN], maintaining Ca^{2+} homeostasis [ANK2_HUMAN, CPNE3_HUMAN], exhibited metalloendopeptidase activity [CAN1_HUMAN, KELL_HUMAN] or acting as a Ca^{2+} [S10A6_HUMAN] sensor.

4.3.6.2. Zinc

In the current proteomic study, zinc-associated proteins constitute the majority of detected *Plasmodium* metalloproteins and zinc was the second most abundant trace metal measured in the parasite as discussed in Chapter 3. When monitored over the 48 h intraerythrocytic life cycle, the amount of total Zn found was less than that of host RBC during the early to mid-trophozoite stage; however, as the parasite developed and progressed into late trophozoite to schizont stages, total Zn had increased and was detected in amounts higher than that of the host cell. In both the label-free and qualitative proteomic studies, the majority of characterised and uncharacterised metal-associated proteins were found to be Zn-binding or contained a Zn-finger motif. These proteins were identified to be involved in nuclear processes such as DNA replication, transcription, DNA repair, cell cycle events as well as intracellular protein transport and protein biosynthesis. This was not surprising since the trophozoites used were a mix of mid- to late-stage trophozoites also containing schizonts. Late in the parasite life cycle, parent cells prepare to undergo nuclear division thereby resulting in increased DNA and RNA content coinciding with the early schizont stage[307], hence the increase in the number of nuclear-related proteins as well as total Zn content observed.

Label-free proteomics identified the M1 family aminopeptidase [AMP1_PLAFQ] to be in high abundance in T_{CYT} and low abundance in DV. This aminopeptidase was also identified in the qualitative study in both Hz_{SP} and Hz_{Dis}. This enzyme was amongst the high abundance proteins in the *Plasmodium* proteome ranked in the top 5% with an abundance of 2 962 *ppm* (PaxDb). Aminopeptidases are grouped as enzymes which catalytically cleave at the *N*-terminus of proteins and peptides and in some cases are zinc metalloenzymes. This M1 family aminopeptidase, actively transcribed during the intraerythrocytic stage of the *P. falciparum* life cycle, was thought to localise within the

acidic DV and where it is involved in haemoglobin digestion and generation of a reserve of amino acids.[308, 309] Immunofluorescent imaging studies by Ragheb *et al* suggests the nucleus as a second location for this metalloenzyme; however, the exact function here remains unknown.[310] This supports the finding of M1 aminopeptidase in high abundance in the T_{CYT} fraction. In this study, adenosine deaminase [W4IFN3_PLAFA], was also found to be in high abundance in T_{CYT}. This is a zinc-binding enzyme which catalyses the reaction of adenosine to inosine and is located in the ribosome and involved in purine salvage pathways in *Plasmodium*.[311] Additionally, uncharacterised proteins A0A024WGY1_PLAFA and PF14_0517 were found to be in high abundance in T_{CYT} (Table 4.2). The first of these two proteins, by database search, was found to be a metalloaminopeptidase belonging to the peptidase M24B family. This uncharacterised protein comprised three characteristic domains as described in Table 4.10 which bind Zn.

Table 4.10. Description of domain and repeats constituting uncharacterised protein A0A024WGY1_PLAFA

Domain No.	Domain Description	Amino Acid Position(s)	Length
1	Creatinase N	119-249	131
2	Peptidase M24	466-679	214
3	Peptidase M24 C	689-756	68

The second of the two aminopeptidases was one which played a role in haemoglobin degradation. Aminopeptidase P [PF14_0517], a putative peptidase, was found exclusively in the dissolved haemozoin fraction (Table 4.7). Similar to the M1 aminopeptidase, this too was a DV metalloenzyme and, even though this has been identified qualitatively, its presence in Hz_{Dis} indicates that it is likely closely associated with the haemozoin formation process and a likely source of the zinc observed in the acidic organelle. This enzyme present at 1 635 ppm in the parasite is moderately abundant. Aminopeptidase P differs from its M1 counterpart in that it hydrolyses peptides with a proline at position 2 and even though active with Zn^{2+} , it is most active with Mn^{2+} as a cofactor. Though this enzyme is present in both the DV and parasite cytoplasm, detection within the DV indicates a role further downstream in the haemoglobin degradation cascade.

A proteomic study reported by Ambele *et al* which focused on identifying the possible proteins involved in haemozoin formation was unable to identify significant DV markers including the well-known metalloenzyme, falcilysin.[296] Using a similar proteomic approach but three times more material, over a thousand proteins were identified. Interestingly, in the proteomic study of the DV by LaMarque *et al*, falcilysin was not identified by mass spectrometry in the protein list reported.[181] Similar issues were experienced in the label-free proteomic approach, but in the current qualitative proteomic study falcilysin [PF13_0322] was successfully identified by mass spectrometry and was found in the dissolved haemozoin fraction. This could be attributed to the ability of gel electrophoresis to reduce sample complexity which in turn reduced signal suppression thereby allowing the associated peptides to be identified. Falcilysin, a metalloprotease unique to the food vacuole, and present at 2 531 ppm in the parasite, forms part of the family of M16 metalloproteases. This protease comprises an inverted active site motif where the histidine residues coordinate to Zn^{2+}.[312] This one is different from other haemoglobin proteases in that it hydrolyses peptides at polar or charged amino acid residues. Inferring from the abundance and localisation in the DV, this is the likely main pool of Zn in the DV.

Turning to the finding that increased Zn levels were higher than those in the host RBC in the early schizont stage, this suggests that the parasite scavenges Zn from its surroundings to meet the enhanced metabolic demands of cell division. For this to occur there needs to be one or more transporters that allow the influx of Zn into the parasite when essential. A putative Zn transporter [PF07_0065] was found present in the dissolved haemozoin fraction indicating this could be present in the DV. It has been reported that this gene exhibits upregulation of expression 30 to 40 h into the intraerythrocytic life cycle.[307] This correlates with the increase in Zn observed in Chapter 3 and the presence of labile Zn seen in imaging studies by Marvin *et al* which supports the presence and function of such a transporter.[216] Interestingly, this zinc transporter has been detected at levels of 172 ppm as shown on PaxDb indicating that this is not very abundant in *Plasmodium*.

The remaining Zn related proteins that were detected in Hz_{SP} and Hz_{Dis} were also detected in T_{CYT} which suggests that these could possibly be contaminants or directly delivered to the DV. Since Q8IB60_PLAF7 and PFD0250c were found to be associated with the COPII

vesicle coat thus indicating they originated from the endoplasmic reticulum, they were considered as contaminants. With respect to the uncharacterised proteins found in the qualitative study, most of these were nuclear-related and shared the Zn-finger motif; others were ER related and were considered as carry through contaminants. These proteins were found to be mainly involved in metabolic processes, protein transport in the parasite and chaperone activity.

Possible sources of zinc from erythrocyte metalloproteins were mainly represented by carbonic anhydrase [CAH1_HUMAN], E3 ubiquitin-protein ligase [UBR4_HUMAN], serum albumin [ALBU_HUMAN], Kell blood group glycoprotein [KELL_HUMAN] and biliverdin reductase A [BIEA_HUMAN] which were likely to be present in the parasite as a result of ingestion of RBC cytoplasm throughout the asexual life cycle. Two of these proteins were detected by label-free proteomics and the relative abundance was determined. Carbonic anhydrase was detected in high abundance in both T_{CYT} and DV whereas E3 ubiquitin-protein ligase was found in low abundance in DV and high abundance in T_{CYT}. Carbonic anhydrase present in 15 669 ppm is one of the most abundant human proteins; therefore, the high relative abundance detected was not surprising.

4.3.6.3. Magnesium

Total magnesium measured in isolated parasites exhibited a similar trend to that observed for Zn; however, in contrast to Zn, Mg levels showed a 2-fold increase from early to mid-trophozoite stage and thereafter almost doubled at the schizont stage. Magnesium, a macronutrient required in fairly large amounts in most living organisms, is responsible for essential metabolic processes such as glycolysis, protein synthesis, lipid biogenesis, metabolism of other cations and most importantly, required as a cofactor in hundreds of enzyme reactions.

As the parasite develops within the host erythrocyte and transitions from ring to trophozoite stage, the metabolic demand drastically increases. In addition, high energy is required during this time as there are a number of essential cellular processes occurring simultaneously. At this point, one of the main processes is haemoglobin catabolism and rapid haemozoin formation which has shown to indicate an enhanced metabolic rate at the trophozoite stage.[313] As the parasite transitions from trophozoite to schizont, the

metabolic demand increases even more due to nuclear division and merozoite formation. The increase in mitochondria was shown to mimic that of DNA replication during merozoite formation; therefore, the late trophozoite to schizont has been marked as the most metabolically-active form of the intraerythrocytic parasite.[216, 314, 315]

This enhanced metabolic demand is supported by the Mg-associated proteins identified in each of the proteomic studies. The majority of identified proteins represent enzymes involved in various metabolic processes from the citric acid cycle to nucleotide biosynthesis [A0A024WSP0_PLAFA, W4IA64_PLAFA, Q8IJ37_PLAF7, Q8IE40_PLAF7, PFC0840w MAL13P1.22, PFF1300w, PF13_0242, PF10_0122, PF13_0349, W4J2N1_PLAFP, A0A024X9M7_PLAFC, W4IV38_PLAFP, A0A024WFW4_PLAFA]. As it was observed that Mg levels were higher than that of the host cell, this implies that a portion of this measured divalent cation was in fact imported from the host cell to meet the requirements of the pathogen. A number of Mg membrane transporters were identified in the study that could play a role in the influx into the cell [W4IA54_PLAFA, A0A024VV81_PLAFA, PFC0840w, PFL0950c, PF11_0210, PF14_0255 PFE1130w].

The semi-quantitative proteomic study found two enzymes, *S*-adenosylmethionine synthase [A0A024VGU2_PLAFA] and enolase [ENO_PLAFG] in high abundance in T_{CYT} fraction with the latter present in low abundance in DV. Since Mg appears to concentrate within the trophozoite cytoplasm with only low abundance in the DV, these two enzymes are likely contributors to this phenomenon. *S*-adenosylmethionine synthase is a moderately abundant enzyme present in the whole organism at 2 388 ppm. This enzyme contains transmembrane domains and belongs to the AdoMet synthase family and binds two Mg^{2+} per subunit. It catalyses the reaction between ATP and methionine forming part of the pathway that produces *S*-adenosylmethionine.[316] Enolase on the other hand is involved in the glycolysis pathway and carbohydrate degradation and is consequently highly abundant constituting 7 650 ppm of the whole integrated proteome of the organism. Enolase requires Mg^{2+} for catalytic activity and to stabilise dimer formation in the production of pyruvate.

Turning to the erythrocyte proteins, five were detected and profiled by their relative abundance between T_{CYT} and DV. Serine/threonine-protein kinase [OXSR1_HUMAN] was detected in higher abundance in T_{CYT} and low in DV whereas sodium/potassium-transporting ATPase subunit alpha-1 [AT1A1_HUMAN] and 6-phosphofructokinase

[K6PF_HUMAN], involved in creating electrochemical gradients and catalytic activity, were detected in low abundance in T_{CYT}. Due to the interaction between Mg and Ca, certain proteins are transporters of both ions or use either as a cofactor as seen in the plasma membrane calcium-transporting ATPase 4 and Kell blood group glycoprotein, both of which are regulators of Ca and Mg ions were found to be high in DV. These proteins and enzymes contribute to the overall content of Mg; however, it is important to note that these molecules were likely detected in the DV as a result of ingestion of host cell cytoplasm and may not be essential in contributing to parasite function or homeostasis. However, this also raises the question as to the final outcome of metal ions ingested by the parasite: are these released by proteins and utilised by the cell or retained by the DV?

4.3.6.4. Manganese

Trace amounts of manganese were found in erythrocytes and in parasite material and total manganese was found to concentrate in the trophozoite cytoplasm with the only noticeable increase observed at the last time-point representing the schizont stage. In both proteomic studies, Mn represented less than 5% of the metalloproteins found. Two uncharacterised proteins, A0A024WGY1_PLAFA and A0A024WGY1_PLAFA were found to be present in high abundance in T_{CYT} and low in DV thus supporting the observations described in Chapter 3. These proteins were found to be potential Zn binders as discussed in Section 4.3.6.2; however, since they belong to the M24B aminopeptidase family, they were also considered as potential Mn^{2+} metalloenzymes. Mn-associated enzymes identified in the Hz_{SP} and Hz_{Dis} fractions originated from various subcellular locations such as the cytoplasm [A0A024V7Z4_PLAFA, A0A024VMG0_PLAFA, PF14_0439], protein complexes [PF14_0630, RTCB_PLAF7] or were associated with the nucleus [A0A024VFU2_PLAFA]. This cohort of proteins are involved in cellular processes including but not limited to cleavage of *N*-terminal methionine from newly formed proteins, diverse aminopeptidase activity, catalytic activity of proteasome subunits and endonuclease activity.

4.3.6.5. Copper

Both copper and iron are reactive metals which can produce hydroxyl radicals by the Fenton reaction making it imperative to maintain intracellular Cu homeostasis in cells.[223] From the metallomics study, total copper detected in the parasite gradually increased over the 48 h life cycle with most concentrating in the DV. Due to its redox active nature, the accumulation or maldistribution of ionic copper can be lethal to the cell; therefore, various mechanisms are found in strategic subcellular locations to gather labile ions. Host erythrocytes contain micromolar amounts of copper of which 70% is found in the form of Cu/Zn SOD. As the parasite develops and feeds on the host cytoplasm, Cu/Zn SOD along with haemoglobin are trafficked to the DV and is the likely form of localised copper detected in this study. Even though Cu/Zn SOD is a fairly abundant enzyme, it was not detected by mass spectrometry. However, two human proteins that could also be a potential origin of the detected copper in the DV were identified in the Hz_{SP} fraction. These were cytoplasmic serum albumin [ALBU_HUMAN] and membrane-associated copper-transporting ATPase 1 [ATP7A_HUMAN] which are likely to follow the same fate as haemoglobin in terms of where it ultimately ends up.

Four specific *Plasmodium* specific copper proteins were identified, of which one was an uncharacterised protein. The uncharacterised protein [A0A024VMK0_PLAFA] was found to be associated with the haemozoin wash as well as in the trophozoite cytoplasm. This protein was characterised as membrane-associated, exhibited copper ion transmembrane transport activity and was capable of peroxiredoxin activity. Similarities were found to thioredoxin in that it has a thioredoxin domain at amino acid positions 3-162, thereby implying that its capable of forming an integral part of the antioxidant defence system.

A mitochondrial related protein, CG3 [O15798_PLAFA] was identified, and known to be a copper ion transporter involved in cytochrome c oxidase complex formation. As mentioned before, copper levels were observed to increase as the parasite matures. This complements the enhanced metabolic demand resulting in an increase in the mitochondrial content; therefore, this is likely a form of the observed copper ions detected in the parasite cytoplasm. Two putative transporters were found present in the dissolved haemozoin fraction: Cu^{2+} transporting ATPase [PFI0240c] and a copper

transporter [PF14_0369]. The former has been characterised to be involved in copper efflux and present in the parasite periphery and within the cytoplasm.[224, 317]

4.3.6.6. Selenium

Selenium was not measured by ICP-MS; however, human selenium-binding protein 1 [SBP1_HUMAN, A6PVW9_HUMAN] was detected to be highly abundant in the DV and this was further supported by the detection of this protein in Hz_{SP} and Hz_{Dis}. This erythrocyte cytoplasmic protein involved in protein transport and catalytic activity is better known for its grouping with glutathione oxidase and thioredoxin reductase which form the antioxidant network.[318] Selenium plays an important role as an antioxidant protein by providing protection against ROS. This trace element exhibits its antioxidant properties in the form of selenoproteins which contain selenocysteine, of which 25 are encoded in the human genome.[319]

Even though the Sec motif that describes selenoproteins is highly redox active and *Plasmodia* are highly susceptible to oxidative stress, especially in the DV during haemozoin formation, the selenoproteome specific to *P. falciparum* has not been extensively explored. Bioinformatic studies by Lobanov *et al* found there to be four unique parasite-specific selenoproteins (Table 4.11) which appear to be present in low abundance in the parasite itself.[320] A follow up study by Roseler *et al* using radioactive selenium in the parasite culture showed selenoproteins to localise in the ribosomes and nucleus.[321] However, such proteins were not identified in the current proteomic study.

Table 4.11. Description of four selenoproteins identified in *Plasmodium* as reported by Lobanov *et al*.[320]

PlasmoDB Accession Code	Protein Name	Abundance (ppm)
PF14_0033/ PF14_0462	Sel1	6.75
PFI1515w	Sel2	20.6
MAL8P1.86	Sel3	15.8
PF14_0251	Sel4	28.1

4.3.6.7. Iron

As demonstrated in Chapter 3, iron is highly abundant in trophozoites. This is overwhelmingly in the form of haemozoin crystals. However, using proteomics a number of Fe proteins and enzymes were identified which constitute an important part of the metalloproteome. Many of the proteins identified in the qualitative study were found to be Fe-S proteins and involved in various metabolic processes [A0A024V5V4_PLAFA, W4IA10_PLAFA, A0A024WJP7_PLAFA, DPOD1_PLAFK, RIR2_PLAFG, PFL1345c, PF14_0630, PFF1070c, PFI0380c]. A subset of these proteins were classified as uncharacterised proteins [A0A024VG17_PLAFA, W4IHP5_PLAFA, A0A024WG81_PLAFA, A0A024WQR6_PLAFA] with Fe-binding capacity and involved in metabolic functions and cell redox homeostasis. Interestingly, multidrug resistance protein 2 (MDR2) [Q8IKZ6_PLAF7] and methionine aminopeptidase 1[A0A024V7Z4_PLAFA] were found in Hz_{SP}. MDR2 belongs to the ATP-binding cassette (ABC) superfamily of transporters and found located in the DVM. This DV marker is actively involved in drug transport across the membrane and in maintaining iron homeostasis.[322, 323]

In the same qualitative study, Fe-SOD [PF08_0071] and ferredoxin reductase-like protein [PF07_0085] were found in Hz_{Dis}. Both enzymes incorporate Fe which indicates the likely form in which Fe is present in addition to haemozoin and are uniquely involved in the parasite enzymatic cellular redox network. *Plasmodium* Fe-SOD is distinct from human Cu/Zn SOD and Mn-SOD, binds one Fe cation per subunit and is responsible for destroying superoxide anions formed during cellular processes, more specifically during the oxidation of Fe^{2+} to Fe^{3+} in the DV.[324] An uncharacterised protein [W7K445_PLAFA] was identified by label-free proteomics to be present in high abundance in DV and low in T_{CYT}. This protein was found to contain ribosomal domains and belongs to the ribosomal protein L30, ferredoxin-like fold domain superfamily.

Eight erythrocytic proteins were identified by semi-quantitative proteomics, of which four were haemoglobin subunits [HBB_HUMAN, HBA_HUMAN, HBD_HUMAN, HBG2_HUMAN] detected in high abundance. Since haemoglobin accounts for more than 90% of the erythrocyte protein content, it was expected to be in high abundance in DV-related fractions and the main source of Fe present in the parasite within the haem cofactor. The other four detected proteins were the erythrocyte membrane protein band 4.2, ATP-binding cassette sub-family B member 6, catalase and flavin reductase and were

detected in high abundance in DV and T_{CYT} with the exception of the first two which were in low abundance in T_{CYT}. These proteins, although minor contributors to the total Fe content of the parasite, are integral components of erythrocytes where they function in iron homeostasis, haem catabolism and maintaining the shape of the erythrocyte.

Taking into account that Fe was the most abundant trace element measured across parasite fractions and that the major source was haemozoin, an interrogation of the proteins claimed to be involved in haemozoin formation was conducted. To date, HRP II and HDP have been implicated in haemozoin formation as both proteins are rich in histidine residues which are thought to bind haem in the correct orientation to allow dimerisation thus promoting crystal formation.[124, 131, 137] Closer inspection of the qualitative data revealed that neither of these proteins were detected. Despite the number of haemozoin crystals suggesting at least 30 proteins per crystal, these remained a challenge to find. It is well known that when a protein is identified by MS it can be concluded with confidence that the protein is present in that particular sample; however, if a protein is not identified it does not guarantee that the protein is absent owing to effects noted earlier in this chapter. Thus, a further effort was made to identify these proteins.

The label-free quantitative data were then interrogated in depth for HRP II and HDP by using a targeted approach when analysing MS data already obtained. In this case, HDP was detected in the DV lumen, trophozoite cytoplasm, first SDS wash of haemozoin as well as in the dissolved haemozoin fraction (Table 4.12), but HRP II remained elusive. As highlighted in Chapter 1, the majority of HRP II is thought to be located at the parasite periphery with only a small fraction believed to end up in the DV, this low level may have impacted on peptide identification even though mass spectrometry is a sensitive technique. Turning to HDP, the semi-quantitative profile obtained showed that this protein was detected in highest abundance in the dissolved haemozoin fraction; since each of these fractions represented the full sample derived from a common parasite preparation and were made up in equal volumes, this seems to suggest a specific association of HDP with haemozoin.

Table 4.12: Identification of HDP, 25 kDa (M_r), Q8IL04 (accession number) by mass spectrometry

Parasite fraction	No. unique peptides (*N*=4)	% Sequence coverage	Relative abundance
Trophozoite cytoplasm [a]	61.0 ± 9.7	100	Low
Digestive vacuole [b]	103.8 ± 34.3	100	Low
1st SDS wash of Haemozoin	42.8 ± 6.1	100	Low
Dissolved Haemozoin	48.5 ± 13.9	100	High

[a] *Excluding the digestive vacuole and haemozoin,* [b] *Excluding haemozoin*

4.3.7. Collation of additional proteins identified in relation to the DV

The increase in number of haemozoin crystals used in the qualitative study afforded a higher number of proteins that were identified in the haemozoin wash and dissolved haemozoin fractions. Focusing on dissolved haemozoin, several known DV markers, proteins involved in trafficking, vesicle formation and the haemoglobin digestion pathway were found (Table 4.13) and this subset was in accordance to that previously reported to constitute the DV proteome by LaMarque *et al*.[181]

In addition to HDP, other components of the multi-enzyme complex proposed by Chugh *et al* suggested to be involved in the process from haemoglobin catabolism to haemozoin formation were identified in this study.[51] With the exception of falcipain 2, all three of plasmepsin II, plasmepsin IV and HAP were found to be associated with the haemozoin fractions. Plasmepsin I was also detected with the result that all four aspartic proteases were found in intimate association with haemozoin. This finding also supports the approach of preparing an enriched haemozoin sample which seemingly affords an enriched representation of the proteins present in the DV during the most metabolically-active stage of the parasite life cycle.

Cysteine protease falcipain 1, which is quite biochemically different to its isoenzymes, was detected. Cysteine proteases falcipain 2 and 3 play active role in site specific cleavage of host haemoglobin, however, even though expressed during the intraerythrocytic cycle, falcipain 1 may not be essential to parasite functions.[325-327] The detection of DVM markers, PfCRT and PfMDR1 in this study is consistent with what may be expected if haemozoin is in direct contact with the DVM as suggested by Kapishnikov *et al*.[151] The detection of

merozoite surface protein 9 which is known to be present even before merozoite formation was likely detected either due to a mixed parasite culture or because it was taken up as part of the PPM/PVM. Knob-associated HRP, membrane associated HRP, parasitophorous vacuolar protein 1 and exported proteins all comprising the parasite surface were likely to be detected because of the trafficking route discussed earlier in Section 4.3.1.

Haemozoin washings representing weakly-associated proteins comprised mainly metabolic proteins and those involved in the antioxidant network in the parasite. Additional V-type ATPase subunits were detected. These are proton pumps or used for cation exchange across the DVM and are important for regulating DV pH.[328] Interestingly, two out of the three DV proteins not detected by LaMarque *et al* were identified in this proteomic study, namely *N*-ethylmaleimide sensitive fusion protein and CG2. These proteins were found in Hz_{Dis} and Hz_{SP}, respectively. CG2, a high molecular weight protein of 320-330 kDa was likely detected in this study due to the higher percentage gel used (15 vs 12%) compared to that of LaMarque *et al* which allowed the detection of high molecular weight proteins. CG2 has been shown to be expressed at the parasite periphery detected in the PVM, cytoplasm and DV by electron microscopy and expression was shown to increase along with haemoglobin uptake and digestion, therefore supporting the finding of an association with haemozoin formation.[329] *N*-ethylmaleimide-sensitive factor is a protein that promotes vesicle transport from one membrane component to another forming an integral part of the secretory pathway. Electron microscopy studies showed this protein to be associated with the DV.[330] Uroporphyrinogen decarboxylase, an enzyme involved in haem biosynthesis, was detected in surface washings. A number of hypothetical/uncharacterised proteins were found but none displayed any similarity to HRP II in terms of function or sequence and none appeared to be potential key mediators in haemozoin formation.

Table 4.13: DV marker proteins identified from in Hz_{SP} and Hz_{Dis} from in-gel samples

Accession No.	Protein Description	Associated Functions	Haemozoin Fraction
PF14_0282	Acid phosphatase, putative	Acid phosphatase	Hz_{Dis}
MAL8P1.82	Vacuolar sorting protein VPS9, putative	Ubl conjugation pathway, Protein targeting to vacuole	Hz_{Dis}
PFC0140c	*N*-ethylmaleimide sensitive fusion protein, putative	Vesicle-mediated transport	Hz_{Dis}
PFL1385c	Merozoite surface protein 9	Pathogenesis	Hz_{Dis}
PF13_0065	Vacuolar ATP synthase subunit a	Proton-transporting ATPase activity, Vacuolar acidification	Hz_{Dis}
PF14_0201	Surface protein, Pf113		Hz_{Dis}
PF14_0615	ATP synthase (C/AC39) subunit, putative	Hydrogen ion transmembrane transporter activity; vacuolar acidification	Hz_{Dis}
PF13_0034	Vacuolar ATP synthase subunit h, putative	Vacuolar acidification	Hz_{Dis}
PF11_0302	Parasitophorous vacuolar protein 1		Hz_{Dis}
PFD0090c	Plasmodium exported protein		Hz_{Dis}
PF14_0678	Exported protein 2		Hz_{Dis}
PF10_0329	Plasmepsin VII	Aspartic-type endopeptidase activity; proteolysis	Hz_{Dis}
PF14_0078	Histo-aspartic protease	Aspartic-type endopeptidase activity; proteolysis	Hz_{Dis}
PF14_0075	Plasmepsin IV	Aspartic-type endopeptidase activity, haemoglobin catabolic process	Hz_{Dis}
PF13_0133	Plasmepsin V	Aspartic-type endopeptidase activity; proteolysis	Hz_{Dis}
PF14_0077	Plasmepsin II	Aspartic-type endopeptidase activity, haemoglobin catabolic process	Both
PF14_0076	Plasmepsin I	Aspartic-type endopeptidase activity, haemoglobin catabolic process	Both
MAL7P1.27	Chloroquine Resistance Transporter	Drug transmembrane transport	Both
PFE1150w	Multidrug resistance protein	Transmembrane movement of substances	Both

PF14_0553	Cysteine proteinase falcipain 1	Cysteine-type peptidase activity, haemoglobin catabolism	Hz_{Dis}
PF14_0428	Histidine tRNA ligase, putative	tRNA aminoacylation for protein translation	Hz_{Dis}
PFB0100c	Knob-associated histidine-rich protein		Hz_{Dis}
MAL13P1.413	Membrane associated histidine-rich protein		Hz_{Dis}
PF13_0276	Membrane-associated histidine rich protein 2, (MARHP2)		Hz_{Dis}
O15797_PLAFA	CG4	ATP binding	Hz_{SP}
O15791_PLAFA	CG2		Hz_{SP}
O15798_PLAFA	CG3	Cu ion transport and homeostasis	Hz_{SP}
A0A024V9Z4_PLAFA	Uroporphyrinogen decarboxylase	Protoporphyrin IX biosynthesis	Hz_{SP}
Q9NBA7_PLAFA	Cysteine protease falcipain-3	Cysteine type peptidase activity	Hz_{SP}
E7DX59_PLAFA	Glutathione reductase	Oxidoreductase	Hz_{SP}
W4IDL5_PLAFA	Glutathione peroxidase	Glutathione peroxidase activity, response to oxidative stress	Hz_{SP}
Q8I461_PLAF7	Cation transporting P-ATPase	Cation transport, metal ion binding, ATP binding	Hz_{SP}
A0A024UY38_PLAFA	V-type H(+)-translocating pyrophosphatase	Proton transport	Hz_{SP}
A0A024WGA1_PLAFA	V-type ATPase, C subunit	Ion transport	Hz_{SP}
VATB_PLAFA	V-type proton ATPase subunit B	Ion transport, ATP activity	Hz_{SP}
Q8ID33_PLAF7	NADH-cytochrome B5 reductase, putative	Electron carrier, redox activity	Hz_{SP}
A0A024WL88_PLAFA	Vacuolar protein sorting-associated protein 26	Protein transport	Hz_{SP}

4.4. Chapter Summary

Parasite material was analysed for potential metal-associated proteins using both qualitative and semi-quantitative proteomic-based mass spectrometry methods. A fractionation approach was strategically employed when preparing parasite samples to reduce overall complexity but more specifically with respect to haemozoin to try to limit contamination. By interrogating the *P. falciparum* and *H. sapiens* genomes, thousands of proteins were identified in this study, but only a subset was deemed likely to be specifically involved in processes related to haemozoin formation or the DV, while others detected were likely contaminants carried through the isolation process.

Increasing the number of haemozoin crystals used allowed the detection of more proteins. Specific DV markers and those implicated in haemoglobin digestion and haemozoin formation were successfully identified. Several metal-associated proteins were identified across the trophozoite cytoplasm and DV and label-free proteomics generated relative abundance profiles for a number of these. Supporting the metal content measured across the parasite, key metalloproteins constituting the metalloproteome of the DV were represented by haemoglobin, Fe SOD, Cu/Zn SOD, falcilysin, M1 aminopeptidase and *S*-adenosylmethionine synthase. These are the likely major proteins in which Fe, Cu, Zn and Mg, respectively detected in Chapter 3 are found.

The haem iron-associated metalloprotein, HDP, was identified across the parasite but was detected in high abundance in the dissolved haemozoin fraction. This protein has been previously implicated in haemozoin formation and its identification suggests that it has a specific affinity for haem in the DV. However, since the surface of haemozoin crystals are unlikely to be completely free of biomaterial prior to base dissolution, it is possible that biomolecules other than proteins are present as well and could be potential mediators of β-haematin formation. The potential role of recombinant HDP in β-haematin formation will be explored in Chapter 5.

Chapter 5

Expression, Characterisation and Activity Studies of Haem Detoxification Protein

5.1. Introduction

Haemozoin formation in haematophagous organisms such as *Rhodnius prolixus, Schistosoma mansoni* and, most importantly, *P. falciparum* proceeds via an intricate biocrystallisation process that is thought to be mediated by biomolecules.[73, 74] To date, there is much contention as to which specific biomolecules, be it proteins or lipids, are responsible for this essential process in the malaria parasite. Biomineralisation across organisms ranging from invertebrates to vertebrates is driven by the cell, coupled with the unique binding properties of specific proteins to crystal components.[331] The involvement of these proteins in biomineralisation processes such as kidney stone formation[109], formation of mollusc shells[332], spicules of sea urchins[106], human bone matrix,[111] and the hermatypic coral skeleton[108] have been extensively researched and identified using mass spectrometry techniques in an attempt to elucidate the biomineral proteome which is organism-specific.

Turning to the *Plasmodium* proteome, native and recombinant HRP II was amongst the earliest proteins shown to efficiently promote β-haematin formation which sparked further interest in attempting to identify other proteins as key mediators in this biocrystallisation process.[124] HDP, a functionally conserved protein across the *Plasmodium* genus and shown to be crucial to parasite survival, was reported to be potent in converting free haem into β-haematin.[131] The involvement of HDP in haemozoin

formation and its association with other proteins within the DV was later investigated using coimmunoprecipitation, SDS-PAGE and LC-MS/MS leading to the conclusion that HDP forms part of a 200 kDa multienzyme complex responsible for haemoglobin degradation and haemozoin formation as discussed in Chapter 1.

LC-MS/MS data in Chapter 4 (Table 4.12) identified HDP to be present in high abundance in the dissolved haemozoin fraction therefore suggesting that it was occluded by the crystals during formation and has a specific association with haemozoin. Expression of recombinant HDP (rHDP) in bacterial cell lines has proven to be rather challenging, yielding very low to no soluble protein with an abundance of HDP precipitating out as inclusion bodies.[51, 131] Due to these difficulties, all studies carried out thus far have used refolded HDP which is not the best option as there is no guarantee that the protein will be in its native conformation after solubilising with denaturants followed by refolding. These factors raise questions as to whether HDP is, in fact, the key mediator in promoting haemozoin formation and what impact the soluble form would have on β-haematin formation. This chapter focuses on presenting the design and optimisation for the expression and purification of soluble rHDP. The characterisation of expressed target protein and its role in β-haematin formation will be explored.

5.2. Experimental Methods

5.2.1. Plasmid preparation and gene synthesis

Transformation of a chemically competent DH5-α cell line with the cold shock expression vector, pCold I, was carried out using a standard heat-shock technique. The transformed DH5-α cells were plated onto agar plates containing ampicillin (100 µg/mL) and incubated upside down at 37°C overnight. Successfully transformed DH5-α colonies were selected and transferred into an autoclaved bottle containing 5 mL Luria Broth containing ampicillin (100 µg/mL) using aseptic techniques. These cells were gently agitated in a shaking incubator at 30˚C overnight. A 1 mL aliquot of the overnight culture was then transferred into a sterile Eppendorf tube and centrifuged at 10 000 rpm for 30 s using a benchtop mini-spin. The supernatant was discarded, and this step repeated until all cells from the overnight culture were recovered. Plasmid DNA was extracted from pelleted cells using the BioFlux Biospin Plasmid DNA Extraction Kit (Hangzhou Bioer Technology)

as per the manufacturer's instructions. DNA concentration was measured by monitoring the absorbance 260 nm using a NanoDrop™ obtaining an absorbance ratio of DNA to protein (A_{260}/A_{280}) of ≈ 2.0 confirming pure DNA to be present. Agarose gels were used to separate DNA fragments and to validate and further check purity.

Gene synthesis of HDP was performed by GeneArt GmbH (Thermo Fisher Scientific, Germany). The synthesised gene was cloned into the pCold I expression vector with codon optimisation for expression in *E. coli* using 5' Nde1 and 3' BamH1 as restriction enzyme sites. Codon usage was adapted to *E. coli* genes; regions that were GC rich (> 80%) and GC deficient (< 30%) were avoided. Gene optimisation was successful with a codon adaptation index (C.A.I) of 0.94 which indicates that this gene would allow for high and stable expression rates in the respective *E. coli* strains.

5.2.2. Transformation

Plasmids incorporating the synthesised HDP gene were reconstituted in 50 µL autoclaved water to produce a stock solution of 100 ng/µL. A 1 µL aliquot of reconstituted plasmid was added to 100 µL of competent cells in a sterile Eppendorf tube, which was gently tapped to encourage mixing. Expression vector pCold I was processed as the experiment and pMK-T used as a negative control. Cells containing the plasmid were activated by heat shock treatment by being placed on ice for 20 min, followed by a 30 s incubation at 42°C and, finally, on ice for a further 2 min. 900 µL of Luria Broth was transferred into a 15 mL Falcon tube, into which 100 µL of cells were added giving a final volume of 1 mL. Cells were incubated at 37°C for an hour while shaking, after which the cells were centrifuged at 3 500 rpm for 2 min. Agar plates containing ampicillin were poured and stored at 4°C after solidifying.

Using sterile bacterial culturing techniques, 200 µL of cells were loaded onto the agar plate and evenly distributed using a sterile glass spreader. Plates were secured with parafilm and incubated at 37°C overnight. After incubation, these were inspected for the formation of single colonies and thereafter stored at 4°C until starter cultures were prepared. Single colonies were observed in the experimental plate thus indicating that HDP had successfully been expressed in this cell line. No satellite colonies were observed indicating that the cells grew for an appropriate amount of time. Starter cultures were

prepared using aseptic techniques. Autoclaved 10 mL culture media aliquots containing ampicillin at 100 µg/mL were prepared and maintained at room temperature. Agar plates stored at 4°C were allowed to equilibrate at room temperature prior to use. Sterilised tweezers were used to pick a single colony off the surface of the agar plate which was transferred directly into the culture medium and incubated with shaking at 37°C overnight. The same procedure was followed for each new cell strain evaluated as well as the incorporation of chaperone plasmids. Additional methods regarding the preparation and use of chaperone plasmids were followed as per the manufacturer's instructions (Chaperone Plasmid Set, Takara).

5.2.3. Expression of rHDP

Protein was expressed using the C41 *E. coli* cell line in Terrific Broth, a nutrient-rich medium, supplemented with 1% glucose to suppress leaky expression and ampicillin at 100 µg/mL for plasmid maintenance. Overnight cultures were used to inoculate a bulk culture by transferring 5 mL of these cells into 1 L culture medium containing the appropriate antibiotic and incubated at 37°C for 3 h with gentle shaking. Cell growth was monitored by measuring the optical density (O.D.) at 600 nm of the cell culture between 3-4 h after incubation until mid-log phase growth (O.D. of 0.6-0.8) was reached. The O.D. was measured using a Thermo Electron Helios Gamma Spectrophotometer (Thermo Fisher Scientific). At mid-log phase, cell cultures were removed from the incubator and immediately placed on ice in preparation for induction with isopropyl β-D-1-thiogalactopyranoside (IPTG). IPTG is a non-hydrolysable lactose analogue that releases repression of the *lac* operon thereby inducing protein expression when the gene is under the control of a *lac* operator.[333] In trial experiments utilising δ-aminolevulinic acid (ALA), culture media were supplemented with 0.5 mM ALA and 2.5 mL/L trace element solution prepared by combining 2.7 g $FeCl_3.6H_2O$, 0.2 g $ZnCl_2.4H_2O$, 0.2 g $CoCl_2.6H_2O$, 0.2 g $Na_2MoO_4.2H_2O$, 0.1 g $CaCl_2.2H_2O$, 0.13 g $CuCl_2.6H_2O$, 0.05 g H_3BO_3, 10 mL concentrated HCl and making up to 100 mL in distilled water.

Bacterial cultures harbouring the pCold I-HDP expression plasmid were induced with 0.5 mM IPTG at 15°C with shaking for 48 h in a C24KC refrigerated incubator shaker (New Brunswick Scientific) and topped up with ampicillin at regular intervals. Cells were harvested by centrifugation at 4 000 *g* for 20 min at 4°C using an Allegra X-30R centrifuge

(Beckman Coulter). The supernatant was gently discarded so as not to disturb the cell pellet. The cell pellet was then resuspended in lysis buffer (0.05 M Tris-HCl, pH 8.0, 0.5 M NaCl at pH 8.0 containing 1× SigmaFAST™ EDTA-free protease inhibitor cocktail) and incubated on ice for 60 min with intermittent homogenisation. Cells were then sonicated for a total processing time of 4 min at 45 W in 15 s bursts using a Misonix Sonicator 3000 Ultra Sonic Cell Disruptor (Cole-Palmer) to lyse them. Thereafter the cell suspension was centrifuged at 20 000 *g* for 30 min at 4°C in pre-chilled high-spin centrifuge tubes. The supernatant, which contained soluble rHDP, was used for purification and the pellet containing rHDP in the form of inclusion bodies, was isolated and refolded as described later in this chapter.

5.2.4. Purification of soluble rHDP

Soluble rHDP was purified from the supernatant obtained after cell lysis using a HisTrap™ Chelating High Performance Column (GE Healthcare) containing nickel-nitrilotriacetic acid (Ni-NTA) His•Bind® Resin (Merck). This nickel affinity column was attached to an AKTA Explorer (GE Healthcare, Life Sciences) automated chromatography system. The column was equilibrated with freshly-prepared binding buffer comprising 0.02 M $NaHPO_4$, pH 7.4 and 0.5 M NaCl. Protein samples were filtered through a 0.45 µm cellulose acetate syringe filter prior to being loaded onto the column. Nickel affinity purification proceeded via a two-step process, first through a low pH wash with 0.02 M $NaHPO_4$, pH 6.5, 0.5 M NaCl followed by competitive elution with 0.5 M imidazole in 0.02 M $NaHPO_4$, 0.5 M NaCl at pH 7.4 to generate an imidazole gradient at an elution rate of 5 mL/min. The software used to monitor affinity chromatography, modify methods and interpret chromatograms was UNICORN™, version 4.11, Amersham Biosciences.

Fractions were evaluated by gel electrophoresis and those containing a band at ~25 kDa were pooled and concentrated to 5 mL using an Amicon-Ultra Filter Unit with a molecular nitrocellulose membrane (10 kDa molecular weight cut-off). Size-exclusion chromatography (SEC) was used as a polishing purification step by loading 1 mL of the concentrated affinity purified protein onto a Superdex 200 10/300 GL High Performance Column, Tricorn (GE Healthcare) equilibrated with 1× PBS, pH 7.4 and eluted at 1 mL/min. The software used to monitor SEC and interpret chromatograms was Gilson UniPoint™.

Progression and optimisation of protein expression and purification methods were monitored by SDS-PAGE. Protein concentrations were determined using a NanoDrop™ as well as Bradford assay (Bio-Rad) as per the manufacturer's protocol. Fractions containing pure rHDP were pooled, concentrated and stored in 1× PBS buffer, pH 7.4 supplemented with 10% (*v/v*) glycerol at -80°C until further use.

5.2.5. Detection of His-Tag fusion proteins

Following SDS-PAGE of protein fractions, gels were sequentially stained using InVision™ His-Tag In-Gel Stain (Life Technologies, Novex, ThermoFisher Scientific #LC6030) which allows for specific detection of His-Tag proteins. Briefly, the gels were first incubated in 200 mL fixing solution comprising ethanol, acetic acid and water (5:1:4 *v/v*) for 1 h with gentle shaking at 1.5 revolution per second on an orbital shaker. The fixing solution containing acetic acid caused the gel to shrink which was then rehydrated first by two 10 min washes with MilliQ water after which the gel was incubated in 25 mL His-Tag In-Gel Stain for 1 h in the dark. Immediately after incubation the stain was decanted, and the gel rinsed using phosphate buffer (0.02 M, pH 7.8) for 10 min. After staining, gels were stored in 100 mL phosphate buffer and immediately imaged using a Bio-Rad ChemiDoc XRS+ with ImageLab software (Version 5.2.1, BioRad Laboratories, Inc.).

5.2.6 Mass Spectrometry

Qualitative proteomics was employed for target protein identification from protein expression experiments.

i. Preparation of Gel Samples

Protein bands of interest were processed as described earlier in Chapter 2. Coomassie stained gel pieces were destained with 0.2 M NH_4HCO_3/Acetonitrile (50:50 *v/v*) until transparent.

ii. In-Gel Digest

In-gel trypsin digest was performed as described in Section 2.5.11 with the modification that these samples were dried down and resuspended in 30 µL of a solution comprising 2% acetonitrile/water and 0.1% formic acid following digest.

iii. Desalting

Residual digest reagents were removed using an in-house manufactured C_{18} stage tip (Empore Octadecyl C_{18} extraction discs; Supelco). First, the C_{18} membrane was activated with 30 µL methanol followed by equilibration with 30 µL 2% acetonitrile/water containing 0.1 % FA. The sample was loaded onto the stage tip following equilibration, bound sample was washed with 30 µL 2% acetonitrile/water containing 0.1% FA. The bound peptides were then eluted with 30 µL 50% acetonitrile/water and 0.1% FA, thereafter the eluent was evaporated to complete dryness. The dried peptides were then dissolved in 2% acetonitrile/water and 0.1% FA in preparation for LC-MS analysis.

iv. Liquid Chromatography

Liquid chromatography was performed using a Thermo Scientific Ultimate 3000 RSLC equipped with a 5 mm × 300 µm C_{18} trap column and a 35 cm × 75 µm in-house manufactured C_{18} column (Aeris C_{18}, 3.6 µm; Phenomenex) analytical column. The solvent systems employed were: Loading: 2% acetonitrile/water; 0.1% FA

Solvent A: 2% acetonitrile/water; 0.1% FA

Solvent B: 100% acetonitrile/water

The samples were loaded onto the trap column using loading solvent at a flow rate of 20 µL/min from a temperature controlled autosampler set at 7°C. Loading was performed for 10 min before the sample was eluted onto the analytical column. Flow rate was set to 300 nL/min and the gradient generated as follows: 2% B constant over 10 min; 2-10% B from 10-15 min; 10-35% B from 15-75 min using Chromeleon non-linear gradient 6 and 35-50% B from 75-85 min. Chromatography was performed at 50°C and the outflow delivered to the mass spectrometer through a stainless steel nano-bore emitter.

v. Mass Spectrometry

Mass spectrometry was performed using a Thermo Scientific Fusion mass spectrometer equipped with a Nanospray Flex ionization source. The sample was introduced through a stainless-steel emitter. Data were collected in positive mode with spray voltage set to 2 kV and ion transfer capillary set to 280°C. Spectra were internally calibrated using polysiloxane ions at *m/z* = 445.12003 and 371.10024. MS1 scans were performed using the orbitrap detector set at 120 000 resolutions over the scan range 350-1650 with AGC target at 3×10^5 and maximum injection time of 40 ms with data acquired in profile mode. MS2 acquisitions were performed using monoisotopic precursor selection for ions with charges +2 to +6 with the error tolerance set to ± 10 ppm. Precursor ions were excluded from fragmentation once for a period of 30 s and were selected for fragmentation in HCD mode using the quadrupole mass analyser with HCD energy set to 32.5%. Fragment ions were detected in the orbitrap mass analyser set to 30 000 resolutions. The AGC target was set to 1×10^4 and the maximum injection time to 45 ms. These data were acquired in centroid mode.

vi. Data Analysis

The raw files generated by the mass spectrometer were imported into Proteome Discoverer version 1.4 (Thermo Scientific) and processed using the Sequest algorithm. Database interrogation was performed against a concatenated database created using the Uniprot *E. coli* database and the supplied HDP sequence with semi-tryptic cleavage allowing for 2 missed cleavages. Precursor mass tolerance was set to 10 ppm and fragment mass tolerance set to 0.1 Da. Protein *N*-terminal acetylation, deamidation (NQ) and oxidation (M) was allowed as dynamic modifications and thiomethyl of C as static modification. Peptide validation was performed using the peptide validator node set to search against a decoy database with strict FDR 1%. The results files were imported into Scaffold 1.4.4 and identified peptides validated using the X! Tandem search algorithm included in Scaffold. Peptide and protein validation were performed using the Peptide and Protein Prophet algorithms.

5.2.7. Circular Dichroism Spectroscopy

Circular dichroism spectra of purified soluble and refolded rHDP were recorded in 0.01 M sodium acetate, pH 5.2 and 0.1 M sodium phosphate, pH 7.4 at a protein concentration of 0.2 mg/mL. Protein samples were aliquoted into a 0.1 mm cuvette and spectra recorded in the far UV region (185-280 nm) using a Chirascan™–plus Circular Dichroism Spectrometer at room temperature. Spectral data were processed using Applied Photophysics Pro-Data Chirascan software version 4.2.6.

5.2.8. Fluorescence Spectroscopy

Working solutions of 0.2 mg/mL soluble and refolded rHDP in 0.01 M phosphate buffer, pH 7.4 were transferred to a Hellma, Suprasil® fluorescence quartz cuvette with a volume capacity of 50 µL. Fluorescence emission spectra were recorded using a Varian Cary Eclipse Fluorescence Spectrophotometer where all steady-state fluorescent measurements were carried out at 25°C controlled by a regulated temperature cell holder with excitation at 290 nm.

5.2.9. Spectrophotometric Titrations

Due to the nature of haem and its tendency to adhere to glass and plastic, all haem solutions were freshly prepared and stored only for the duration of each experiment in a glass vial.[334] All quartz cuvettes, Hamilton syringes and glassware used in haem-related experiments were thoroughly washed with 0.1 M NaOH, 1 M HNO_3 and finally distilled water and then allowed to dry in an oven at 37°C.

UV-vis spectra were recorded using a Shimadzu UV-1800 spectrophotometer over the range 250 to 800 nm. Due to the limited amount of rHDP, all reactions were carried out on a small scale using a 660 µL quartz cuvette (Hellma, Suprasil) with a 1 cm pathlength maintained at a constant temperature of 25°C. Spectrophotometric titrations were performed by adding aliquots of a freshly prepared 0.02 M haemin solution in 0.1 M NaOH, into a 1 µM solution of rHDP in 400 µL of HEPES (0.1 M, pH 7.4) buffer. Additions to the buffered protein solution were performed using a 25 µL Hamilton syringe in increments until a final concentration of 5 µM haem was added, with stirring after each

addition. Absorbance spectra were corrected for dilution and titration data were analysed using GraphPad Prism version 4.

5.2.10. Exchange studies with rHDP

Isolated haemozoin and synthesised β-haematin (1 mg) crystals were incubated in a 1 mL sodium acetate (0.5 M, pH 5.2) buffered solution containing 2 μM rHDP for 30 min at 37°C. In a parallel experiment, β-haematin was synthesised in the presence of rHDP using the model lipid blend (Section 6.2.3) where rHDP was added to the lipid/haem mixture to afford a final concentration of 2 μM protein as described above. Following the 30 min incubation period, samples were centrifuged at 13 500 rpm for 10 min and the supernatant set aside. The remaining pellet was extensively washed, first with sodium acetate buffer (0.5 M, pH 5.2) followed by four washes each with 4% (*w/v*) SDS solution and PBS (10 mM, pH 7.4), after which the pellet was dissolved in 0.1 M sodium hydroxide. The β-haematin precipitate prepared using lipids in the presence of rHDP was washed with an aqueous pyridine solution containing 5% (*v/v*) pyridine, 30% (*v/v*) acetone and 0.02 M HEPES (pH 7.4) before proceeding with detergent and buffer washes as described above. A nitrilase from *Synechocystis sp*. strain PCC6803 (Nit6803), a non-related His-tagged protein, was used as a positive control. Experiments comprising only rHDP and the nitrilase in buffer were subjected to the same incubation conditions and used as controls.

Control proteins, washings and dissolved pellets were used to prepare gel samples as described in Chapter 2. A 5 μL aliquot of Colour Prestained Protein Standard, Broad Range 11 to 245 kDa (New England BioLabs #P7712S) was loaded into the first lane of each gel (15% SDS-PAGE); thereafter, 15-20 μL of the respective samples were loaded sequentially. Gel electrophoresis was run at 30 mA for 75 min for double gels using a Bio-Rad Power-Pac Basic unit. Gels were stained for specific detection of histidine tags following the procedure described in the InVision™ His-Tag In-Gel Stain (ThermoFisher Scientific #LC6030) product guide and imaged as described earlier in Section 5.2.5.

5.2.11. β-Haematin Formation Assay

The role that rHDP plays in haemozoin formation was investigated following previously reported methods which investigated the activity of HRPII in β-haematin formation as reported by Sullivan *et al* with modifications.[124]

Haemin stock solution (0.01 M) was prepared in *N, N*-dimethylformamide prior to use. The β-haematin formation assay was set up in a 1 mL glass reaction vial containing 600 µM haem and 0.5 µM rHDP in sodium acetate buffer (0.5 M, pH 5.2) and incubated at 37°C for 1 h. A control experiment was set up in the same way but without the addition of any protein. After incubation, SDS was added to a final detergent concentration of 0.1% (*w/v*). Samples were then transferred into individual Eppendorfs and centrifuged at 15 000 rpm for 15 min at room temperature. The supernatant was discarded and the pellet washed using 5% (*v/v*) pyridine in HEPES (0.02 M pH 7.4). Pyridine at this concentration and pH is known to solubilise unreacted free haem that is present while β-haematin remains insoluble. The remaining precipitate was further washed with 1 mL MilliQ water followed by three 1 mL washes with acetone/methanol (1:9 *v/v*). The resulting washed pellet was dried and characterised using FT-IR, pXRD, SEM and TEM.

5.3. Results and Discussion

5.3.1. Soluble Recombinant HDP

5.3.1.1. Rationale behind using pCold I as a suitable expression vector

E. coli utilised as expression hosts are highly advantageous as they are versatile microorganisms with an easily manipulable genome. They successfully host foreign DNA, produce protein in high yield, are simple to use and affordable. Even though *E. coli* is routinely used as a workhorse for heterologous protein expression across diverse organisms, expressing soluble recombinant *Plasmodium* proteins remains a challenge due to its AT-rich genome and low complexity regions.[135] This high AT vs GC content is thought to bring about early termination of mRNA translation resulting in recombinant proteins forming aggregates and precipitating out as inclusion bodies within the expression host.[335] Attempting to solubilise inclusion bodies using chaotropic agents followed by

refolding is unique to each protein and requires in-depth troubleshooting and optimisation which is both labour intensive and costly.[336]

In addition, once refolded, one is not guaranteed correct and complete refolding of the protein into its native conformation, making this material less desirable for structure and activity studies. There are distinct differences in the amino acid content between *Plasmodium* and *E. coli* proteins imposing a metabolic burden on the host cell thereby rendering the *Plasmodium* proteins as 'toxic' thus further contributing to the difficult task of expressing such proteins.[337]

Thus far, rHDP has been synthesised using the pET101 and pQE30 expression vectors in BL21 and M15 *E. coli* cell lines, respectively. These strategies resulted in HDP being expressed largely as inclusion bodies that were refolded and used to investigate its role in haemozoin formation.[51, 131] Nakatani *et al* reported the application of pCold IV as an expression vector using BL21(DE3) cells in which a minute fraction of soluble HDP in addition to the high yield of inclusion bodies was observed.[138]

The aim of this study was to optimise the expression of soluble rHDP, thereby producing material that closely resembles its native conformation and so providing further insight into its properties and activity. In an attempt to optimise soluble expression of rHDP and overcome the formation of inclusion bodies, a variety of expression conditions were explored starting with the choice of expression vector. The strategy chosen extended on that of Nakatani *et al* whereby rHDP-pCold IV (Figure 5.1a) was expressed in BL21(DE3) cell line. Application of the pCold vector suite allows for low temperature protein expression. Expression at high temperature encourages cells to grow rapidly due to a faster rate of metabolism resulting in the cell drastically overexpressing the recombinant protein and subsequently struggling to optimise its folding mechanisms. This results in the majority of recombinant protein being shunted to inclusion bodies. In contrast, growing cells at a lower temperature slows the rate of growth, therefore allowing for its cell machinery to correctly fold the recombinant protein of interest.

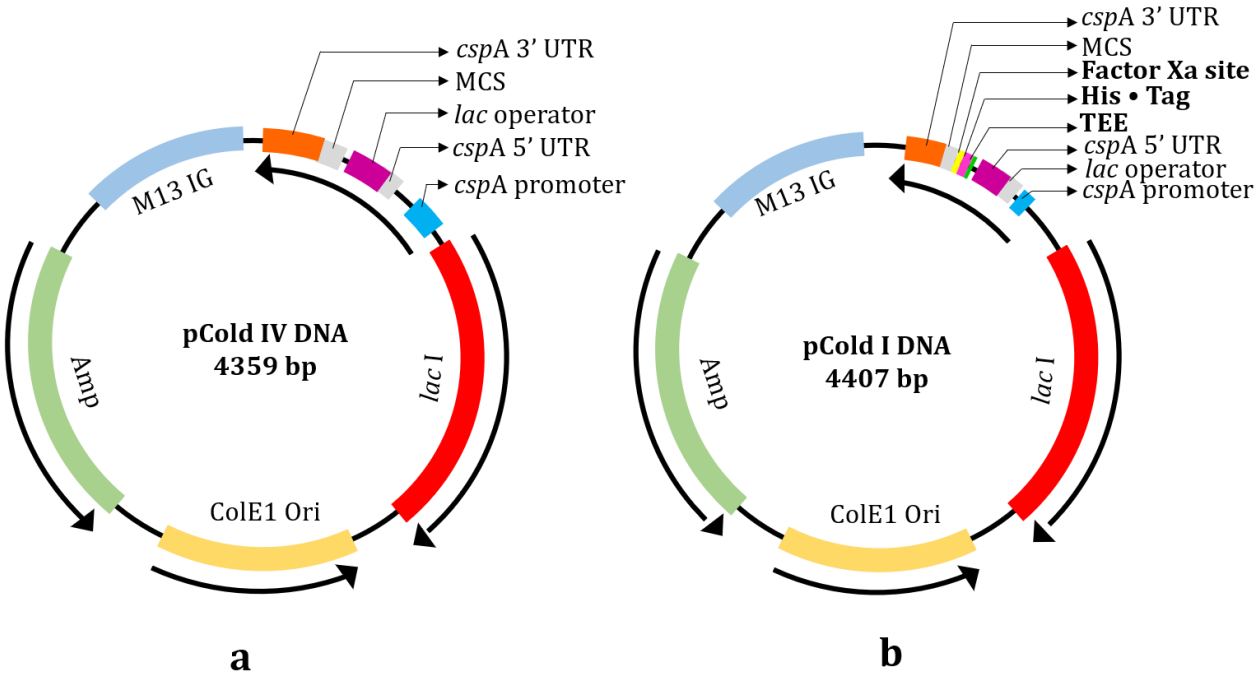

Figure 5.1. Vector maps representing pCold expression vectors of interest. Schematic vector maps of pCold IV **(a)** and pCold I **(b)** illustrating essential differences between the two expression vectors.

Cold Shock Expression System pCold I (Figure 5.1b and 5.2) encodes a hexahistidine tag upstream (*N*-terminus) of the open reading frame (ORF) allowing the use of nickel affinity chromatography to form part of the protein purification strategy. Protein expression is controlled by the cold shock promoter, *csp*A, factor Xa cleavage site allows for post expression cleavage of the His-tag if needed and the translating enhancement element (TEE) located downstream of *csp*A allows for optimised low temperature expression.[338] Utilisation of pCold I offered an advancement over the previously reported pCold IV vector with the above-mentioned advantages.

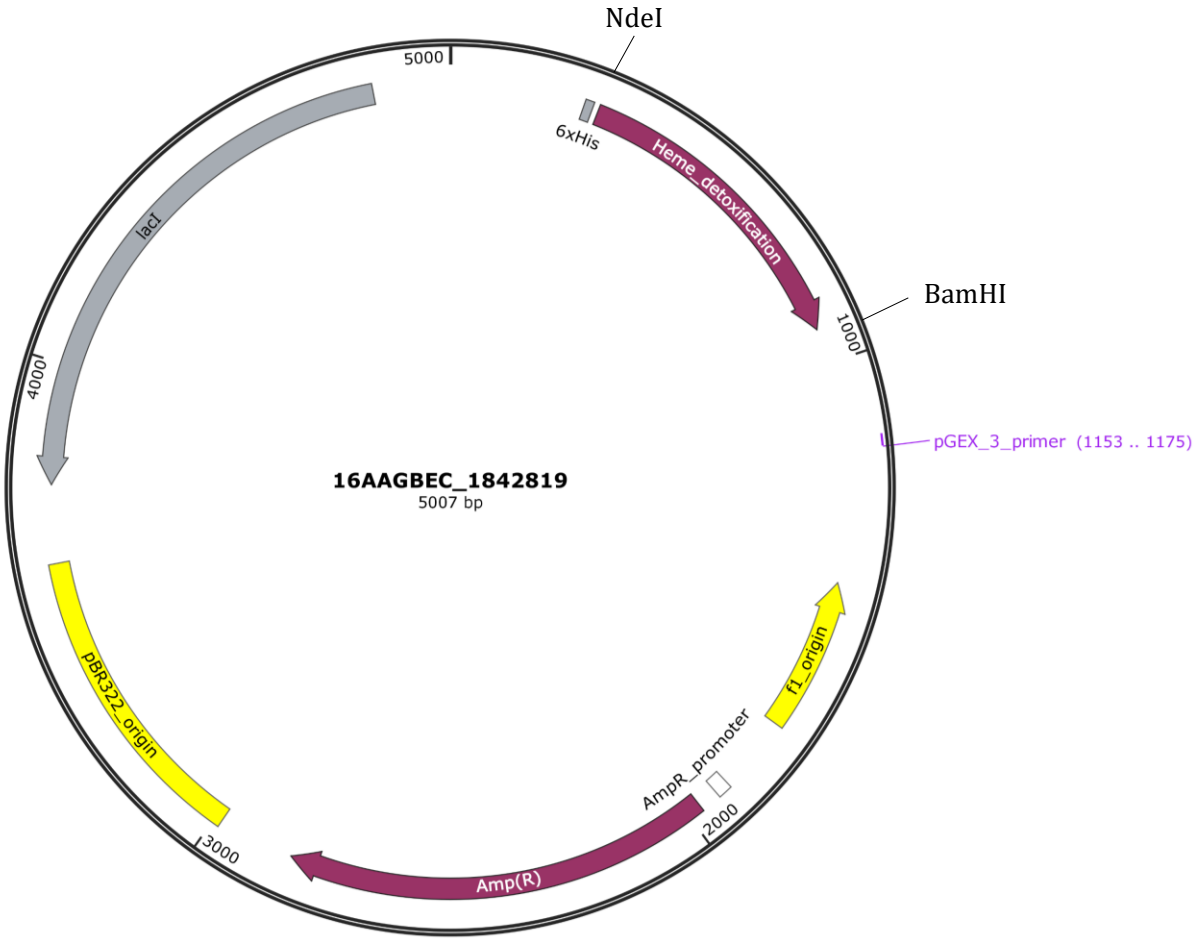

Figure 5.2. Vector map of synthesised expression plasmid pCold I-HDP. This was utilised to optimise soluble expression of rHDP with haem detoxification gene ligated within *Nde*1/*Bam*H1 restricted enzyme sites, ampicillin resistant promoter (AmpR) and polyhistidine tag (6×His). Vector map generated using SnapGene Viewer software, GSL Biotech.

5.3.1.2. Strategies for optimised expression of soluble rHDP

The *E. coli* cell line, BL21(DE3), was transformed with *p*HDP (pCold I-HDP) and expressed using standard previously reported conditions (Table 5.1-I), yielding miniscule amounts of soluble rHDP as expected (Figure 5.3a- Lanes 4 and 5). This culture was scaled up by 4× in an attempt to obtain an overall higher amount of soluble material that could progress through to purification producing an adequate amount for further characterisation and activity studies. However, this attempt offered no further improvement to the smaller scale preparation and in fact resulted in the formation of even more inclusion bodies (Figure 5.3b- Lane 4).

Table 5.1. Summary of experimental expression conditions for soluble rHDP

Reaction	Cell Line	Growth Medium	[IPTG] in mM	Antibiotic	T (°C)	Induction Time (h)
I	BL21	LB[a]	1.0	amp[d]	15	18
II	BL21	LB[a], 0.5 mM δ-ALA[b], trace metal solution	0.5	amp[d]	25	24
III	C41	LB[a]	1.0	amp[d]	15	18
IV	C41	LB[a], 0.5 mM δ-ALA[b], trace metal solution	0.5	amp[d]	25	24
V	C41	TB[c]	1.0	amp[d]	15	18
VI	C41	TB[c], 1% glucose	0.25	amp[d]	15	18, 24
VII	**C41**	**TB[c], 1% glucose**	**0.5**	**amp[d]**	**15**	**24, 48**
VIII	C41	TB[c], 1% glucose, L-arabinose, KJE8 chaperone plasmid	0.5	tet[e]	15	24, 48
IX	C41	TB[c], 1% glucose, Tf2 chaperone plasmid	0.5	tet[e]	15	24, 32

[a]LB: Luria Broth, [b]δ-ALA: δ-aminolevulinic acid, [c]TB: Terrific Broth, [d]amp: ampicillin, [e]tet: tetracycline

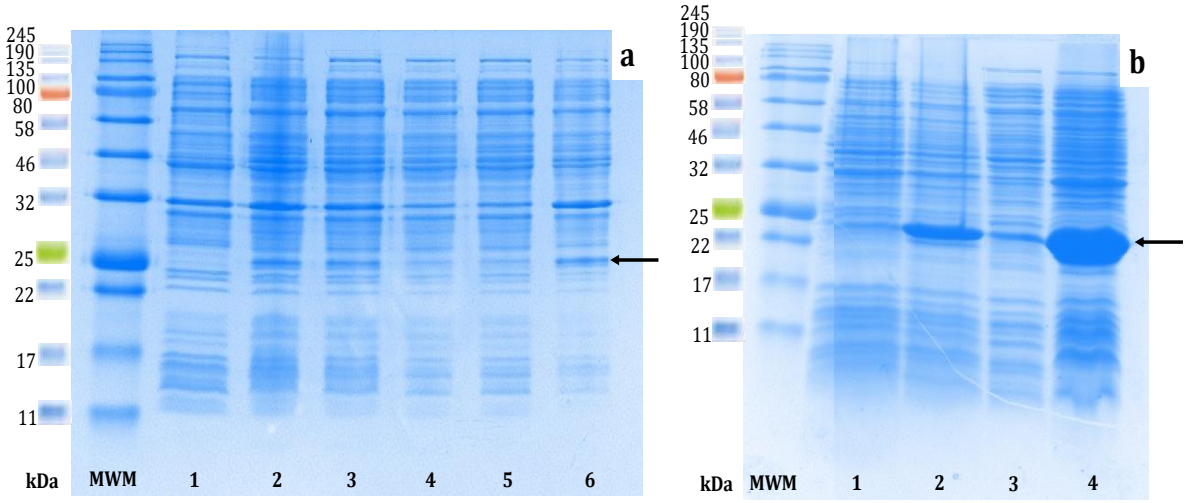

Figure 5.3. SDS-PAGE analysis representing initial expression using the BL21 cell line under standard growth conditions. (a) 15% gel showing very low yield of soluble rHDP. Key: molecular weight marker (MWM), before induction with IPTG (1), after induction with IPTG (2), crude lysate after cell lysis (3), soluble (4 & 5) and insoluble (6) protein fractions. **(b)** Scaled up preparation under the same expression conditions as in a, illustrating majority of rHDP present as inclusion bodies. Key: before induction with IPTG (1), after induction with IPTG (2), soluble (3) and insoluble (4) protein. rHDP indicated by arrows in line with 25 kDa marker.

Cytochrome P450 (CYP450) represents a superfamily of haem-containing metabolising enzymes that play an essential role in cellular functions. Previous studies have shown that the incorporation of ALA, the first rate-limiting intermediate in the haem biosynthesis pathway and Fe^{3+}, dramatically enhanced expression levels of soluble CYP450 in *E. coli*.[339,

[340] Building on this premise, and assuming that HDP is also a haem-containing protein and involved in haem binding, BL21 cells containing *p*HDP were grown in media supplemented with δ-ALA and trace element solution with the major component being the cofactor Fe^{3+} and smaller amounts of other trace metal ions. The rationale for this intervention was that porphyrin may be essential to the structure and synthesis of functional rHDP and that these additions would promote intrinsic folding, thereby resulting in a greater yield of soluble protein (Table 5.1-II). Expression conditions were further modified in an aim to promote haem biosynthesis. Temperature and induction time were increased from 15 to 25°C and 18 to 24 h respectively. When compared to the control experiment, the addition of the haem precursor showed no significant improvement in the expression of soluble rHDP under these new conditions (Figure 5.4a- Lane 3 vs 8).

During each expression trial, rHDP precipitated out as inclusion bodies. As challenging as this was, this offered a new perspective in finding an alternate approach to expression. Overexpression, misfolding, protein aggregates and low protein production are some of the key signs that indicate that rHDP has a detrimental effect on the chosen *E. coli* host. Under such circumstances an alternative would be to use a cell line that is genetically modified and adapted to counteract the effects of potential toxicity whilst attempting to encourage protein expression.

A new strategy for overcoming this problem during recombinant expression of HDP was to utilise the C41 cell line, an *E. coli* mutant that is adapted to resist effects of toxic proteins.[341] C41 cells were transformed with *p*HDP and expressed following the same conditions as with the BL21 cells (Table 5.1-III) as well as an experimental set up with the addition of δ-aminolevulinic acid and trace elements (Table 5.1-IV). Upon close inspection of SDS-PAGE gels after electrophoresis, a slight improvement in the soluble fraction was observed (Figure 5.4b- Lane 3); however, as seen with the BL21 cell line, the addition of δ-aminolevulinic acid did not drastically enhance expression (Figure 5.4b- Lane 7). These observations resulted in all further expression studies being conducted using the C41 cell line.

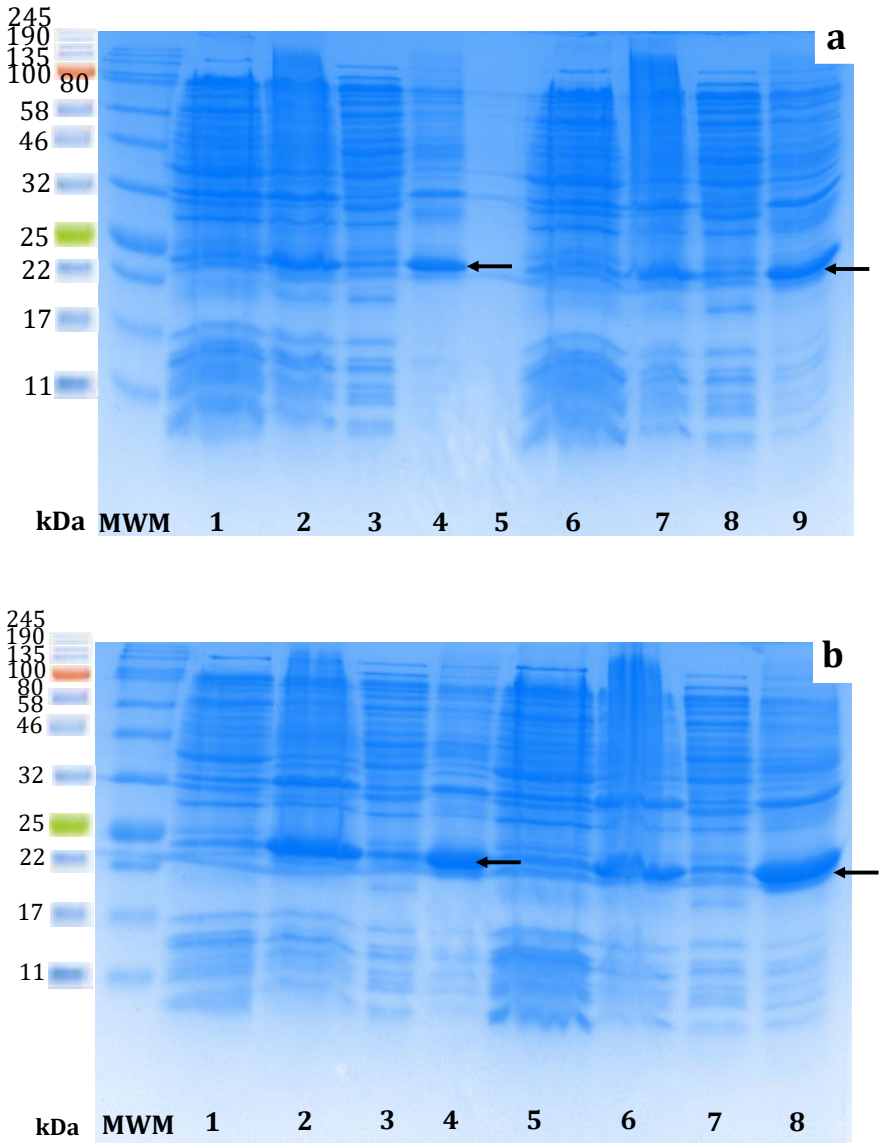

Figure 5.4. SDS-PAGE analysis illustrating expression of rHDP following treatment with δ-aminolevulinic acid and trace elements. (a) Expression of rHDP using BL21 cell line, control (1-4) and treated cells (6-9) Key: no IPTG (1, 6), with IPTG (2, 7), soluble fraction (3, 8), insoluble fraction (4, 9), blank lane (5). **(b)** Expression of rHDP using C41 cell strain control (1-4) and treated cells (5-8). Key: no IPTG (1, 5), with IPTG (2, 6), soluble fraction (3, 7) and insoluble fraction (4, 8).

Terrific Broth was developed to improve the protein yield of plasmid containing *E. coli* cells by extending the growth phase of recombinant strains.[342] In this study, Luria Broth was substituted with Terrific Broth using the optimised cell line (Table 5.1-V) to further improve expression of soluble rHDP. This medium was then supplemented with 1% glucose to suppress leaky expression and expression was monitored over various induction time points and concentrations of IPTG (Table 5.1-VI and VII).[343] Analysis of

SDS-PAGE (Figure 5.5a) showed that incorporating 1% glucose in Terrific Broth and inducing expression using 0.5 mM IPTG for 48 h while replenishing with fresh ampicillin at regular intervals afforded optimised expression conditions that, for the first time, yielded adequate amounts of soluble rHDP for further characterisation and activity studies.

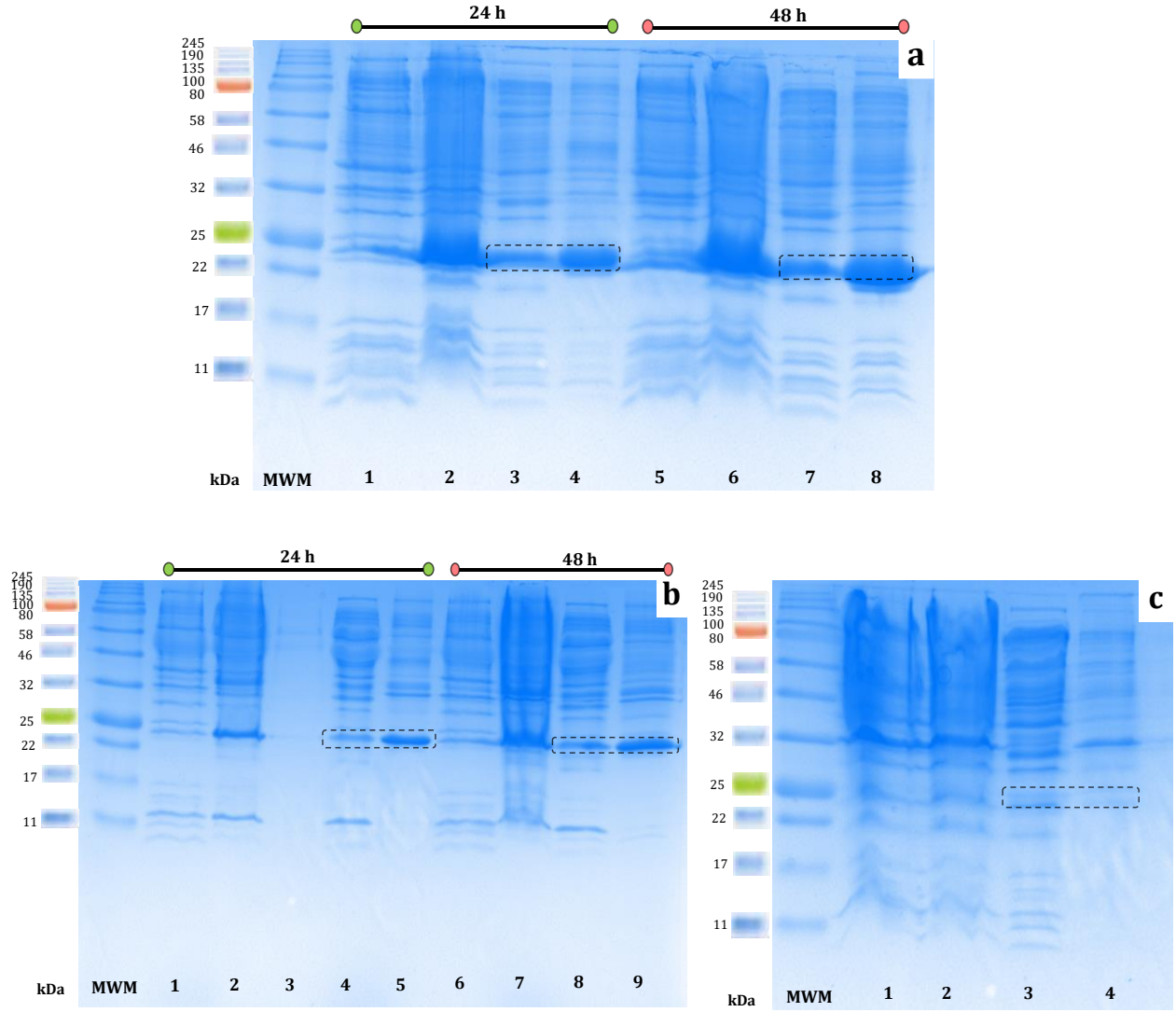

Figure 5.5. 15% SDS-PAGE illustrating expression of pCold I-rHDP using *E. coli* C41 cell line. **(a)** Gel showing successful expression of soluble rHDP following induction at 24 and 48 h under optimised expression conditions. Key: no IPTG (1,5), with IPTG (2,6), soluble fraction (3,7) and insoluble fraction (4,8). **(b)** pCold I-rHDP expressed in C41 cells with chaperone plasmid KJE8, induction monitored at 24 and 48 h. Key: no IPTG (1,6), with IPTG (2,7), blank lane (3), soluble (4,8) and insoluble (5,9) fractions. **(c)** pCold I-rHDP expressed in C41 cells with chaperone plasmid Tf2 at 32 h. Key: no IPTG (1), with IPTG (2), soluble (3) and insoluble (4) fractions. Soluble and insoluble rHDP fractions highlighted by black dotted rectangle.

Molecular chaperones are responsible for preventing newly-synthesised polypeptides from misfolding and forming inclusion bodies. Co-expression of molecular chaperones with recombinant protein has been previously reported to promote stable expression and prevent aggregation.[344] After successfully optimising expression of soluble rHDP a further attempt to improve the yield was to co-express molecular chaperones with rHDP. Similar expression conditions were applied with the inclusion of chaperone plasmids KJE8 (Table 5.1-VIII) and Tf2 (Table 5.1-IX) comprising dnaK-dnaJ-grpE/groES-groEL and groES-groEL-tig chaperones respectively. The aim was to aid correct protein folding thereby reducing aggregation. In the case of pKJE8, however, most of the protein continued to aggregate in the form of inclusion bodies (Figure 5.5b- Lanes 5 and 9) and in the case of Tf2, a lower level of total expression was observed and expression of soluble rHDP in particular was diminished (Figure 5.5c). The use of molecular chaperones in expression of rHDP did not improve the soluble expression or yield.

The final strategy was to express soluble rHDP using the C41 cell line in Terrific Broth supplemented with 1% glucose, lower concentration of IPTG and longer induction at low temperature as indicated in Table 5.1-VII.

5.3.1.3. Purification strategies

In order to understand the chemical and physical properties of any target protein, the isolation and purification processes involved play a crucial role in obtaining suitable material. Purifying recombinant protein in the least number of steps, and high yield whilst maintaining protein stability, are key factors in developing an ideal purification scheme. Cell lysis was the first crucial step in this process which involves disrupting the host cell wall using a suitable buffer system thereby releasing an ensemble of biomolecules; specifically, soluble proteins and protein aggregates precipitated as inclusion bodies (Figure 5.6). Exploiting the physical properties of the target protein allows the use of chromatographic methods for fractionation. However, it is important to note that the proteomic content of the cell is quite complex, thus making it imperative to use a combination of complementary techniques in the fractionation process to obtain pure protein while minimising contamination.

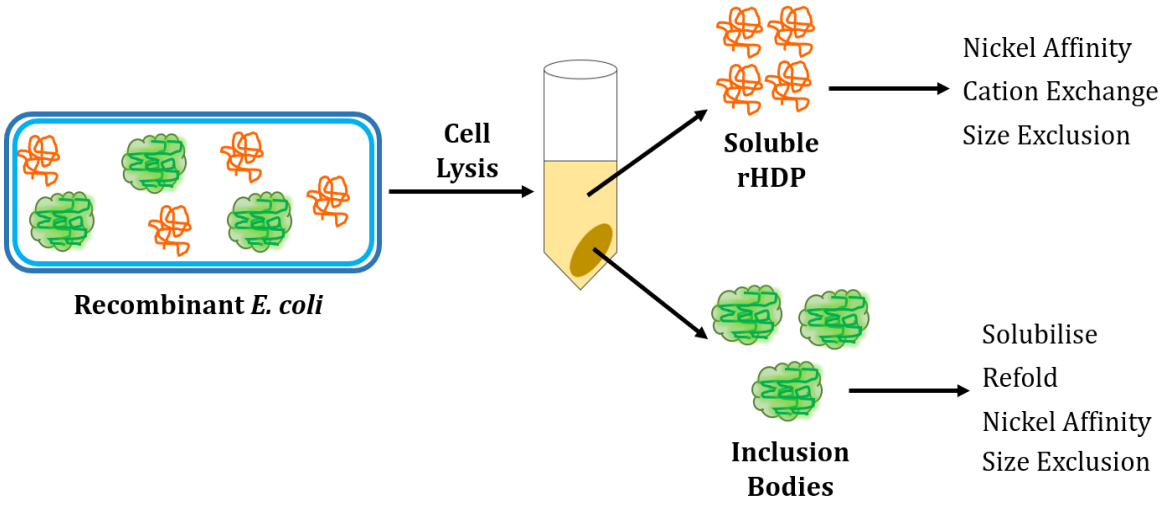

Figure 5.6. Workflow illustrating cell lysis and various strategies to isolate and purify rHDP from *E. coli*.

An additional advantage of utilising the pCold I expression vector was the incorporation of a hexahistidine tag adjacent to the HDP sequence which allowed for the application of nickel affinity chromatography in purification. This proceeded via specific His binding to a Ni^{2+}-NTA column followed by competitive elution with imidazole.

Calculation of the theoretical parameters for HDP using an online bioinformatic tool known as ProtParam (Swiss Institute of Bioinformatics) estimated a theoretical pI of 9.29 for this protein. This unique characteristic of HDP offered an added advantage when compared to *E. coli* proteins with a pI range of 4 to 5 thus allowing the application of cation exchange chromatography as an additional method of purification.[345] SEC is a robust technique that focuses on separation of macromolecules based on molecular size or hydrodynamic volume. The mild eluent conditions preserve the protein, making it stable throughout separation whilst the elution profile offers insights into protein interactions and possible aggregation or quaternary structure.

Following cell lysis under conditions described earlier in section 5.2.3, the homogenised solution was centrifuged to separate soluble and insoluble material as well as cell debris. The soluble protein fraction was isolated for further purification. Exploiting the presence of the hexahistidine tag, nickel affinity chromatography using the buffer system noted in Table 5.2-I was employed. Proteins bound to the Ni^{2+}-NTA column were released by competitive elution using a high concentration of imidazole. The elution profile (Figure

5.7a) showed that most of the proteins eluted in the flow-through with the remaining bound proteins eluting with the early addition of imidazole. The second peak comprises smaller overlapping peaks suggesting poor separation with an overall undesirable result.

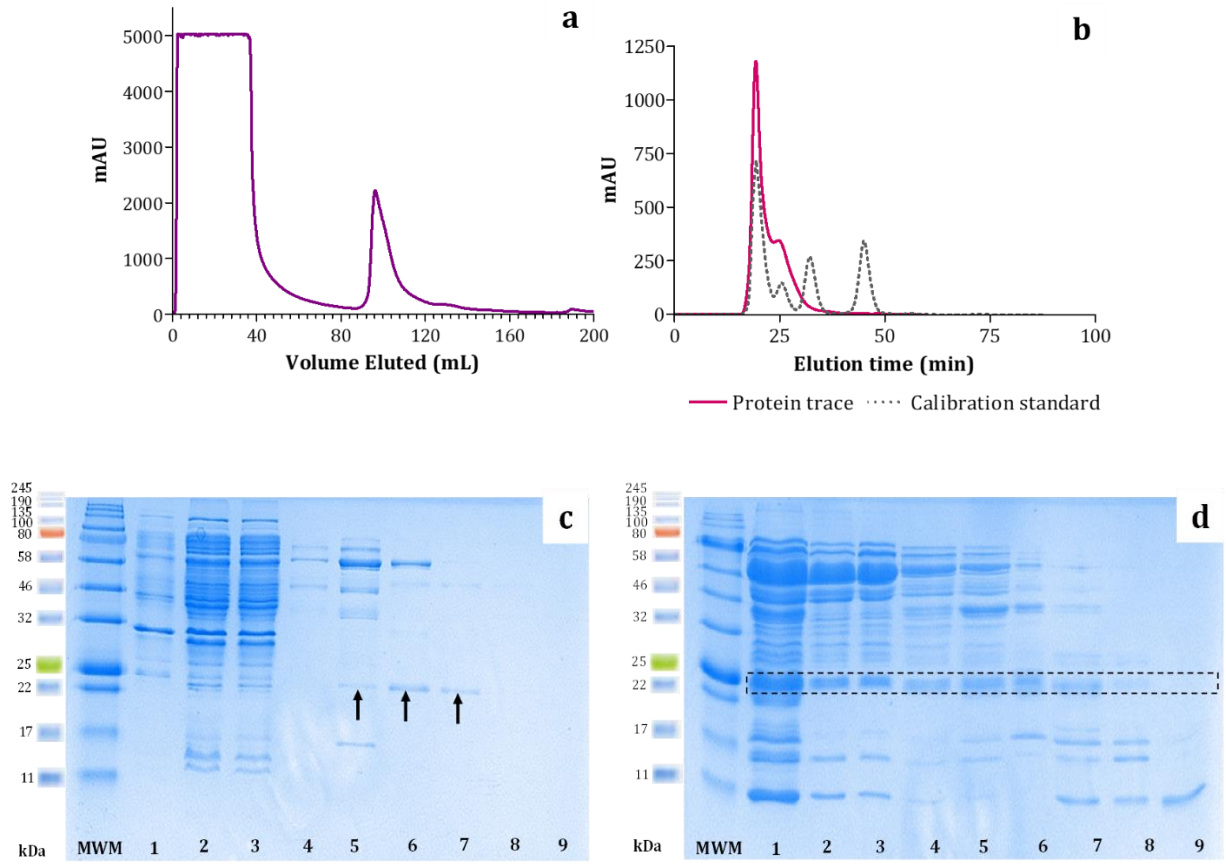

Figure 5.7. Chromatographic elution profiles and SDS-PAGE analysis of purification steps. **(a)** Elution profile obtained using 0.5 M imidazole to elute proteins bound to Ni^{2+}-NTA during initial purification attempt. Nickel affinity fractions were collected at 1 mL/min. **(b)** Size-exclusion elution profile using a 0.05 M Tris, pH 8-0.15 M NaCl buffer system. Fractions were collected at 5 mL/min. **(c)** 15% acrylamide SDS-PAGE depicting initial purification attempt of rHDP expressed in BL21 *E. coli* cell strain. rHDP present in lanes 5-7 as indicated by the arrows**.** Key: molecular weight marker (MWM), insoluble rHDP (1), unbound proteins (2,3) and proteins bound to Ni^{2+}-NTA column (4-9). **(d)** SDS-PAGE of pooled rHDP containing fractions purified by size-exclusion chromatography. Key: Concentrated rHDP loaded onto column (1) and fractions eluted off size-exclusion column (2-9). rHDP is monitored at 25 kDa enclosed in dotted rectangle.

Analysis of the corresponding acrylamide gel (Figure 5.7c) monitored at 25 kDa supports this conclusion and further shows that a portion of rHDP was lost in the flow-through. Fractions corresponding to the second peak were seen to contain soluble rHDP along with other contaminating proteins at a higher molecular weight. Fractions containing soluble

rHDP were pooled, concentrated and subjected to SEC using a Superdex 75 column and Tris (50 mM, pH 8), 0.15 M NaCl buffer for elution. The overlapping peaks in the resulting elution profile (Figure 5.7b) illustrates poor separation with most of the protein having been eluted in the void volume as indicated by the early elution time. The corresponding acrlyamide gel (Figure 5.7d) showed rHDP to be present in all fractions in addition to a number of contaminating *E. coli* proteins, suggesting that these conditions were not optimal for isolation and purification of the target protein.

The original affinity purification method was altered by adding 40 mM imidazole to the binding buffer (Table 5.2-II) to reduce non-specific binding to the Ni^{2+}-NTA column. All proteins eluted in the flow-through and no other peaks were observed during the linear gradient of imidazole which indicated weak interaction between the protein of interest and the column. Further adjustment (Table 5.2-III) involved a shallow initial imidazole gradient from 0-30% which resulted in improved separation and considerably reduced contamination (Figure 5.8a). Fractions potentially containing rHDP were then pooled and the imidazole was removed by desalting using Sørensen's buffer (50 mM, pH 7.0) prior to cation exchange.

Table 5.2. Buffer conditions for method development towards optimising purification using nickel affinity chromatography

Trial No.	Binding Buffer	Elution Buffer	Additional Buffers
I	0.05 M Tris-HCl, pH 8, 0.5 M NaCl	0.05 M Tris-HCl, pH 8, 0.5 M NaCl, 0.5 M imidazole	-
II	0.05 M Tris-HCl, pH 8, 0.5 M NaCl, 0.04 M Imidazole	0.05 M Tris-HCl, pH 8, 0.5 M NaCl, 0.5 M imidazole	-
III	0.05 M Tris-HCl, pH 8, 0.5 M NaCl	0.05 M Tris-HCl, pH 8, 0.5 M NaCl, 0.5 M imidazole	-
IV	0.02 M $NaHPO_4$, pH 7.4, 0.5 M NaCl	0.02 M $NaHPO_4$, pH 7.4, 0.5 M NaCl, 0.5 M imidazole	-
V	0.02 M $NaHPO_4$, pH 7.4, 0.5 M NaCl	0.02 M $NaHPO_4$, pH 7.4, 0.5 M NaCl, 0.5 M imidazole	0.02 M $NaHPO_4$, pH 6.5, 0.5 M NaCl

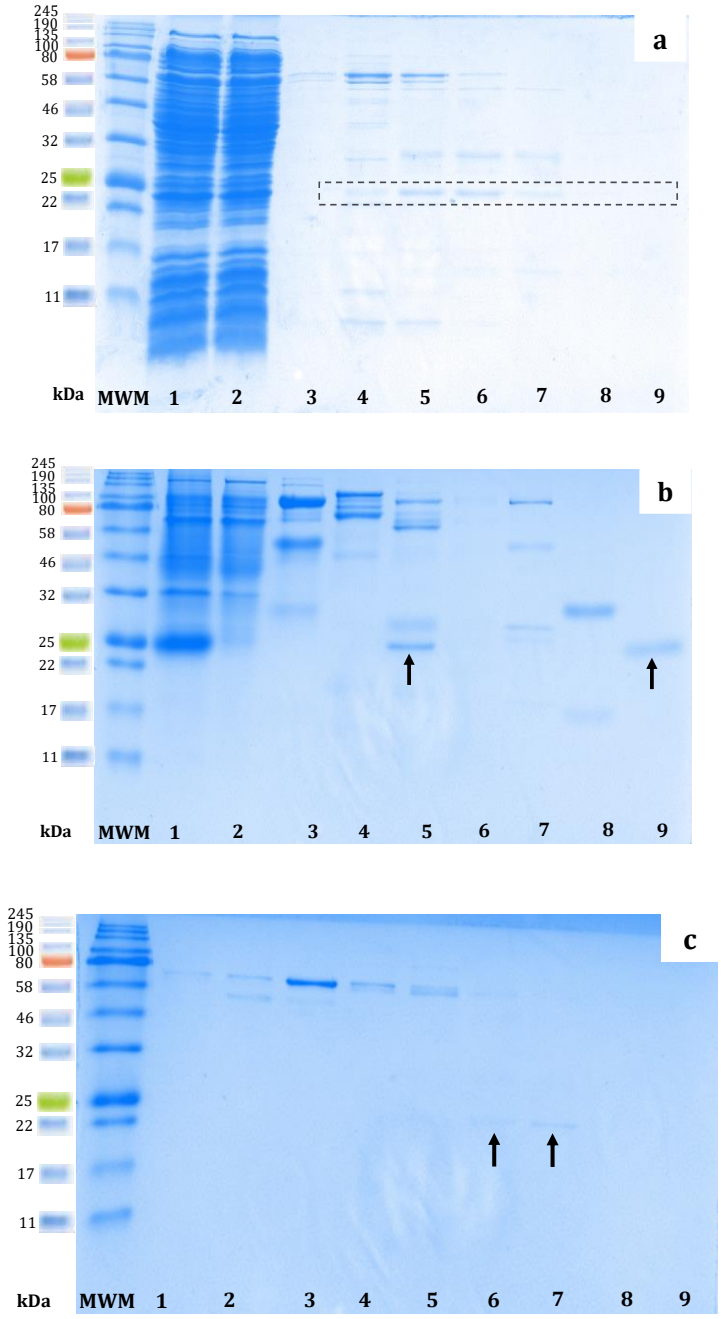

Figure 5.8. SDS-PAGE analysis representing purification of rHDP including a linear imidazole gradient. (a) 15% acrylamide SDS-PAGE representing nickel affinity chromatography, the first step in purification scheme using a shallow imidazole gradient. Key: molecular weight marker (MWM), unbound proteins (1,2), bound proteins monitored at 280 nm (3-7) and strongly bound proteins eluted only with 0.5 M imidazole (8, 9). **(b)** Purification gel representing the second purification step, cation exchange chromatography. Key: cell lysate after induction (1), soluble protein fraction (2) and eluted fractions (3-9) where rHDP is present indicated by the arrows. **(c)** Pooled and concentrated eluted fractions corresponding to lanes 6 through to 10 followed by size-exclusion chromatography affording pure rHDP present in fractions as indicated by the arrows. Key: Fractions eluted off size-exclusion column (1 to 9).

Even though the inclusion of cation exchange improved the purity of rHDP, it also required an additional step in the purification process which further diminished the amount of material from an already low yield of expressed protein (Figure 5.8 b and c). The aim was to further optimise the purification strategy by minimising the number of steps in the purification scheme thereby maximising the yield.

In order to minimise protein loss through buffer exchange processes, $NaHPO_4$ (20 mM, pH 7.4) was utilised from the first chromatographic step in the purification process since it was shown to maintain protein stability (Table 5.2-IV). Incorporating these new binding and elution buffers allowed for method optimisation by first introducing a linear imidazole gradient of 0-50% which resulted in elution of proteins quite early with poor resolution. A linear 0-30% imidazole gradient showed an improvement in separation; however, it was still difficult to distinguish between individual peaks and track fractions in which rHDP was the sole or the dominant protein as monitored by gel electrophoresis. It is noteworthy to mention that through the different nickel affinity trials there were proteins that associated very strongly with the nickel column and only eluted with 0.5 M (100%) imidazole. These were observed to be at a different molecular weight from the target protein.

In addition to the optimal imidazole gradient, a low pH wash preceding the multistep imidazole gradient was introduced. This low pH wash encouraged the early elution of non-specific proteins that may contain proximal His residues in their structure thus promoting better separation from rHDP. Various combinations using imidazole were tried in an attempt to optimise the multistep gradient. Size-exclusion chromatography was employed after each attempt, after which the yield and purity for each unique method was determined.

After several attempts at improving this purification scheme, buffer conditions detailed in Table 5.2-V proved to be optimal. Since there were still traces of contaminating proteins that eluted with rHDP, an additional step of 2.5% imidazole was incorporated in the multistep gradient establishing the optimised method using affinity chromatography as illustrated in Figure 5.9a.

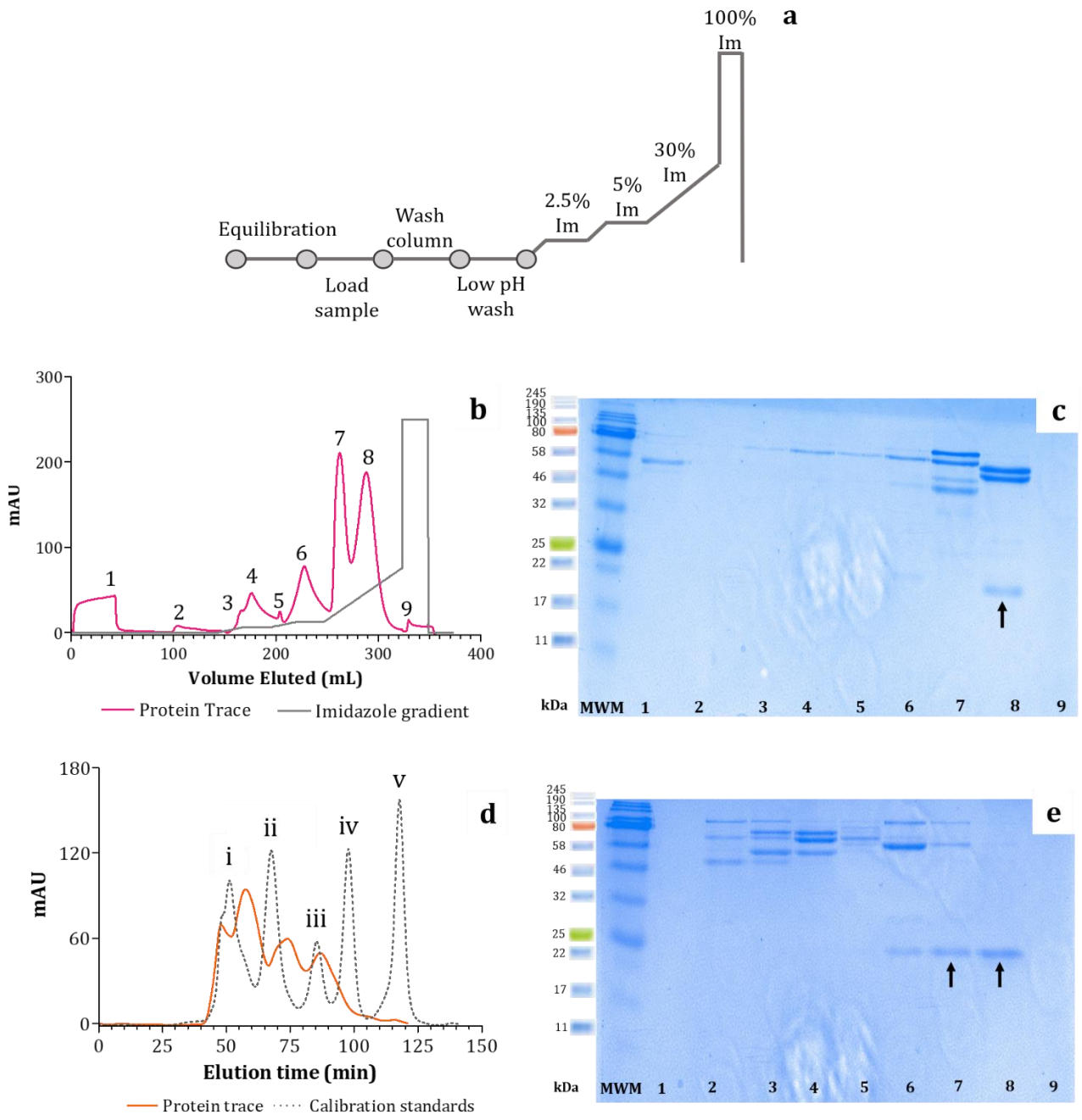

Figure 5.9. Chromatographic and SDS-PAGE analysis of optimised purification of rHDP. (a) Schematic of optimised linear imidazole (Im) gradient used. **(b)** Optimised elution profile including a low pH wash and a multi-step imidazole gradient from 2.5 to 100% to elute proteins bound to Ni^{2+}-NTA. **(c)** Nickel affinity fractions eluted using buffer comprising 0.02 M $NaHPO_4$ (pH 7.4), 0.5 M NaCl and 0.5 M imidazole at 1 mL/min. Key: Distinct protein separation peaks (1-9) and corresponding 15% SDS-PAGE gel. **(d)** Elution profile representing size-exclusion in 1× PBS (pH 7.4) at 5 mL/min and **(e)** 15% SDS-PAGE with each lane (1-9) corresponding to peaks observed in the elution profile. Size-exclusion calibration standards representing 670 kDa (i), 158 kDa (ii), 44 kDa (iii), 17 kDa (iv) and 1.35 kDa (v). Fractions containing purified rHDP are indicated by the arrows.

The resulting elution profile (Figure 5.9b) shows successful separation with distinct peaks. Each peak, 1 to 9, corresponding to lanes 1 to 9 (Figure 5.9c) illustrates enhanced separation of rHDP from contaminating *E. coli* proteins prior to SEC without the need of the intermediate cation exchange method. Size-exclusion was optimised using an S200 column (10/300) and PBS (1×, pH 7.4) as the equilibration and elution buffer. This afforded excellent separation with symmetrical peaks and the overlay of this profile with calibration standards (Figure 5.9b) provides an idea of the hydrodynamic volume of rHDP.

The size-exclusion elution profile indicated that monomeric rHDP eluted at approximately 83 min which corresponds to the expected molecular weight of 25 kDa. Eluted fractions corresponding to these peaks were analysed using gel electrophoresis (Figure 5.9e) showing improvement in the final purification step affording pure rHDP (Figure 5.9e- Lane 8) in higher yield compared to all previous purification attempts.

Table 5.3. Comparison of expression and purification conditions affording 12-fold increase in yield of soluble rHDP

	Initial Trial	**Optimised Conditions**
***E. coli* Cell line**	BL21	C41
Growth medium	Luria Broth	Terrific Broth
Induction time	16 h	48 h
Total soluble rHDP obtained from a 4 L bulk culture	150 µg	1.8 mg
Other	Monomer	Monomer and possible higher order oligomer
Nickel Affinity Chromatography	Poor separation	Excellent separation incorporating a low pH wash and multistep imidazole gradient
Size-Exclusion Chromatography	Poor separation using S75 column and Tris Buffer	Symmetrical peaks and excellent separation using S200 column and 1× PBS buffer

Optimised expression as noted in Table 5.3, in combination with these purification methods, afforded a 12-fold increase in yield of soluble rHDP when compared to initial expression and purification trials producing, for the first time, adequate amounts of soluble rHDP for characterisation and activity studies. In addition, the presence of

symmetric peaks in SEC profile and the high molecular weight bands that appear to track monomeric rHDP suggests that this protein could possibly be present in the form of higher order oligomers. These warrant future investigation but, for the purposes of this study, only monomeric rHDP was further investigated.

5.3.2. Protein Refolding from Inclusion Bodies

Synthesising recombinant proteins in an overexpression system such as *E. coli* where the rate of protein aggregate formation surpasses correct folding results in the formation of inclusion bodies.[346] This is an undesirable event since the protein particles precipitate in a non-native form in which correct refolding into its bioactive form must be empirically determined for each target protein making this a cumbersome process and a major bottleneck in recombinant protein synthesis. Here an attempt was made to refold rHDP using previously-reported methods with modifications in order to be able to make comparisons with literature data and with soluble rHDP.

5.3.2.1 Solubilisation and storage of protein from protein aggregates

Various buffers as described in Table 5.4 were prepared to solubilise and store insoluble recombinant protein until refolding was attempted.

Table 5.4: Buffers used for solubilising inclusion bodies using urea

Buffer System	Buffer Components
I	0.05 M Tris, pH 7.5, 0.2 M NaCl
II	Buffer I supplemented with 1% Triton X-100
III	Buffer II supplemented with 1 M urea
IV	0.05 M Tris (pH 7.5), 0.2 M NaCl, 8 M urea, 0.001 M DTT and 1× protease inhibitors

Insoluble pellets obtained after cell lysis were resuspended in 10 mL Buffer I and centrifuged at 20 000 *g* for 20 min at 4°C. The supernatant was discarded, and the wet cell weight determined in order to calculate the amount of urea required, following a suggested protocol requiring 1 M urea per gram wet cell weight. An additional wash using 25 mL of Buffer I was carried out. The resulting pellet was then resuspended in 25 mL of

Buffer II containing detergent to encourage solubility of cellular lipids thereby contributing to a cleaner cell pellet, homogenised using a Dounce homogeniser and centrifuged as before. This step was repeated twice before a further two washings using Buffer III and a final wash with Buffer I to remove detergent with homogenisation between each wash step prior to centrifugation at 25 000 *g* for 30 min at 4°C.

Urea was used as a denaturant to aid in further solubilisation to produce monomers from existing protein structures and was therefore incorporated into the buffers after partial solubilisation had been achieved.[347] The resulting washed and solubilised pellet was resuspended in 15 mL extraction buffer (Buffer IV). The protein concentration was determined using a NanoDrop™ spectrophotometer and the material stored in 2 mL aliquots at -20°C until further use. Dithiothreitol acted as a reducing agent to break any disulfide bonds present.

5.3.2.2. On-column refolding

On-column refolding was attempted according to the method of Oganesyun *et al* by binding the urea-denatured His-tagged rHDP to a nickel column prior to refolding.[348]

Table 5.5: Buffers used for on-column refolding and affinity purification

Buffer System	Buffer Components
I	0.02M Tris (pH 8), 0.1 M NaCl, 8 M urea
II	Buffer I supplemented with 0.02 M imidazole
III	0.02M Tris (pH 8), 0.1 M NaCl
IV	Buffer III supplemented with 0.1% Triton X-100
V	Buffer III supplemented with 0.005 M β-cyclodextrin
VI	0.02M Tris (pH 8), 0.1 M NaCl supplemented with 0.6 M imidazole

Aliquots of solubilised inclusion bodies were thawed at 4°C prior to use. Ni-NTA His•Bind® Resin was pre-equilibrated using Buffer I, a denaturing buffer denoted in Table 5.5, prior to protein loading. Solubilised inclusion bodies were bound to Ni-NTA resin by batch absorption overnight whilst gently shaking at room temperature. Protein-bound resin was packed into a glass column and washed with Buffer II to remove non-specific contaminating proteins. This was followed by sequential washes with Buffers IV and V, of which the latter removes the detergent and encourages protein refolding. Remaining

contaminants and β-cyclodextrin were removed with an additional wash with Buffer III. Soluble refolded rHDP was then eluted off the column with Buffer VI by competitive elution with a high concentration of imidazole (0.6 M). All fractions were monitored for target protein content and purity by SDS-PAGE.

Analysis of the resulting acrylamide gel (Figure 5.10) showed that there was no protein present in the fractions eluted off the column using imidazole as indicated by the blank lanes seen in the gel below. Reviewing the earlier fractions eluted off during the various washing steps showed trace amounts of proteins present; however, the large volume of buffer used diluted the samples resulting in an undesirably low yield recovery. The remaining protein could possibly have still been bound to the column, but even with varying concentrations of imidazole it was not possible to recover this portion. Unfortunately, this one-step refolding and purification attempt of rHDP from inclusion bodies was unsuccessful.

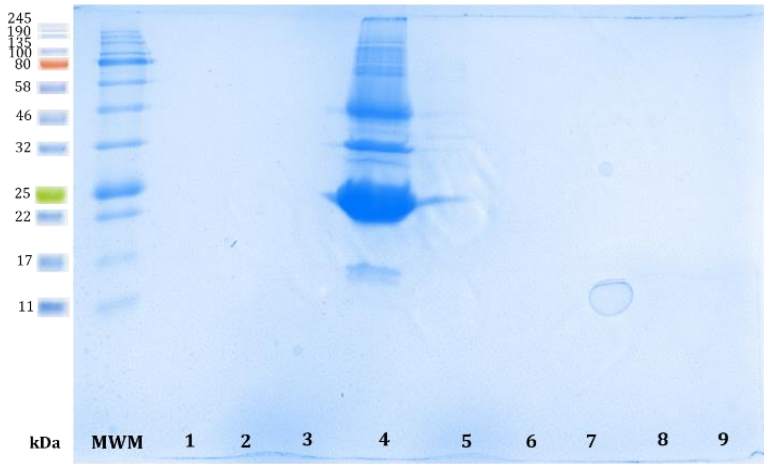

Figure 5.10. 15% SDS-PAGE of fractions eluted using on-column refolding method to refold rHDP from insoluble inclusion bodies. Key: molecular weight marker (MWM), solubilised protein sample loaded onto column (4) and fractions eluted with 600 mM imidazole after refolding protocol was complete (1-3 and 5-9).

5.3.2.3. In-solution refolding

To date, literature regarding refolding of rHDP from inclusion bodies has followed a reported method used in refolding recombinant *Plasmodium* circumsporozoite protein (CSP) with a modified purification step.[349] This led to the application of this rapid dilution

technique as reported by Rathore *et al* in an attempt to refold rHDP. Briefly, solubilised material was slowly dispensed in small aliquots into a large volume of refolding buffer comprising 0.1 M Tris (pH 8), 0.5 M L-arginine-HCl, 2 mM EDTA and 0.9 mM oxidised glutathione resulting in a 100-fold final dilution. Arginine is known to effectively suppress protein aggregation; therefore, incorporating this amino acid in the refolding buffer also offers protein stability. This solution was maintained at 10°C for 36 h. The renatured material was concentrated using an Amicon® stirred cell equipped with a 10 kDa membrane to a manageable volume prior to dialysis against a Tris-urea buffer (0.02 M Tris, pH 8, 0.1 M urea). Following dialysis, the sample was further concentrated and purified by SEC using 1× PBS, pH7.4 as the mobile phase. Analysis of the resulting SEC elution profile exhibited a series of several smaller peaks whereas two distinct symmetrical peaks were observed at a later elution time. The elution time for each of these peaks was approximately at 105 and 120 min, respectively. This late elution suggests that rHDP present was of a different hydrodynamic volume compared to soluble rHDP indicating that the protein may not have successfully folded.

5.3.2.4. Optimised refolding of rHDP

Refolding proteins requires a change in conformation from the denatured aggregated state to renatured soluble protein. Since this process is laborious with numerous possible permutations, using the unique characteristics pertaining to the target protein were essential in finding a successful method in combination with the techniques at hand. Given that on-column refolding and rapid dilution using established refolding buffers was deemed to be unfavourable with respect to rHDP refolding, various aspects that these methods and those reported by Jani *et al* offered were used in combination to optimise an improved refolding method.

After cell lysis and centrifugation, the pellet comprising insoluble material was temporarily stored at -20°C with no additions of any denaturants such as urea. Cell pellets were thawed over ice prior to use after which wash buffer I (Table 5.6) of 3× the pellet volume was added. The suspension was homogenised using a Dounce homogeniser and centrifuged at 20 000 *g* for 20 min at 4°C. The supernatant was examined and discarded after confirming that it did not contain the target protein. Wash buffer supplemented with

Triton X-100 (buffer II) was used to resuspend the pellet after which this was homogenised and centrifuged as previously described and this wash step was repeated once more. The resulting pellet comprising inclusion bodies was washed three more times with wash buffer I. Solubilisation buffer containing 50 mM CAPS, pH 11.0 was used to resuspend the pellet. The suspension was transferred into a 50 mL falcon tube and allowed to gently shake using an orbital shaker for 30 min at room temperature.

Table 5.6: Buffers used for optimised refolding and purification of rHDP

Buffer System	Buffer Components
Wash Buffer I	0.05 M Tris, pH 7.5, 0.2 M NaCl
Wash Buffer II	0.05 M Tris, pH 7.5, 0.2 M NaCl, 1% Triton X-100
Solubilisation/Binding	0.05 M CAPS, pH 11, 1.5% *N*-lauroylsarcosine, 0.3 M NaCl
Affinity Wash Buffer	0.05 M CAPS, pH 11, 0.3% *N*-lauroylsarcosine, 0.3 M NaCl
Affinity Elution Buffer	0.05 M CAPS, pH 11, 0.3% *N*-lauroylsarcosine, 0.3 M NaCl, 0.5 M imidazole
Dialysis	0.025 M CAPS, pH 11, 0.15 M NaCl
Size-Exclusion	1× PBS, pH 7.4

N-Cyclohexyl-3-aminopropanesulfonic acid (CAPS) offers a buffering range of 9.7 to 11.1, enabling one to work above the theoretical pI of HDP and incorporation of the detergent. *N*-Lauroylsarcosine in this buffer encouraged further solubilisation of the material which was the first crucial step in promoting refolding. The solubilised material was then centrifuged at 10 000 *g* for 30 min at 4°C, liberating a pellet white in colour which was set aside and the supernatant containing soluble protein processed further.

The viscous supernatant was sonicated prior to loading onto a Ni-NTA column in binding buffer. This affinity chromatography method incorporated a washing step using 0.05 M CAPS, pH 11, 0.3% *N*-lauroylsarcosine, 0.3 M NaCl prior to elution with a linear imidazole gradient. This additional wash step was included to help the protein slowly refold while bound to the column due to the gradual change in *N*-lauroylsarcosine concentration from 1.5% to 0.3% before competitive elution with imidazole. The elution profile showed two peaks, the first being rather broad representing the flow-through indicating that not all the protein bound to the column. This could be improved by using a slower flow rate when

loading the sample and the second was sharp and symmetrical and appeared at the start of the imidazole gradient.

Analysis of the resulting acrylamide gel (Figure 5.11a- Lane 2) showed that a substantial amount was lost in the flow-through but the fractions making up the second peak exhibited distinct bands at the correct molecular weight for rHDP with minimal contamination seen in the respective lanes (Figure 5.11a- Lanes 4 and 5).

All eluted fractions exhibiting a distinct band at 25 kDa were pooled and concentrated using a centrifugal filter unit with a 3 kDa molecular weight cut-off. The concentrated sample was transferred into dialysis tubing in a beaker filled with dialysis buffer and allowed to dialyse for 3 to 4 h at room temperature with gentle stirring to reduce salt and detergent concentrations. The dialysed sample was purified by SEC using a Sephadex 200 column and 1× PBS, pH 7.4 for equilibration and elution. The elution profile (Figure 5.11b) exhibited a symmetrical peak indicating the same hydrodynamic volume suggesting successful folding of rHDP. The elution time was approximately at 84 min which was very similar to the 83 min elution time observed for purified soluble rHDP. Overlay of the protein trace with calibration standards further supported the expected molecular weight for monomeric rHDP. The blunt peak, even though symmetrical, was likely due to overloading of sample onto column.

Analysis of SDS-PAGE (Figure 5.11c) showed a band at 25 kDa across all fractions making up the symmetrical peak seen in the elution profile indicating that this was, in fact, rHDP that had folded with minimal contamination. There was also a second band seen consistently above the monomeric band which could be due to the presence of strong disulfide bonds not being completely reduced with β-mercaptoethanol or the possibility of higher order oligomers of rHDP present once purified. Pure refolded rHDP was stored in 1× PBS supplemented with 10% glycerol at -80°C until further use.

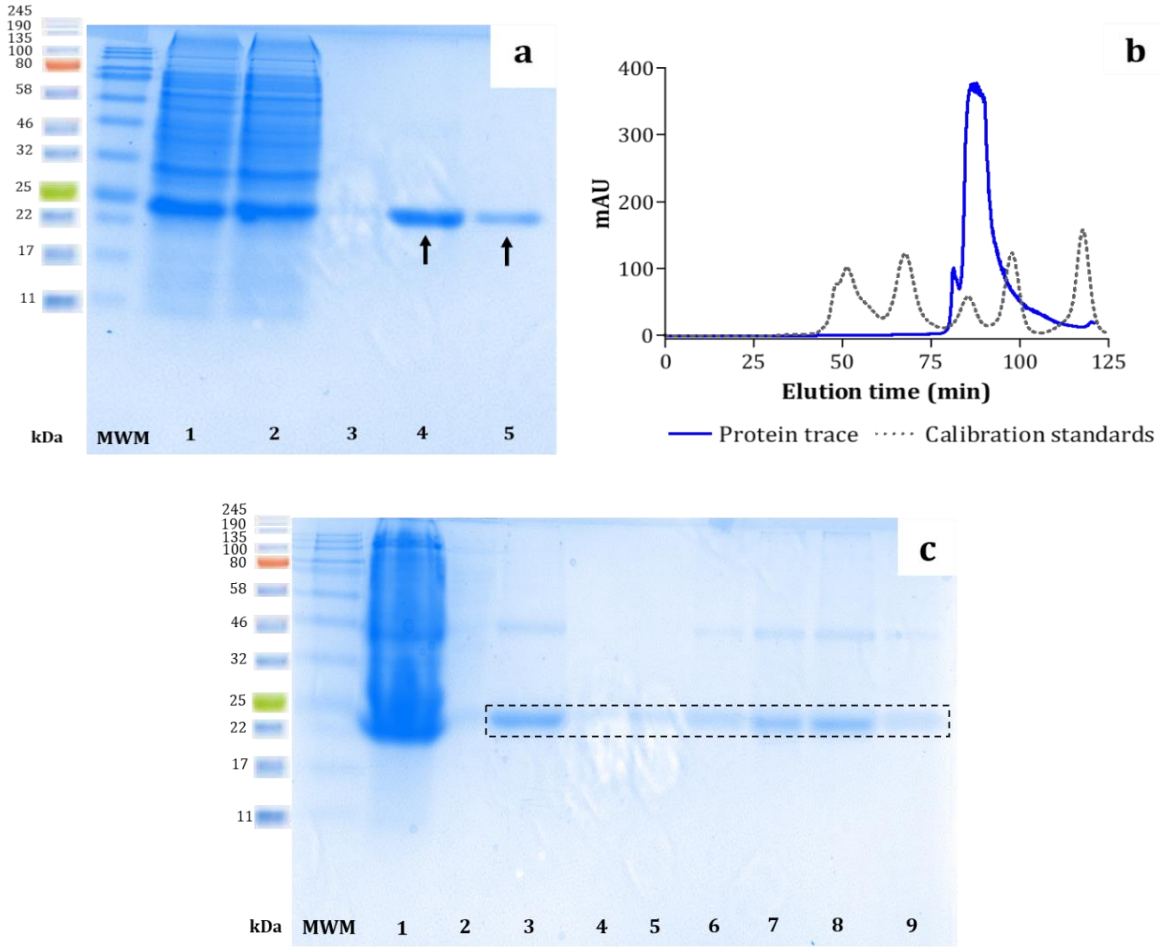

Figure 5.11. SDS-PAGE and chromatographic analysis representing purification of refolded rHDP. (a) 15% SDS-PAGE of purification after refolding rHDP from inclusion bodies using nickel affinity chromatography. Key: molecular weight marker (MWM), protein sample loaded onto column (1), flow through (2), fractions corresponding to single peak in chromatogram (3 to 5). **(b)** Size-exclusion elution profile showing a single symmetric peak. Key: calibration standards (i to v). **(c)** SDS-PAGE representing final purification step in the refolding procedure using size-exclusion chromatography. Key: precipitate formed after incubation with sarcosine (1), protein in solution after solubilisation (2), protein sample loaded onto SEC column (3), fractions corresponding to peak in elution profile (4 to 9).

5.3.3. Identification of expressed rHDP

The elution profile obtained from the final purification step in obtaining both pure soluble and refolded rHDP using SEC comprised multiple peaks. In order to gain a more precise idea of which fractions contained rHDP and to confirm that the refolded product was in fact the target protein, following electrophoresis, gels were stained using InVision™ His-tag In-gel stain. This fluorescent dye is conjugated to a Ni-NTA complex allowing Ni^{2+} to bind to the domain of a His tag thus allowing for selective

detection of His tagged fusion proteins and provides a faster alternative to the traditional western blot. Analysis of the stained gels visualised using an ethidium bromide filter revealed distinct fluorescent bands corresponding to the expected monomeric molecular weight for rHDP, thereby positively identifying the target protein (Figure 5.12-2a and 3a). The same gels were then stained with Coomassie Blue to compare the location of the bands (Figure 5.12-2b and 3b).

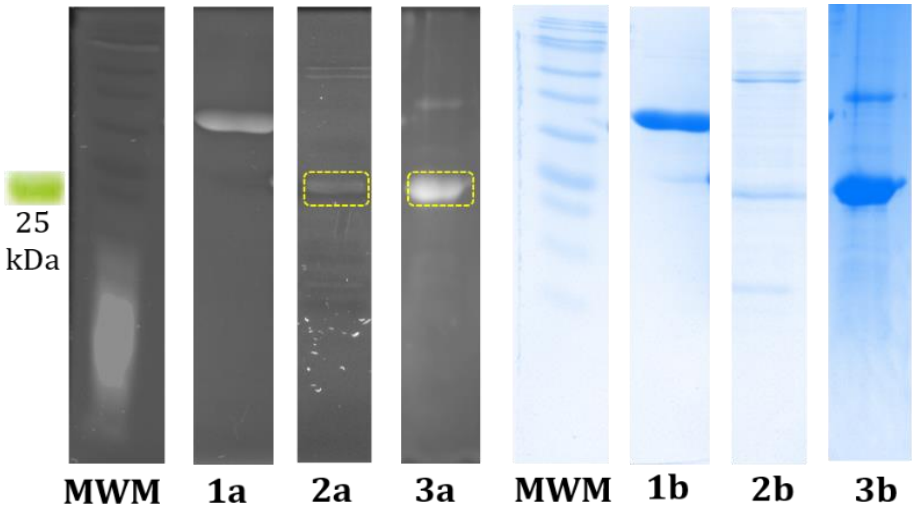

Figure 5.12.Visualisation of recombinant HDP by specific His-tag staining. (a) 15% SDS-PAGE visualised using InVision™ His-tag In-gel stain followed by staining with **(b)** Coomassie Blue to identify pure rHDP. Key: Molecular weight marker (MWM), recombinant His-tagged nitrilase from *Synechocystis sp.* Strain PCC6803 (Nit6803) used as a positive control (1), soluble (2) and refolded (3) rHDP.

Qualitative proteomics was employed for target protein identification from protein expression experiments as an additional technique to identify the gel bands that corresponded to the target protein. In order to reduce the amount of *E. coli* contaminants, rHDP fractions were carried through the complete purification scheme and only fractions obtained after SEC were analysed for protein content.

Following digestion, separation and LC-MS/MS, peptide fragments were interrogated against a concatenated database created using the Uniprot *E. coli* database and the HDP sequence obtained from the NCBI database (Accession number: PKC49565.1). These data confirmed that the band that has been tracked throughout all experiments at approximately 24.3 kDa was, in fact, HDP. This was identified with a protein identification

probability of 100% and an exclusive unique peptide count of 4. Upon closer analysis of the purification gel shown in Figure 5.9e, the identification of the higher molecular weight bands which also fluoresced when stained with the InVision™ His-tag In-gel stain were investigated using mass spectrometry. By reducing the peptide identifiers to only one unique peptide, traces of HDP were identified in a band at a molecular weight corresponding to approximately 68 kDa suggesting that there could be higher order forms of this protein, but this would require further investigation in the future.

5.3.4. Occlusion of labelled rHDP by β-haematin

HDP was detected in the DV lumen, trophozoite cytoplasm, washings of haemozoin as well as in dissolved crystals by LC-MS/MS as shown in Chapter 4. Having used a label-free semi-quantitative proteomic approach where quantitation was based on relative abundance, this protein was detected in high abundance in the dissolved haemozoin fraction following extensive washing relative to the other listed parasite components. Since each of these fractions represented the full sample derived from a common parasite preparation and were made up in equal volumes, they suggest a specific association of HDP with haemozoin.

Given that haemozoin formation is a biocrystallisation process analogous to biomineralisation and that the latter has been shown to incorporate matrix proteins or occlude material during various biomineralisation processes as highlighted in Chapter 1, the occlusion of rHDP by β-haematin was investigated. His-tagged rHDP was used as a probe to examine this hypothesis as well as to determine whether occluded biomolecules, in this case protein, are capable of exchanging with the external milieu. This was done by incubating pre-formed β-haematin and isolated haemozoin crystals with rHDP in sodium acetate buffer (0.5 M, pH 5.2) as detailed in Section 5.2.10. In a parallel experiment, β-haematin was synthesised in the presence of rHDP. All crystals were extensively washed with 4% SDS and PBS buffer prior to base dissolution and the respective fractions separated by SDS-PAGE. Conjugation of the His-tag allowed for specific in-gel detection thus allowing for visualisation of rHDP across protein samples. The InVision stain has a detection limit of 0.5 picomole of a hexahistidine tagged fusion protein thereby allowing for sensitive detection of the target protein.[350]

Preformed β-haematin exposed to rHDP appeared to have adsorbed this protein to a certain extent. This was apparent from the fact that rHDP could be washed off β-haematin crystals with 4% SDS following prior washing with acetate buffer (pH 5.2) as illustrated in Figure 5.13 (Lane 5). The protein, which was only found to be present in the first SDS wash, was visualised using the In-Gel His-Tag specific fluorescent stain. Following extensive further washing with SDS and PBS buffer, no further rHDP was detected when β-haematin crystals were then dissolved in 0.1 M NaOH (Figure 5.13- Lane 10).

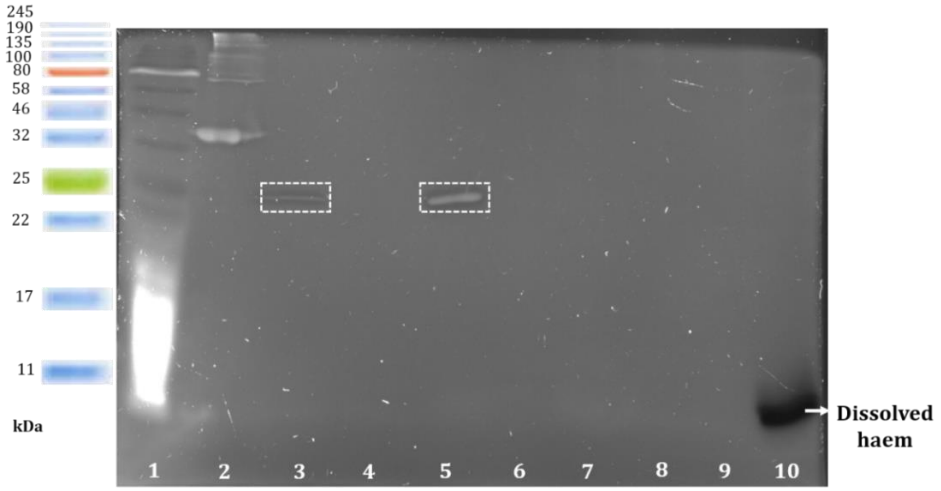

Figure 5.13. 15% SDS-PAGE stained with InVision His-tag stain showing pre-formed β-haematin incubated with rHDP. Key: molecular weight marker (lane 1), positive protein control (lane 2), rHDP (lane 3), supernatant (lane 4), 1st SDS wash (lane 5), 4th SDS wash (lane 6), 1st PBS wash (lane 7), 4th PBS wash (lane 8), sample application buffer (lane 9) and dissolved β-haematin (lane 10). rHDP highlighted by white dotted rectangle.

Haemozoin crystals isolated from purified DVs obtained from the NF54 strain of *P. falciparum* were exposed to rHDP in the same manner as with preformed β-haematin. In this study, crystals were observed to have adsorbed rHDP since the protein was detected in the first SDS wash following prior washing with acetate buffer (Figure 5.14- Lane 5). After extensive further detergent and buffer washes, followed by dissolution of haemozoin in 0.1 M NaOH, no further His-tagged rHDP was detected (Figure 5.14- Lane 10). These results demonstrated that haemozoin crystals exhibited similar behaviour to that of preformed crystals in that, once formed, these crystals do not irreversibly adsorb the protein from the external milieu.

By contrast, when β-haematin was synthesised in the presence of rHDP, adsorbed protein was again detected in the first SDS wash (Figure 5.15- Lane 6) but, when these crystals were subsequently dissolved in 0.1 M NaOH following extensive detergent and buffer washing, additional occluded rHDP was readily detected (Figure 5.15- Lane 10). Therefore, these results unequivocally illustrate that β-haematin crystals occlude rHDP in a non-exchangeable manner when the protein is present at the time of formation and imply that HDP detected in the dissolved haemozoin fraction was almost certainly present when the haemozoin formed.

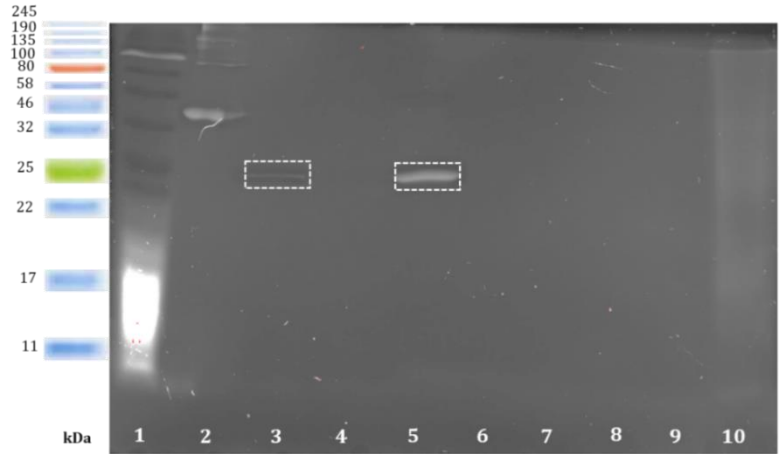

Figure 5.14. 15% SDS-PAGE stained with InVision His-tag stain showing isolated haemozoin crystals incubated with rHDP. Key: molecular weight marker (lane 1), positive protein control (lane 2), rHDP control (lane 3), supernatant (lane 4), 1st SDS wash (lane 5), 4th SDS wash (lane 6), 1st PBS wash (lane 7), 4th PBS wash (lane 8), blank (lane 9) and dissolved haemozoin (lane 10). rHDP highlighted by white dotted rectangle.

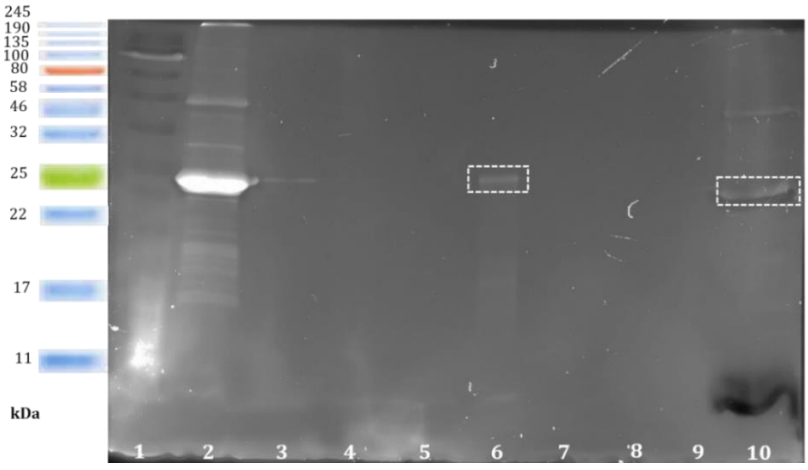

Figure 5.15. 15% SDS-PAGE stained with InVision His-tag stain from β-haematin formed in the presence of rHDP. Key: molecular weight marker (lane 1), rHDP control (lanes 2 and 3), haematin control (lane 4), supernatant (lane 5), 1st SDS wash (lane 6), 5th SDS wash (lane 7), 1st PBS wash (lane 8), 4th PBS wash (lane 9) and dissolved β-haematin (lane 10). rHDP highlighted by white dotted rectangle.

5.3.5. Characterisation and Activity Studies of rHDP

5.3.5.1. Circular dichroism and fluorescence spectroscopy

Circular dichroism (CD) spectroscopy was used to determine if there were conformational differences between soluble and refolded rHDP. Chiral macromolecules, specifically proteins, can absorb and transmit circularly polarised light generating a unique CD trace based on their inherent structural characteristics making this an essential tool for gaining information about its secondary structure and folding.[351] CD spectra recorded in the far UV-vis region of 180-280 nm revealed significant differences between refolded and soluble rHDP both at pH 5.2 and 7.4 (Figure 5.16 a and b). The CD spectra of refolded rHDP appeared to be very similar to that previously reported by Jani *et al* recorded at physiological pH.[131] All spectra exhibited minima at 228 nm and 208 nm as well as maxima at 192 nm with these being characteristic of α-helical proteins. Notably, soluble rHDP displayed distinct differences in α-helical content upon change in pH whereas its refolded counterpart retained its characteristic conformation.

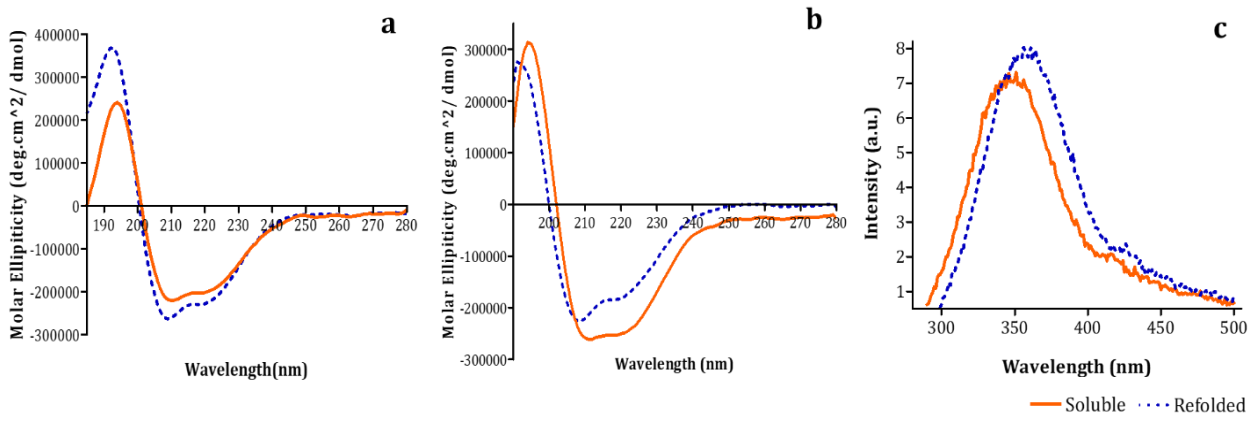

Figure 5.16. Circular dichroism spectra of soluble and refolded rHDP recorded at 0.2 mg/mL in **(a)** 0.01 M sodium acetate buffer, pH 5.2 and **(b)** 0.01 M phosphate buffer, pH 7.4. **(c)** Intrinsic fluorescence spectra recorded in 0.01 M phosphate buffer, pH 7.4.

Fluorescence spectroscopy used to investigate biomolecules such as DNA and lipids usually requires complex labelling of fluorophores specific to the research need. Out of the twenty amino acids, three are aromatic (Figure 5.17a-c), making their intrinsic fluorescence a unique photophysical property of proteins that is used to gain a better understanding of tertiary structure. Tryptophan (Trp, W) is the most dominant of the three owing to its high quantum yield and greater sensitivity while tyrosine (Tyr, Y) and

phenylalanine (Phe, F) offer weaker signals.[352] In the native state, tryptophan and tyrosine are located within the hydrophobic core of the protein whereas, in a partially-folded state, these residues are exposed to the solvent.

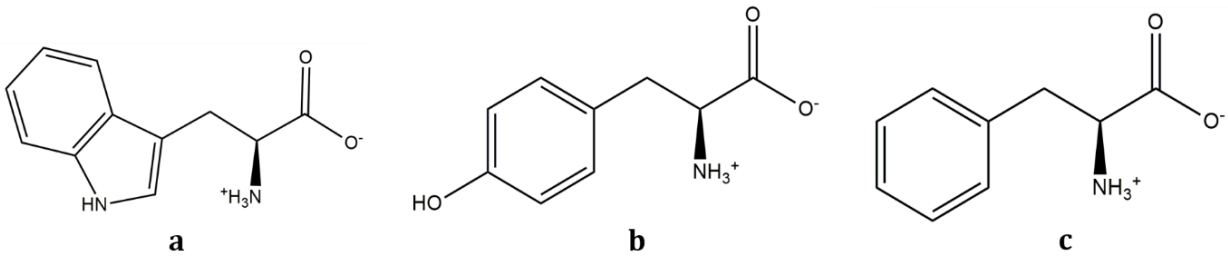

Figure 5.17. Chemical structures of the three amino acids which are intrinsically fluorescent: (a) tryptophan, **(b)** tyrosine and **(c)** phenylalanine.

Fluorescence spectra of soluble and refolded rHDP showed a shift in the peak maximum, indicating differences in the tertiary structure (Figure 5.16c). This distinct shift indicates increased Tyr to Trp energy transfer in the refolded protein in which one or more of the three Trp residues are closer to Tyr emphasising conformational differences between the soluble and refolded protein.

5.3.5.2. Spectrophotometric titrations to determine binding strength and stoichiometry

Spectrophotometric titrations of haemin with soluble rHDP showed a shift in λ_{max} from 398 to 396 nm (Figure 5.18a). Titrations under the same experimental conditions using refolded rHDP exhibited a shift in λ_{max} from 413 to 411 nm (Figure 5.18d). The observed changes in the UV-vis spectrum of haem upon interaction with the protein are consistent with association. A plot of absorbance vs the ratio of haemin to rHDP indicated the formation of a 1:1 haemin-protein complex for both soluble and refolded rHDP (Figure 5.18b and e) in contrast to previous reports which indicated a stoichiometry of 2 to 2.7 molecules of haem to refolded HDP respectively.[138, 131]

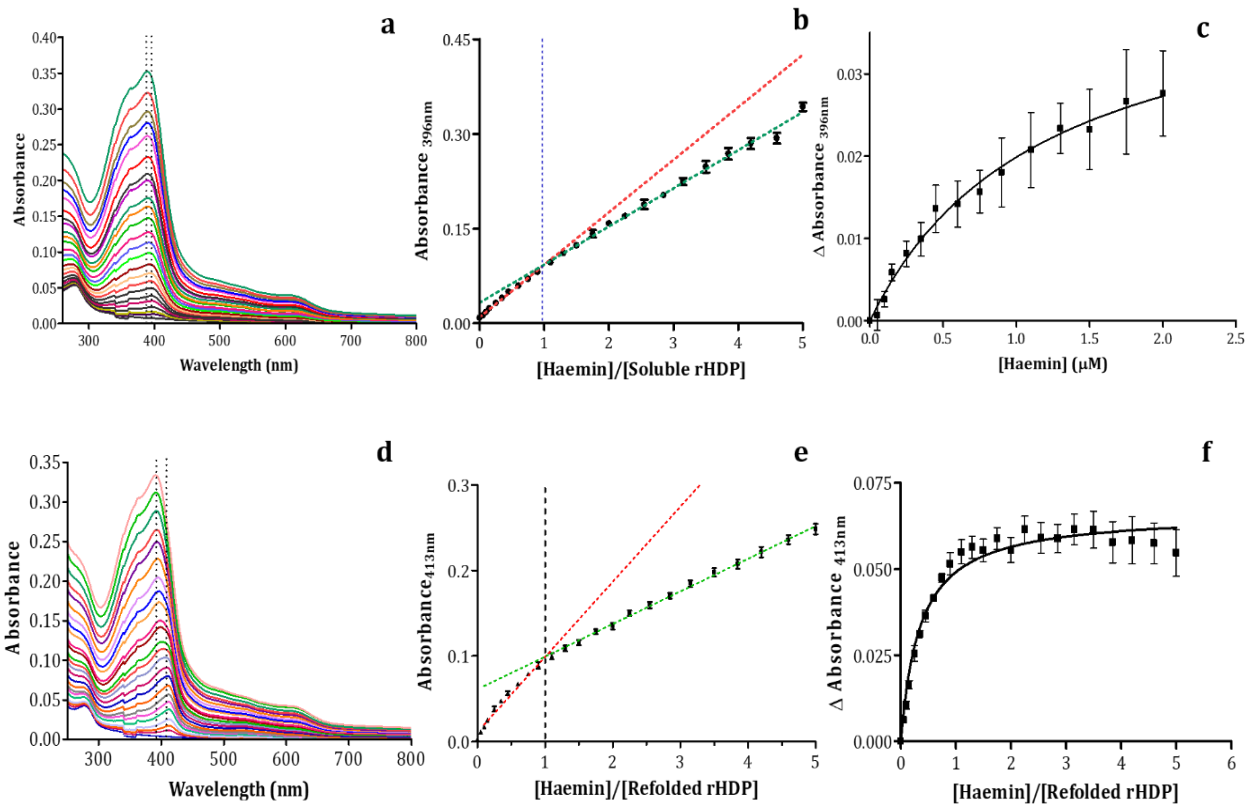

Figure 5.18. UV-Vis spectra and titration curves representing the interaction of haemin with rHDP. (a) Spectrophotometric titrations of haemin titrated into 1 μM soluble and **(d)** refolded rHDP at pH 7.4 in increments from 0 to 5 μM monitored by UV-vis absorbance spectroscopy. **(b)** A plot of absorbance vs haemin to soluble rHDP ratio showed a 1:1 binding stoichiometry with ε_A = 8.302 ± 0.002 × 10^4 $M^{-1}cm^{-1}$ corresponding to the Fe(III)PPIX-rHDP complex and ε_B = 6.031 ± 0.001 × 10^4 $M^{-1}cm^{-1}$ corresponding to free Fe(III)PPIX dimer. **(e)** Similarly, a plot of absorbance vs haemin to refolded rHDP ratio comprised ε_A = 8.776 ± 0.003 × 10^4 $M^{-1}cm^{-1}$ and ε_B = 3.813 ± 0.001 × 10^4 $M^{-1}cm^{-1}$. Spectrophotometric titrations showing ΔA vs concentration of haemin was fitted using a 1:1 dissociation equation with **(c)** R^2 = 0.69 and **(f)** R^2 = 0.90 for soluble and rHDP respectively, where $\Delta A = A_{obs} - \varepsilon_B[haemin] - A_0$.

Plasmodium HRP II, which was previously implicated in haemozoin formation, exhibiting a K_d of 340 nM is 4-fold stronger than the reported K_d of 80 nM for refolded HDP.[132,131] In this study, a K_d of 1.2 ± 0.5 μM and 0.35 ± 0.04 μM for soluble and refolded rHDP respectively (Figure 5.18c and f) was determined, indicating a 4-fold weaker affinity for refolded rHDP than previously reported, but still weaker affinity for the soluble protein.

5.3.5.3. Activity studies of rHDP

HDP has attracted attention over the past decade for its insinuated role in haemozoin formation. Previous studies have shown that blood-stage parasites in which the HDP gene was knocked out were not viable, signifying that HDP is an essential protein in this stage of the parasite's lifecycle. However, there are a number of shortfalls surrounding the reported function of HDP as a haemozoin formation enzyme. Previous studies have relied solely on refolded recombinant protein which probably differs in conformation from its native form since as seen here, it certainly differs from its soluble form. As noted in Chapter 1, the HDP sequence comprises nine His residues at positions 44, 58, 70, 79, 122, 172, 175, 192 and 197, of which site-directed mutagenesis studies have claimed four to be essential in β-haematin formation, namely His122, 172, 175 and 197. However, mutation of any one, or all nine, His residues to Ala did not eliminate activity, but simply reduced it by about 50% when compared to the wild type.[137]

Table 5.7: Sequence alignment[a] comparing H172 *P. falciparum* HDP to other human-infecting *Plasmodium* species

Organism	Accession Number	His residue not conserved	% Sequence Identity	E-value	Score
P. vivax	A0A1G4HHQ7_PLAVI	H172N	76.5	2.7×10^{-115}	856
P. ovale	A0A1C3KWC8_9APIC	H172N	79.5	5×10^{-120}	887
P. malariae	A0A1A8W7M9_PLAMA	H172N	82.3	4.7×10^{-122}	900
P. knowlesi	A0A384L7P6_PLAKH	H172N	79.1	3.3×10^{-117}	870

[a] Sequence alignment carried out using The UniProt Consortium, UniProt: the universal protein knowledgebase

Sequence analysis of the HDP sequence with other human-infecting *Plasmodium* species (Table 5.7) shows that His172 is not conserved but instead an Asn residue is found at this position. Given that the mutagenesis study indicated that mutation of this residue had as much effect on β-haematin formation as mutation of all four essential His residues, it questions the role of this protein in directly catalysing this process given that the other *Plasmodium* species still produce haemozoin. Studies focusing on amino acid exchangeability in proteins indicate a relatively low probability of His to Asn mutation

with conservation of function.[353] Though this may not entirely rule out Asn playing the same role as His172, it does create doubt. In addition, HDP homologues were found in other non-haemozoin forming organisms including blood-infecting parasites such as *Babesia* in which the His residues are not conserved, with other amino acid residues being present in those positions (Table 5.8). This suggests that HDP plays a different role to that previously believed but a similar one that may be common to these other organisms. For these reasons, the ability of rHDP to mediate β-haematin formation was investigated.

Table 5.8: Sequence alignment[a] comparing key *P. falciparum* HDP His residues to non-haemozoin forming organisms

Organism	Accession Number	His residue	% Sequence Identity	E-value	Score
C. velia	A0A0G4H2Z3_9ALVE	H44F H172D H175R	44.8	1.8×10^{-50}	434
T. parva	Q4N158_THEPA	H58N H70E H172K H175K	44.6	3.6×10^{-52}	440
B. bovis	A7APP5_BABBO	H58N H70P H172V H175D	41.4	4.5×10^{-43}	380
B. microti	A0A1N6LWP5_BABMR	H58I H70Q H172E H175(-)	38.4	1.2×10^{-33}	317

[a]Sequence alignment carried out using The UniProt Consortium, UniProt: the universal protein knowledgebase

The activity of soluble and refolded rHDP in mediating β-haematin formation was evaluated using FT-IR to confirm formation of the product using characteristic signals as illustrated in Figure 5.19a. Experimental conditions used were identical to those previously reported by Sullivan *et al*, Jani *et al* and Nakatani *et al* with the modification that 5% pyridine (pH 7.4) was used instead of bicarbonate to wash out unreacted haemin.[124, 131, 137] Studies were carried out to determine the influence of various concentrations and buffers on the formation of β-haematin in which final experiments proceeded using 0.5 M sodium acetate, pH 5.2 (Figure 5.19b). Following established

protocols, SDS was added at the end of the reaction. This was done with the intention that it would denature rHDP, thereby rendering it inactive and terminating the reaction. Under these conditions, in agreement with previous studies, β-haematin was formed when soluble and refolded rHDP were incorporated in the reaction (Figure 5.20). A control experiment containing neither rHDP nor SDS produced no detectable β-haematin (Figure 5.19b and 5.20).

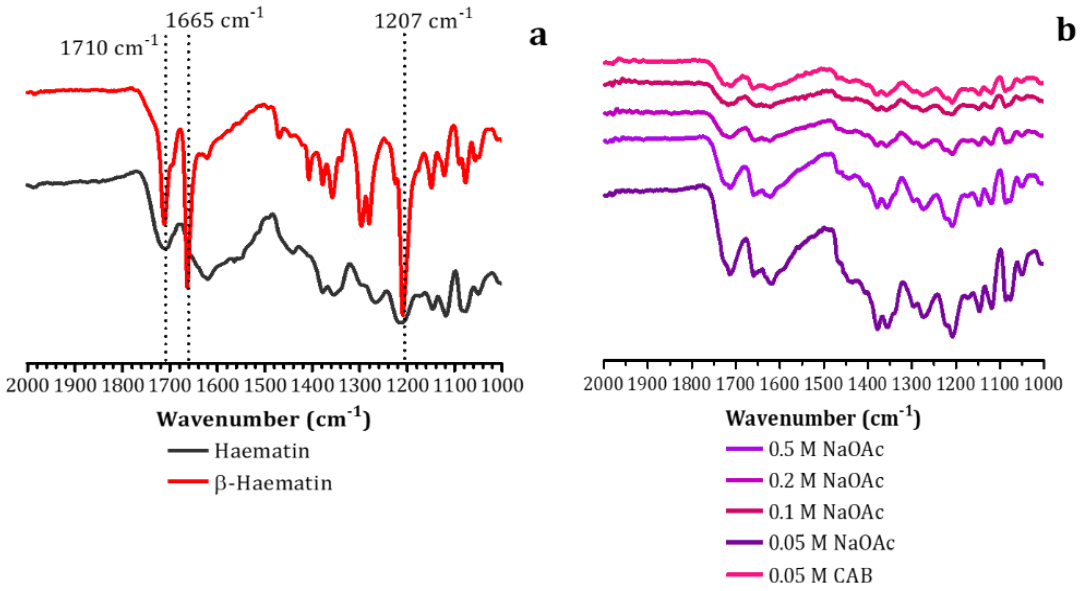

Figure 5.19. Overlay of FT-IR spectra representing haematin control and β-haematin synthesised using the acetate method as a positive control. (a) Dashed lines indicate characteristic peaks representing the C=O at 1665 cm^{-1} and C-O at 1207 cm^{-1} vibrational stretches. **(b)** FT-IR spectra representing the precipitate obtained from a buffer study to optimise experimental conditions. These showed that there was no detectable β-haematin present, confirming that the chosen buffer did not contribute to formation. Key: Citrate buffer (CAB)

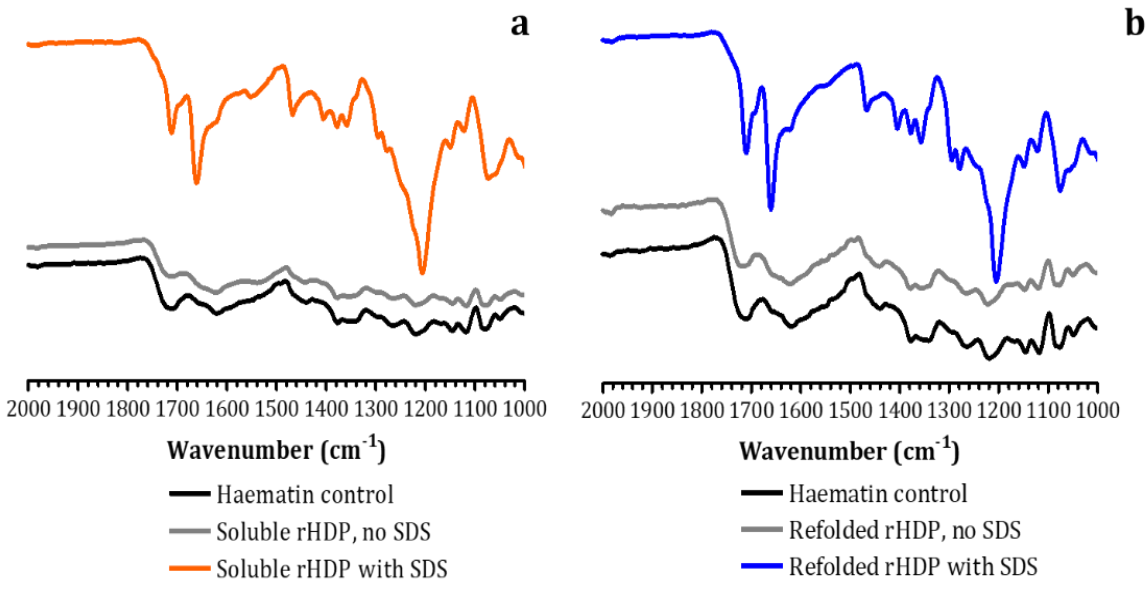

Figure 5.20. FT-IR spectra representing precipitate obtained from the first control reaction comprising 600 μM haemin (black line), second control reaction comprising 600 μM haemin and 0.5 μM rHDP (grey line) and experimental reaction comprising 600 μM haemin, 0.5 μM rHDP and 0.1% SDS (coloured lines). Spectra representing soluble rHDP and refolded rHDP are seen in **a** and **b** respectively. All reactions were carried out in 0.5 M sodium acetate, pH 5.2 at 37°C for 1 h.

It is well known that detergents are able to mediate β-haematin formation; therefore, an investigation of the reaction in the absence of rHDP, whilst keeping all other reaction conditions and the method constant whilst maintaining the addition of SDS at the end of the reaction, was carried out. The product of this reaction was characterized using FT-IR spectroscopy, pXRD, SEM and TEM (Figure 5.21) which unequivocally identified the product as β-haematin. Using these insights, an experiment was performed with soluble and refolded rHDP omitting SDS. In these cases, no β-haematin formed, illustrating that SDS was in fact entirely responsible for crystal formation in the original experiment (Figure 5.20). Various concentrations of SDS were investigated to determine the range at which β-haematin was capable of forming. The products of this reaction monitored by FT-IR showed that formation proceeded over a range of 0.025 to 5% SDS, while anything above 5% illustrated deviations in the corresponding spectra (Figure 5.22).

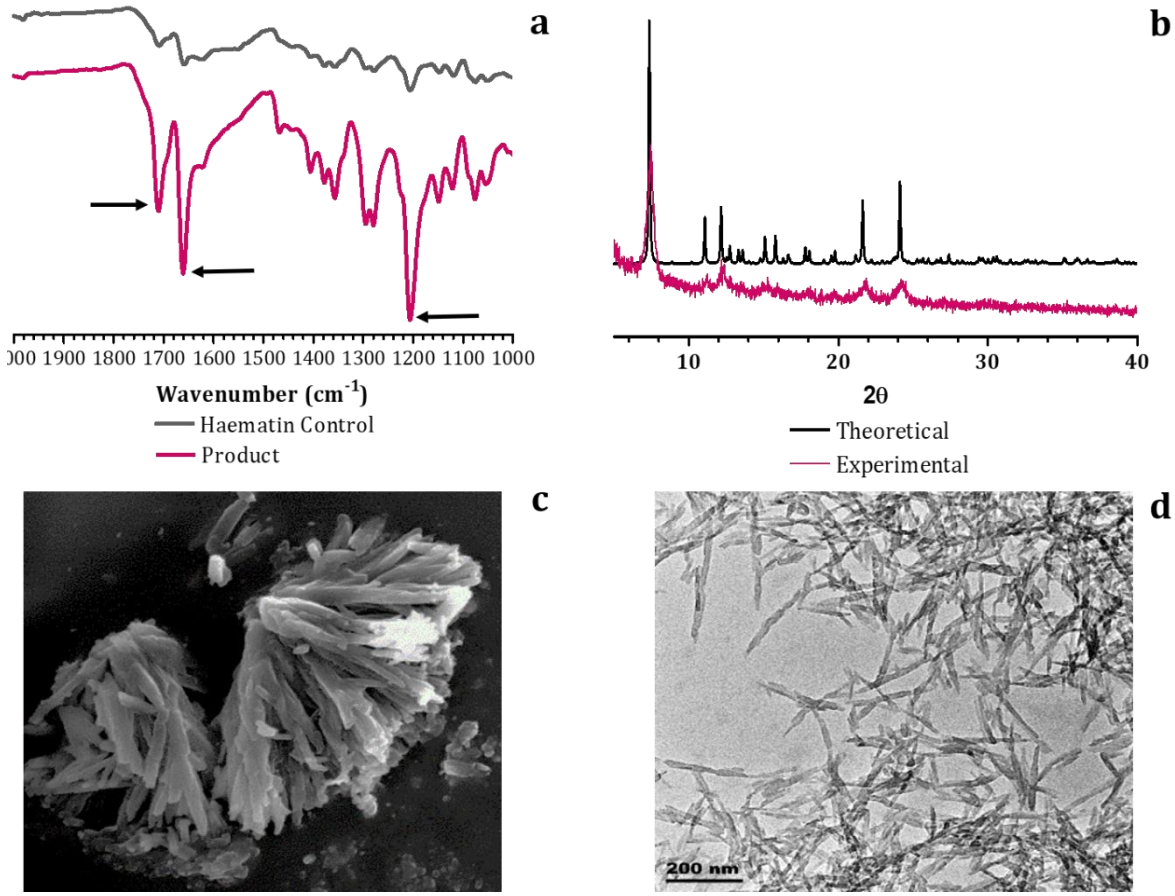

Figure 5.21. Characterisation of synthesised product with SDS only. (a) Peaks in the FT-IR spectrum at 1710 cm^{-1}, 1665 cm^{-1} and 1207 cm^{-1} indicated by the arrows. **(b)** Calculated pXRD pattern aligned with the theoretical pattern. **(c)** Scanning and **(d)** transmission electron micrographs illustrating external morphology of the crystals formed.

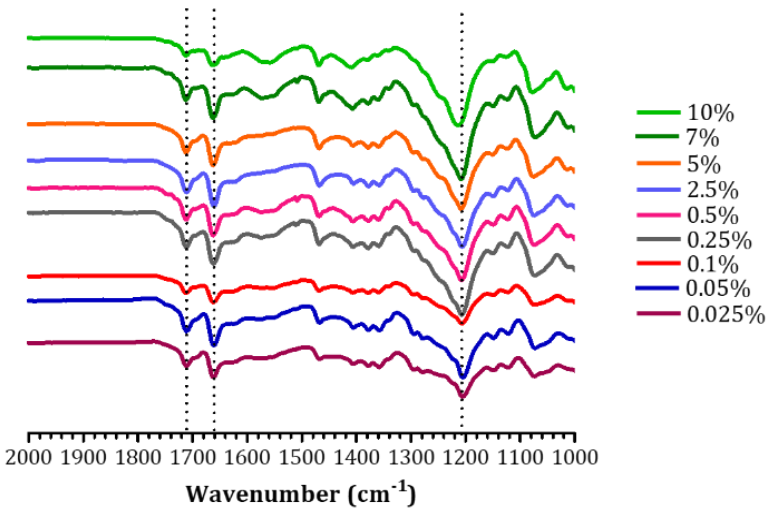

Figure 5.22. FT-IR spectra representing β-haematin formation using different concentrations of SDS (*w/v*). Spectra illustrate a range of 0.025-5% to be viable for successful β-haematin formation. Dashed lines trace the characteristic peaks at 1710 cm^{-1}, 1665 cm^{-1} and 1207 cm^{-1}.

Under previously reported conditions, including the use of 0.1% SDS to terminate the reaction, mixtures independently containing soluble and refolded rHDP were found to produce β-haematin.[131, 51, 137] However, when SDS was omitted, no β-haematin formed, demonstrating that it was in fact the detergent that was responsible for mediating this process. Further experiments in which the reaction proceeded in the absence of rHDP but incorporated the SDS termination step successfully produced β-haematin. The FT-IR spectrum and pXRD pattern obtained were characteristic of β-haematin and the crystals produced were similar in external morphology to haemozoin crystals when visualised using electron microscopy. Extended incubation times of rHDP with haemin from 1 to 4 h, as well as initial dissolution of haemin in solvents other than DMF, had no effect on the outcome of the reaction when SDS was omitted.

These findings strongly indicate that HDP is not responsible for mediating or catalysing haemozoin formation since rHDP on its own has no capacity to mediate β-haematin formation, and neither does it play a role as a haem dimerisation protein as previously suggested since it binds haemin in a 1:1 ratio. It may be that the weak association allows HDP to play a role in sequestering excess haem as a transport or chaperone protein rather than an enzyme directly responsible for haemozoin formation although the K_d is very high for such a function.

5.4. Chapter Summary

This chapter has described the optimised expression and purification of soluble and refolded rHDP. Using the pCold I expression vector in the C41 *E. coli* cell line, low-temperature induction conditions and nutrient enriched media supplemented with 1% glucose, resulted in the production of adequate amounts of soluble rHDP. Inclusion bodies were washed, solubilised and homogenised in a sarcosine-containing buffer system operating at a pH higher than the theoretical pI of HDP. Inclusion body material was refolded and purified using a detergent gradient incorporated into a nickel affinity method followed by dialysis and SEC which afforded pure protein in high yield. The identity of expressed protein was confirmed by using an In-gel His-tag stain complemented by tandem mass spectrometry.

Circular dichroism and fluorescence spectroscopy confirmed that soluble and refolded rHDP differ in their secondary and tertiary structures. Soluble rHDP is more likely to resemble the native conformation in the parasite compared to its refolded counterpart. A 1:1 binding stoichiometry of rHDP to haem was found for both soluble and refolded rHDP compared to the previously reported 2:1 value for the refolded protein. rHDP bound haem relatively weakly with a K_d of 1.2 ± 0.5 μM and 0.35 ± 0.04 μM for soluble and refolded rHDP, respectively. While quite weak, this would be strong enough to be able to bind free haem present in the DV and to shuttle it to where haemozoin is formed given the high haem concentration in the DV.

Published β-haematin formation assay conditions incorporating protein were rigidly followed and were reproducible in forming β-haematin. In this study, it was discovered that it was the addition of SDS that was responsible for promoting β-haematin formation under these conditions. It was established that both soluble and refolded rHDP were incapable of catalysing β-haematin formation without the aid of the detergent which calls into question the theory postulating it as a haemozoin-forming enzyme. While these findings have illustrated that rHDP is not directly responsible for haemozoin formation, the earlier evidence that this protein is occluded by haemozoin crystals in relatively high abundance and that it exhibits an interaction with haem suggests that it could potentially play a role as a haem chaperone protein. Since detergents were responsible for nucleation of β-haematin and have been used lipid mimetics, the role of lipids as potential mediators of haemozoin formation will be explored in Chapter 6.

Chapter 6

The Investigation of Lipids Occluded by Haemozoin and their Role in Crystal Formation

6.1. Introduction

Having demonstrated that rHDP is not a key mediator of haemozoin formation, but rather the anionic detergent, SDS, is responsible for catalysing β-haematin formation as illustrated in Chapter 5, it was decided to further explore the role of lipids in this biocrystallisation process. Biomineralisation relies on the coalescence of macromolecules such as polysaccharides, lipids and proteins in creating a balanced yet dynamic environment which closely interacts with the inorganic mineral phase thus promoting crystallisation within an organism. Lipid assemblies constituting matrix vesicles have been shown to regulate the location, composition, size and, in some cases, the shape of biominerals such as magnetosomes found in magnetotactic bacteria, coccoliths from the marine alga *E. huxleyi* as well as in bone and dentin formation.[354,98,112] In these non-related organisms, phospholipid-rich vesicles and membranes create specialised compartments which direct where biomineralisation occurs.

Prior to reports that HDP was responsible for haemozoin formation in *Plasmodium*, an alternate theory was based on lipids being the biomolecules responsible for crystal nucleation. As discussed in Chapter 1, lipids were first implicated in haemozoin formation when acetonitrile derived parasite extracts successfully produced β-haematin.[139] To date, it is only the surface-associated lipids that have been profiled; however, the method of isolation creates a cause for contention as this process can carry through contaminants

from the parasite itself.[146] In addition, derivatising lipids prior to analysis involves chemical modifications that in some cases may alter the system in a manner that results in a loss of the exact identity of the lipids actually present. Confocal and fluorescent imaging techniques previously used to visualise lipid bodies afforded images in which it was unclear whether the lipid bodies were located inside or outside the DV due to inadequate resolution. Even though the evidence suggesting that lipids are important to haemozoin formation is convincing, the shortfalls that accompany it opens the area to further interrogation. This chapter focuses on demonstrating that haemozoin and β-haematin can occlude lipids in a non-exchangeable manner, profiling the specific lipids occluded by these crystals at the time and site of their formation and investigating their activity in β-haematin formation. The composition and location of lipid bodies with respect to haemozoin were also examined.

6.2. Experimental Methods

6.2.1. Qualitative lipid profiling using TLC

Lipids were extracted from washings or dissolved haemozoin obtained from extensively washed crystals using chloroform/methanol (2:1 *v/v*) and separated using TLC following previously reported conditions.[143, 146] This first involved separating the phospholipid component using a chloroform/methanol/water (50:20:3 *v/v*) mobile phase, after which the TLC plates (TLC Silica gel 60 F_{254} aluminium backed plates, Merck) were air-dried and immersed into the second mobile phase comprising hexane/diethyl ether/acetic acid (16:10:1 *v/v*) to facilitate separation of neutral lipids. Commercially available lipids, *rac*-1-monostearoylglycerol (MSG), *rac*-1-monopalmitoylglycerol (MPG), 1,3-dipalmitoylglycerol (DPG), 1,3-dioleoylglycerol (DOG), 1,3-dilinoleoylglycerol (DLG), 1,2-dioleoyl-*sn*-glycero-3-phosphocholine (DOPC), cholesterol (CHL) and cholesteryl oleate (CE) were purchased from Sigma-Aldrich and used as standards in this study. Lipid standards were reconstituted in either acetone/methanol (1:9 v/v) or chloroform/methanol (2:1 *v/v*) at a stock concentration of 3.31 mM and were subjected to the same TLC system as described above. Following separation, TLC plates were stained with 0.05% (*w/v*) Primuline, a non-destructive lipid-specific fluorescent dye prepared in acetone/water (4:1 *v/v*) and visualised using a UV lamp at 365 nm.[355]

β-Haematin (25 mg) prepared using a 4.5 M acetate solution as reported in Chapter 2, was incubated in 1 mL parasite lysate at 37°C for 15 min. This mixture was allowed to equilibrate at room temperature for a further 15 min before crystals were collected via centrifugation. Synthetic crystals were extensively washed in the same manner as that described for isolated haemozoin. The impact of NaOH on lipid profiles was investigated by treating parasite lysate and 3.31 mM phospholipid standards (DOPC) and cholesteryl oleate with 0.1 M NaOH in a ratio of 2:1 (*v/v*) and separated using TLC in the same manner as described above.

6.2.2. Exchange studies using labelled NBD-Cholesterol

To determine whether cholesterol were exchangeable with haemozoin and β-haematin, preformed crystals (1 mg) were incubated in a 1 mL solution buffered with sodium acetate (0.5 M, pH 5.2) containing NBD-cholesterol (2.5 mM) for 30 min at 37°C. In a parallel experiment, β-haematin was synthesised in the presence of NBD-cholesterol using the model lipid blend (Section 6.2.4.1) where the labelled lipid was used to substitute a portion of the cholesterol content to afford a final concentration of 1.5 mM. Following incubation, the product was obtained by centrifugation at 13 500 rpm for 10 min. The pellet was extensively washed, first with sodium acetate buffer (0.5 M, pH 5.2) then by four washes with an acetone/methanol (1:9 *v/v*) solution and finally by three washes with PBS (10 mM, pH 7.4) after which the pellet was dissolved in 0.1 M sodium hydroxide.

β-haematin prepared in the presence of NBD-cholesterol was first washed with an aqueous pyridine solution containing 5% (*v/v*) pyridine, 30% (*v/v*) acetone and 0.02 M HEPES (pH 7.4) before proceeding with organic solvent and buffer washes. Lipids were extracted from samples using acetone/methanol (1:9 *v/v*) and separated using TLC following methods detailed in Section 6.2.1. Following separation, TLC silica gel plates hosting fluorescently-labelled cholesterol were air dried and visualised using a UV lamp at 365 nm.

6.2.3. Lipid profiling by MS

MS experiments and data collection were performed at the Lipidomics Core Facility, Columbia University Medical Centre.

6.2.3.1. Extraction of lipids from parasite material

Lipids were extracted from RBCs, trophozoite cytoplasm, washings of haemozoin crystals and dissolved crystals using the Bligh-Dyer method with modifications.[356] The number of parasites were determined through counting using a haemocytometer, and total protein content measured using the Quick Start Bradford Protein Assay (Bio-Rad) as per the manufacturer's instructions. All buffers and solutions were preserved on ice throughout the lipid extraction process.

Each sample was first homogenised using chloroform/methanol (2:1 *v/v*) in a sample-to-organic-solvent ratio of 1:2 (*v/v*). This mixture was further homogenised by adding 900 µL chloroform/methanol (5:4 *v/v*), after which it was vigorously vortexed for 30 s then incubated on ice for 1 min. This process was repeated twice more. Homogenised material was then centrifuged at 13 000 rpm for 4 min producing two distinct layers. The lower organic layer, comprising lipids, was carefully transferred into a new Eppendorf tube and dried under nitrogen gas until all solvent had evaporated. Dried samples were resuspended in minimum volume of chloroform/methanol (2:1 *v/v*) and dosed with internal lipid standards obtained from Avanti Polar Lipids (Alabaster, AL). The neutral lipid standards used were D7-cholesterol, cholesterol ester (CE) 17:0, monoacylglycerol (MG) 17:0, 4-methyl diether diacylglycerol (DG), D5-triacylglycerol (TG) 16:0/18:0/16:0. Phospholipid and sphingolipid standards comprised phosphatidic acid (PA) 14:0/14:0, phosphatidylcholine (PC) 14:0/14:0, phosphatidylethanolamine (PE) 14:0/14:0, phosphatidylglycerol (PG) 15:0/15:0, phosphatidylinositol (PI) 16:0/16:0, phosphatidylserine (PS) 14:0/14:0, acyl phosphatidylglycerol (APG) 14:0/14:0/14:0, bis (monoacylglycero)phosphate (BMP) 14:0/14:0, lysophosphatidylcholine (LPC) 13:0, lysophosphatidylethanolamine (LPE) 14:0, lysophosphatidylinositol (LPI) 13:0 and ceramide (Cer) d18:1/17:0, sphingomyelin (SM) d18:1/12:0, dihydrosphingomyelin dhSM d18:0/12:0, galactosylceramide (GalCer) d18:1/12:0, sulfatide (Sulf) d18:1/12:0, glucosylceramide (GlcCer) d18:1/12:0 and lactosylceramide (LacCer) d18:1/12:0, respectively.

6.2.3.2. Lipidomics based mass spectrometry

Lipid extracts were analysed using a LC-MS/MS platform comprising a 1260 Infinity LC system coupled to a 6490 Triple Quadrupole MS system (Agilent Technologies, Santa Clara, CA) following optimised mass spectrometry protocols reported by Chan *et al.* and Gulati *et al* with modifications.[357,203] Briefly, sterols and glycerolipids were separated by employing reverse-phase HPLC using an Agilent Zorbax Eclipse XDB-C18 column (4.6 x 100 mm) and an isocratic mobile phase (Table 6.1) at a flow rate of 250 µL/min.

Separation of glycerophospholipids and sphingolipids proceeded by normal-phase HPLC using an Agilent Zorbax Rx-Sil column (inner diameter 2.1 x 100 mm) at a flow rate of 300 µL/min. This was used in conjunction with mobile phases A and B (Table 6.1) to produce the following liner gradients that promoted separation: 95% A for 2 min, progressing to 30% A over 18 min and held for 3 min leading to 95% A over 2 min which was held for 6 min. Dynamic multiple reaction monitoring (MRM) transitions under negative and positive ionisation modes were used to obtain quantitative lipid profiles across all samples by jointly referencing the signal intensities of relevant internal standards. Lipid levels were calculated based on the number of moles of lipid measured and normalised to total cell protein with concentrations expressed as nmol/mg of total cellular protein.

Table 6.1. Mobile phases used in mass spectrometry experiments for separation of lipid classes

	Mobile phase constituents	**Ratio (*v/v*)**
Isocratic Mobile Phase	Chloroform/methanol/ ammonium acetate (0.1 M)	100:100:4
Mobile Phase A	Chloroform/methanol/ammonium hydroxide (1 M)	89.9:10:0.1
Mobile Phase B	Chloroform/methanol/water/ammonium hydroxide	55:39.9:5:0.1

6.2.4. Formation of β-haematin by model lipid blends

6.2.4.1. Experimental methods for synthesis of β-haematin

β-haematin was prepared by following previously reported methods with modifications.[153] 2 mL sodium acetate buffer (0.5 M, pH 5.2) was pre-incubated in a glass reaction vial for 45 min at 37°C. A fresh solution of Fe(III)PPIX was prepared by dissolving 2 mg haemin (Fluka) in 400 µL NaOH (0.1 M) which was sonicated for 10 min and further

solubilised using 600 µL acetone/methanol (1:9 *v/v*). Stock solutions of individual lipids; namely, MSG, MPG, MOG, DPG, DOG, DLG, cholesterol, cholesteryl oleate, glycerol trioleate (TG) and phosphatidylcholine (PC) were prepared in chloroform/methanol (2:1 *v/v*) or acetone/methanol (1:9 *v/v*) at a stock concentration of 3.31 mM.

A monoglyceride blend (MG_b) was prepared by combining MPG/MSG/MOG in a ratio of 2:1:1 (*v/v*) and a diglyceride blend (DG_b) prepared by combining DOG/DPG/DLG in equal amounts. These constituent lipids were used to produce a model lipid blend (Blend A) based on the actual lipids identified to be occluded by haemozoin using mass spectrometry. Blend A was prepared by mixing CHL/CE/MG_b/DG_b/TG/PC in a ratio of 94.2:2.2:0.2:0.2:0.1:3.1 (*v/v*). A 1:1 lipid/Fe(III)PPIX mixture was freshly prepared before use, 600 µL carefully layered over the pre-incubated buffer using a 21 G syringe and incubated for 60 min at 37°C. The product was collected by centrifugation at 13 500 rpm for 5 min after which the β-haematin pellet was sequentially washed with 1 mL sodium acetate buffer (0.5 M, pH 5.2), 600 µL of freshly prepared 5% pyridine solution, 1 mL MilliQ water followed by multiple acetone/methanol washes (1:9 *v/v*) and allowed to air-dry overnight. A control reaction was set up simultaneously under the same experimental conditions, but lipid was substituted with acetone/methanol (1:9 *v/v*). Each experiment was performed in triplicate.

6.2.4.2. Quantifying the amount of β-haematin formed

After 60 min incubation and first buffer wash, the supernatant was discarded, and the resulting pellet was used to determine the percentage yield of β-haematin formed. A modified version of the pyridine-ferrichrome assay was employed by monitoring the coloured low-spin complex that Fe(III)PPIX forms with pyridine at its maximum absorption of 405 nm by UV-vis spectroscopy.[358] Aqueous pyridine (5% *v/v*) does not solubilise β-haematin but rather, selectively solubilises free Fe(III)PPIX present making it an ideal solvent for detecting free Fe(III)PPIX. The pellet was washed using 600 µL freshly prepared 5% pyridine solution. Following centrifugation, the coloured supernatant was diluted 1:20 in 5% pyridine solution and the absorbance measured at 405 nm using a SpectraMax Microplate Reader (Molecular Devices).

The yield was determined by calculating the ratio of measured absorbances of the test and control experiments at 405 nm using the equation below:

$$\%\ Yield\ of\ \beta - Haematin\ formed = 1 - \left(\frac{Abs\ at\ 405nm\ of\ Test}{Abs\ at\ 405nm\ of\ Control}\right)\ x\ 100$$

6.2.4.3. Preparation of derivative lipid blends

Lipid stock solutions (3.31 mM) were used to prepare four additional lipid blends derived from Blend A by combining various lipids as outlined in Table 6.2.

Table 6.2. Composition of lipids used to prepare alternative blends

	Lipid Components	Ratio (*v/v*)
Blend B	CHL/CE/MG_b/DG_b/TG	97.2:2.3:0.2:0.2:0.1
Blend C	CHL/CE	97.7:2.3
Blend D	CHL/MG_b/DG_b/TG	99.4:0.2:0.2:0.1
Blend E	CHL/ MG_b/DG_b/TG/PC	96.3:0.2:0.2:0.1:3.2

6.2.4.4. Effect of different methods used to dispense lipid/Fe(III)PPIX mixture on yield of β-haematin

The technique in which lipids and Fe(III)PPIX were introduced into the buffer system was investigated. β-Haematin was prepared as described above in Section 6.2.3.1 but instead of gently layering the lipid/Fe(III)PPIX mixture over the buffer using a syringe, the mixture was vortexed and rapidly transferred into the pre-incubated buffer using a pipette. The suspension was mixed and then incubated. After incubation and washing, the yield of β-haematin formed was determined as described above.

6.2.4.5. Kinetic investigation of β-haematin formation using lipid Blend A

Kinetic studies were carried out for Blend A at a lipid/Fe(III)PPIX ratio of 1:1. β-haematin was prepared using the same experimental procedure described Section 6.2.3.1. The reaction was allowed to proceed at varying lengths of time and stopped at specific time intervals up to 60 min. The yield was calculated as described in Section 6.2.3.2; however, yields obtained in this experiment corresponded to different time points which was used to generate a kinetic plot.

6.2.4.6. Determination of the minimum amount of lipid needed to promote β-haematin formation

The lowest concentration of model lipid blend needed to produce β-haematin was determined. This proceeded by preparing β-haematin as described in Section 6.2.3.1. but a constant concentration of Fe(III)PPIX was maintained whilst varying the concentration of lipid (Blend A) from 2.3 to 600 μM corresponding to lipid/Fe(III)PPIX mole ratios of 7.8×10^{-3} to 2. The immediate pellet obtained after incubation was examined by FT-IR to determine if the product had successfully formed.

6.2.5. Live-cell fluorescent imaging by laser scanning confocal microscopy

6.2.5.1. General experimental methods

Imaging medium was prepared by combining 10.4 g/L RPMI 1640 and 24.0 g/L HEPES in 100 mL MilliQ water. The pH was adjusted to 7.5 with NaOH (5 M) and the solution filtered using a 0.22 μm nylon syringe filter prior to use. Stock solutions of Hoechst 33342 (Life Technologies), HCS LipidTOX™ Green (Thermo Scientific) and Nile red (Sigma-Aldrich) were prepared in DMSO. These fluorescent probes were diluted using imaging medium to afford concentrations of 2 μM, 500 nM and 200 nM respectively and were incubated at 37°C for 30 min prior to use. Nunc® Lab-tek® II eight-well chamber slides with cover glass No. 1.5 (Thermo Fisher Scientific) were coated with 200 μL of 0.01 % (*w/v*) poly-L-lysine solution and incubated at room temperature for 15 min after which excess solution was carefully removed and the chamber slides air dried overnight.

Parasitised erythrocytes (NF54) were collected at 6 h intervals over the 48 h life cycle where t_0 is the time point at which merozoites re-invaded host erythrocytes. Parasite cultures were centrifuged at 750 rcf for 5 min, after which 5 μL of the pellet was transferred into a falcon tube containing 5 mL imaging medium and immediately vortexed to avoid cell aggregation. 150 μL of the cell suspension was transferred onto the centre of each well in the chamber slide and incubated at 37°C for 20 min to allow cells to adhere. Imaging medium was then used to gently wash each well which removed unwanted free cells. This solution was replaced with 150 μL imaging medium containing the appropriate concentrations of the respective fluorophores as mentioned above.

6.2.5.2. Laser scanning confocal microscopy of the development of lipid bodies

Laser scanning confocal microscopy was performed at the Confocal and Light Microscope Imaging Facility at the University of Cape Town using a Zeiss Axiovert 200 M LSM 150-META confocal microscope. Cells were incubated at 37°C during imaging. A 20x low objective lens was first used to locate cells of interest after which a Plan-Apochromat 63x/1.4 Oil DIC M27 objective lens was used for fluorescent imaging. Hoechst was excited at 750 nm using a two-photon laser and emission detected using a 415-500 nm spectral filter. HCS LipidTOX™ Green was excited at 488 nm and fluorescence was detected using a 500-550 nm bandpass filter. Nile red was excited using a 561 nm laser and fluorescence was detected using a 575-630 nm bandpass filter. Images were captured and processed using Zen 2011 software package (Carl Zeiss Microscopy GmbH).

6.2.6. Live cell fluorescent imaging by spinning disk confocal microscopy

6.2.6.1. General experimental methods

Preparation of cells and fluorescent probes proceeded as described in Section 6.2.4.1. with modifications. Imaging medium was prepared by combining 32.1 g/L RPMI 1640 without phenol red, 5.94 g/L HEPES and 0.05 g/L hypoxanthine in 1 L MilliQ water and stirred at low heat for 60 min. The pH was adjusted to 7.4 and the solution filtered prior to use. HCS LipidTOX™ Red (Thermo Scientific) and NBD-cholesterol (Thermo Scientific) were prepared from stock solutions to afford concentrations of 200 nM each. Mature, trophozoite stage NF54 and Dd2 green fluorescent protein (GFP) conjugated PfCRT parasite cultures were collected by centrifugation after which 5 µL of the resulting pRBC pellet was added to 5 mL imaging media containing fluorescent probes used in this study. 150 µL of this cell suspension was transferred into borosilicate coated wells of a Nunc® Lab-tek® II eight-well chamber slide with cover glass No. 1.5 (Thermo Scientific) and incubated at 37°C for 20 min. After incubation, cells were gently washed with 150 µL imaging medium. This was gently removed and replaced with 150 µL new medium containing fluorescent probes.

6.2.6.2. Spinning disk confocal microscopy

Live cell imaging using spinning disk confocal microscopy was performed at the Confocal and Specialised Microscopy Shared Resource Facility at Columbia University using a Nikon Stochastic Optical Reconstruction Microscope (N-STORM) equipped with a Nikon Ti Eclipse Inverted microscope stand (Nikon Instruments, Melville, NY) and an EMCCD camera (Andor DU-897 and Evolve) coupled with a CSU-X1 spinning disk scanner unit (Yokogawa). Cells were maintained at 37°C in a stage-top incubator (Tokai) throughout imaging. High resolution *z*-stacks were collected using a 100×/1.49 TIRF Nikon oil objective lens.

Images were processed using NIS-Elements based on a stochastic optical reconstruction algorithm. Prior to fluorescence imaging, transmittance was focused on haemozoin within the parasites until the DV was clearly visible as previously described.[359] Hoechst was excited using a 405 nm laser and emission detected using an ET455/50m filter. LipidTOX™ Red was excited using a 561 nm laser and detected using the ET600/60m emission filter. GFP-conjugated parasites and NBD-cholesterol were excited with a 488 nm laser and emission detected using an ET525/50m emission filter. Chromatic correction and channel alignment were performed using multicolour fluorescent TetraSpeck™ Microspheres as a calibration tool (0.1 µm, #T7279, Thermo Fischer). 3D reconstruction and deconvolution were performed using the Volocity® software package from Quorum Technologies utilising the iterative restoration algorithm developed by PerkinElmer allowing for calculated and experimentally-determined point spread functions (PSFs).

6.3. Results and Discussion

6.3.1. Qualitative Profile of Lipids Associated with Haemozoin

Development of the malaria parasite within the host erythrocyte is contingent on cell remodelling which occurs through various essential processes of which most are lipid dependent. These include protein trafficking, cell signalling, haemoglobin trafficking and degradation as well as membrane, vesicle and organelle biogenesis, to name a few, which together illustrate the importance of lipid bioavailability for growth and survival during

the blood stage of the parasite's life cycle.[189, 360] Apicomplexan parasites, specifically *Plasmodium*, meet this intense nutritional demand by scavenging lipids from the host cell or through the type II fatty acid synthesis (FAS II) pathway.[135, 361]

Biological samples yield crude extracts comprising a complex mixture of macromolecules such as DNA, proteins, metabolites and lipids. To reduce the complexity associated with parasite lysate and to obtain a qualitative profile of the lipids associated with haemozoin, thin layer chromatography was employed. This established technique often used in lipid analysis provides separation of various lipid classes present in a given sample based on the difference in polarity between the stationary phase and the non-polar lipids which migrate on the silica plate along with the solvent front.[362] TLC is advantageous in that it is cost-effective, allows simultaneous analysis of multiple samples, excludes memory effects owing to the use of a new stationary phase for each experiment, is reproducible and allows for efficient detection of compounds when treated with specific dyes.[363, 364]

By TLC analysis, Pisciotta *et al*. identified lipids associated with the surface of isolated haemozoin where a minor phospholipid component was observed as well as predominantly monoacylglycerols and diminished amounts of diacyl- and triacylglycerols compared to trophozoites.[146] In an attempt to minimise lipid loss during isolation, haemozoin crystals were obtained by sucrose cushion centrifugation. Due to this being a gentle technique, it is likely that the contents of the DV lumen as well as membrane material were carried through the isolation process thus possibly contaminating the isolated crystals.

Haemozoin used in this study was isolated from purified DVs, as observed by TEM noted earlier in Chapter 4 (Figure 4.1 b), using trituration and freeze–thawing methods as detailed earlier in Chapter 2 in order to identify lipids associated with haemozoin. Isolated haemozoin was extensively washed with SDS, acetone/methanol and PBS solutions in order to remove all lipids associated with the surface of the crystals. During washing, liberated crystals were monitored by TEM (Figure 6.1) where, at the microscopic level, such crystals appeared to be free from cellular matter.

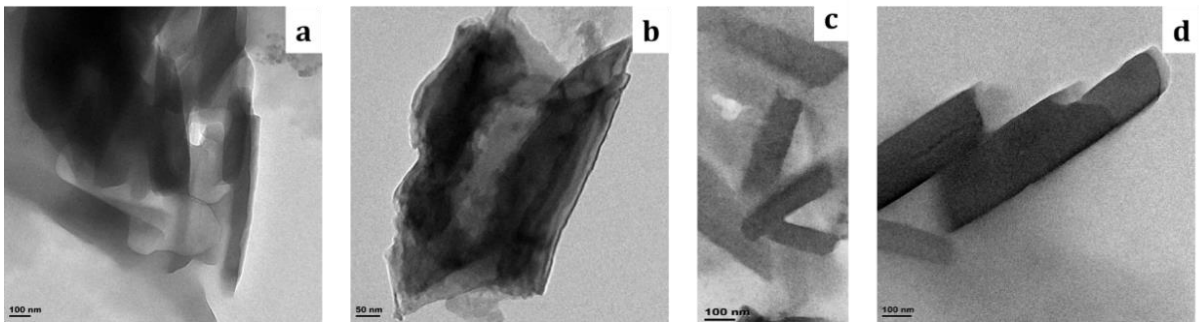

Figure 6.1. Transmission electron micrographs of haemozoin crystals isolated from the DVs of NF54 strain *P. falciparum.* (a) Haemozoin isolated following freeze-thaw cycles, **(b)** crystals during the washing process and **(c and d)** following extensive washing with organic solvents and buffer.

It is important to bear in mind that, as observed in proteomic studies of haemozoin (Chapter 4), like proteins, it is possible that lipids may have been carried through the isolation process thus acting as a source of contamination. Even though haemozoin crystals were isolated from purified DVs, it is probable that RBC as well as DVM could strongly adhere to the surface of the crystals thereby influencing the lipid content associated with the surface of haemozoin. This premise also applies to the study carried out by Pisciotta *et al* where lipids examined were, in fact, mostly surface-associated and may not provide a true reflection of the lipid material exclusively associated with haemozoin at the time of formation.

Lipids extracted from washings using organic solvents were subjected to separation by TLC utilising a two-phase solvent system previously reported by Pisciotta *et al*, first to separate phospholipids followed by separation of neutral lipids as described in Section 6.2.1. Lipids were visualised on TLC plates with Primuline, a non-destructive fluorescent lipophilic stain.[355] TLC analysis representing the washings of haemozoin crystals were conducted until there were no detectable lipids associated with the surface (Figure 6.2) after which extensively washed crystals were dissolved using 0.1 M NaOH. The above-mentioned shortfalls with respect to contaminating external lipids were addressed by utilising this extensive washing process which finally released material occluded by haemozoin, thereby providing a more pristine and reliable sample of the lipids present at the time and site of haemozoin formation.

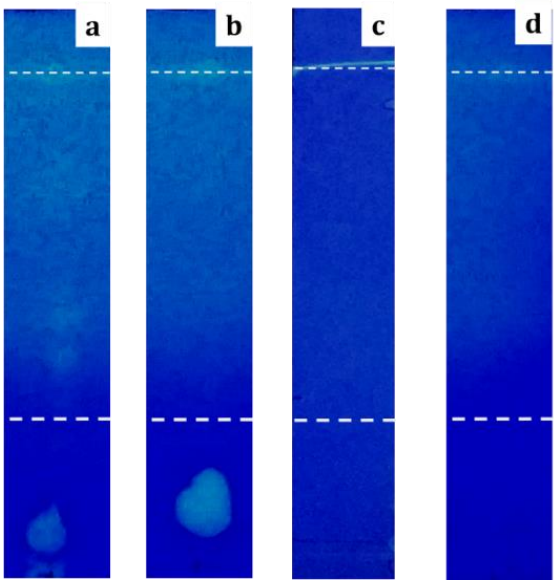

Figure 6.2. TLC plates representing lipids extracted from various washings of haemozoin. Lipids extracted from the **(a)** second and **(b)** fifth washings of isolated haemozoin crystals using a 4% SDS (*w/v*) solution, **(c)** second wash with acetone/methanol (1:9 *v/v*) and **(d)** final wash with PBS.

Since glycerolipids were previously thought to be the major component of haemozoin related lipids, several glycerolipid standards were separated using this two-phase TLC system described above (Figure 6.3 a-f). Considering the trafficking of RBC content to the DV, cholesterol and cholesterol ester (CE) standards were run alongside for comparison (Figure 6.3 g and h). Analysis of lipid standards showed there to be distinct differences between the retention factor (R_f) of monoacyl-, diacyl- and triacylglycerols; however, overlap between cholesterol and cholesterol ester with diacyl- and triacylglycerols respectively was observed. The schematic in Figure 6.4-a illustrates the TLC observations where cholesterol and DPG exhibit a similar R_f and CE appeared to migrate along with the second solvent front, having a similar R_f to that of triacyglycerols.

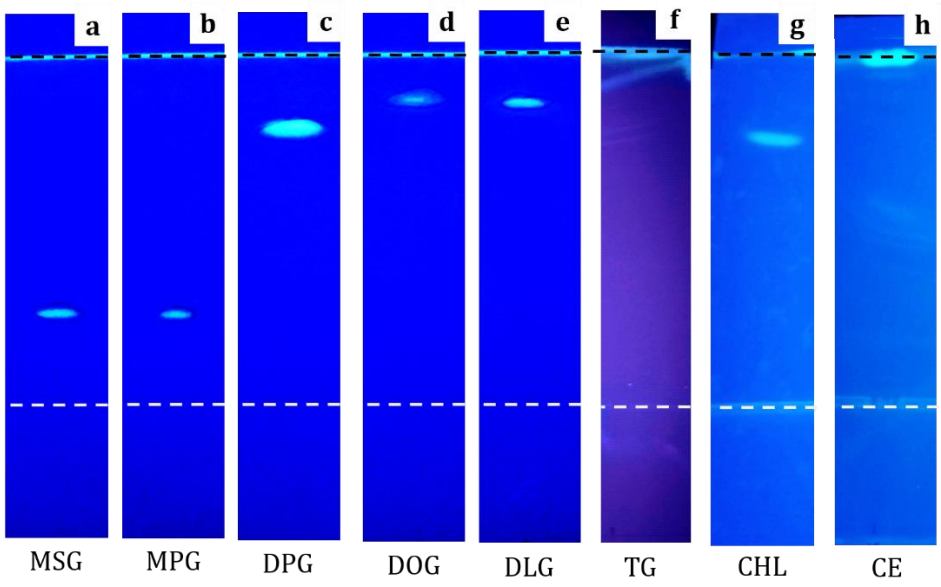

Figure 6.3. TLC silica plates of glycerolipid and sterol standards stained with Primuline and visualised under UV-vis. (a) Monostearoylglycerol, MSG, **(b)** monopalmitoyl glycerol, MPG, **(c)** dipalmitoyl glycerol, DPG, **(d)** dioleoyl glycerol, DOG, **(e)** dilineoyl glycerol, DLG, **(f)** triacyl glycerol, TG, **(g)** cholesterol and **(h)** cholesteryl oleate, CE. First and second solvent fronts represented by white and black dashed lines, respectively.

Lipid material from 3.7×10^{11} haemozoin crystals was spotted onto TLC plates which were stained with Primuline after separation. This translated to approximately 7 μmol haem present in the 2 μL aliquot containing crystals which in turn approximated to 2.7×10^{-3} nmol (951 ng) of lipid dispensed onto the plate which was within the detection limit of Primuline.[355] TLC analysis showed that the first washing off the surface of haemozoin comprised mainly phospholipids as well as what was initially thought to be diacylglycerols and triacylglycerols, with trace amounts of monoacylglycerols (Figure 6.4b).

These observations are similar to that reported by Pisciotta *et al*; however, the relative abundance of monoacylglycerols and diacylglycerols observed in the current study appeared to be lower and higher respectively and is likely as a result of the different methods used during isolation of haemozoin. However, since certain lipids were found to overlap (Figure 6.4a), what was initially thought to have been strictly diacylglycerols now appears to be a mixture of sterols and acylglycerols. Therefore, TLC could be used only to obtain a qualitative profile of the lipids associated with various fractions of haemozoin

prompting the use of a more sensitive technique like mass spectrometry to identify the specific lipids present.

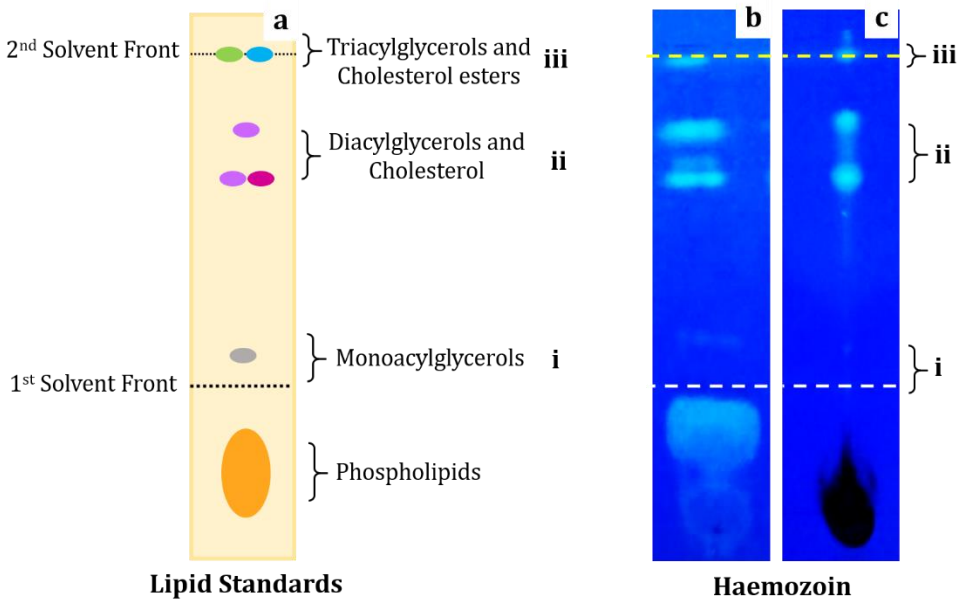

Figure 6.4. Comparison of lipid standards to the qualitative profile of lipids associated with haemozoin. (a) Schematic representing the migration patterns of various lipid standards by TLC. TLC silica plates illustrating the qualitative profile of lipids associated with haemozoin isolated from mature trophozoites. Separation of extracts **(b)** from the first washing and from **(c)** extensively washed crystals that were dissolved. First and second solvent fronts are represented by the white and yellow dashed lines, respectively.

Analysis of the organic phase indicates that haemozoin occludes mainly a mixture of neutral lipids, and not as much phospholipids as seen associated with the surface (Figure 6.4 b vs c). Dissolved haemozoin exhibited a unique lipid profile compared to the surface washing, indicating that the lipids occluded by the crystals are specific. In this case, potentially diacylglycerols and cholesterol (lipids denoted by area II of the TLC plate) seemed to be the most abundant whereas monoacylglycerols (area I) were the least abundant. Detectable amounts of lipid which could either be triacylglycerols, cholesterol esters or a combination of both denoted by area III were also found occluded by haemozoin.

To establish whether the absence of phospholipids in dissolved haemozoin was an artefact of headgroup dephosphorylation during the dissolution process under basic conditions and whether such conditions impacted the R_f of other lipids, phospholipid

standard, cholesterol ester standard and lipid extracts from parasite lysate were treated with 0.1 M NaOH. TLC analysis showed that the R_f of DOPC and CE remained the same showing that these lipids were not affected by treatment with base (Figure 6.5 a to d). Parasite lysate extracts continued to exhibit their characteristic phospholipid and neutral lipid TLC spots even after treatment with NaOH (Figure 6.5e and f).

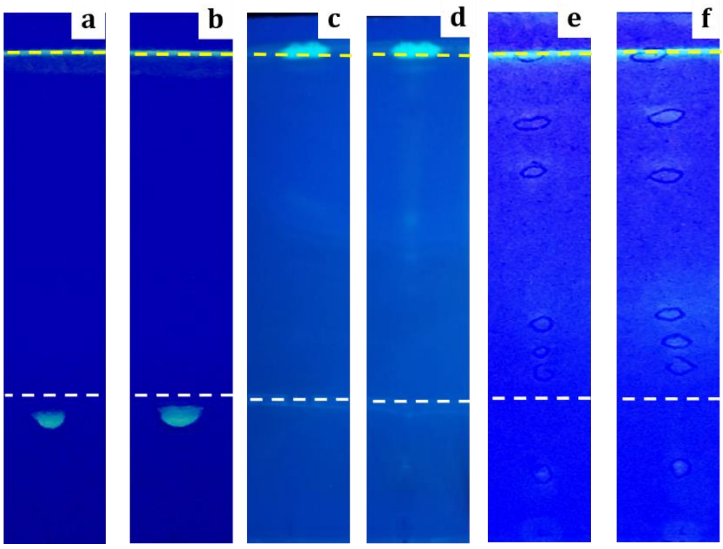

Figure 6.5. TLC plates illustrating the effect of 0.1 M NaOH on lipid standards and parasite lysate. Phospholipid standard, DOPC (a and b), cholesterol ester (c and d) and lipid extracts from parasite lysate (e and f) treated with (a, c, e) and without (b, d, f) base.

Transmission electron micrographs of isolated and washed haemozoin crystals reported by Ambele *et al* have supported the highly crystalline nature of these crystals and were shown to exhibit regular lattice fringes.[153] Although haemozoin is non-porous, it is probable that small amounts of lipid occluded by haemozoin are tolerated by the crystal and are unlikely to disrupt the crystal matrix.

To investigate the possibility that these glycerolipids were as a result of cell debris strongly adhering to the surface of crystals which could not be removed through extensive washing, β-haematin was chemically prepared in the absence of lipids. The crystalline material (Figure 6.6) was incubated in lipid extracts obtained from parasite lysate from which haemozoin was extracted. Incubated β-haematin was subjected to extensive washing and processed in the same manner as for natural haemozoin. Surface washings from β-haematin crystals exhibited a similar lipid profile to that observed for haemozoin

even though the neutral lipid spots appeared to be far weaker (Figure 6.7a). Extensively washed β-haematin crystals which were then dissolved exhibited no lipids on the TLC plate (Figure 6.7b). These findings definitively show that the neutral lipids detected to be occluded by haemozoin crystals were not simply strongly adhered to the surface. A similar profile was observed for regions I to III as seen in Figure 6.4 b and c.

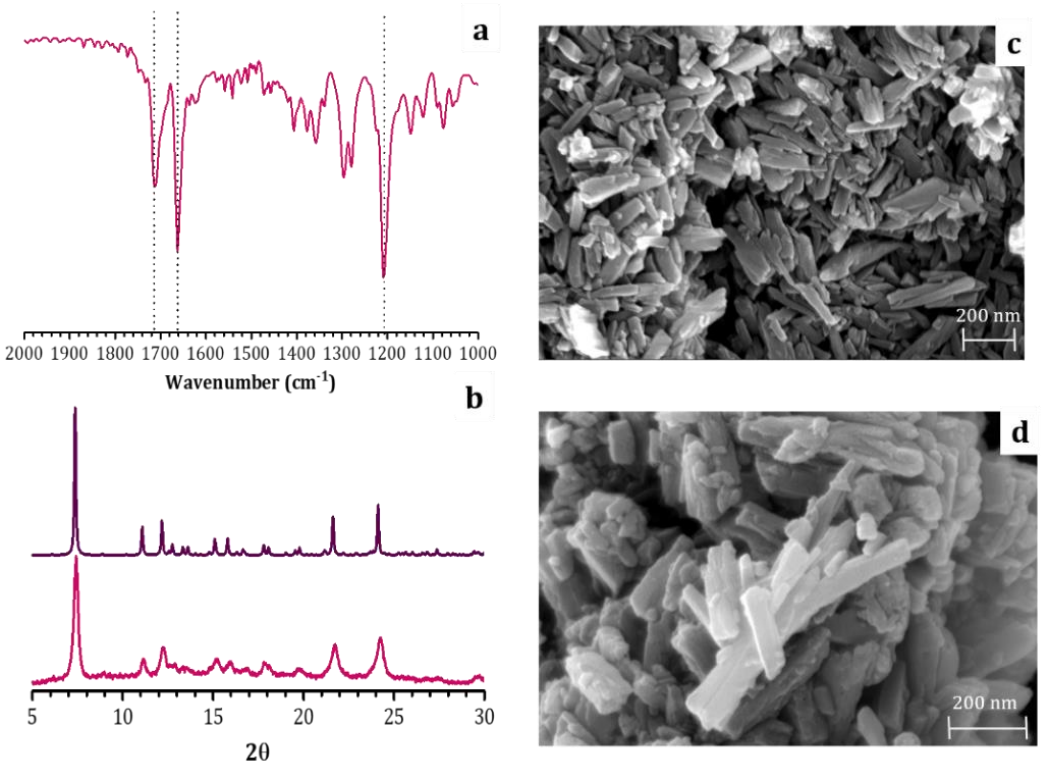

Figure 6.6. Characterisation of β-haematin synthesised from acetate buffered solution. (a) Infrared spectrum showing characteristic signals at 1712 cm^{-1}, 1665 cm^{-1} and 1207 cm^{-1} confirming formation of product. **(b)** Powder x-ray diffraction pattern and **(c, d)** scanning electron micrographs illustrating crystallinity. Calculated pXRD pattern from the reported crystal structure shown in purple and the observed in pink.[70]

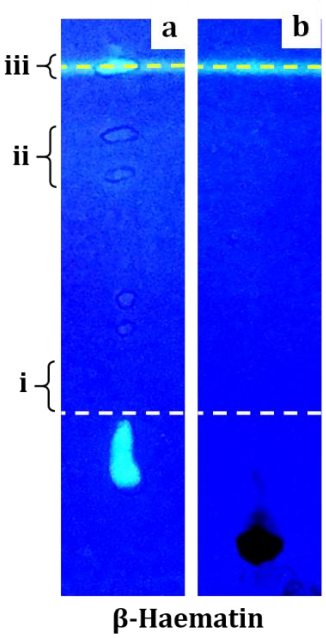

Figure 6.7. TLC silica plates illustrating the lipid profile associated with synthesised β-haematin. Lipid extracts obtained from β-haematin synthesised using the acetate method that had been exposed to parasite lysate. Separation of extracts **(a)** from the first washing and **(b)** from extensively washed and dissolved crystals. First and second solvent fronts are represented by the white and yellow dashed lines, respectively.

A similar approach to that employed in Chapter 5 to test whether proteins can be occluded by haemozoin was used to determine whether lipids can do the same. NBD-labelled cholesterol was used in this study where the fluorescent NBD moiety allowed for visualisation by fluorescence. Preformed β-haematin crystals incubated with NBD-cholesterol was shown to have adsorbed a certain amount of the labelled lipid as it was observed to have specifically washed off the surface with acetone/methanol following a wash with acetate buffer (pH 5.2). Following extensive further washing with acetone/methanol and PBS, these crystals were dissolved in 0.1 M NaOH. TLC of dissolved haemozoin illustrated there was no further NBD-cholesterol that was released (Figure 6.8a- Lane 4).

In contrast, β-haematin synthesised in the presence of NBD-cholesterol revealed that the labelled lipid could be released off the surface in the first acetone/methanol wash (Figure 6.8b- Lane 1). Following extensive washing with organic solvent and PBS buffer, base dissolution of these crystals further released easily detectable NBD-cholesterol (Figure 6.8b- Lane 4). Similar to the experiment with preformed β-haematin, isolated haemozoin crystals were exposed to labelled cholesterol and similar trends were

observed. The NBD-cholesterol appeared to have adsorbed to the crystals but, after washing, was released with no further lipid present upon base dissolution (Figure 6.8 c- Lane 1 vs 4).

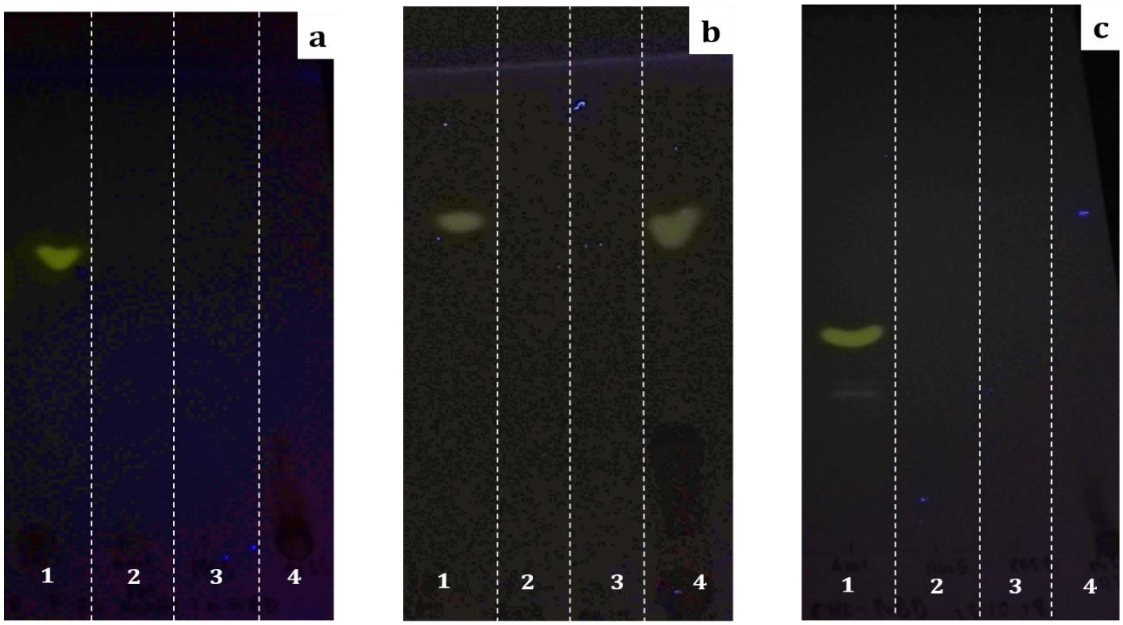

Figure 6.8. TLC analysis of the association of fluorescently labelled cholesterol with β-haematin and haemozoin. (a) TLC of β-haematin incubated with NBD-cholesterol, **(b)** β-haematin made in the presence of NBD-cholesterol and **(c)** haemozoin incubated with NBD-cholesterol. Key: 1st wash with acetone/methanol (lane 1), 5th wash with acetone/methanol (lane 2), 3rd wash with PBS (lane 3) and dissolved crystals (lane 4).

These findings demonstrate that lipids are adsorbed by haemozoin and β-haematin but are not occluded by preformed crystals and that lipids were adsorbed strongly enough that they were not easily displaced when washing with the buffer; however, they were completely displaced by washing with the organic solvent. However, when β-haematin was prepared in the presence of this molecule, such biomolecules were only released upon dissolution of the crystals. In addition, these findings also show that material is occluded in a non-exchangeable manner with the external milieu. Slit-shaped macropores have been reported to be present in β-haematin.[365] However, these seem to be unlikely candidates as potential sites of occlusion since these appear to be spaces between individual crystals which ought to be relatively accessible to exchange.

6.3.2. Identification of Lipids Occluded by Haemozoin

6.3.2.1. Lipidomics based MS approach to identify lipids occluded by haemozoin

LC-tandem MS was employed in the lipidomics analysis of haemozoin isolated from *P. falciparum* according to the experimental workflow illustrated in Figure 6.9. The most significant technological advancement provided by this technique has been the ability to measure precise concentrations of the analytes present. Precursor scanning and neutral loss scanning were amongst the well-established LC-MS methods used for quantification that have been previously applied to other biomolecules like proteins.

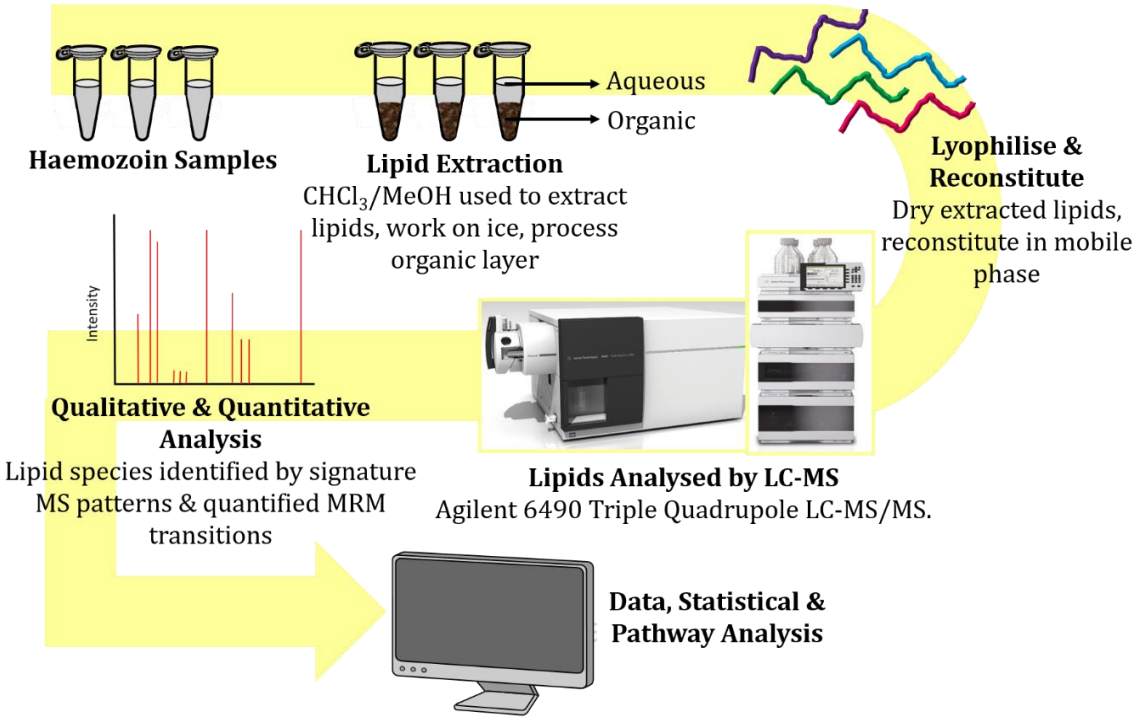

Figure 6.9. LC-MS approach used for profiling lipids occluded by haemozoin. Lipids were extracted from extensively washed haemozoin crystals ($N = 6$) using organic solvents, lyophilised and processed using LC-MS which afforded qualitative and quantitative profiles. Lipids were quantified by MRM transitions optimised by the method of Chan *et al.*[357]

For the purposes of the current study, the focus was on MRM transitions. MRM is a non-scanning spectrometric technique achieved only with triple quadrupole mass spectrometers. MRM transitions are highly sensitive and extremely selective towards the

target analyte since it utilises two different mass filters to produce precursor and fragment ions, generating unique *m/z* values for quantification.

The aim of this lipidomics study was to identify and quantify lipids associated with, or occluded by, haemozoin crystals. Previously reported LC-MS methods were used and are rationalised two-fold; firstly on the advanced technology available for such analysis and, secondly, on the method used for quantification.[203]

Mass spectrometric analysis of extracted lipids proceeded using a 6490 LC-MS (Agilent Technologies) which offered the technological innovation needed for the meticulous measurements required. Liquid phase fractionation was performed prior to MS analysis using optimised solvent systems for mapping of the full lipidome comprising phospholipids, sphingolipids and neutral lipids as described in Section 6.2.2.2. Following fractionation, lipid extracts were ionised using Jet Stream technology which increased sample signal intensity thus allowing a triple quadrupole to detect above femtogram levels of the analyte after which the generated ions enter a hexabore capillary (Figure 6.10). A triple quadrupole MS reduced chemical noise in the accompanying LC-MS system more significantly than a single quadrupole would. From the hexabore capillary, the ions passed through a dual ion funnel where the first funnel which was under high pressure (7-14 Torr), propelled ions forward followed by the low pressure (1-3 Torr) funnel which then encouraged ion enrichment.[366]

The ions then progressed through the octopole ion guide which provided high efficiency transmission over a wider mass range. The ion transfer optics carefully selected ions and reduced contamination after which the sample was filtered through the first quadrupole mass filter (MS1) which produced precursor ions that corresponded to the target mass which proceeded to the collision cell which, due to its curvature, maximised ion transmission over a wider mass range. The curved collision cell's linear axial acceleration ensured rapid MS/MS fragmentation with high sensitivity. Selected ions were then further filtered through the second quadrupole mass filter (MS2) which produced fragment ions that were detected in either positive or negative mode using a detector modified for improved signal conversion.

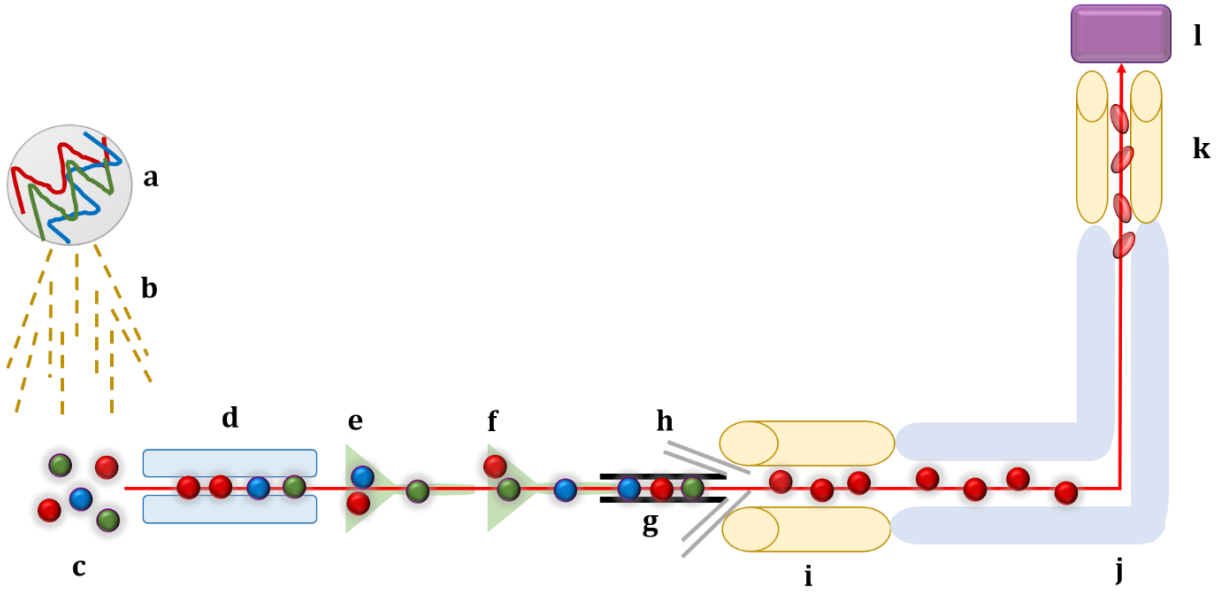

Figure 6.10. Schematic representing LC-MS technology designed by Agilent Technologies used in the current lipidomics study. Lipid extract (a), Jet Stream ionisation (b), ionised lipid sample (c), hexabore capillary (d), 1st ion funnel (e), 2nd ion funnel (f), octopole (g), optic lens (h), quadrupole mass filter- MS1 (i), curved collision cell (j), quadrupole mass filter- MS2 (k) and mass detector (l).

Ions were then quantified by MRM transitions, a method previously used for proteins but which has been modified and optimised, making it unique to lipid analysis as described in studies carried out by Chan *et al* and Shui *et al*.[367,368,357,369] Applying any technique to lipids was challenging and required method development since, in general, these molecules are more complex to work with and more often than not generate immense noise and signal overlap due to the various head groups and fatty acid chains.

Briefly, lipid standards were initially quantified by MRM transitions and pre-screened based on unique *m/z* values and their specific retention times. A MS spectrum comprising signals from the target lipid as well as background ions was first generated. All ions passed through the octopole and MS1 and only the target ion proceeded (precursor ion) with all other contaminants filtered out. The precursor ion then proceeded through the collision cell where a characteristic fragmentation pattern was generated. Specific fragments then proceeded to MS2 where intense signals characteristic of a particular analyte were used to quantify the species providing absolute quantification, and a mass signal confirmed the identification. This level of selectivity removed the chemical background and reduced interference. Only analytes that coincided with the specific

precursor-fragmentation ion pair were isolated by the mass spectrometer where a signal was detected thus minimising chemical noise. These data were generated for each lipid standard and used to create tables within the software prior to analysis of complex lipid extracts.

6.3.2.2. Profile of lipids associated with haemozoin

Mass spectrometry-based lipidomics was employed to identify and quantify lipids associated with and occluded by haemozoin (See Appendix for a complete list of lipids identified). Parasite isolates were obtained following the same process used in the proteomics study discussed in Chapter 4, Section 4.3.1. Even though mature trophozoites (NF54 strain of *P. falciparum*) were isolated by saponin treatment of pRBCs which is known to disrupt RBC membranes whilst maintaining the structural integrity of the parasite, RBC ghosts were likely to have remained following lysis. DVs were released by trituration thereby affording a fraction of the trophozoite cytoplasm. In the case of trophozoite cytoplasm, is it likely that this fraction may contain traces of intact DVs that were carried through the isolation process. Lipids were then extracted from RBCs, T_{CYT}, the first haemozoin wash and dissolved crystals. Those lipids weakly associated with the crystal surface and occluded by haemozoin are denoted as Hz_{SL} and Hz_{Dis}, respectively.

Lipidomics analysis identified over 800 lipid species across various samples which were categorised into phospholipids, sphingolipids and neutral lipids constituting the three major lipid classes. Phospholipids are essential to membrane development playing a predominantly structural role at the cellular level.[370] These lipids are characterised by the presence of a phosphate head group and two fatty acid residues attached to a glycerol molecule (Figure 6.11a). Each phospholipid attains its unique structure and properties by incorporating chemical moieties such as choline or ethanolamine which modify the head group, thereby generating a variety of species such as phosphatidylcholine and phosphatidylethanolamine.

Sphingolipids are characterised by their 18-carbon amino alcohol backbone, often referred to as sphingosine. Creation of an *O*-link attaches charged head groups such as ethanolamine to the sphingosine backbone during cellular or synthetic processes, resulting in the formation of an array of complex lipids (Figure 6.11b). Sphingolipids play

a key role in membrane fluidity as well as cell growth in addition to contributing to cell structure and membrane signalling, making the combination of phospho- and sphingolipids crucial to any living system.[204] Neutral lipids on the other hand are commonly known as 'simple lipids' and are molecules that lack charged groups. This specific group of lipids are sequestered from the cytosol and, due to their non-polar nature, tend to aggregate within the cell forming dense lipid droplets or bodies. These lipid bodies act as a reservoir to meet the energy and nutrient demands of the cell.[371] Neutral lipids are made up of cholesterol, cholesterol esters and glycerolipids (Figure 6.11c) which differ in structure and exhibit dynamic properties within cells.

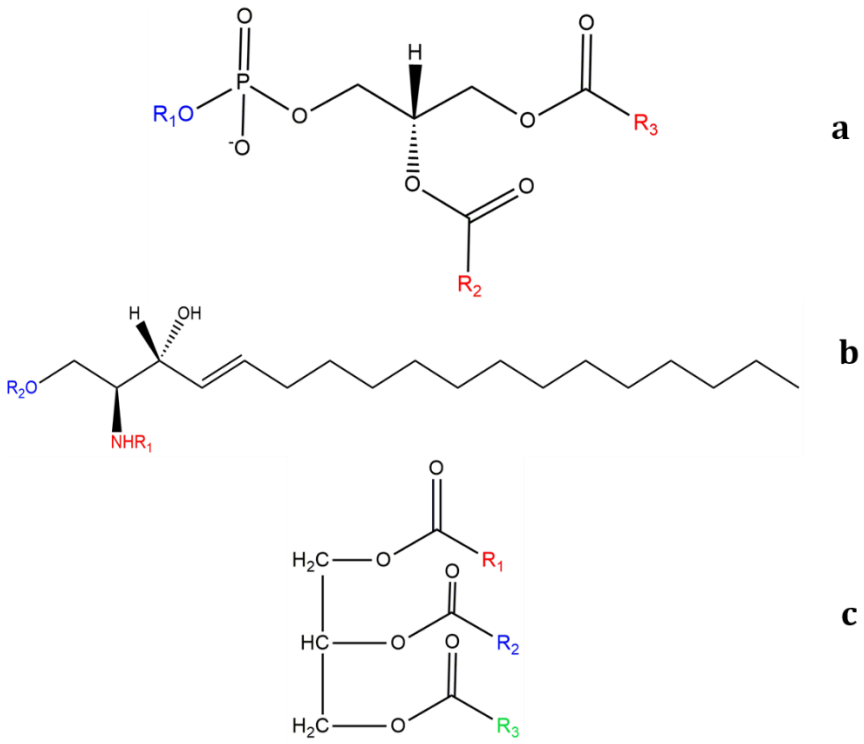

Figure 6.11. General lipid structures representing the three major lipid classes. **(a)** Phospholipids with a modified polar head group (R_1) and fatty acid chains (R_2 and R_3). **(b)** Sphingolipids comprise a sphingosine backbone, fatty acid residue (R_1) linked to a charged head group (R_2) and **(c)** triglycerides comprise a glycerol backbone and fatty acid residues (R_1- R_3). Fatty acids are of variable lengths and degrees of saturation.

Pooled samples of uninfected RBCs were used as control cells and subjected to lipidomic analysis which afforded a distribution of the three major lipid classes as shown in Figure 6.12a. Neutral lipids accounted for 75% of total RBC lipid content with phospho-

and sphingolipids together comprising the remaining quarter. Cholesterol was found to dominate the neutral lipid class accounting for approximately 98% (Figure 6.12b) and the measured amount of 199 ± 39.9 nmol/mg was found to be within range of that previously reported.[372, 373] The remaining fraction consisted of 60% acyl carnitine and trace amounts of cholesterol esters and acylglycerols The most abundant phospholipid constituents detected in RBCs were phosphatidylcholine (PC), phosphatidylethanolamine (PE) and plasmalogen phosphatidylethanolamine (PEp) which accounted for approximately 85% of detected phospholipids whereas sphingomyelin (SM) was observed to be the dominant sphingolipid pertaining to that lipid class. The overall lipid distribution indicated that RBCs are made up of equal parts of cholesterol and phospholipids by weight which is in agreement with the reported composition of the RBC membrane.[374]

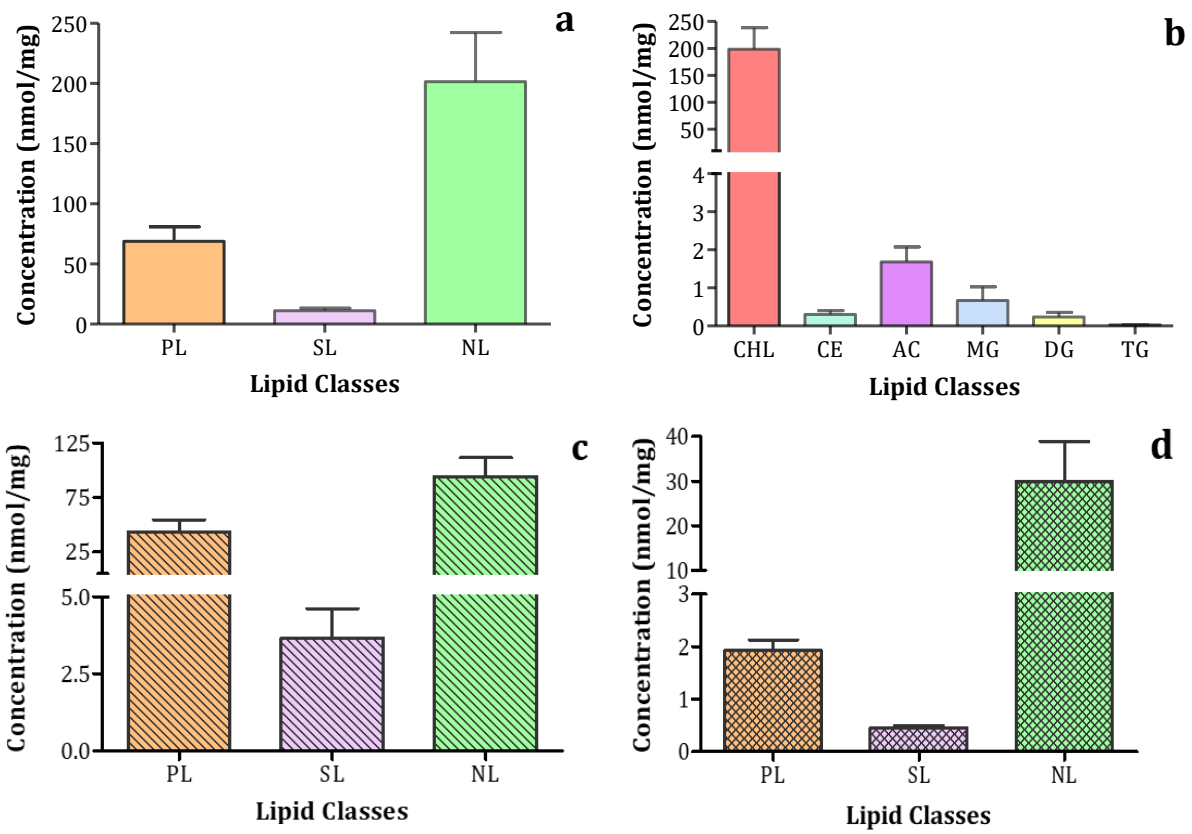

Figure 6.12. Global distribution of phospho-, sphingo- and neutral lipids from control cells and haemozoin extracts. (a) General lipid profile and **(b)** detected neutral lipids from red blood cell extracts. Material **(c)** weakly associated with the surface of and **(d)** in dissolved haemozoin material. Key: Phospholipids (PL), sphingolipids (SL) and neutral lipids (NL), cholesterol (CHL), cholesterol esters (CE), acyl carnitine (AC), monoacylglycerols (MG), diacylglycerols (DG) and triacylglycerols (TG). Units = nmol/mg total cell protein.

Lipidomics analysis identified 405 lipid species that were weakly associated with the surface of haemozoin and revealed that approximately 66% consisted of neutral lipids comprising cholesterol, cholesterol esters, acyl carnitines and glycerolipids. Phospholipids made up 90% of the remaining lipids with sphingolipids comprising the rest (Figure 6.12c). It is noteworthy to mention that, with respect to surface lipids, this may not only represent lipids directly associated with the surface of crystals but rather a combination including possible RBC and DV membranes that may have been carried through the isolation process.

The overall distribution of lipid classes in Hz_{Dis} exhibited a similar trend to Hz_{SL} where neutral lipids were observed to be the most abundant class, also consisting of cholesterol, cholesterol esters, acyl carnitines and glycerolipids contributing approximately 94%. The remaining portion of lipids in dissolved material comprised 80% phospholipids with trace amounts of sphingolipids (Figure 6.12d). The most abundant phospholipid constituents present in Hz_{SL} and Hz_{Dis} were phosphatidylcholine and phosphatidylethanolamine whereas sphingomyelin was observed to be the dominant sphingolipid similar to that observed for RBCs. Interestingly, phosphatidylinositol was found to be amongst the abundant phospholipids in Hz_{SL} with amounts approximately 20-fold higher than RBCs. Based on the earlier results that demonstrated that haemozoin occludes biomolecules in a non-exchangeable way, occluded material best represents the lipids actually present during haemozoin formation.

Comparison of Hz_{SL} to RBCs illustrated notable decreases in the amount of PE, PEp and SM detected in the haemozoin-associated material, whereas PC remained relatively constant. Phospholipids detected in Hz_{SL} was found to be 7-fold higher compared to Hz_{Dis}. As this former material is representative of lipids associated with the surface, this could possibly also represent what was present within the DV therefore suggesting that the crystals may be in close contact with the inner membrane of the DV, a concept initially hypothesised by Kapishnikov *et al*.[151]

A closer look at the most abundant phospho- and sphingolipid species present revealed three lipids accounted for 49% of total detected phosphatidylcholines, one with saturated fatty acid residues and the other two with unsaturated fatty acid residues, with the remainder made up of minor amounts comprising 47 other lipids (Table 6.3). Four lipids, three of which contain unsaturated fatty acids and one plasmalogen

phosphatidylethanolamine, accounted for 46% of total detected phosphatidylethanolamines with the remainder consisting of smaller amounts of 35 other lipids. Sphingolipids comprised 73% sphingomyelin, 25% ceramides and 2% trace amounts of other detectable sphingolipids. The single, most abundant sphingomyelin consisting of an oleic acid attached at the C_1 position and a palmitic acid attached at the C_2 position accounted for 62% of sphingomyelins. PC 34:0 and PE 38:4 were the most abundant phospholipid species detected across all fractions (Figure 6.13 a and b) whereas SM d18:1/16:0 (Figure 6.13c) was the most abundant sphingolipid species present, yet only trace amounts were detected in Hz_{Dis}.

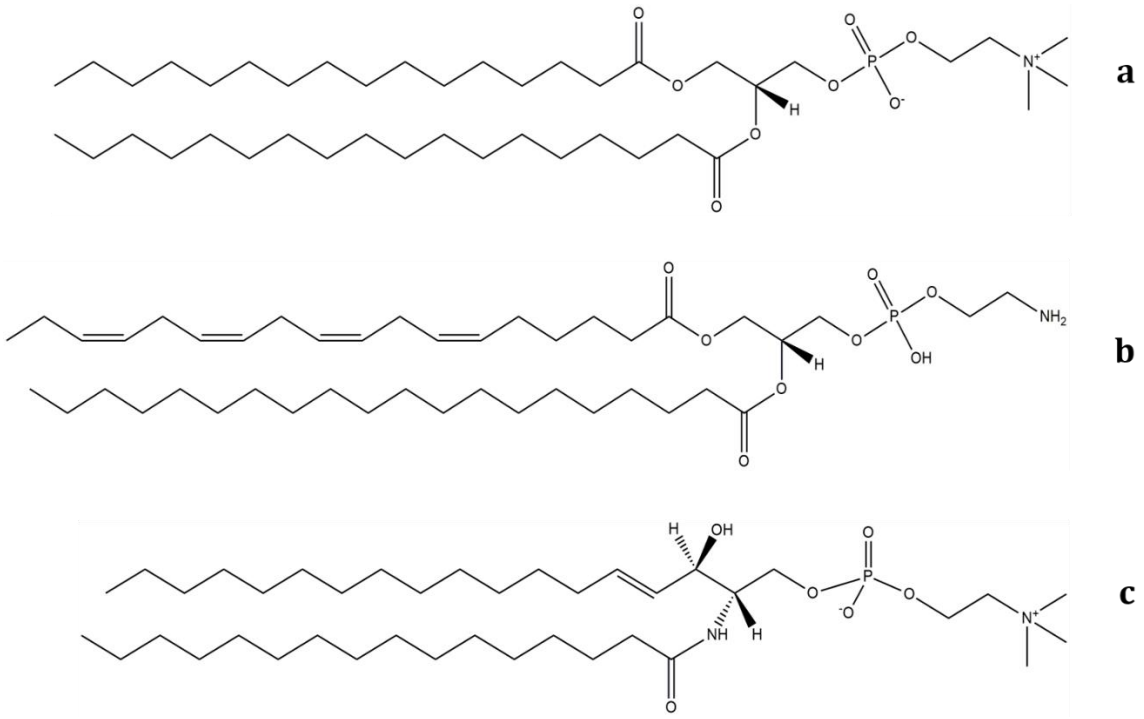

Figure 6.13. Chemical structures of the most abundant species making up the dominant phospho- and sphingolipids detected and measured by lipidomics. (a) Phosphatidylcholine 34:0, **(b)** phosphatidylethanolamine 38:4 and **(c)** sphingomyelin d18:1/16:0.

Fewer lipids were detected in material occluded by haemozoin where 385 lipid species were identified by lipidomics with diminished amounts of phospholipids and sphingolipids. A closer look revealed that phosphatidylcholines and phosphatidylethanolamines were the dominant phospholipid classes accounting for 41% and 25%, respectively. Three lipids, one with saturated fatty acid residues, and the other

two with unsaturated fatty acid residues accounted for 56% of total detected phosphatidylcholines with the remainder made up of minor amounts of 22 other lipids (Table 6.4). Three lipids, one with saturated fatty acid residues and the other two with unsaturated fatty acid residues accounted for 35% of total detected phosphatidylethanolamines with the remainder consisting of lesser amounts of 36 other lipids.

Table 6.3. Abundant lipids associated with the surface of haemozoin

Lipid Class	No. lipid species identified	Most abundant lipid(s)	Concentration (nmol/mg)[a]
Phosphatidic acid	24	PA 30:0	0.003 ± 0.0009
Phosphatidylcholine	50	PC 32:0	4.5 ± 1.3
		PC 34:1	3.5 ± 0.8
		PC 34:2	2.3 ± 0.8
Phosphatidylethanolamine	39	PE 34:1	2.2 ± 0.5
		PE 34:2	2.4 ± 0.6
		PE 36:4	1.5 ± 0.4
		PEp 38:4	0.5 ± 0.1
Phosphatidylserine	17	PS 36:1	0.1 ± 0.03
Other phospholipids	103	PI 34:1	1.0 ± 0.2
		PI 36:1	0.9 ± 0.2
		PI 36:2	0.8 ± 0.2
Ceramides	47	Cer d18:1/16:0	0.5 ± 0.1
		Cer d18:1/24:1	0.1 ± 0.05
Sphingomyelin	14	SM d18:1/16:0	1.2 ± 0.3
		SM d18:1/22:0	0.4 ± 0.1
		SM d18:1/24:0	0.4 ± 0.08
Other sphingolipids	22	GM3 d18:1/16:0	0.02 ± 0.005
Cholesterol	n/a	Free cholesterol	88.2 ± 16.2
Cholesterol esters	10	CE 18:2	0.8 ± 0.1
		CE 20:4	0.2 ± 0.08
		CE 18:1	0.3 ± 0.03
Acyl carnitine	6	AC C16:0	0.1 ± 0.04
Monoacylglycerols	6	MG 16:0	0.1 ± 0.02
		MG 18:0	0.09 ± 0.03
		MG 18:1	0.08 ± 0.002
		MG 18:2	0.07 ± 0.02
Diacylglycerols	29	DG 34:1/16:0	0.7 ± 0.1
		DG 34:2/16:0	0.7 ± 0.1
		DG 36:1/18:0	0.4 ± 0.09
		DG 32:0/16:0	0.3 ± 0.09

		DG 34:0/16:0	0.2 ± 0.05
		DG 36:0/18:0	0.1 ± 0.03
Triacylglycerols	38	TG 48:0/16:0	0.1 ± 0.03
		TG 48:1/16:0	0.1 ± 0.05
		TG 50:3/16:1	0.09 ± 0.05
		TG 52:3/18:1	0.08 ± 0.03

[a] Expressed per mg total parasite protein

Table 6.4. Abundant lipids in dissolved haemozoin

Lipid Class	No. lipid species identified	Most abundant lipid(s)	Concentration (nmol/mg) [a]
Phosphatidic acid	24	PA 36:1	0.0005 ± 0.00005
Phosphatidylcholine	25	PC 32:0	0.1 ± 0.02
		PC 34:1	0.2 ± 0.04
		PC 34:2	0.1 ± 0.02
Phosphatidylethanolamine	39	PE 38:0	0.05 ± 0.01
		PE 38:1	0.04 ± 0.02
		PE 38:4	0.08 ± 0.02
		PEp 40:6	0.06 ± 0.01
Phosphatidylserine	17	PS 40:6	0.07 ± 0.01
Other phospholipids	123	PI 38:4	0.02 ± 0.003
Ceramides	12	dhCer d18:0/16:0	0.003 ± 0.0004
Sphingomyelin	12	SM d18:1/16:0	0.1 ± 0.007
		SM d18:1/24:0	0.06 ± 0.009
Other sphingolipids	58	Sulf d18:0/16:0	0.004 ± 0.0005
Cholesterol	n/a	Free cholesterol	28.9 ± 8.9
Cholesterol esters	9	CE 18:1	0.1 ± 0.01
		CE 18:2	0.4 ± 0.06
Acyl carnitine	6	AC C18:1	0.02 ± 0.003
Monoacylglycerols	6	MG 16:0	0.05 ± 0.005
		MG 18:1	0.05 ± 0.005
Diacylglycerols	23	DG 34:1/16:0	0.01 ± 0.001
		DG 36:0/18:0	0.02 ± 0.004
		DG 36:2/18:1	0.02 ± 0.001
Triacylglycerols	32	TG 48:0/16:0	0.01 ± 0.003

[a] Expressed per mg total parasite protein

It was originally believed that phospholipids were important in haemozoin formation; however, later extensive research suggested haemozoin crystals to be in close proximity to lipid droplets thereby implicating neutral lipids, specifically acylglycerols, as mediators

in haemozoin formation.[139, 140, 143, 146] Owing to the ongoing debate as to which biological molecules are the key mediators in haemozoin formation as well as the uncertainty associated with phospholipids or glycerolipids being responsible for this crucial process, the current lipidomic study sought to track the neutral lipid profile across parasite fractions and to determine the set of lipids occluded by haemozoin crystals.

Neutral lipids were identified and measured in lipid extracts obtained from T_{CYT}, Hz_{SL} as well as Hz_{Dis} and were compared to RBCs. It must be noted that DG and TG species listed in Tables 6.3 and 6.4 are presented as the parent and most abundant daughter fatty acid chains since these acylglycerols do not produce distinctive daughter ions in the same way as seen for phospholipids. For example, in the case of DG 34:0/16:0, the number 34:0 represents the sum of both fatty acid chains present making this the parent ion, and 16:0 represents the most abundant daughter ion present in this lipid molecule. Distinct differences were observed in the neutral lipid content between control RBCs and material occluded by haemozoin. This emphasises that lipids detected were not merely as a result of contamination but was attributed to a unique neutral lipid profile exhibited by haemozoin occluded material, although the presence of contaminating lipids cannot be completely excluded.

The global neutral lipid profile obtained exhibited a decreasing gradient from RBCs to T_{CYT} and Hz_{SL} with Hz_{Dis} containing the least (Figure 6.14a). However, taken together, the combination of parasite fractions shows an increase in total lipid content compared to the RBC indicating enrichment by the parasite. Such enrichment in lipid concentration indicates that the parasite itself actively synthesises its own lipids whereas lipids that remain relatively constant indicates that such lipids are more likely to be scavenged. These differences probably reflect the fact that developing malaria parasites begin to scavenge host lipids as well as synthesise their own glycerolipids to meet the metabolic demands that accompany maturation therefore resulting in an increase in neutral lipid content as the parasite develops.[143, 203]

T_{CYT} comprises 91% cholesterol with the remaining neutral lipid content consisting of 62% acylglycerols in addition to cholesterol esters and acyl carnitine (Figure 6.14b). Diacyl- and triacylglycerols were detected in amounts that were more than an order of magnitude higher than that of RBCs (Figure 6.12b vs 6.14b). Relative to the RBC,

cholesterol esters exhibited a 12-fold increase whereas acyl carnitine remained relatively constant.

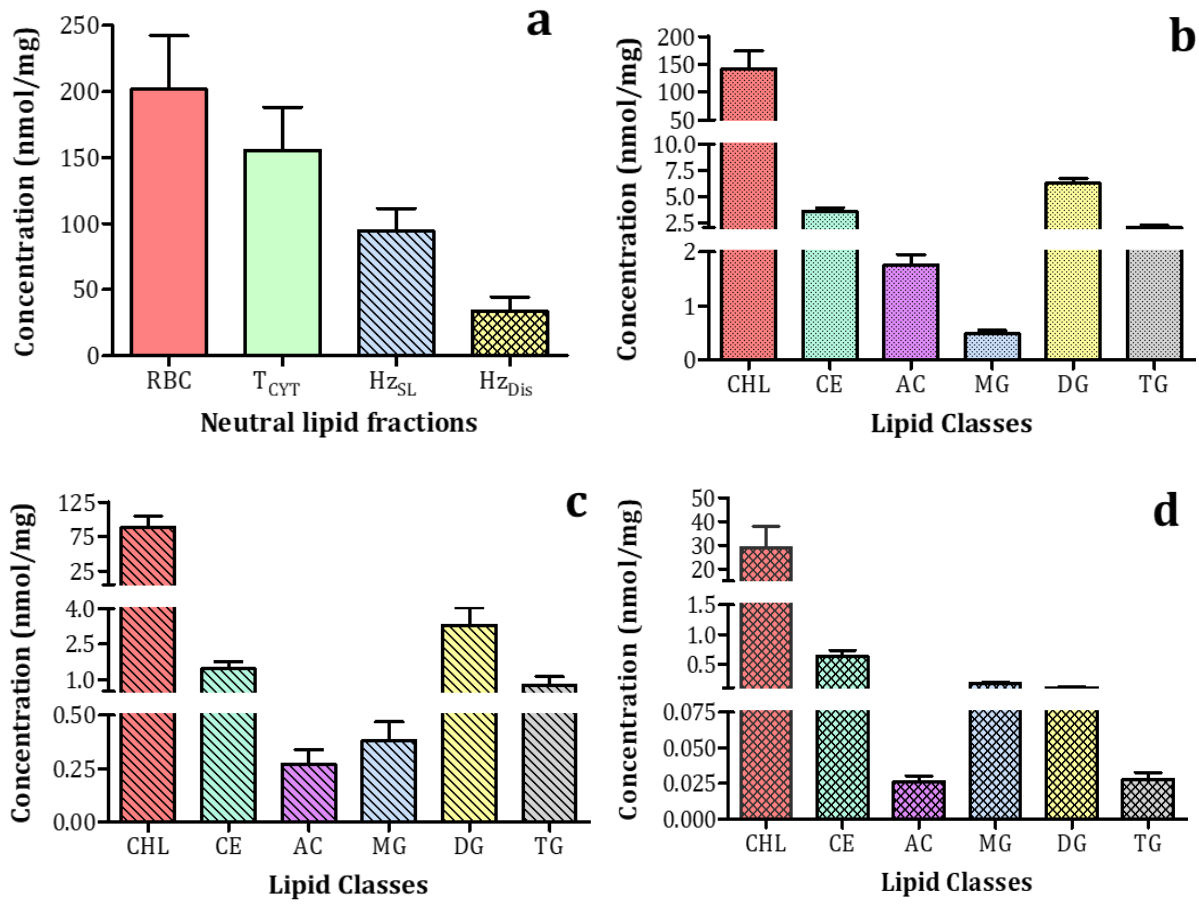

Figure 6.14. Neutral lipid profile across parasite fractions as measured by mass spectrometry. (a) Comparison of total neutral lipid content in parasite fractions and control RBCs. Distribution of neutral lipid species found in **(b)** trophozoite cytoplasm excluding the DV, material **(c)** associated with the surface of and **(d)** in dissolved haemozoin crystals. Key: Red blood cells (RBC), trophozoite cytoplasm (T_{CYT}), surface associated lipids (Hz_{SL}) and occluded lipids (Hz_{Dis}), cholesterol (CHL), cholesterol esters (CE), acyl carnitine (AC), monoacylglycerols (MG), diacylglycerols (DG) and triacylglycerols (TG). Units = nmol/mg total cell protein.

Neutral lipids associated with haemozoin will be discussed in two parts; firstly, those weakly associated with the crystal surface, followed by those occluded by the crystals. Weakly-associated neutral lipids consisted of 93% cholesterol; of the remaining lipids, 72% consisted of acylglycerols, 23% cholesterol esters and lesser amounts of acyl carnitine were detected (Figure 6.14c). A total of 405 individual lipid species were identified in Hz_{SL} with three unsaturated lipids accounting for 88% of the cholesterol esters (Table 6.4). With respect to the acylglycerols, diacylglycerols dominated this

component accounting for 55% whereas monoacylglycerols and triacylglycerols accounted for 6% and 12%, respectively. A closer look at these lipids at a species level revealed that four out of the six identified monoacylglycerols were present in similar amounts with one saturated lipid, monopalmitic glycerol, being the most abundant. Monoacylglycerols were previously reported to be in abundance with lesser amounts of diacyl- and even smaller amounts of triacylglycerols in a study that focused on haemozoin surface-associated lipids.[146] The current lipidomic data afforded a 1:1 ratio of monostearic glycerol (MSG) to monopalmitic glycerol (MPG) which is in contrast to the 2:1 ratio reported by Pisciotta *et al*. Focusing on the diacylglycerols, three unsaturated lipids account for 56% of those detected (Table 6.4). The higher levels of diacylglycerols compared to monoacylglycerols detected by mass spectrometry correlates with the TLC data presented earlier in this chapter. It is notable that smaller amounts of the distearic glycerol and 1-stearic-3-palmitic glycerol were detected in this study. Four triacylglycerols were present in similar concentrations where one was saturated and three unsaturated, accounting for 53% of those detected.

The key finding as presented in Section 6.3.1 showing that haemozoin and its synthetic counterpart, β-haematin, are able to occlude material in a non-exchangeable manner, emphasises the importance of identifying the lipid species present in dissolved haemozoin as this represents what was likely actually present at the time and site of formation. Focusing on the neutral lipids, cholesterol was by far the dominant component, constituting 96% of this class. Of the remaining 4%, about half consisted of cholesterol esters with the rest made up of monoacyl-, diacyl- and triacylglycerols. Acyl carnitines constituted a minor component (Figure 6.14 d).

In total, 386 individual lipids were identified in Hz_{Dis} with just two unsaturated lipids accounting for 83% of the cholesterol esters (Table 6.4). In the case of the monoacylglycerols, two specific lipids, one saturated and one unsaturated, made up 56% of those identified, while for the diacylglycerols three lipids, two saturated and one unsaturated, accounted for 44% of those detected. A single saturated lipid dominated the triacylglycerols accounting for 36% with the remainder made up of trace amounts of 31 other lipids. Notably, neutral lipids occluded by haemozoin are present in substantially lower amounts than those weakly associated with the crystal surface. Diacyl- and triacyglycerols appear to concentrate in Hz_{SL} whereas in the Hz_{Dis} fraction,

higher amounts of monoacyl- and diacylglycerols appear to be present in comparison to triacylglycerols (Figure 6.14c vs d).

It is well known that intraerythrocytic *P. falciparum* is unable to synthesise cholesterol *de novo* but, rather, obtain it from the host RBC membrane.[193, 375] Given that haemoglobin is transported from the RBC cytoplasm to the DV through the cytostome, it is probable that the parasite acquires cholesterol in a similar manner.[42] It is likely that the cholesterol esters are trafficked together with cholesterol, since they are also seen in the RBC membrane albeit at a fraction of the relative abundance compared to haemozoin occluded lipids.

LC-MS/MS successfully provided the sensitivity and accuracy required to identify the specific lipids present as well as quantify them whereas TLC provided a qualitative overview. Based on the finding that cholesterol comprises the majority of neutral lipid content occluded by haemozoin, one would have expected to have observed a single concentrated spot representing predominantly cholesterol and a second, less concentrated spot above it representing diacylglycerols by TLC reported earlier in this chapter. Similar patterns were observed; however, the diacylglycerol spot appeared to fluoresce more intensely. This at first unexpected observation can be explained by the characteristics of the fluorophore used and is not indicative of the concentration of cholesterol actually present in this case. Certain fluorophores, of which Primuline is an example, experience a great enhancement in their fluorescence emission upon interaction with analytes containing long hydrocarbon chains like diacylglycerols.[376] This phenomenon is significantly enhanced when the fluorophore has been irradiated using UV light at 365 nm and the sensitivity further increases upon application of silica gel as the adsorbent.[377, 378]

6.3.3. Mediation of β-Haematin Formation by Model Lipid Blend

Lipids that were found to be occluded by haemozoin in a non-exchangeable manner were investigated to determine their efficacy in facilitating crystal formation. By far the most abundant occluded lipid was cholesterol, which made up almost 90% of the total. This was explored by preparing a model lipid blend comprising the same ratio of specific neutral and phospholipids consisting of cholesterol and commercially available cholesterol ester, mono-, di- and triacylglycerols as well as phosphatidylcholine. Model blend A comprised 94.2% cholesterol, 2.2% cholesteryl oleate, 0.2% monoacylglycerols (consisting of monostearoylglycerol, monooleoylglycerol and monopalmitoylglycerol in a 1:1:2 ratio), 0.2% diacylglycerols (made up of equal parts dioleoylglycerol, dipalmitoylglycerol and dilineoylglycerol), 0.1% trioleoylglycerol and 3.1% phosphatidylcholine.

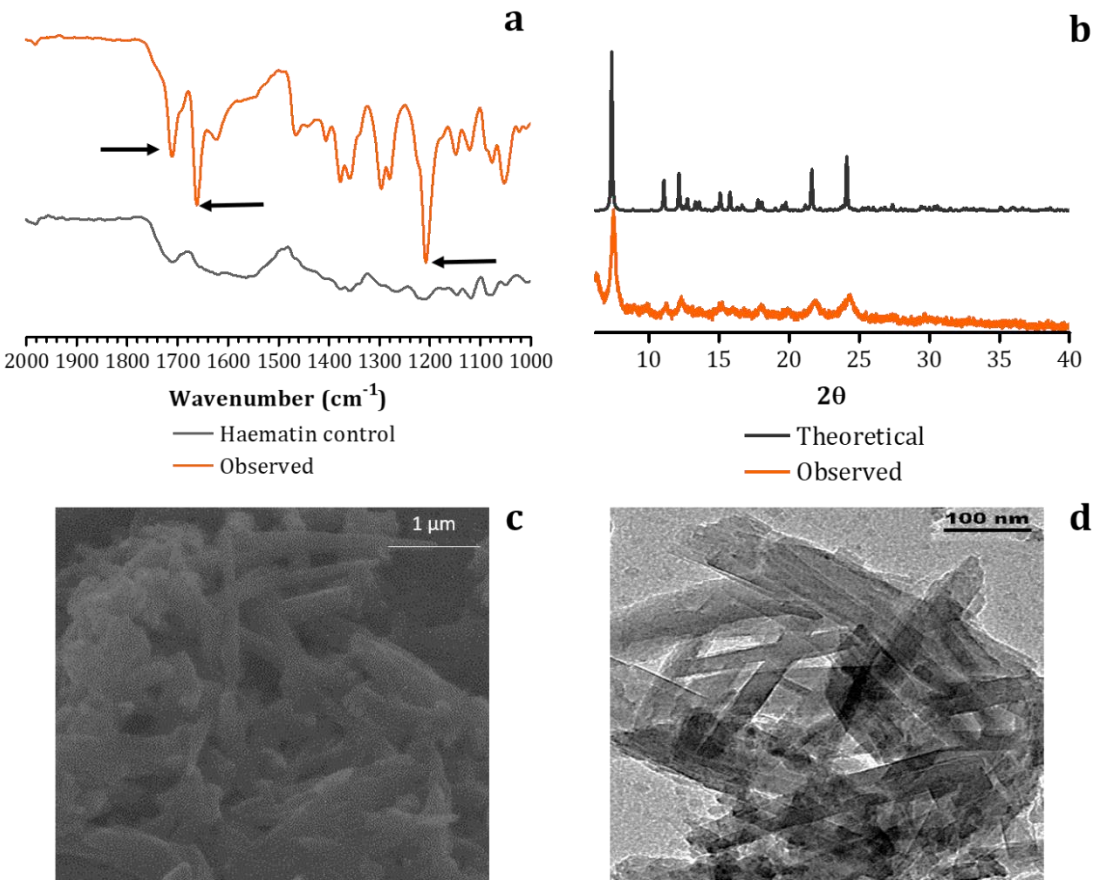

Figure 6.15. Characterisation of β-haematin synthesised using model lipid blend A. (a) FT-IR spectrum showing characteristics peaks at 1207 cm^{-1}, 1665 cm^{-1} and 1710 cm^{-1}. **(b)** Calculated and observed pXRD patterns confirming crystallinity. **(c)** Scanning and **(d)** transmission electron micrographs showing crystal morphology.

This unique lipid blend that closely mimics the lipids specifically occluded by haemozoin discovered in the above mentioned lipidomics study successfully produced β-haematin in aqueous medium in greater than 90% yield as measured from the unconverted Fe(III)PPIX determined by UV-visible spectroscopy as a pyridine complex. To confirm the identity of the synthesised material, FT-IR spectroscopy, pXRD as well as TEM and SEM were performed. All techniques confirmed the formation of β-haematin (Figure 6.15). The crystals produced by this blend were very similar to natural haemozoin in external morphology.

Omission of the phospholipid component from blend A (Table 6.5), affording blend B, resulted in a significant decrease in yield, but the overall yield remained above 70% (Figure 6.16a). Further removal of the acylglycerols (Table 6.5), affording blend C, had little additional effect on the resulting yield (Figure 6.16a). Removal of the cholesterol ester from blend B while retaining the acylglycerols afforded blend D. This produced a similar yield of β-haematin to blends B and C. Omission of only the cholesterol ester from the original model to produce blend E also resulted in a reduced yield, although the reduction was somewhat smaller than in the other cases (Figure 6.16a). Omission of all lipid components other than cholesterol (blend F) completely abolished its ability to mediate β-haematin formation with the observed inactivity of cholesterol being consistent with previous reports.[148]

Table 6.5. Constituents of model blends used to investigate β-haematin formation

Lipids	Blend A	Blend B	Blend C	Blend D	Blend E	Blend F
Cholesterol	+	+	+	+	+	+
CE	+	+	+	-	-	-
MG	+	+	-	+	+	-
DG	+	+	-	+	+	-
TG	+	+	-	+	+	-
PC	+	-	-	-	+	-

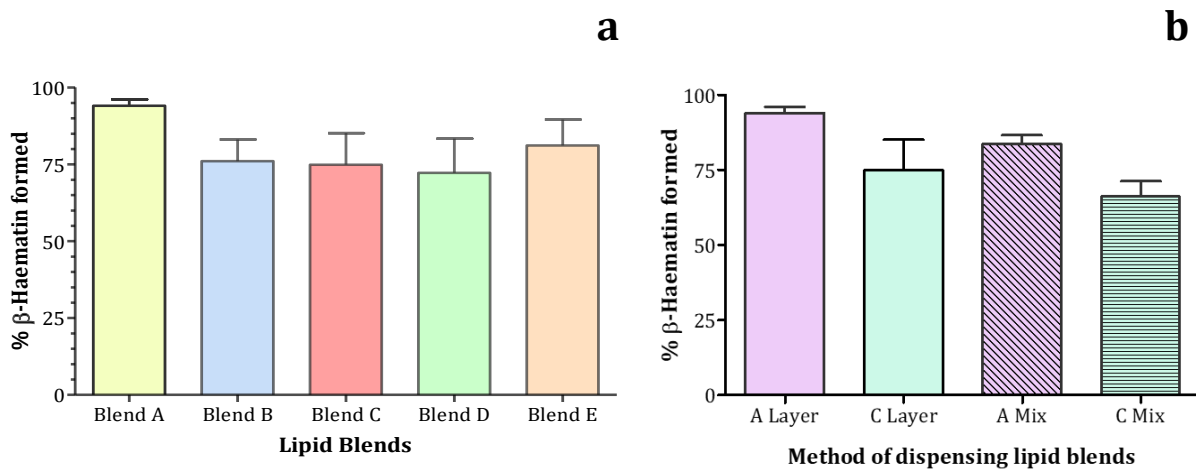

Figure 6.16. The effect of lipid blend composition and addition of lipid/Fe(III)PPIX on yield of β-haematin formation. (a) Lipid blends prepared based on specific lipids identified by mass spectrometry found to be occluded by haemozoin and their effect on the yields of β-haematin formed (*N* = 3, SEM). **(b)** Comparison of the method of delivery of lipid-Fe(III)PPIX to the buffer system.

Previous reports focusing on lipid mediated β-haematin has involved the careful delivery of lipid/Fe(III)PPIX mixture into a buffered system whereby the technical aspect was a major determinant in promoting successful formation of β-haematin. In some studies, lipid/Fe(III)PPIX was gently dispensed onto the surface of organic solvents using a needle where β-haematin was produced under the conditions described when working at the pentanol/water interface or using a lipid blend to assist in crystal formation.[147, 149] Considering these findings, the technical aspects of lipid mediated β-haematin in the current study was investigated using two different lipid blends.

Model blends A and C were combined in a 1:1 ratio and either carefully layered over the buffer surface or added and vigorously mixed prior to incubation (Section 6.2.3.4). The yield of β-haematin produced was determined spectroscopically by measuring the unreacted haematin as a pyridine complex as described above and even though the yield of β-haematin formed by mixing was slightly lower than that of careful layering, the yields remained above 75% (Figure 6.16b). The yield of β-haematin produced using model blend A remained above 80% after mixing thus signifying the robustness of the lipid composition and efficiency of blend A in promoting β-haematin formation irrespective of the method of delivery.

An investigation into the rate of β-haematin formation in the presence of blend A showed that the process is extremely fast, where the reaction was observed to have reached completion in well under ten minutes. Indeed, the reaction was too fast to obtain a reliable rate constant (Figure 6.17)

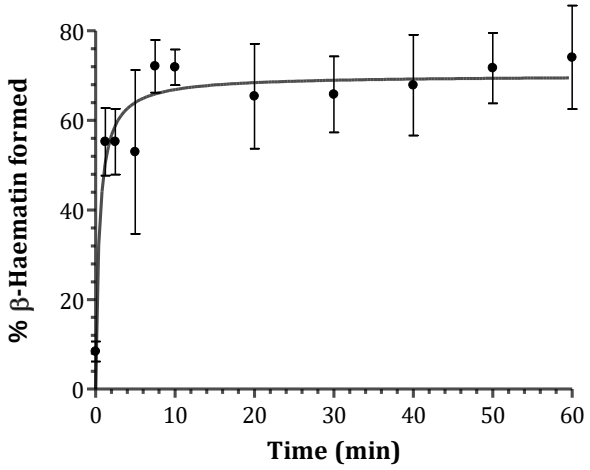

Figure 6.17. Kinetic curve of β-haematin formation using lipid blend A illustrating that the reaction proceeded so rapidly and was completed within 7.5 min. Reaction conditions: Incubation at varying time intervals up to a 60 min period, sodium acetate buffer (0.5 M, pH 5.2), 37°C, using a 1:1 mol ratio of model lipid blend A/Fe(III)PPIX. Error bars represent SEM, *N* = 3.

The minimum concentration of blend A required for the successful formation of β-haematin was investigated and the product determined by FT-IR (Table 6.6). It was found that concentrations of the blend as low as 20 μM could mediate the process. To test whether HDP works together with lipids, inclusion of rHDP at a concentration just below 20 μM was tested. It was found that the inclusion of soluble rHDP into the reaction mixture at a lipid concentration below 18 μM had no effect on its ability to form β-haematin.

The total amount of measured occluded lipid corresponded to 32.3 ± 9 nmol/mg protein (SEM, n = 6). The total protein content as determined by Bradford assay afforded a concentration of $2.2 \pm 0.3 \times 10^{-9}$ mg/cell (SEM, n = 6), therefore the occluded lipid corresponded to $6.7 \pm 1.5 \times 10^{-17}$ fmol/cell, which compares with 1.8 ± 0.2 fmol of haem/cell in the form of haemozoin. This corresponds to one lipid molecule per 74 ± 20 haem molecules of haemozoin. The approximate volume of the DV in a mature trophozoite is 4.0 fL, giving a minimum concentration of these lipids in the DV of 16 ± 3 mM.[359] This is

likely to be a considerable underestimate, since it is likely that only a small portion of the total lipids are occluded by haemozoin. Investigations of the model blend showed that concentrations ≥ 18 μM were capable of mediating β-haematin formation with high yields. Thus, the lipids present in the DV at the time and place of haemozoin formation are almost certainly in amounts more than adequate to efficiently mediate haemozoin formation without the need for any other catalyst.

Taking into account the surface area and volume of the unit cell as described earlier in Section 4.3.5.1, the resulting haemozoin crystal surface area to volume ratio indicates that there is one surface haem for every 50 total haem molecules. Given the 74 haem molecules per lipid, there is just under one lipid molecule per surface haem. This suggests that haemozoin crystals are likely coated in a lipid monolayer that is not easily disrupted but allows for the further weak adsorption of other biomolecules within the DV during crystal formation. This could explain the observation of tenaciously adsorbed atoms reported by Guerra *et al* that remain associated with the surface of haemozoin following attempts to clean the surface.

Table 6.6. The effect of varying concentrations of lipid Blend A on β-haematin formation

Concentration of lipid (μM)	β-haematin formation
600	+
300	+
150	+
75	+
37.5	+
18.8	+
9.4	-
4.7	-
2.3	-

6.3.4. Imaging Intracellular Lipids in *P. falciparum*

Neutral lipid bodies, specifically glycerolipid structures, and phospholipids have been implicated in haemozoin formation. Consequently, the development of lipid bodies was monitored over the 48 h asexual replication cycle. A number of commercially-available fluorescent probes (Figure 6.18) were used to investigate the development and location of lipid bodies as well as subcellular structures within *P. falciparum* by live-cell imaging.

Nile red is a lipophilic dye that has previously been used to monitor cellular lipids (Figure 6.18a).[379] This fluorescent dye has a broad excitation and emission spectrum which allows for the detection of both phospholipids as well as neutral lipids. When excitation is monitored at 561 nm and emission over 650-710 nm in the visible spectrum, the resulting red fluorescent signal is characteristic of phospholipid-rich regions whereas excitation at the same wavelength but emission at lower wavelengths corresponding to 575-630 nm results in a yellow-gold fluorescence signal characteristic of neutral lipids.

Hoechst 33342 (Figure 6.18b) is a supravital bis-benzimidazole fluorescent dye used to stain DNA in both live and fixed cells.[380] This molecule binds to the minor groove of double stranded DNA with enhanced fluorescence observed in DNA regions that are AT-rich, thus making it particularly favourable for studying *P. falciparum* owing to the parasite's AT-rich genome.

LipidTOX™ Green Neutral Lipid stain and its Red counterpart are specific for monitoring intracellular lipids in both live and fixed cells and has mainly been used to study diseases such as atherosclerosis and diabetes.[381] With a high affinity for neutral lipid droplets and the ability for multiplexing with other probes which allows further investigation of other important factors such as subcellular location, the LipidTOX™ series is more versatile compared to conventional probes such as Nile red and Sudan III.[382]

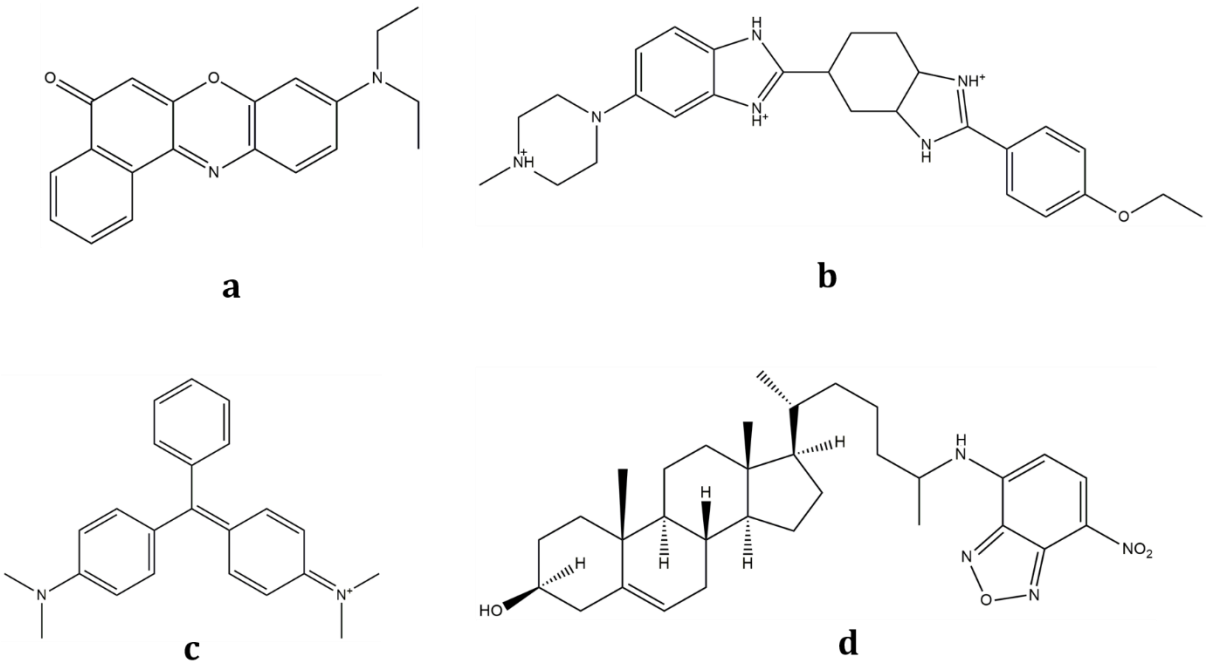

Figure 6.18. Chemical structures of fluorescent dyes used in live-cell confocal imaging studies. (a) Nile red, **(b)** Hoechst, **(c)** Malachite green and **(d)** NBD-cholesterol.

Malachite green (Figure 6.18c) is a triarylmethane dye that is well known for its intense green colour and was originally used in the pigment industry but has gained popularity in electron microscopy. Incorporation of Malachite green into a glutaraldehyde fixative enhances density of lipid bodies within cells by stabilising lipid elements as well as improving contrast of membranes when used in conjunction with tannic acid, offering added advantages when visualising with TEM.[383] NBD-Cholesterol (Figure 6.18d) is a sterol derivative with the NBD fluorophore attached to the hydrophilic end of cholesterol. This is an environment-sensitive probe used to monitor the distribution of cholesterol in living cells.[384]

Parasitised erythrocytes were harvested at 6 h intervals beginning with early rings until the mature segmented schizont. A sample of cells were first fixed and visualised by Giemsa staining using a light microscope to confirm the size and time-point of the parasite over the 48 h life cycle prior to confocal imaging. Parasite maturity was determined by the appearance and development of the DV as well as the number of nuclei present (Figure 6.19a). Laser scanning confocal microscopy was used to monitor the development of lipid bodies at each of the eight time intervals. Parasitised cells were treated with

Hoechst, Nile red and LipidTOX™ Green neutral lipid stain to monitor nuclei, phospholipids and neutral lipids, respectively.

Early to mid-ring stage parasites (6-12 h) were found to be close to the host RBC plasma membrane post invasion and were approximately 1 μm in size. Late rings (18 h) were similar in cellular structure with the main difference being the migration of the parasite towards the centre of the host cell. During the ring stage the phospholipid signal was most prominent with no fluorescent signal observed from the neutral lipid channel. The dominant phospholipid content is expected since this represents the initial growth phase of the parasite which marks the genesis of cell membranes and organelles forming the cell machinery. A single nucleus (blue) was present per cell throughout the ring stage and appeared to be at the periphery, near the PPM.

Giemsa images of parasites at 24 h illustrate the first appearance of haemozoin crystals contained within the DV, with this being characteristic of the early trophozoite stage in the life cycle. The spectroscopic properties of crystalline Fe(III)PPIX is responsible for the natural autofluorescence observed in haemozoin and β-haematin.[385] However, due to this signal being so faint, it does not interfere or overlap with fluorescence from the probes used in this study and even though this was monitored during imaging, it proved to be negligible.

At this time interval, the nucleus moved away from the cell periphery and a higher phospholipid content was observed; however, there were no neutral lipid bodies seen with the first appearance of haemozoin. The 30 h interval represents the most metabolically-active stage of the parasite where an increase in parasite volume was observed as well as the number of haemozoin crystals. The DV was more prominent and an intense fluorescent signal representing a spherical body was observed as indicated by the white arrow in the transmitted light channel. This signal corresponds to the LipidTOX™ Green stain in the dark field channel (Figure 6.19c) indicating that this was a neutral lipid body. The phospholipid region appeared to show more structure and depth indicating organelle development as the parasite matures.

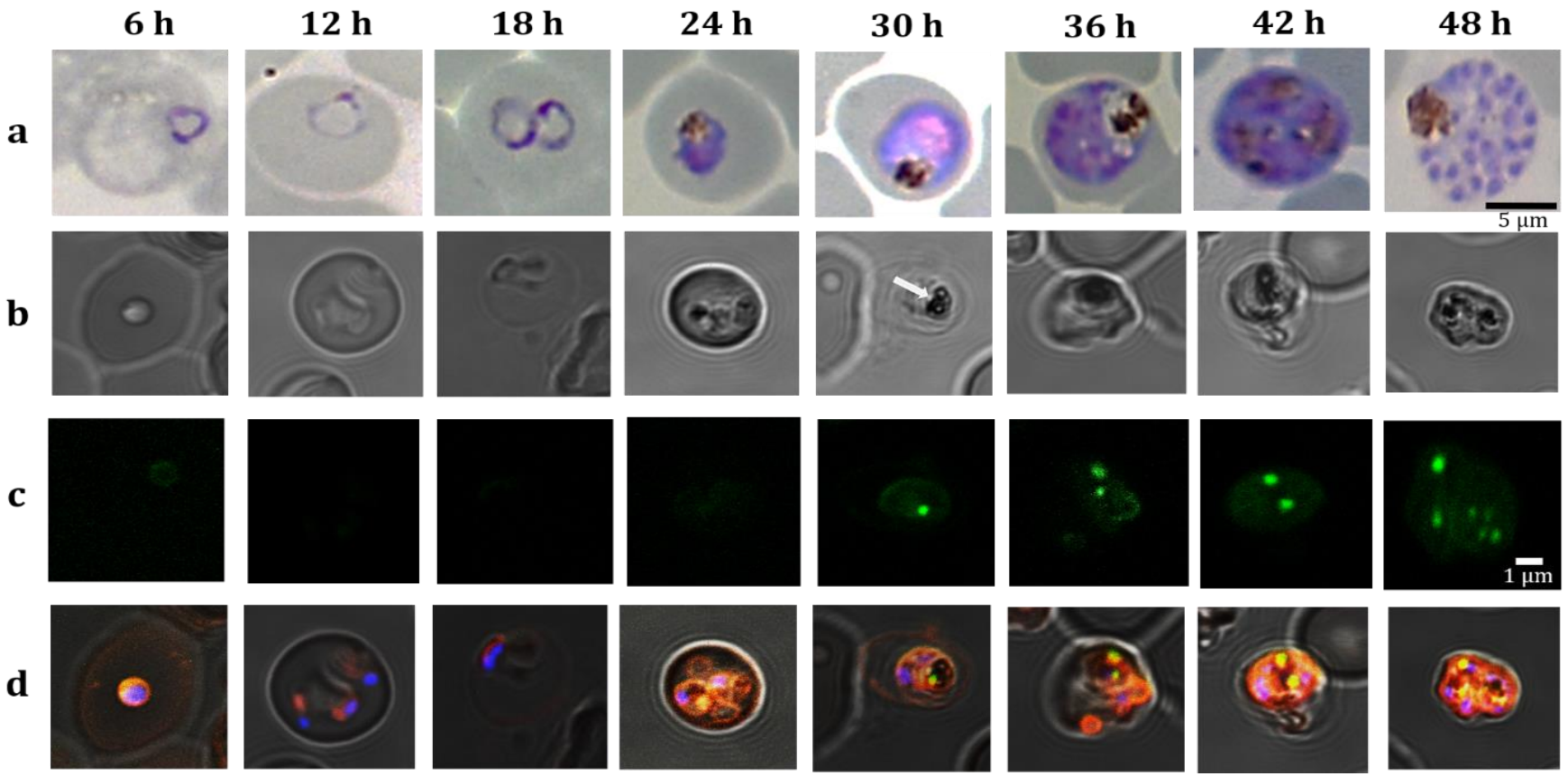

Figure 6.19. Time-point investigation into the development of lipid bodies in NF54 strain of *P. falciparum* over the 48 h asexual replication cycle. Parasites were imaged at 6 h intervals by **(a)** Giemsa staining of fixed cells and **(b-d)** live-cell imaging by confocal microscopy. Panels represent **(b)** DIC images of pRBCs, **(c)** lipid bodies stained with LipidTOX™ Green Neutral Lipid Stain and **(d)** an overlay of the various fluorescent channels of parasites treated with Hoechst (blue), Nile red (red) and LipidTOX™ Green Neutral Lipid Stain (green/yellow). Time intervals represent the early ring (6 h), mid-ring (12 h), late-ring (18 h), early trophozoite (24 h), mature trophozoite (30 h), late trophozoite (36 h), early schizont (42 h) and segmented schizont (48 h).

As the parasite transitioned from mid to mature trophozoite (30-36 h), a 3-fold increase in the size of the parasite was observed as a result of haemoglobin ingestion and catabolism. In addition, notable increases in haemozoin content and the number of lipid bodies of variable size were observed at the 36 h time interval, representing the mature trophozoite. The appearance of several lipid bodies later in the asexual life cycle, corresponding to enhanced haemozoin formation was consistent with previous findings.[142, 143]

Haemozoin crystals were even more pronounced and appeared to be aggregated at the early schizont stage at 42 h as seen in both Giemsa and phase contrast images (DIC). At this time-point, the parasite occupied the entirety of the host RBC with an increase in the number and size of lipid bodies which averaged to be approximately 3 to 4 per parasite from analysed images. In this example (Figure 6.19d), the phospholipid signal from the Nile red channel overlapped to some extent with the neutral lipid stain indicating that lipid bodies comprise heterogenous lipid content; however, due to the observed fluorescence intensity of the neutral lipid stain (green) the major component is in fact neutral lipids corresponding to previously discussed lipidomics data.

The segmented schizont at 46-48 h contained multiple nuclei accompanying several newly-formed daughter merozoites. In some cases, the DV was positioned at the periphery of the cell while, in others, it was seen at the centre; in each case, it was surrounded by several lipid bodies therefore suggesting an intimate association with the DV. However, it was unclear as to whether these neutral lipid bodies were on the inside or outside of the DV and were in close contact with haemozoin. Overall, a visible increase in total lipid content was observed as the parasite developed from the early ring to the segmented schizont with this increase presumably meeting the different metabolic demands of the cell throughout its life cycle.

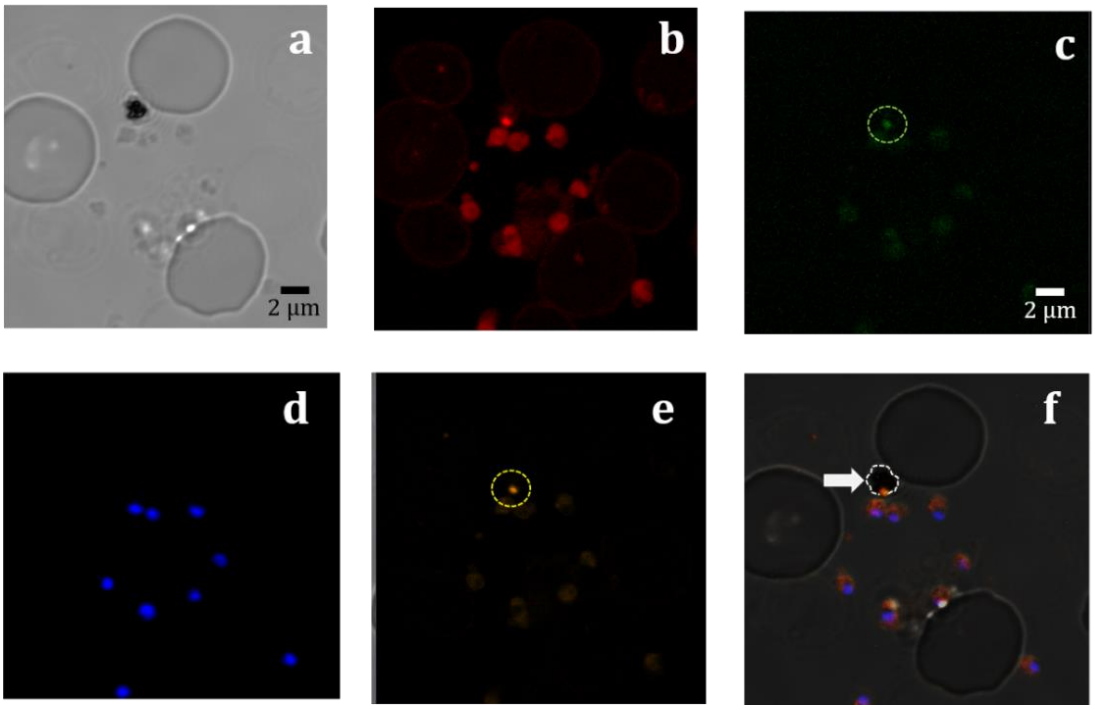

Figure 6.20. Laser scanning confocal microscopy images illustrating the location of a prominent lipid body with the DV following schizont rupture. A ruptured schizont releasing daughter merozoites that reinvade host erythrocytes. Lipid bodies seen to be intimately associated with the DV after rupture as indicated by the white arrow. **(a)** DIC showing released DV represented by the dark haemozoin crystals, **(b)** phospholipid region of Nile red, **(c)** neutral lipid body fluorescing by LipidTOX™ Green neutral lipid channel, **(d)** nuclei stained with Hoechst, **(e)** neutral lipid region of Nile red and **(f)** merged image of all channels.

Following schizont rupture (Figure 6.20), several daughter merozoites each with their own nuclei were released with each seeking to re-invade new RBCs. Monitoring red fluorescent signal intensity shows that the daughter merozoites were phospholipid-rich as indicated by the Nile Red channel. The DV, represented by black crystals in the DIC channel, was released after rupture with at least one neutral lipid body which remained in close contact with it as seen in both the LipidTOX™ Green neutral lipid channel (Figure 6.20c) and the gold fluorescent neutral lipid signal from Nile Red (Figure 6.20e) highlighted by circles in the images above.

Confocal microscopy confirmed the presence of neutral lipid bodies which appeared to be dependent on the life cycle stage and the extent of haemozoin formation. TEM was used as a complementary technique to gain further insight into the location and association of these lipid bodies in relation to the DV and haemozoin within parasitised cells. TEM produces high resolution images with improved magnification and allows detailed

visualisation of organelles within a cell, thereby providing significant advantages over confocal microscopy with respect to resolution and detail. Previous studies using electron microscopy reported lipid nanospheres that enclosed haemozoin crystals within the DV, suggesting that these nanospheres are responsible for the orientation and growth of the crystals.[146]

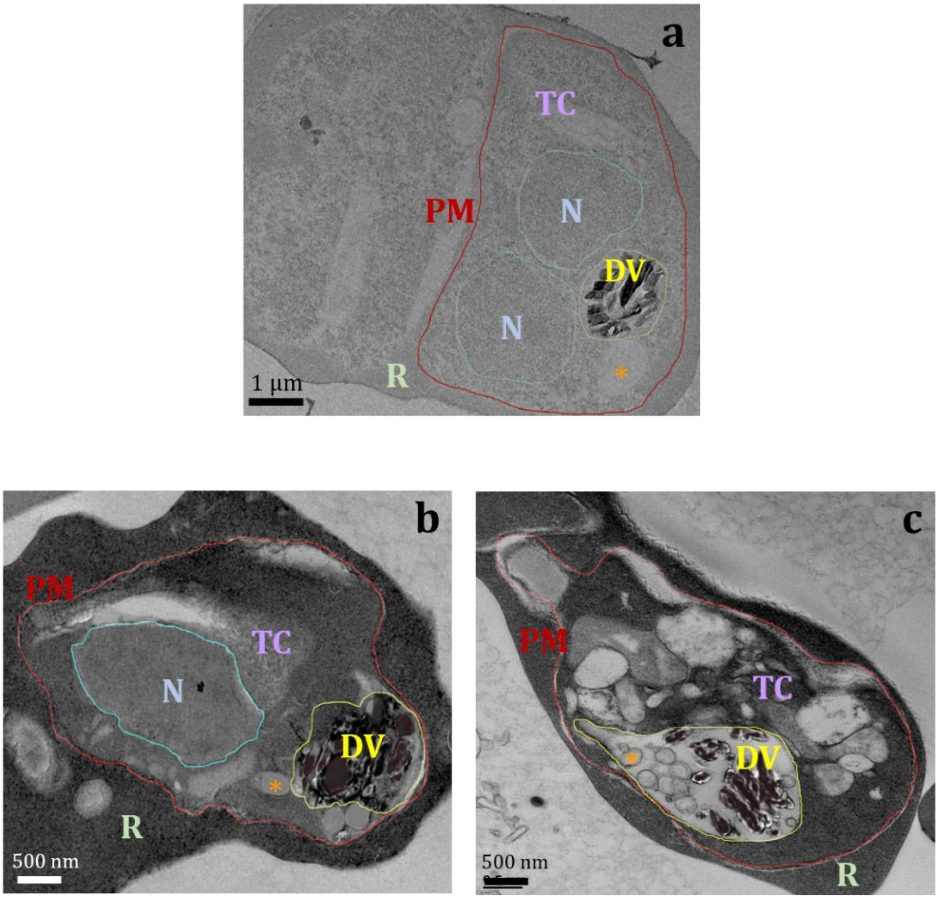

Figure 6.21. Transmission electron micrographs of parasitised cells illustrating lipid bodies in close proximity to the DV. TEM images representing **(a)** mature trophozoite stage control pRBCs and **(b, c)** pRBCs stained with Malachite green. Key: Host RBC (R), parasite membrane (PM), trophozoite cytoplasm (TC), nucleus (N), DV containing haemozoin (DV) and lipid bodies (*).

In the current study, mature trophozoite stage pRBCs were treated with Malachite green, a dye that specifically enhances the electron density of lipids as discussed earlier in this section. Control cells (unstained), prepared in the same way as stained cells for electron microscopy, exhibited a fully developed DV that was tightly packed with haemozoin crystals with a distinct lipid body approximately 1 µm in size found to be closely

associated external to the DV as indicated by the asterisk in Figure 6.21a. The density of lipid bodies and, in some cases, membrane structures were clearly enhanced after treatment with Malachite green improving visualisation.

In this example, three lipid bodies were observed to be in close contact with the outside of the DV similar to that seen in the control cells, but appearing to be smaller in size (Figure 6.21b). A look through a different section showed what the DV looks like when it is cut through and laying on its side (Figure 6.21c). Here there were a number of smaller dense bodies which could be lipid bodies or transport vesicles present within the DV laying adjacent to haemozoin crystals. Incorporating observations from both the control and stained cells, this suggests that lipid bodies may be in close contact with the DV but are unlikely to envelop haemozoin as previously thought.

While this imaging study supports the presence of lipid bodies in association with the DV, it remained unclear as to whether there is any direct contact with haemozoin. Conventional confocal laser scanning microscopy lacks the resolution required to definitively establish whether these lipid bodies are located inside or outside of the DV. Turning to TEM images, it has been claimed on theoretical grounds that there should be no contrast observed between haemozoin and lipids thereby calling into question the reported lipid structures that appear to coat haemozoin crystals. In addition, chemical fixation utilised in sample preparation for electron microscopy, as well as sectioning of embedded samples, have the potential to create artefacts leading to false positive results. Given that *P. falciparum* is one of the smallest eukaryotic cells, less than 8 μm in diameter depending on the stage in the life cycle, advanced live-cell imaging such as spinning disk confocal microscopy is a more appropriate method for envisaging what happens within the cell with minimal perturbation. Taking into consideration the overwhelming dominance of neutral lipids occluded by haemozoin, the localisation of glycerolipids and cholesterol present in *P. falciparum* was further investigated using this technique.

Conventional laser scanning confocal microscopy focuses a small laser beam through a single pinhole which scans an entire specimen point by point, sequentially building an image one pixel at a time. The single beam limits acquisition speed and has a higher potential for phototoxicity resulting in photobleaching of specimens due to prolonged exposure making this technique lower in sensitivity and resolution. By contrast, spinning disk confocal microscopy operates on the premise of passing a laser beam though multiple

pinholes, thereby illuminating the entire specimen at any one time. This imaging technique provides millisecond, high-resolution image acquisition in real-time. Due to the laser being split, the sample is exposed to low power light in very short intervals thereby minimising photodamage to specimens during live-cell imaging.[386] Spinning disk confocal microscopy is ideally suited for 2D and 3D imaging due to the enhanced temporal and spatial resolution offered.[387, 388]

In order to determine whether glycerolipid-rich neutral lipid bodies localised within or external to the DV, a Dd2 strain of *P. falciparum* expressing GFP conjugated PfCRT (GFP-PfCRT) was treated with LipidTOX™ Red, a neutral lipid-specific fluorescent dye, and Hoechst, prior to imaging. PfCRT is a DV-specific marker and GFP-PfCRT offered improved photostability and specificity for the vacuole during live-cell imaging.[389] Spinning disk confocal microscopy was used to acquire images which were used to generate 3D volume reconstructions as described in Section 6.2.5.2 which provided higher resolution and clarity at the organelle level.

Mature, late-stage trophozoites (Figure 6.22a-c) and segmented schizont-stage (Figure 6.22d-e) pRBCs exhibited intense fluorescence from all three channels representing the DV (green), nuclei (blue) and glycerolipid-rich neutral lipid bodies (red). The DV, approximately 2 μm in cross-section, was well developed and located towards the centre of the cell in trophozoites and more towards the edge at the segmented schizont stage.

Spinning disk confocal microscopy definitively showed that the glycerolipid-rich neutral lipid bodies were intimately associated with but located outside the DV and were not in contact with haemozoin crystals (Figure 6.22). There were approximately three lipid bodies associated with the DV on average. This supports the transmission electron micrographs that portrayed similar features. It is likely that these lipid bodies are present as a source of stored lipids and a portion may be trafficked into the DV where only minute amounts, as demonstrated earlier by lipidomics, is required to promote haemozoin formation.

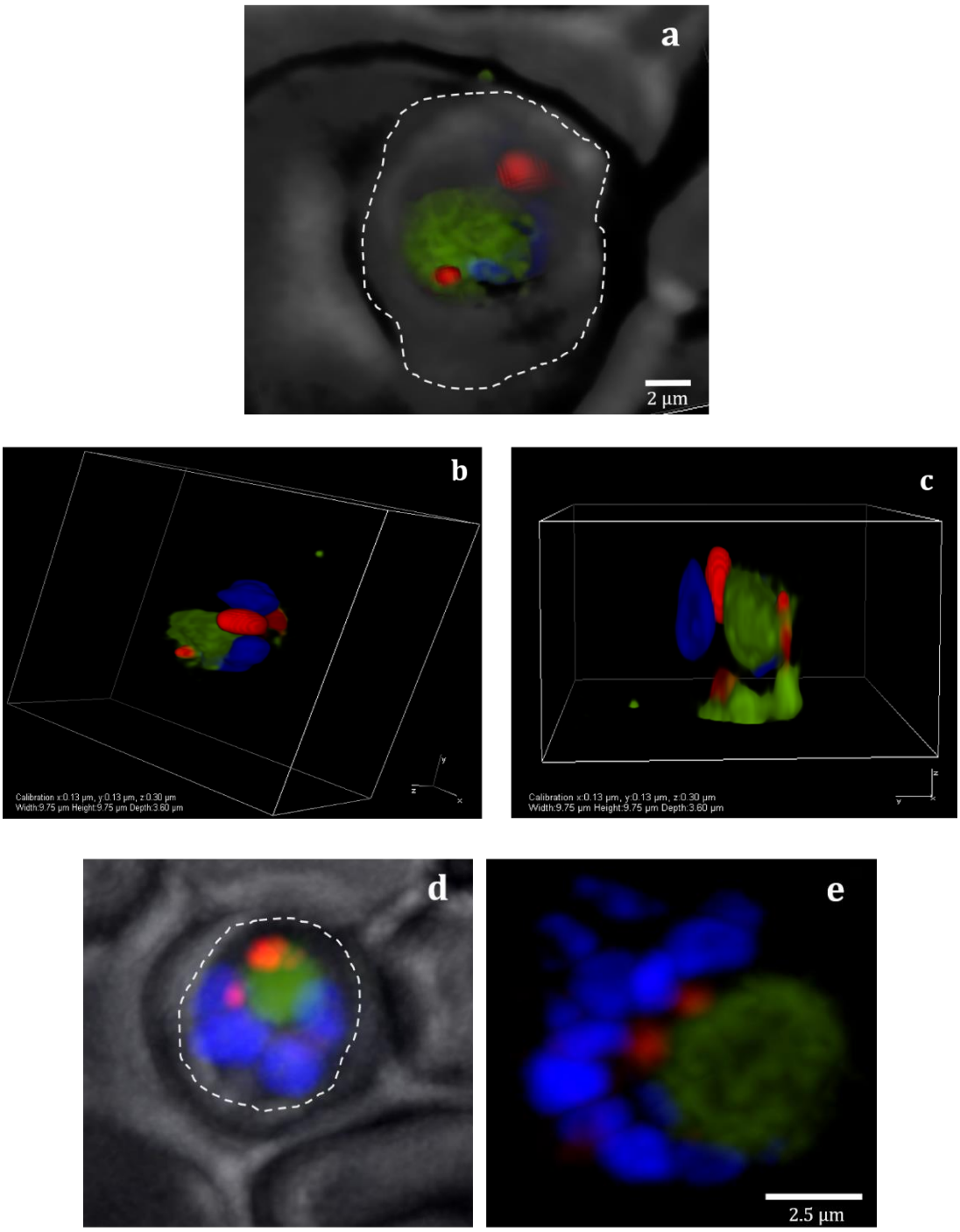

Figure 6.22. Spinning disk confocal images illustrating the location of lipid bodies in relation to haemozoin by 3D volume reconstruction. Images represent **(a)** a mature trophozoite and **(d)** segmented schizont GFP-PfCRT expressing parasites. **(b, c, e)** 3D volume reconstructions of the corresponding fluorescent channels illustrating that the neutral lipid bodies are located external to the DV and are not in intimate, continuous contact with haemozoin crystals. Key: parasite plasma membrane (white dashed lines), DV membrane (green), nuclei stained with Hoechst (blue) and lipid bodies stained with LipidTOX™ Red Neutral Lipid Stain (red).

The distribution of cholesterol and its relation to neutral lipid bodies within parasitised cells was investigated by exposing NF54 strain of *P. falciparum* infected RBCs to NBD-cholesterol and LipidTOX™ Red Neutral Lipid Stain (Figure 6.23). An accumulation of labelled cholesterol was observed to be located near haemozoin within the parasite (Figure 6.23a and c). In addition, partial colocalisation was observed between LipidTOX™ Red Neutral Lipid Stain and NBD-cholesterol distal to the region occupied by haemozoin, suggesting that the labelled cholesterol was in contact with, or in very close proximity to, haemozoin crystals.

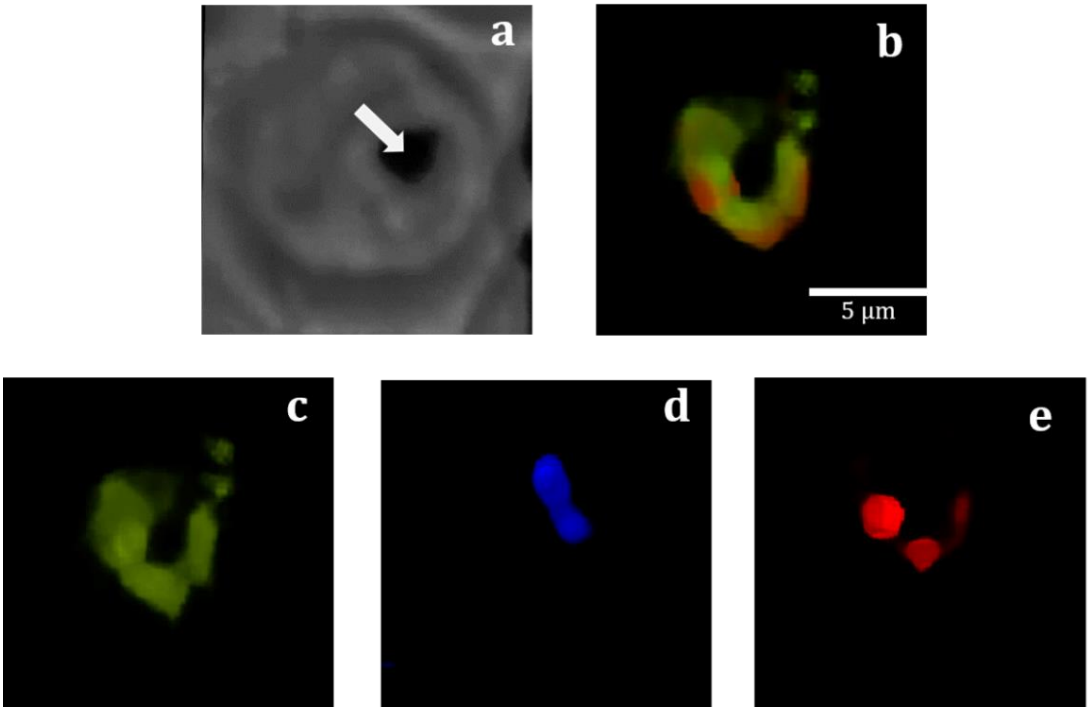

Figure 6.23. Spinning disk confocal images showing the distribution of NBD-cholesterol in a mature trophozoite. NBD-Cholesterol highlighted areas surrounding the haemozoin pocket illustrated by **(a)** the arrow in a phase contrast image exhibiting partial colocalisation of **(b)** NBD-cholesterol with LipidTOX™ Red Neutral Lipid Stain. Distribution of **(c)** NBD-cholesterol, **(d)** multiple nuclei indicating a mature parasite and **(e)** distribution of neutral lipid bodies stained with LipidTOX™ Red.

It has been reported that the concentration of cholesterol in the PPM is considerably lower than in the RBC membrane, with pRBCs illustrating an increase in the levels of membrane cholesterol relative to control RBCs.[202] As the parasite matures, the increase in demand for lipids enhances the concentration of non-sterol lipids inevitably leading to

a dilution effect of cholesterol. This creates a gradient in membrane cholesterol content with infected RBC > tubulovesicular network and Maurer's clefts > PVM > PPM.[202] The role of the cytostome in transporting cholesterol is likely to be the origin of this lipid found to be occluded by haemozoin. Notably, while cholesterol is the most abundant lipid occluded, this does not imply that this sterol is exceptionally abundant in the parasite, or even the DV relative to the RBC. The idea that cholesterol can be transported to the DV is supported by the fact that externally added NBD-cholesterol finds its way to the vicinity of haemozoin relatively quickly as observed in the above images. Considering the changes in DVM thickness reported by Kapishnikov *et al* discussed in Chapter 1, the observed patches could be indicative of cholesterol-rich lipid rafts that are likely in contact with haemozoin.[152] As highlighted earlier, glycosylphosphatidylinositol-anchored proteins (GPIs) are characteristic components of lipid rafts. Interestingly, the qualitative proteomic study of haemozoin identified two uncharacterised proteins which appeared to be associated with lipid rafts. One protein [W4IBF0_PLAFA] was detected in material found to be weakly-associated with haemozoin and the other [Pf11_0229] in material occluded by the crystal. Database analysis of these proteins revealed that they exhibited 100% similarity in sequence identity to *P. falciparum* specific GPI anchor attachment 1 protein and the GPI transamidase complex, respectively.

6.4. Chapter Summary

The lipidomic study presented in this chapter provides a first comprehensive insight into the lipids specifically occluded by haemozoin that were present at the site and time of crystal formation.

TLC was used as a qualitative technique which demonstrated distinct differences between surface-associated lipids and those occluded by haemozoin. Overlap between lipids was observed, making it difficult to unequivocally identify the lipid constituents by TLC. Additionally, TLC studies demonstrated that haemozoin and β-haematin occlude lipids in a non-exchangeable manner. Lipidomics-based mass spectrometry identified 386 different lipids that were occluded by haemozoin, with neutral lipids being the most abundant class with smaller amounts of phospholipids and sphingolipids. Cholesterol was identified to be the dominant neutral lipid accounting for over 90% of this class with cholesterol esters being the next most abundant and the remaining lipids comprising trace amounts of glycerolipids.

Lipidomics data was used to guide preparation of a model lipid blend A that mimicked the lipids occluded by haemozoin. Blend A, comprising 94.2% cholesterol, 2.2% cholesterol ester, 0.2% monoacylglycerols, 0.2% diacylglycerols, 0.1% triacylglycerols and 3.1% phosphatidylcholine, was used to synthesise β-haematin under conditions modelling the environment of the DV (pH 5.2, 37°C). This blend efficiently promoted β-haematin formation in yields exceeding 90% and the reaction reached completion within 7.5 min. The crystals produced were similar in external morphology to haemozoin formed *in vivo*. A study investigating the lowest concentration of this blend of lipids that was successful in promoting β-haematin formation revealed that the cut-off was below 20 μM. This shows that the lipids present at the time and site of nucleation are extremely efficient in mediating β-haematin formation in high yields at concentrations likely to be easily attained in the DV.

Spinning disk confocal microscopy unequivocally demonstrated that neutral lipid bodies that were glycerolipid-rich were located outside the DV in Dd2 parasites expressing GFP-PfCRT. In addition, these bodies appeared to be in close contact with the exterior of the DV membrane and partially co-localised with NBD-cholesterol suggesting that they may be able to exchange material with the DV. These findings have conclusively identified

the lipids that are in intimate contact with Fe(III)PPIX or haemozoin during nucleation and growth, making it highly likely that these are the biomolecules responsible for mediating haemozoin formation in the malaria parasite. Further investigations are necessary to establish the origin of occluded lipids as well as to determine the mechanistic role of specific lipids in haemozoin formation.

Chapter 7

Conclusions and Future Work

7.1. Overall conclusions

Apicomplexa are pathogens known to be master manipulators of host cell machinery which, in turn, strategically promote immune evasion thus enabling survival in harsh environments. Of these pathogens, *P. falciparum* is the deadliest causative agent of malaria affecting humans due to its ability to rapidly replicate within host erythrocytes which sequentially drives the devastating disease and its global socio-economic burden. Even though there have been reports of the malaria incidence rate portraying a plateaux effect, this severely virulent pathogen is responsible for the high morbidity and mortality rates still evident in the developing world due to emerging resistance to current antimalarial regimens.[2] A major cause for concern centres around the lack of knowledge or controversy regarding essential parasite-specific pathways that enable immune evasion and survival, specifically during the intraerythrocytic cycle. Therefore, it is of paramount importance to meticulously investigate such mechanisms and biological processes which have the potential to form novel defence strategies against emerging resistance and stimulate future drug design.

There exists a continuous interplay between host and pathogen as the parasite sequesters within the erythrocyte, an intrinsic event inherently directed by molecules such as proteins, lipids, carbohydrates and metal ions. The parasite obtains nutrients that are essential to growth and development whilst not imposing drastic changes that may be detrimental to the host cell. Divalent transition metals are essential to vital biological processes in host-pathogen systems as these elements provide stability, form part of the

antioxidant defence system or function as cofactors.[275, 390] Of particular interest in this study, and previously not extensively explored, is the distribution of trace metal ions in *P. falciparum* as it develops over the 48 h intraerythrocytic cycle.

Sequestering within the erythrocyte triggers ingestion of haemoglobin by endocytosis through the cytostome, making this the only proven mechanism by which the parasite easily overcomes the triple membrane barrier (RBC membrane, PVM and PPM) in order to obtain nutrients. This alludes to the premise that specific transporters are likely present to equip the parasite with the machinery needed to meet metabolic demands. To date it is known that at least 2.5% of the *Plasmodium* genome encodes for various transporters; however, due to the complexity associated with unequivocally determining the exact role and subcellular location of each, very little is known about these in detail.[231]

Ingestion of large amounts of haemoglobin and catabolism thereof has been thought to provide the parasite with increasing amounts of Fe in the form of free haem. Furthermore, oxidation of toxic free haem and conversion into haemozoin within the acidic DV has been the target of antimalarials such as chloroquine and quinine as well as artemisinin partner drugs used in ACT. Haemozoin formation, the final stage in the haem detoxification pathway, remains a promising target in that it is parasite- specific, not genome-encoded and critical for survival. However, the mechanistic details regarding crystal formation has remained contentious.

Consequently, the broad aims of the current study were two-fold, (i) to explore the bioinorganic complement of *P. falciparum* and (ii) to investigate the mediators of haemozoin formation. In this work, the bioinorganic component comprised the exploration of the trace metal distribution in the malaria parasite over the intraerythrocytic cycle. This was complemented by a proteomics-based approach which was employed to identify potential metal-associated proteins. In order to comprehensively investigate the biomolecules involved in haemozoin formation, a fractionation approach was used to isolate haemozoin from mature parasites. This was followed by extensive washing with detergents and organic solvents and, finally, base dissolution to release occluded material. These biological extracts independently comprising proteins and lipids were analysed by mass spectrometry to identify potential haemozoin-forming proteins as well as to profile lipids.

Using a molecular biology approach, the protein of interest, HDP, was synthesised, purified and characterised. The association of previously implicated lipid bodies with respect to haemozoin was examined by using commercially-available fluorophores and live-cell spinning disk confocal microscopy. Finally, activity studies exploring the formation of β-haematin were performed with purified protein and identified lipids found through lipidomics, thus providing a holistic approach to further gain insights into haemozoin formation. A summary of the overall insights pertinent to this study is illustrated in Figure 7.1.

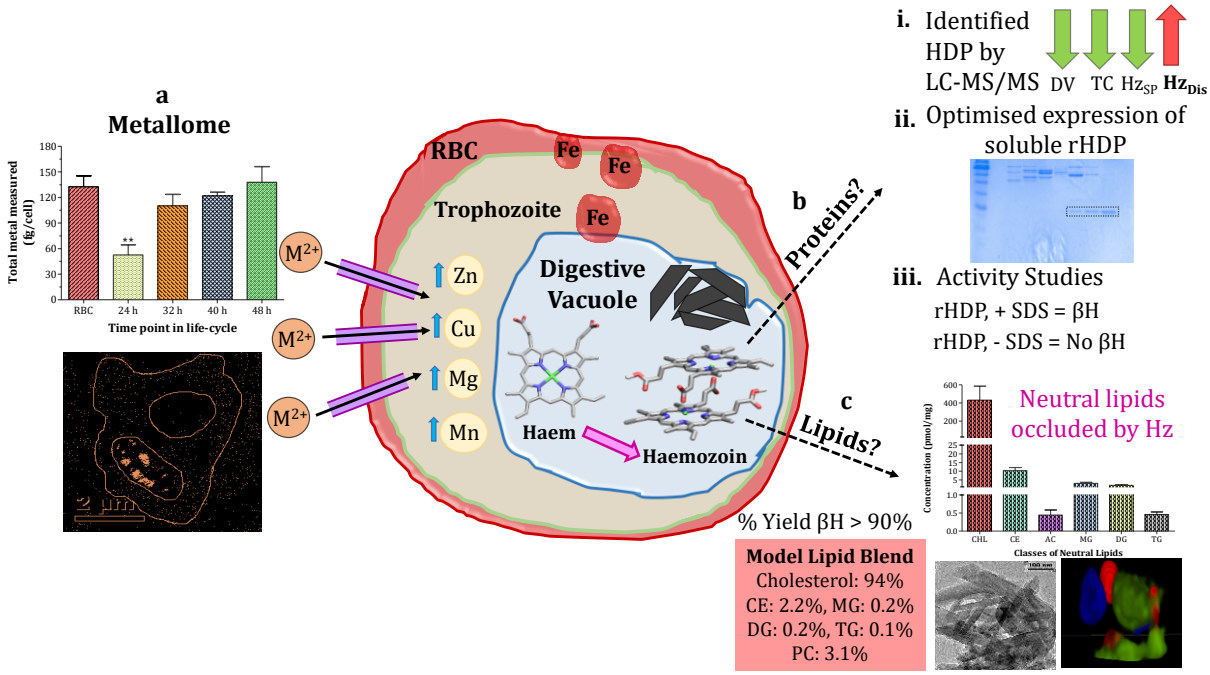

Figure 7.1. Schematic representing overall findings from this study. (a) Investigation of the parasite metallome and discovery of potential metal influx pathways. **(b)** Exploring the impact of HDP as a potential mediator of β-haematin formation. **(c)** The role of occluded lipids in β-haematin formation. Key: Divalent trace metal ions (M^{2+}), red blood cell (RBC), β-haematin (βH), haemozoin (Hz), cholesterol esters (CE), monoacylglycerols (MG), diacylglycerols (DG), triacylglycerols (TG) and phosphatidylcholine (PC).

Trace metal content was measured at various time intervals as the parasite matured from young trophozoite (24 h) to schizont stage (48 h). Data obtained confirmed that over 90% of metal content was represented by Fe in the form of haem which validated previously reported studies. Throughout the intraerythrocytic cycle, the amount of Fe remained less than that of the uninfected host cell and total Fe in pRBC relatively constant as the parasite matured. This suggests that the amount of Fe was likely regulated by, and in proportion

to the amount of haemoglobin ingested since this protein contains over 95% of the cellular haem. In contrast, albeit measured in smaller amounts, the Mg, Zn, Cu and Mn content all exhibited increases at various time-points over the 48 h cycle (Figure 7.1a). Additionally, these metals were detected in amounts higher than those present in the uninfected host cell. Even though the erythrocyte served as a rich source of Fe, it is unlikely to be a pool for other transition metals like Mg and Zn. Thus, these findings are indicative of the parasite having unique metal transporters which enable active uptake of trace metals from sources external to the host cell. Interestingly, in addition to various other metal-associated proteins distinguished by their characteristic metal binding motifs that were identified by LC-MS/MS, several Mg and Cu transporters were found thereby supporting the hypothesis of metal uptake pathways exclusive to the parasite. This in turn warrants further investigation into understanding the mechanistic details regarding exactly how the parasite promotes metal uptake.

Mass spectrometry analysis of proteins found in the surface washings of haemozoin and in dissolved material revealed a number of proteins characteristic of the DV, therefore corroborating those previously reported.[181] Most significant was the detection of HDP which was found in high relative abundance in the dissolved haemozoin fraction (Figure 7.1b). Several hypotheses regarding the biocrystallisation of haemozoin have evolved from the initial theory of this being an autocatalytic process to one catalysed by proteins such as HRP II and currently dominated by the claimed potency of HDP as a haem dimerisation protein.[139,146,131,137] The role of lipids in the form of neutral lipid bodies have gained much attention over the past decade.[141,146] However, there has been a lack of evidence regarding the specific association of these molecules with haemozoin.

In order to evaluate the role of HDP in haemozoin formation, recombinant HDP was synthesised and investigated. The expression and purification of rHDP proved to be quite complex and labour intensive due to the conflicting physical properties of this protein. Optimised expression of soluble rHDP involved the use of the pCold I expression plasmid in the C41 *E. coli* cell line at low temperature accompanied by longer induction periods. This optimised method afforded adequate amounts of soluble protein for further evaluation, seemingly for the first time. Circular dichroism and fluorescence spectroscopy both illustrated that soluble rHDP was different in conformation to its refolded

counterpart. Spectrophotometric titrations revealed that both soluble and refolded rHDP bound a single molecule of Fe(III)PPIX with weak protein-haem association.

The activity of soluble and refolded rHDP was determined by employing previously reported β-haematin assay conditions whereby the addition of SDS was incorporated in the washing steps following incubation of protein and haem in aqueous buffer.[124, 131] This study showed that the reaction including rHDP and SDS had successfully promoted β-haematin formation; however, omission of SDS under the same reaction conditions resulted in no β-haematin being formed. These results demonstrated that the detergent was solely responsible for promoting β-haematin formation under these conditions; therefore, claims by previous investigators that HDP acts as a potent enzyme in catalysing crystal formation appear to be highly improbable. Even though rHDP exhibited a different haem binding ratio to that reported and was found not to be competent in mediating β-haematin formation, these findings in fact explain the inconsistencies observed in point mutation studies where parasites that lacked essential His residues in the HDP sequence were still able to produce haemozoin.[137] This suggests that it is highly unlikely that any of the previously implicated proteins are the biomolecules that are responsible for crystallisation, thereby supporting that this may be a lipid-mediated process.

Lipidomics-based mass spectrometry successfully identified and quantified a unique set of lipids present in dissolved haemozoin (Figure 7.1c). Neutral lipids were found to be the dominant class in this study with cholesterol accounting for approximately 90% of lipids detected, with smaller amounts of cholesterol esters, acyl carnitine and glycerolipids. A synthetic model lipid blend that mimicked the detected lipid profile specific to dissolved haemozoin was used to investigate the role of these lipids in β-haematin formation. This model blend was found to be exceptionally efficient in mediating β-haematin formation in terms of rate and high yield with just micromolar quantities being sufficient for nucleation. Transmission and scanning electron microscopy of lipid mediated product illustrated that these crystals were similar in morphology to haemozoin observed *in vivo*.

Imaging studies by confocal microscopy confirmed the development of neutral lipid bodies to be interrelated with parasite maturation over the asexual cycle. Transmission electron micrographs of mature trophozoites treated with Malachite green depicted neutral lipid bodies adjacent to haemozoin or external to the DV. This observation was further supported by live-cell imaging of GFP-labelled PfCRT parasites using spinning disk

confocal microscopy which afforded the enhanced resolution required to accurately determine the disposition of neutral lipid bodies. Three-dimensional volume reconstruction showed that neutral lipid bodies were located external to the DV, or in certain instances, were in close contact with the DV membrane but were never found in the immediate vicinity of haemozoin. This association between the observed lipid bodies and DV membrane also exhibited colocalisation with NBD-cholesterol, therefore suggesting a possible exchange mechanism.

In this study, exposure of pre-formed β-haematin and haemozoin to His-tagged rHDP and NBD-cholesterol illustrated that these crystals strongly adsorbed labelled molecules as these were not released from the surface by mere washing with aqueous buffer but only following treatment with detergent or organic solvents. β-Haematin synthesised in the presence of the respective labelled molecules was observed to have retained these molecules following extensive washing and only released them upon base dissolution signifying occlusion by the crystals.

Significantly, the findings that preformed β-haematin and haemozoin did not occlude labelled molecules as was the case for crystals formed in the presence of such molecules implies that these crystals occlude material in a manner non-exchangeable with the external milieu. Admittedly, due to the adhesive nature of haemozoin it is probably unlikely that the surface could be completely stripped of all associated biomaterial; nevertheless, extensive washing releases molecules most strongly adsorbed, while dissolution releases significant amounts of occluded material thereby providing a window into those molecules present at the time and site of crystal formation which were observed for the first time.

In its entirety, these studies produced the trace metal distribution profile in *P. falciparum* and unequivocally identified the biomolecules that are in intimate contact with haemozoin during crystal formation. The increases in trace metals measured, and identification of metal transporters, suggest that the parasite has unique metal uptake pathways. Notably, the intimate contact of biomolecules with haemozoin does not insinuate specific association or function of these molecules, but rather supports their presence in the DV at the time and site of formation. Having confirmed that soluble and refolded rHDP were equally incapable of mediating β-haematin formation, the detection of HDP in dissolved haemozoin alludes to a critical role within the parasite. Since HDP

weakly binds Fe(III)PPIX, a possible role might be as a haem transporter or chaperone protein, but further investigation would be required to validate this hypothesis. The efficiency of the model lipid blend resembling the unique lipid profile established for haemozoin in mediating β-haematin formation emphasises the intrinsic importance of these molecules, making them highly likely to be the biomolecules responsible for promoting haemozoin formation in the parasite.

It is intriguing that a unicellular protist like the malaria parasite has such advanced mechanisms making it incredibly resilient to not only survive within various hosts, but also be able to modify the host's cellular complement entirely for its own benefit. Indeed, there have been decades of research devoted to better understanding various biological processes unique to *Plasmodium*; however, well-known survival mechanisms such as haemozoin formation remain elusive. The continuous threat of parasite resistance rendering current treatment obsolete appears to be an inevitably fast-approaching and daunting reality. This work, encompassing a multidisciplinary approach, provides novel insights into the conundrum regarding the specific biomolecules responsible for haemozoin formation as well as generating new ideas regarding potential metal uptake within the parasite. Together, these contribute to the creation of new knowledge which can be exploited to strategically address the structural and mechanistic implications of such proteins and lipids in the parasite especially as potential metabolic pathways that can be perturbed, hence making these possible viable targets of novel chemotherapeutic agents. Pursuing these future investigations has the potential to discover further novel insights that will ultimately culminate in assisting with the eradication of this dreadful disease.

7.2. Future work

As demonstrated earlier, the observed changes in trace metal distribution and identification of metal transporters offer novel insights into the metallome of *P. falciparum*, consequently making this study unique compared to those previously reported for the bioinorganic component of the malaria parasite which have mainly centred around macroelements such as Fe and Ca. A comprehensive understanding of parasite-specific metal uptake mechanisms would be highly advantageous as this would provide unprecedented details of crucial biochemical pathways that could evolve into the discovery of new drug targets. Therefore, further investigation and full characterisation of trace metal transporters should be pursued.

The significance of these metal transporters to intraerythrocytic parasite development can be explored by treating parasites with compounds that would selectively inhibit optimum functioning of these proteins. This proposed experiment would be based on the premise that the metal transporters are crucial for parasite growth as it transitions from young trophozoite to schizont. Alternatively, a genomics-based approach could be employed to monitor gene regulatory events specific to genetic switches unique to metal transporters over the asexual cycle. A possible technique to locate on/off genetic switches could be ChIP- sequencing which combines chromatin immunoprecipitation with DNA sequencing to determine the activity of particular proteins.[391, 392] Data generated from this study would be able to identify at which exact point over the 48 h asexual cycle metal influx transporter genes are switched on which could lead to a new target within the blood stage. If successful, this approach would not be limited to *Plasmodium* but could be applied to other Apicomplexan pathogens.

With this being the first study to systematically investigate soluble rHDP as a potential mediator of β-haematin formation, these new findings steer the research area of HDP in a different direction. The main focus of further studies would entail refocusing interest and determining the biological function and importance of this protein in the DV of the malaria parasite. Since HDP appears to be crucial to parasite survival, the most strategic way forward would be to gain structural insights into this protein. In order to attempt protein crystallisation studies, the expression of soluble HDP would need to be further optimised to produce large enough quantities that would be sufficient for solubility experiments and crystal trials. Having shown improved soluble expression of rHDP using the pCold I

expression plasmid, further optimisation could focus on using an alternative *E. coli* cell line such as ArcticExpress competent cells that further enhance expression at lower temperatures.

Since HDP has a strong affinity for haemozoin and was found to bind Fe(III)PPIX, further functional studies should focus on validating whether HDP is in fact a haem chaperone protein. This could be explored by conducting haem binding and release studies where the rates can be experimentally determined by UV-vis spectrophotometry. Insights into the subcellular location of HDP can be envisaged by generating mutant parasites by conjugating specific organelle markers and HDP to various fluorescent proteins such as green or red fluorescent protein (GFP or RFP). The fluorescent conjugates in mutant parasites could be designed as photo-switchable probes which will allow for more stable, sensitive and enhanced high-resolution cellular imaging where technologies such as Stochastic Optical Reconstruction Microscopy (STORM) or Photoactivated Localization Microscopy (PALM) could be employed. [393, 394]

Finally, the unequivocal discovery that detected occluded lipids were solely responsible for mediating β-haematin formation results in the urgent need to supplement this knowledge by elucidating the structural and mechanistic implications of the various lipid constituents. *P. falciparum* is known not to synthesise its own cholesterol but obtains it from the host erythrocyte. Therefore, understanding the importance and function of cholesterol in the DV and its association with haemozoin is now crucial to provide detailed mechanistic insight into haemozoin formation.

Cryogenic transmission electron as well as super-resolution microscopy are informative tools that can be used to monitor cholesterol trafficking in the malaria parasite. Interrogating this trafficking pathway will provide novel insights into the involvement of lipids in this biocrystallisation process and will open new areas of research for exploring intracellular lipids within parasitic cells. The mechanism of lipid-mediated β-haematin formation may be unravelled by determining the effect on the kinetics of variations of the model lipid blend. The incorporation of well-known antimalarials in lipid kinetic studies can be used to decipher how the overall rate of reaction is affected by interaction with drugs in unique lipid-haem systems.

Chapter 8

References

1. S. Chakraborty, S. Roy, H. U. Mistry, S. Murthy, N. George, V. Bhandari and P. Sharma, *Front. Immunol*., 2017, **8**, 15.
2. World Health Organisation, *World Malaria Report 2018*, WHO Press, Geneva, 2018.
3. T. E. Wellems and C. V. Plowe, *J. Infect. Dis*., 2001, **184**, 770.
4. C. Roper, R. Pearce, S. Nair, B. Sharp, F. Nosten and T. Anderson, *Science*, 2004, **305**, 1124.
5. M. Imwong, T. T. Hien, N. T. Thuy-Nhien, A. M. Dondorp and N. J. White, *Lancet Infect. Dis*., 2017, **17**, 1022.
6. R. Amato, R. D. Pearson, J. Almagro-Garcia, C. Amaratunga, P. Lim, S. Suon, S. Sreng, E. Drury, J. Stalker, O. Miotto, R. M. Fairhurst and D. P. Kwiatkowski, *Lancet Infect. Dis*., 2018, **18**, 337.
7. E. A. Ashley, M. Dhorda, R. M. Fairhurst, C. Amaratunga, P. Lim, S. Suon, S. Sreng, J. M. Anderson, S. Mao, B. Sam, C. Sopha, C. M. Chuor, C. Nguon, S. Sovannaroth, S. Pukrittayakamee, P. Jittamala, K. Chotivanich, K. Chutasmit, C. Suchatsoonthorn, R. Runcharoen, T. T. Hien, N. T. Thuy-Nhien, N. V. Thanh, N. H. Phu, Y. Htut, K. T. Han, K. H. Aye, O. A. Mokuolu, R. R. Olaosebikan, O. O. Folaranmi, M. Mayxay, M. Khanthavong, B. Hongvanthong, P. N. Newton, M. A. Onyamboko, C. I. Fanello, A. K. Tshefu, N. Mishra, N. Valecha, A. P. Phyo, F. Nosten, P. Yi, R. Tripura, S. Borrmann, M. Bashraheil, J. Peshu, M. A. Faiz, A. Ghose, M. A. Hossain, R. Samad, M. R. Rahman, M. M. Hasan, A. Islam, O. Miotto, R. Amato, B. MacInnis, J. Stalker, D. P. Kwiatkowski, Z. Bozdech, A. Jeeyapant, P. Y. Cheah, T. Sakulthaew, J. Chalk, B. Intharabut, K. Silamut, S. J. Lee, B. Vihokhern, C. Kunasol, M. Imwong, J. Tarning, W. J. Taylor, S. Yeung, C. J. Woodrow, J. A. Flegg, D. Das, J. Smith, M. Venkatesan, C. V. Plowe, K. Stepniewska, P. J. Guerin, A. M. Dondorp, N. P. Day, N. J. White and T.R.A.C., *N. Engl. J. Med*., 2014, **371**, 411.
8. D. L. Saunders, P. Vanachayangkul and C. Lon, *N. Engl. J. Med*., 2014, **371**, 484.
9. B. M. Greenwood, D. A. Fidock, D. E. Kyle, S. H. Kappe, P. L. Alonso, F. H. Collins and P. E. Duffy, *J. Clin. Invest*., 2008, **118**, 1266.
10. D. L. Medica and P. Sinnis, *Infect. Immun*., 2005, **73**, 4363.
11. R. Amino, S. Thiberge, B. Martin, S. Celli, S. Shorte, F. Frischknecht and R. Menard, *Nat. Med.*, 2006, **12**, 220.
12. A. Sturm, R. Amino, C. van de Sand, T. Regen, S. Retzlaff, A. Rennenberg, A. Krueger, J. M. Pollok, R. Menard and V. T. Heussler, *Science*., 2006, **313**, 1287.
13. M. Prudencio, M. M. Mota and A. M. Mendes, *Trends Parasitol*., 2011, **27**, 565.
14. A. G. Maier, B. M. Cooke, A. F. Cowman and L. Tilley, *Nat. Rev. Microbiol*., 2009, **7**, 341.
15. S. E. Francis, D. J. Sullivan and D. E. Goldberg, *Annu. Rev. Microbiol.*, 1997, **51**, 97.

16. S. K. Nilsson, L. M. Childs, C. Buckee and M. Marti, *PLoS Pathog.*, 2015, **11**, 17.
17. R. E. Sinden, *Parasitology*, 1982, **84**, 1.
18. T. Bousema and C. Drakeley, *Clin. Microbiol. Rev.*, 2011, **24**, 377.
19. F. Frischknecht and K. Matuschewski, *Cold Spring Harb. Perspect. Med.*, 2017, **7**, a025478.
20. L. H. Bannister, J. M. Hopkins, R. E. Fowler, S. Krishna and G. H. Mitchell, *Parasitol. Today*, 2000, **16**, 427.
21. M. Aikawa, C. G. Huff and H. Sprinz, *J. Cell Biol.*, 1967, **34**, 229.
22. H. Ginsburg, *Blood Cells.*, 1990, **16**, 225.
23. M. Marti, R. T. Good, M. Rug, E. Knuepfer and A. F. Cowman, *Science*, 2004, **306**, 1930.
24. N. Abu Bakar, N. Klonis, E. Hanssen, C. Chan and L. Tilley, *J. Cell Sci.*, 2010, **123**, 441.
25. M. Aikawa, P. K. Hepler, C. G. Huff and H. Sprinz, *J. Cell Biol*, 1966, **28**, 355.
26. P. J. Rosenthal and S. R. Meshnick, *Mol. Biochem. Parasit.*, 1996, **83**, 131.
27. C. Spycher, M. Rug, E. Pachlatko, E. Hanssen, D. Ferguson, A. F. Cowman, L. Tilley and H. P. Beck, *Mol. Microbiol.*, 2008, **68**, 1300.
28. T. Y. Sam-Yellowe, *Trends Parasitol.*, 2009, **25**, 277.
29. E. Hanssen, P. J. McMillan and L. Tilley, *Int. J. Parasit.*, 2010, **40**, 1127.
30. G. G. van Dooren, M. Marti, C. J. Tonkin, L. M. Stimmler, A. F. Cowman and G. I. McFadden, *Mol. Microbiol.*, 2005, **57**, 405.
31. S. Glushakova, D. Yin, T. Li and J. Zimmerberg, *Curr. Biol.*, 2005, **15**, 1645.
32. V. L. Hale, J. M. Watermeyer, F. Hackett, G. Vizcay-Barrena, C. van Ooij, J. A. Thomas, M. C. Spink, M. Harkiolaki, E. Duke, R. A. Fleck, M. J. Blackman and H. R. Saibil, *Proc. Natl. Acad. Sci. U. S. A.*, 2017, **114**, 3439.
33. L. Blanc, A. De Gassart, C. Geminard, P. Bette-Bobillo and M. Vidal, *Blood Cells Mol. Dis.*, 2005, **35**, 21.
34. M. Moras, S. D. Lefevre and M. A. Ostuni, *Front. Physiol.*, 2017, **8**, 1076.
35. Y. Tong and M. Guo, *Arch. Biochem. Biophys.*, 2009, **481**, 1.
36. N. D. Hammer and E. P. Skaar, *Annu. Rev. Microbiol.*, 2011, **65**, 129.
37. J. M. Combrinck, T. E. Mabotha, K. K. Ncokazi, M. A. Ambele, D. Taylor, P. J. Smith, H. C. Hoppe and T. J. Egan, *ACS Chem. Biol.*, 2013, **8**, 133.
38. V. L. Lew, T. Tiffert and H. Ginsburg, *Blood*, 2003, **101**, 4189.
39. D. A. Elliott, M. T. McIntosh, H. D. Hosgood, S. Chen, G. Zhang, P. Baevova and K. A. Joiner, *Proc. Natl. Acad. Sci. U. S. A.*, 2008, **105**, 2463.
40. G. J. Doherty and H. T. McMahon, *Annu. Rev. Biochem.*, 2009, **78**, 857.
41. L. Lanzetti, *Curr. Opin. Cell Biol.*, 2007, **19**, 453.
42. K. J. Milani, T. G. Schneider and T. F. Taraschi, *Eukaryot. Cell*, 2015, **14**, 415.
43. D. E. Goldberg, A. F. G. Slater, A. Cerami and G. B. Henderson, *Proc. Natl. Acad. Sci. U. S. A.*, 1990, **87**, 2931.
44. I. Y. Gluzman, S. E. Francis, A. Oksman, C. E. Smith, K. L. Duffin and D. E. Goldberg, *J. Clin. Invest.*, 1994, **93**, 1602.
45. P. J. Rosenthal, *Exp. Parasitol.*, 1995, **80**, 272.
46. S. E. Francis, I. Y. Gluzman, A. Oksman, D. Banerjee and D. E. Goldberg, *Mol. Biochem. Parasitol.*, 1996, **83**, 189.
47. R. Banerjee, J. Liu, W. Beatty, L. Pelosof, M. Klemba and D. E. Goldberg, *Proc. Natl. Acad. Sci. U. S. A.*, 2002, **99**, 990.
48. P. J. Rosenthal, *Int. J. Parasit.*, 2004, **34**, 1489.
49. K. K. Eggleson, K. L. Duffin and D. E. Goldberg, *J. Biol. Chem.*, 1999, **274**, 32411.
50. M. Klemba, I. Gluzman and D. E. Goldberg, *J. Biol. Chem.*, 2004, **279**, 43000.

51. M. Chugh, V. Sundararaman, S. Kumar, V. S. Reddy, W. A. Siddiqui, K. D. Stuart and P. Malhotra, *Proc. Natl. Acad. Sci. U. S. A.*, 2013, **110**, 5392.
52. I. W. Sherman, *Bull. World Health Organ.*, 1977, **55**, 265.
53. M. Krugliak, J. Zhang and H. Ginsburg, *Mol. Biochem. Parasitol.*, 2002, **119**, 249.
54. J. Liu, E. S. Istvan, I. Y. Gluzman, J. Gross and D. E. Goldberg, *Proc. Natl. Acad. Sci. U. S. A.*, 2006, **103**, 8840.
55. R. J. W. Allen and K. Kirk, *Trends Parasitol.*, 2004, **20**, 7.
56. V. Jeney, J. Balla, A. Yachie, Z. Varga, G. M. Vercellotti, J. W. Eaton and G. Balla, *Blood*, 2002, **100**, 879.
57. S. Kumar and U. Bandyopadhyay, *Toxicol. Lett.*, 2005, **157**, 175.
58. S. T. Fraser, R. G. Midwinter, B. S. Berger and R. Stocker, *Adv. Hematol.*, 2011, **2011**, 473709.
59. H. Atamna and H. Ginsburg, *Mol. Biochem. Parasitol.*, 1993, **61**, 231.
60. K. Becker, L. Tilley, J. L. Vennerstrom, D. Roberts, S. Rogerson and H. Ginsburg, *Int. J. Parasit.*, 2004, **34**, 163.
61. S. Müller, *Mol. Microbiol.*, 2004, **53**, 1291.
62. L. W. Scheibel, I. W. Sherman, *Malaria: Principles and Practice of Malariology*, Churchill Livingstone, Edinburgh, 1988.
63. R. Virchow, *Virchows Arch. Pathol. Anat. Physiol. Klin. Med.*, 1849, **2,** 587.
64. L. J. Brucechwatt, *J. R. Soc. Med.*, 1981, **74**, 531.
65. W. H. Brown, *J. Exp. Med.*, 1911, **13,** 290.
66. C. D. Fitch and P. Kanjananggulpan, *J. Biol. Chem.*, 1987, **262**, 15552.
67. A. F. Slater, W. J. Swiggard, B. R. Orton, W. D. Flitter, D. E. Goldberg, A. Cerami and G. B. Henderson, *Proc. Natl. Acad. Sci. U. S. A.*, 1991, **88**, 325.
68. D. S. Bohle, R. E. Dinnebier, S. K. Madsen and P. W. Stephens, *J. Biol. Chem.*, 1997, **272**, 713.
69. D. S. Bohle, P. Debrunner, P. A. Jordan, S. K. Madsen and C. E. Schulz, *J. Am. Chem. Soc.*, 1998, **120**, 8255.
70. S. Pagola, P. W. Stephens, D. S. Bohle, A. D. Kosar and S. K. Madsen, *Nature*, 2000, **404**, 307.
71. J. Gildenhuys, T. le Roex, T. J. Egan and K. A. de Villiers, *J. Am. Chem. Soc.*, 2013, **135**, 1037.
72. A. V. Graca-Souza, C. Maya-Monteiro, G. O. Paiva-Silva, G. R. Braz, M. C. Paes, M. H. Sorgine, M. F. Oliveira and P. L. Oliveira, *Insect Biochem. Mol. Biol.*, 2006, **36**, 322.
73. M. F. Oliveira, J. R. Silva, M. Dansa-Petretski, W. de Souza, U. Lins, C. M. Braga, H. Masuda and P. L. Oliveira, *Nature*, 1999, **400**, 517.
74. M. F. Oliveira, J. C. d'Avila, C. R. Torres, P. L. Oliveira, A. J. Tempone, F. D. Rumjanek, C. M. Braga, J. R. Silva, M. Dansa-Petretski, M. A. Oliveira, W. de Souza and S. T. Ferreira, *Mol. Biochem. Parasitol.*, 2000, **111**, 217.
75. M. M. Chen, L. Shi and D. J. Sullivan, *Mol. Biochem. Parasitol.*, 2001, **113**, 1.
76. M. F. Oliveira, S. W. Kycia, A. Gomez, A. J. Kosar, D. S. Bohle, E. Hempelmann, D. Menezes, M. A. Vannier-Santos, P. L. Oliveira and S. T. Ferreira, *FEBS Lett.*, 2005, **579**, 6010.
77. J. R. Silva, F. B. Mury, M. F. Oliveira, P. L. Oliveira, C. P. Silva and M. Dansa-Petretski, *Insect Biochem. Mol. Biol.*, 2007, **37**, 523.
78. R. Stiebler, D. Majerowicz, J. Knudsen, K. C. Gondim, D. W. Wright, T. J. Egan and M. F. Oliveira, *PLoS One*, 2014, **9**, e88976.
79. M. F. Oliveira, J. C. d'Avila, A. J. Tempone, J. B. Soares, F. D. Rumjanek, A. Ferreira-Pereira, S. T. Ferreira and P. L. Oliveira, *J. Infect. Dis.*, 2004, **190**, 843.

80. J. B. R. C. Soares, C. M. Maya-Monteiro, P. R. B. Bittencourt-Cunha, G. C. Atella, F. A. Lara, J. C. P. d'Avila, D. Menezes, M. A. Vannier-Santos, P. L. Oliveira, T. J. Egan and M. F. Oliveira, *FEBS Lett.*, 2007, **581**, 1742.
81. C. F. Arias, *R. Soc. Open Sci.*, 2017, **4**, 12.
82. C. White, X. Yuan, P. J. Schmidt, E. Bresciani, T. K. Samuel, D. Campagna, C. Hall, K. Bishop, M. L. Calicchio, A. Lapierre, D. M. Ward, P. Liu, M. D. Fleming and I. Hamza, *Cell Metab.*, 2013, **17**, 261.
83. G. Kovtunovych, M. C. Ghosh, W. Ollivierre, R. P. Weitzel, M. A. Eckhaus, J. F. Tisdale, A. Yachie and T. A. Rouault, *Blood*, 2014, **124**, 1522.
84. R. H. Pek, X. Yuan, N. Rietzschel, J. Zhang, L. K. Jackson, Eiji. Nishibori, A. Ribeiro, W. R. Simmons, J. Jagadeesh, H. Sugimoto, M. Z. Alam, L. J. Garrett, M. Haldar, M. Ralle, J. Phillips, D. Bodine, and I. Hamza, *bioRxiv*, 2019, **629725**, DOI: 10.1101/629725.
85. C. Delaby, C. Rondeau, C. Pouzet, A. Willemetz, N. Pilard, M. Desjardins and F. Canonne-Hergaux, *PLoS One*, 2012, **7**, e42199.
86. R. Crichton, *Biological Inorganic Chemistry: A New Introduction to Molecular Structure and Function*, Elsevier, United Kingdom, 2018.
87. J. Cuif and Y. Dauphin, *J. Struct. Biol.*, 2005, **150**, 319.
88. E. D. Sone, S. Weiner and L. Addadi, *J. Struct. Biol.*, 2007, **158**, 428.
89. S. Matsumura, S. Kajiyama, T. Nishimura and T. Kato, *Small*, 2015, **11**, 5127.
90. R. T. DeVol, C. Y. Sun, M. A. Marcus, S. N. Coppersmith, S. C. Myneni and P. U. Gilbert, *J. Am. Chem. Soc.*, 2015, **137**, 13325.
91. Y. Chen, Y. Feng, J. G. Deveaux, M. A. Masoud, F. S. Chandra, H. Chen, D. Zhang and L. Feng, *Minerals*, 2019, **9**, 68.
92. H. C. Anderson, *J. Cell Biol.*, 1967, **35**, 81.
93. G. W. Bernard and V. Marvaso, *Am. J. Anat.*, 1969, **125**, 271.
94. R. E. Wuthier, *Fed. Proc.*, 1976, **35**, 117.
95. B. R. Genge, L. N. Wu and R. E. Wuthier, *J. Biol. Chem.*, 2008, **283**, 9737.
96. L. N. Wu, B. R. Genge and R. E. Wuthier, *J. Biol. Chem.*, 2008, **283**, 3827.
97. D. G. Reid, C. M. Shanahan, M. J. Duer, L. G. Arroyo, M. Schoppet, R. A. Brooks and R. C. Murray, *J. Lipid Res.*, 2012, **53**, 1569.
98. J. R. Young, J. M. Didymus, P. R. Bown, B. Prins and S. Mann, *Nature*, 1992, **356**, 516.
99. R. Blakemore, *Science*, 1975, **190**, 377.
100. A. Arakaki, J. Webb and T. Matsunaga, *J. Biol. Chem.*, 2003, **278**, 8745.
101. Y. Amemiya, A. Arakaki, S. S. Staniland, T. Tanaka and T. Matsunaga, *Biomaterials*, 2007, **28**, 5381.
102. T. Prozorov, S. K. Mallapragada, B. Narasimhan, L. Wang, P. Palo, M. Nilsen-Hamilton, T. J. Williams, D. A. Bazylinski, R. Prozorov and P. C. Canfield, *Adv. Funct. Mater.*, 2007, **17**, 951.
103. A. Arakaki, H. Nakazawa, M. Nemoto, T. Mori and T. Matsunaga, *J. R. Soc. Interface*, 2008, **5**, 977.
104. D. Murat, A. Quinlan, H. Vali and A. Komeili, *Proc. Natl. Acad. Sci. U. S. A.*, 2010, **107**, 5593.
105. D. M. Hershey, P. J. Browne, A. T. Iavarone, J. Teyra, E. H. Lee, S. S. Sidhu and A. Komeili, *J. Biol. Chem.*, 2016, **291**, 17941.
106. K. Mann, A. J. Poustka and M. Mann, *Proteome Sci.*, 2008, **6**, 22.
107. K. Mann, E. Edsinger-Gonzales and M. Mann, *Proteome Sci.*, 2012, **10**, 28.
108. J. L. Drake, T. Mass, L. Haramaty, E. Zelzion, D. Bhattacharya and P. G. Falkowski, *Proc. Natl. Acad. Sci. U. S. A.*, 2013, **110**, 3788.

109. N. Okumura, M. Tsujihata, C. Momohara, I. Yoshioka, K. Suto, N. Nonomura, A. Okuyama and T. Takao, *PLoS One*, 2013, **8**, e68624.
110. F. A. Witzmann, A. P. Evan, F. L. Coe, E. M. Worcester, J. E. Lingeman and J. C. Williams, *Proteome Sci.*, 2016, **14**, 4.
111. R. D. Alves, J. A. Demmers, K. Bezstarosti, B. C. van der Eerden, J. A. Verhaar, M. Eijken and J. P. van Leeuwen, *J. Proteome Res.*, 2011, **10**, 4725.
112. H. C. Anderson, *Clin. Orthop. Rel. Res.*, 1995, **314**, 266.
113. T. J. Egan, J. M. Combrinck, J. Egan, G. R. Hearne, H. M. Marques, S. Ntenteni, B. T. Sewell, P. J. Smith, D. Taylor, D. A. van Schalkwyk and J. C. Walden, *Biochem. J.*, 2002, **365**, 343.
114. A. F. Slater and A. Cerami, *Nature*, 1992, **355**, 167.
115. T. J. Egan, D. C. Ross and P. A. Adams, *FEBS Lett.*, 1994, **352**, 54.
116. T. Were, G. C. Davenport, E. O. Yamo, J. B. Hittner, G. A. Awandare, M. F. Otieno, C. Ouma, A. S. Orago, J. M. Vulule, J. M. Ong'echa and D. J. Perkins, *Microbes Infect.*, 2009, **11**, 811.
117. C. K. Carney, A. C. Schrimpe, K. Halfpenny, R. S. Harry, C. M. Miller, M. Broncel, S. L. Sewell, J. E. Schaff, R. Deol, M. D. Carter and D. W. Wright, *J. Biol. Inorg. Chem.*, 2006, **11**, 917.
118. C. Casals-Pascual, O. Kai, J. O. Cheung, S. Williams, B. Lowe, M. Nyanoti, T. N. Williams, K. Maitland, M. Molyneux, C. R. Newton, N. Peshu, S. M. Watt and D. J. Roberts, *Blood*, 2006, **108**, 2569.
119. B. K. Wilson, M. R. Behrend, M. P. Horning and M. C. Hegg, *Opt. Express*, 2011, **19**, 12190.
120. E. Y. Lukianova-Hleb, K. M. Campbell, P. E. Constantinou, J. Braam, J. S. Olson, R. E. Ware, D. J. Sullivan and D. O. Lapotko, *Proc. Natl. Acad. Sci. U. S. A.*, 2014, **111**, 900.
121. B. T. Grimberg and K. O. Grimberg, *Expert Rev. Anti-Infect. Ther.*, 2016, **14**, 879.
122. A. Dorn, R. Stoffel, H. Matile, A. Bubendorf and R. G. Ridley, *Nature*, 1995, **374**, 269.
123. T. E. Wellems and R. J. Howard, *Proc. Natl. Acad. Sci. U. S. A.*, 1986, **83**, 6065.
124. D. J. Sullivan, I. Y. Gluzman and D. E. Goldberg, *Science*, 1996, **271**, 219.
125. A. Lynn, S. Chandra, P. Malhotra and V. S. Chauhan, *FEBS Lett.*, 1999, **459**, 267.
126. J. Ziegler, R. T. Chang and D. W. Wright, *J. Am. Chem. Soc.*, 1999, **121**, 2395.
127. V. Papalexis, M. A. Siomos, N. Campanale, X. Guo, G. Kocak, M. Foley and L. Tilley, *Mol. Biochem. Parasitol.*, 2001, **115**, 77.
128. T. Akompong, M. Kadekoppala, T. Harrison, A. Oksman, D. E. Goldberg, H. Fujioka, B. U. Samuel, D. Sullivan and K. Haldar, *J. Biol. Chem.*, 2002, **277**, 28923.
129. D. J. Sullivan, *Int. J. Parasit.*, 2002, **32**, 1645.
130. G. S. Noland, N. Briones and D. J. Sullivan, *Mol. Biochem. Parasit.*, 2003, **130**, 91.
131. D. Jani, R. Nagarkatti, W. Beatty, R. Angel, C. Slebodnick, J. Andersen, S. Kumar and D. Rathore, *PLoS Pathog.*, 2008, **4**, e1000053.
132. E. L. Schneider and M. A. Marletta, *Biochemistry*, 2005, **44**, 979.
133. S. Kapishnikov, D. Grolimund, G. Schneider, E. Pereiro, J. G. McNally, J. Als-Nielsen and L. Leiserowitz, *Sci. Rep.*, 2017, **7**, 7610.
134. K. N. Olafson, M. A. Ketchum, J. D. Rimer and P. G. Vekilov, *Proc. Natl. Acad. Sci. U. S. A.*, 2015, **112**, 4946.
135. M. J. Gardner, N. Hall, E. Fung, O. White, M. Berriman, R. W. Hyman, J. M. Carlton, A. Pain, K. E. Nelson, S. Bowman, I. T. Paulsen, K. James, J. A. Eisen, K. Rutherford, S. L. Salzberg, A. Craig, S. Kyes, M. S. Chan, V. Nene, S. J. Shallom, B. Suh, J. Peterson, S. Angiuoli, M. Pertea, J. Allen, J. Selengut, D. Haft, M. W. Mather, A. B. Vaidya, D. M. A. Martin, A. H. Fairlamb, M. J. Fraunholz, D. S. Roos, S. A. Ralph, G. I. McFadden, L. M. Cummings, G. M. Subramanian, C. Mungall, J. C. Venter, D. J. Carucci, S. L. Hoffman, C. Newbold, R. W. Davis, C. M. Fraser and B. Barrell, *Nature*, 2002, **419**, 498.

136. G. J. Seifert, *Int. J. Mol. Sci*., 2018, **19**, e1628.
137. K. Nakatani, H. Ishikawa, S. Aono and Y. Mizutani, *Sci. Rep*., 2014, **4**, 6137.
138. K. Nakatani, H. Ishikawa, S. Aono and Y. Mizutani, *Biochem. Biophys. Res. Commun*., 2013, **439**, 477.
139. K. Bendrat, B. J. Berger and A. Cerami, *Nature*, 1995, **378**, 138.
140. A. Dorn, S. R. Vippagunta, H. Matile, A. Bubendorf, J. L. Vennerstrom and R. G. Ridley, *Biochem. Pharmacol*., 1998, **55**, 737.
141. C. D. Fitch, G. Z. Cai, Y. F. Chen and J. D. Shoemaker, *Biochim. Biophys. Acta*., 1999, **1454**, 31.
142. N. M. Palacpac, Y. Hiramine, F. Mi-ichi, M. Torii, K. Kita, R. Hiramatsu, T. Horii and T. Mitamura, *J. Cell Sci*., 2004, **117**, 1469.
143. K. E. Jackson, N. Klonis, D. J. P. Ferguson, A. Adisa, C. Dogovski and L. Tilley, *Mol. Microbiol*., 2004, **54**, 109.
144. O. Vielemeyer, M. T. McIntosh, K. A. Joiner and I. Coppens, *Mol. Biochem. Parasitol*., 2004, **135**, 195.
145. I. Coppens and O. Vielemeyer, *Int. J. Parasit*., 2005, **35**, 597.
146. J. M. Pisciotta, I. Coppens, A. K. Tripathi, P. F. Scholl, J. Shuman, S. Bajad, V. Shulaev and D. J. Sullivan, *Biochem. J*., 2007, **402**, 197.
147. T. J. Egan, J. Y. J. Chen, K. A. de Villiers, T. E. Mabotha, K. J. Naidoo, K. K. Ncokazi, S. J. Langford, D. McNaughton, S. Pandiancherri and B. R. Wood, *FEBS Lett*., 2006, **580**, 5105.
148. A. N. Hoang, K. K. Ncokazi, K. A. de Villiers, D. W. Wright and T. J. Egan, *Dalton Trans*., 2010, **39**, 1235.
149. A. N. Hoang, R. D. Sandlin, A. Omar, T. J. Egan and D. W. Wright, *Biochemistry*, 2010, **49**, 10107.
150. M. A. Ambele and T. J. Egan, *Malar. J*., 2012, **11**, 337.
151. S. Kapishnikov, A. Weiner, E. Shimoni, P. Guttmann, G. Schneider, N. Dahan-Pasternak, R. Dzikowski, L. Leiserowitz and M. Elbaum, *Proc. Natl. Acad. Sci. U. S. A.*, 2012, **109**, 11188.
152. S. Kapishnikov, A. Weiner, E. Shimoni, G. Schneider, M. Elbaum and L. Leiserowitz, *Langmuir*, 2013, **29**, 14595.
153. M. A. Ambele, B. T. Sewell, F. R. Cummings, P. J. Smith and T. J. Egan, *Cryst. Growth Des*., 2013, **13**, 4442.
154. T. J. Egan, W. W. Mavuso and K. K. Ncokazi, *Biochemistry*, 2001, **40**, 204.
155. R. Stiebler, A. N. Hoang, T. J. Egan, D. W. Wright and M. F. Oliveira, *PLoS One*, 2010, **5**, e12694.
156. N. T. Huy, D. T. Uyen, A. Maeda, D. T. X. Trang, T. Oida, S. Harada and K. Kamei, *Antimicrob. Agents Chemother*., 2007, **51**, 350.
157. Y. Y. Kim, K. Ganesan, P. Yang, A. N. Kulak, S. Borukhin, S. Pechook, L. Ribeiro, R. Kröger, S. J. Eichhorn, S. P. Armes, B. Pokroy and F. C. Meldrum, *Nat. Mater*., 2011, **10**, 890.
158. C. Liu, L. Xie and R. Zhang, *Sci. Rep*., 2015, **5**, e18338.
159. D. C. Green, J. Ihli, P. D. Thornton, M. A. Holden, B. Marzec, Y. Y. Kim, A. N. Kulak, M. A. Levenstein, C. Tang, C. Lynch, S. E. D. Webb, C. J. Tynan and F. C. Meldrum, *Nat. Commun*., 2016, **7**, 13524.
160. E. D. Guerra, F. Baakdah, E. Georges, D. S. Bohle and M. Cerruti, *J. Inorg. Biochem*., 2019, **194**, 214.
161. F. C. Fang and A. Casadevall, *Infect. Immun*., 2011, **79**, 1401.
162. R. Noguera-Solano, R. Ruiz-Gutierrez and J. M. Rodriguez-Caso, *Endeavour*, 2013, **37**, 213.
163. V. E. Velculescu, L. Zhang, W. Zhou, J. Vogelstein, M. A. Basrai, D. E. Bassett, P. Hieter, B. Vogelstein and K. W. Kinzler, *Cell*, 1997, **88**, 243.

164. M. Wilkins, *Expert Rev. Proteomics*, 2009, **6**, 599.
165. S. G. Oliver, M. K. Winson, D. B. Kell and F. Baganz, *Trends Biotechnol.*, 1998, **16**, 373.
166. F. Sanger, S. Nicklen and A. R. Coulson, *Proc. Natl. Acad. Sci. U. S. A.*, 1977, **74**, 5463.
167. R. Bumgarner, *Current Protocols in Molecular Biology*, John Wiley & Sons, 2013.
168. E. L. van Dijk, H. Auger, Y. Jaszczyszyn and C. Thermes, *Trends Genet.*, 2014, **30**, 418.
169. M. Mesri, *Adv. Med.*, 2014, **2014**, e238045.
170. N. Iwamoto and T. Shimada, *Pharmacol. Ther.*, 2018, **185**, 147.
171. K. J. Karczewski and M. P. Snyder, *Nat. Rev. Genet.*, 2018, **19**, 299.
172. E. R. Pearson, *Diabet. Med.*, 2016, **33**, 712.
173. S. Chakraborty, M. I. Hosen, M. Ahmed and H. U. Shekhar, *Biomed. Res. Int.*, 2018, **2018**, e9836256.
174. M. M. Khan, O. Ernst, N. P. Manes, B. L. Oyler, I. D. C. Fraser, D. R. Goodlett and A. Nita-Lazar, *ACS Infect. Dis.*, 2019, **5**, 493.
175. N. L. Anderson and N. G. Anderson, *Electrophoresis*, 1998, **19**, 1853.
176. C. Pinswasdi, S. Thaithong, G. H. Beale, B. Fenton, H. K. Webster and K. Pavanand, *Mol. Biochem. Parasitol.*, 1987, **23**, 159.
177. G. Horgan, A. Creasey and B. Fenton, *Electrophoresis*, 1992, **13**, 871.
178. L. Florens, M. P. Washburn, J. D. Raine, R. M. Anthony, M. Grainger, J. D. Haynes, J. K. Moch, N. Muster, J. B. Sacci, D. L. Tabb, A. A. Witney, D. Wolters, Y. Wu, M. J. Gardner, A. A. Holder, R. E. Sinden, J. R. Yates and D. J. Carucci, *Nature*, 2002, **419**, 520.
179. E. Lasonder, Y. Ishihama, J. S. Andersen, A. M. Vermunt, A. Pain, R. W. Sauerwein, W. M. Eling, N. Hall, A. P. Waters, H. G. Stunnenberg and M. Mann, *Nature*, 2002, **419**, 537.
180. K. E. Swearingen and S. E. Lindner, *Trends Parasitol.*, 2018, **34**, 945.
181. M. Lamarque, C. Tastet, J. Poncet, E. Demettre, P. Jouin, H. Vial and J. F. Dubremetz, *Proteomics. Clin. Appl.*, 2008, **2**, 1361.
182. K. G. Le Roch, Y. Zhou, P. L. Blair, M. Grainger, J. K. Moch, J. D. Haynes, P. De la Vega, A. A. Holder, S. Batalov, D. J. Carucci and E. A. Winzeler, *Science*, 2003, **301**, 1503.
183. K. J. Saliba, R. J. W. Allen, S. Zissis, P. G. Bray, S. A. Ward and K. Kirk, *J. Biol. Chem.*, 2003, **278**, 5605.
184. M. R. Wenk, *Nat. Rev. Drug Discov.*, 2005, **4**, 594.
185. A. D. Watson, *J. Lipid Res.*, 2006, **47**, 2101.
186. X. Han and R. W. Gross, *J. Lipid Res.*, 2003, **44**, 1071.
187. K. Yang and X. Han, *Trends Biochem. Sci.*, 2016, **41**, 954.
188. M. R. Wenk, *FEBS Lett.*, 2006, **580**, 5541.
189. C. Ben Mamoun, S. T. Prigge and H. Vial, *Drug Dev. Res.*, 2010, **71**, 44.
190. R. B. Mikkelsen, M. Kamber, K. S. Wadwa, P. S. Lin and R. Schmidt-Ullrich, *Proc. Natl. Acad. Sci. U. S. A.*, 1988, **85**, 5956.
191. S. C. Murphy, N. L. Hiller, T. Harrison, J. W. Lomasney, N. Mohandas and K. Haldar, *Mol. Membr. Biol.*, 2006, **23**, 81.
192. E. Sezgin, I. Levental, S. Mayor and C. Eggeling, *Nat. Rev. Mol. Cell Biol.*, 2017, **18**, 361.
193. I. W. Sherman, *Microbiol. Rev.*, 1979, **43**, 453.
194. S. Besteiro, S. Vo Duy, C. Perigaud, I. Lefebvre-Tournier and H. J. Vial, *Parasitology*, 2010, **137**, 1343.
195. K. Hanada, M. Nishijima, Y. Akamatsu and R. E. Pagano, *J. Biol. Chem.*, 1995, **270**, 6254.
196. R. Schroeder, E. London and D. Brown, *Proc. Natl. Acad. Sci. U. S. A.*, 1994, **91**, 12130.
197. D. A. Brown and J. K. Rose, *Cell*, 1992, **68**, 533.

198. B. U. Samuel, N. Mohandas, T. Harrison, H. McManus, W. Rosse, M. Reid and K. Haldar, *J. Biol. Chem*., 2001, **276**, 29319.
199. S. Külzer, M. Rug, K. Brinkmann, P. Cannon, A. Cowman, K. Lingelbach, G. L. Blatch, A. G. Maier and J. M. Przyborski, *Cell Microbiol*., 2010, **12**, 1398.
200. S. Frankland, A. Adisa, P. Horrocks, T. F. Taraschi, T. Schneider, S. R. Elliott, S. J. Rogerson, E. Knuepfer, A. F. Cowman, C. I. Newbold and L. Tilley, *Eukaryot. Cell*, 2006, **5**, 849.
201. A. Behl, V. Kumar, A. Bisht, J. J. Panda, R. Hora and P. C. Mishra, *Sci. Rep*., 2019, **9**, 2664.
202. F. Tokumasu, G. Crivat, H. Ackerman, J. Hwang and T. E. Wellems, *Biol. Open*, 2014, **3**, 529.
203. S. Gulati, E. H. Ekland, K. V. Ruggles, R. B. Chan, B. Jayabalasingham, B. Zhou, P. Mantel, M. C. S. Lee, N. Spottiswoode, O. Coburn-Flynn, D. Hjelmqvist, T. S. Worgall, M. Marti, G. Di Paolo and D. A. Fidock, *Cell Host Microbe*, 2015, **18**, 371.
204. C. R. Gault, L. M. Obeid and Y. A. Hannun, *Sphingolipids as Signaling and Regulatory Molecules*, Springer-Verlag Berlin, Berlin, 2010.
205. J. I. Macrae, S. Lopaticki, A. G. Maier, T. Rupasinghe, A. Nahid, A. F. Cowman and M. J. McConville, *Mol. Microbiol*., 2014, **91**, 762.
206. F. M. Goni and A. Alonso, *Prog. Lipid Res*., 1999, **38**, 1.
207. M. A. Welte and A. P. Gould, *Biochim. Biophys. Acta Mol. Cell Biol. Lipids*, 2017, **1862**, 1260.
208. L. A. Finney and T. V. O'Halloran, *Science*, 2003, **300**, 931.
209. R. J. P. Williams, *Coord. Chem. Rev*., 2001, **216**, 583.
210. K. J. Waldron, J. C. Rutherford, D. Ford and N. J. Robinson, *Nature*, 2009, **460**, 823.
211. S. Mounicou, J. Szpunar and R. Lobinski, *Chem. Soc. Rev*., 2009, **38**, 1119.
212. H. Haraguchi, *J. Anal. At. Spectrom*., 2004, **19**, 5.
213. J. Szpunar, *Anal. Bioanal. Chem*., 2004, **378**, 54.
214. H. Haraguchi, *Metallomics*, 2017, **9**, 1001.
215. J. M. Combrinck, K. Y. Fong, L. Gibhard, P. J. Smith, D. W. Wright and T. J. Egan, *Malar. J*., 2015, **14**, 253.
216. R. G. Marvin, J. L. Wolford, M. J. Kidd, S. Murphy, J. Ward, E. L. Que, M. L. Mayer, J. E. Penner-Hahn, K. Haldar and T. V. O'Halloran, *Chem. Biol*., 2012, **19**, 731.
217. E. Carafoli and J. Krebs, *J. Biol. Chem*., 2016, **291**, 20849.
218. C. R. S. Garcia, *Parasitol. Today*, 1999, **15**, 488.
219. S. Glushakova, V. Lizunov, P. S. Blank, K. Melikov, G. Humphrey and J. Zimmerberg, *Malar. J*., 2013, **12**, 41.
220. A. Vaid, D. C. Thomas and P. Sharma, *J. Biol. Chem*., 2008, **283**, 5589.
221. C. Andresen, M. Niklasson, S. C. Eklöf, B. Wallner and P. Lundström, *PLoS One*, 2017, **12**, e018721.
222. S. Absalon, K. Blomqvist, R. M. Rudlaff, T. J. DeLano, M. P. Pollastri and J. D. Dvorin, *mBio*, 2018, **9**, e0013-18.
223. P. Wardman and L. P. Candeias, *Radiat. Res*., 1996, **145**, 523.
224. D. Rasoloson, L. Shi, C. R. Chong, B. F. Kafsack and D. J. Sullivan, *Biochem. J*., 2004, **381**, 803.
225. D. L. Choveaux, J. M. Przyborski and J. P. D. Goldring, *Malar. J*., 2012, **11**, 397.
226. D. L. Choveaux, R. G. E. Krause, J. M. Przyborski and J. P. D. Goldring, *Exp. Parasitol*., 2015, **148**, 30.
227. P. Dean, P. Major, S. Nakjang, R. P. Hirt and T. M. Embley, *Front. Plant Sci*., 2014, **5**, e00153.
228. S. M. Landfear, Methods Mol. Biol., 2010, **637**, 245.
229. C. J. Woodrow, R. J. Burchmore and S. Krishna, *Proc. Natl. Acad. Sci. U. S. A*., 2000, **97**, 9931.
230. K. J. Saliba, R. E. Martin, A. Bröer, R. I. Henry, C. S. McCarthy, M. J. Downie, R. J. W. Allen, K. A. Mullin, G. I. McFadden, S. Bröer and K. Kirk, *Nature*, 2006, **443**, 582.

231. R. E. Martin, H. Ginsburg and K. Kirk, *Mol. Microbiol*., 2009, **74**, 519.
232. K. Slavic, S. Krishna, A. Lahree, G. Bouyer, K. K. Hanson, I. Vera, J. K. Pittman, H. M. Staines and M. M. Mota, *Nat. Commun*., 2016, **7**, e10403.
233. D. Walliker, I. A. Quakyi, T. E. Wellems, T. F. McCutchan, A. Szarfman, W. T. London, L. M. Corcoran, T. R. Burkot and R. Carter, *Science*, 1987, **236**, 1661.
234. R. M. Ekong, K. J. H. Robson, D. A. Baker and D. C. Warhurst, *Parasitology*, 1993, **106**, 107.
235. F. Guinet, J. A. Dvorak, H. Fujioka, D. B. Keister, O. Muratova, D. C. Kaslow, M. Aikawa, A. B. Vaidya and T. E. Wellems, *J. Cell Biol*., 1996, **135**, 269.
236. D. A. Joy, X. Feng, J. Mu, T. Furuya, K. Chotivanich, A. U. Krettli, M. Ho, A. Wang, N. J. White, E. Suh, P. Beerli and X. Su, *Science*, 2003, **300**, 318.
237. W. Trager and J. B. Jensen, *Science*, 1976, **193**, 673.
238. L. F. Meisner, T. W. Chuprevich and S. L. Inhorn, *Nat. New Biol*., 1973, **245**, 145.
239. E. H. Ekland, M. H. Akabas and D. A. Fidock, *Cell*, 2011, **145**, 645.
240. M. A. Lacaille-Dubois and H. Wagner, *Phytomedicine*, 1996, **2**, 363.
241. H. Ginsburg, O. Famin, J. Zhang and M. Krugliak, *Biochem. Pharmacol*., 1998, **56**, 1305.
242. A. Shevchenko, H. Tomas, J. Havlis, J. V. Olsen and M. Mann, *Nat. Protoc*., 2006, **1**, 2856.
243. W. Mertz, *Science*, 1981, **213**, 1332.
244. L. Poulsen, L. B. Møller, K. Plunkett, J. Belmont, Z. Tümer and N. Horn, *Genet. Test*., 2004, **8**, 286.
245. H. Irving and R. J. P. Williams, *Nature*, 1948, **162**, 746.
246. F. Imperi, F. Tiburzi and P. Visca, *Proc. Natl. Acad. Sci. U. S. A*., 2009, **106**, 20440.
247. C. M. Jones, R. M. Wells, A. V. R. Madduri, M. B. Renfrow, C. Ratledge, D. B. Moody and M. Niederweis, *Proc. Natl. Acad. Sci. U. S. A*., 2014, **111**, 1945.
248. M. Solioz, *Metallomics*, 2016, **8**, 824.
249. R. J. C. Brown and M. J. T. Milton, *TrAC-Trend Anal. Chem*., 2005, **24**, 266.
250. A. Montaser and D. W. Golightly, *Inductively Coupled Plasmas in Analytical Atomic Spectrometry*, VCH Publishers Inc, New York, 1992.
251. R. Docampo and S. N. J. Moreno, *Encyclopedia of Malaria,* Springer Science, New York, 2013.
252. K. Neubauer, *Spectroscopy*, 2010, **25**, 30.
253. M. Segura, Y. Madrid and C. Cámara, *J. Anal. At. Spectrom*., 2003, **18**, 1103.
254. R. M. Greendyke, W. A. Meriwether, E. T. Thomas, J. D. Flintjer and M. W. Bayliss, *Am. J. Clin. Path*., 1962, **37**, 429.
255. E. Urrechaga, *Int. J. Lab. Hematol*., 2009, **31**, 528.
256. H. Millart, V. Durlach and J. Durlach, *Magnes. Res.*, 1995, **8**, 65.
257. J. I. MacRae, M. W. A. Dixon, M. K. Dearnley, H. H. Chua, J. M. Chambers, S. Kenny, I. Bottova, L. Tilley and M. J. McConville, *BMC Biol*., 2013, **11**, 67.
258. K. Kirk, H. A. Horner and J. Kirk, *Mol. Biochem. Parasitol*., 1996, **82**, 195.
259. K. Slavic, U. Straschil, L. Reininger, C. Doerig, C. Morin, R. Tewari and S. Krishna, *Mol. Microbiol*., 2010, **75**, 1402.
260. A. Sturm, V. Mollard, A. Cozijnsen, C. D. Goodman and G. I. McFadden, *Proc. Natl. Acad. Sci. U. S. A.*, 2015, **112**, 10216.
261. S. Frassinetti, G. L. Bronzetti, L. Caltavuturo, M. Cini and C. D. Croce, *J. Environ. Pathol. Toxicol. Oncol*., 2006, **25**, 597.
262. C. Andreini, L. Banci, I. Bertini and A. Rosato, *J. Proteome Res*., 2006, **5**, 196.
263. R. S. MacDonald, *J. Nutr*., 2000, **130**, 1500S.
264. K. Jomova and M. Valko, *Toxicology*, 2011, **283**, 65.
265. H. Asahi, M. E. M. Tolba, M. Tanabe and H. Ohmae, *Can. J. Microbiol*., 2013, **59**, 485.

266. H. Asahi, M. E. M. Tolba, M. Tanabe, S. Sugano, K. Abe and F. Kawamoto, *BMC Microbiol*., 2014, **14**, 167.
267. H. Yesilkaya, A. Kadioglu, N. Gingles, J. E. Alexander, T. J. Mitchell and P. W. Andrew, *Infect. Immun*., 2000, **68**, 2819.
268. S. Puri, T. H. Hohle and M. R. O'Brian, *Proc. Natl. Acad. Sci. U. S. A*., 2010, **107**, 10691.
269. S. Kehr, N. Sturm, S. Rahlfs, J. M. Przyborski and K. Becker, *PLoS Pathog*., 2010, **6**, e1001242.
270. L. Banci and I. Bertini, *Metallomics and the Cell. Metal Ions in Life Sciences*, Springer, Dordrecht, 2013.
271. C. L. Dupont, A. Butcher, R. E. Valas, P. E. Bourne and G. Caetano-Anolles, *Proc. Natl. Acad. Sci. U. S. A*., 2010, **107**, 10567.
272. W. Shi and M. R. Chance, *Cell. Mol. Life Sci*., 2008, **65**, 3040.
273. M. F. Perutz, J. C. Kendrew and H. C. Watson, *J. Mol. Biol*., 1965, **13**, 669.
274. J. M. McCord and I. Fridovic, *J. Biol. Chem*., 1969, **244**, 6049.
275. G. Weiss and P. L. Carver, *Clin. Microbiol. Infect*., 2018, **24**, 16.
276. J. E. Cassat and E. P. Skaar, *Semin. Immunopathol*., 2012, **34**, 215.
277. K. H. Rohde and D. W. Dyer, *Front. Biosci*., 2003, **8**, D1186.
278. K. S. Chaturvedi and J. P. Henderson, *Front. Cell. Infect. Microbiol*., 2014, **4**, e00003.
279. T. J. Egan, *J. Inorg. Biochem*., 2008, **102**, 1288.
280. R. Bissinger, P. Modicano, K. Alzoubi, S. Honisch, C. Faggio, M. Abed and F. Lang, *Int. J. Hematol*., 2014, **100**, 51.
281. K. J. Saliba, P. I. Folb and P. J. Smith, *Biochem. Pharmacol*., 1998, **56**, 313.
282. A. S. Paul, E. S. Egan and M. T. Duraisingh, *Curr. Opin. Hematol*., 2015, **22**, 220.
283. P. R. Gilson and B. S. Crabb, *Int. J. Parasit*., 2009, **39**, 91.
284. J. Baum, D. Richard, J. Healer, M. Rug, Z. Krnajski, T. W. Gilberger, J. L. Green, A. A. Holder and A. F. Cowman, *J. Biol. Chem*., 2006, **281**, 5197.
285. M. J. Boyle, D. W. Wilson, J. S. Richards, D. T. Riglar, K. K. A. Tetteh, D. J. Conway, S. A. Ralph, J. Baum and J. G. Beeson, *Proc. Natl. Acad. Sci. U. S. A*., 2010, **107**, 14378.
286. R. Aebersold and M. Mann, *Nature*, 2003, **422**, 198.
287. W. H. Zhu, J. W. Smith and C. M. Huang, *J. Biomed. Biotechnol*., 2010, **2010**, e840518
288. H. B. Liu, R. G. Sadygov and J. R. Yates, *Anal. Chem*., 2004, **76**, 4193.
289. X. Lai, L. Wang, H. Tang and F. A. Witzmann, *J. Proteome Res*., 2011, **10**, 4799.
290. X. Lai, L. Wang and F. A. Witzmann, *Int. J. Proteomics*, 2013, **2013**, e756039.
291. Proteome Software, *Scaffold User Manual*, Portland, 2014.
292. M. Wang, M. Weiss, M. Simonovic, G. Haertinger, S. P. Schrimpf, M. O. Hengartner and C. von Mering, *Mol. Cell. Proteomics*, 2012, **11**, 492.
293. X. Pei, X. An, X. Guo, M. Tarnawski, R. Coppel and N. Mohandas, *J. Biol. Chem*., 2005, **280**, 31166.
294. G. C. D. Carrocini, P. J. A. Zamaro and C. R. Bonini-Domingos, *Rev. Bras. Hematol. Hemoter*., 2011, **33**, 231.
295. R. Buller, M. L. Peterson, Ö. Almarsson and L. Leiserowitz, *Cryst. Growth Des*., 2002, **2**, 553.
296. M. A. Ambele, PhD Thesis, University of Cape Town, 2013.
297. D. E. Clapham, *Cell*, 1995, **80**, 259.
298. M. J. Dreyer, *Medical Technology SA*, 2011, **25**, 29.
299. A. Bogdanova, A. Makhro, J. Wang, P. Lipp and L. Kaestner, *Int. J. Mol. Sci*., 2013, **14**, 9848.
300. S. Singh, M. M. Alam, I. Pal-Bhowmick, J. A. Brzostowski and C. E. Chitnis, *PLoS Pathog*., 2010, **6**, e1000746.

301. M. Wasserman, J. P. Vernot and P. M. Mendoza, *Parasitol. Res*., 1990, **76**, 681.
302. M. N. Leida, J. R. Mahoney and J. W. Eaton, *Biochem. Biophys. Res. Commun*., 1981, **103**, 402.
303. B. Mahajan, A. Selvapandiyan, N. J. Gerald, V. Majam, H. Zheng, T. Wickramarachchi, J. Tiwari, H. Fujioka, J. K. Moch, N. Kumar, L. Aravind, H. L. Nakhasi and S. Kumar, *J. Biol. Chem*., 2008, **283**, 31871.
304. M. A. Fierro, B. Asady, C. F. Brooks, D. W. Cobb, A. Villegas, S. N. J. Moreno and V. Muralidharan, *bioRxiv*, 2019, e457481.
305. M. Klimecka and G. Muszyńska, *Acta Biochim. Pol*., 2007, **54**, 219.
306. K. Kadian, Y. Gupta, P. Kempaiah, N. Gupta, A. Sharma and M. Rawat, *Curr. Top. Med. Chem*., 2017, **17**, 2215.
307. Z. Bozdech, M. Llinás, B. L. Pulliam, E. D. Wong, J. Zhu and J. L. DeRisi, *PLoS. Biol*., 2003, **1**, 85.
308. S. Dalal and M. Klemba, *J. Biol. Chem*., 2007, **282**, 35978.
309. P. M. Jones, M. W. Robinson, J. P. Dalton and A. M. George, *PLoS One*, 2011, **6**, e28589.
310. D. Ragheb, S. Dalal, K. M. Bompiani, W. K. Ray and M. Klemba, *J. Biol. Chem*., 2011, **286,** 27255.
311. A. Ivanov and I. Matsumura, *J. Mol. Graph. Model.*, 2012, **35**, 43.
312. C. E. Murata and D. E. Goldberg, *Mol. Biochem. Parasitol*., 2003, **129**, 123.
313. C. Grüring, A. Heiber, F. Kruse, J. Ungefehr, T. W. Gilberger and T. Spielmann, *Nat. Commun*., 2011, **2**, 1169.
314. M. Clark, N. C. Fisher, R. Kasthuri and C. C. Hand, *Br. J. Haematol*., 2013, **161**, 262.
315. A. Srivastava, N. Philip, K. R. Hughes, K. Georgiou, J. I. MacRae, M. P. Barrett, D. J. Creek, M. J. McConville and A. P. Waters, *PLoS Pathog*., 2016, **12**, e1006094.
316. P. K. Chiang, M. E. Chamberlin, D. Nicholson, S. Soubes, X. Su, G. Subramanian, D. E. Lanar, S. T. Prigge, J. P. Scovill, L. H. Miller and J. Y. Chou, *Biochem. J*., 1999, **344**, 571.
317. S. Kenthirapalan, A. P. Waters, K. Matuschewski and T. W. A. Kooij, *Mol. Microbiol*., 2014, **91**, 315.
318. S. R. Goodman, A. Kurdia, L. Ammann, D. Kakhniashvili and O. Daescu, *Exp. Biol. Med*., 2007, **232**, 1391.
319. G. V. Kryukov, S. Castellano, S. V. Novoselov, A. V. Lobanov, O. Zehtab, R. Guigo and V. N. Gladyshev, *Science*, 2003, **300**, 1439.
320. A. V. Lobanov, C. Delgado, S. Rahlfs, S. V. Novoselov, G. V. Kryukov, S. Gromer, D. L. Hatfield, K. Becker and V. N. Gladyshev, *Nucleic Acids Res*., 2006, **34**, 496.
321. A. Röseler, J. H. Prieto, R. Iozef, B. Hecker, R. H. Schirmer, S. Külzer, J. Przyborski, S. Rahlfs and K. Becker, *Antioxid. Redox Signal*., 2012, **17**, 534.
322. J. P. Rubio and A. F. Cowman, *Exp. Parasitol*., 1994, **79**, 137.
323. E. Rosenberg, I. Litus, N. Schwarzfuchs, R. Sinay, P. Schlesinger, J. Golenser, S. Baumeister, K. Lingelbach and Y. Pollack, *J. Biol. Chem*., 2006, **281**, 27039.
324. I. W. Boucher, A. M. Brzozowski, J. A. Brannigan, C. Schnick, D. J. Smith, S. A. Kyes and A. J. Wilkinson, *BMC Struct. Biol*., 2006, **6**, 20.
325. S. L. Goh, L. L. Goh and T. S. Sim, *Parasitol. Res*., 2005, **97**, 295.
326. S. Subramanian, M. Hardt, Y. Choe, R. K. Niles, E. B. Johansen, J. Legac, J. Gut, I. D. Kerr, C. S. Craik and P. J. Rosenthal, *PLoS One*, 2009, **4**, e5156.
327. P. S. Sijwali and P. J. Rosenthal, *Proc. Natl. Acad. Sci. U. S. A*., 2004, **101**, 4384.
328. K. J. Saliba and K. Kirk, *J. Biol. Chem*., 1999, 274, 33213.
329. R. A. Cooper, J. Papakrivos, K. D. Lane, H. Fujioka, K. Lingelbach and T. E. Wellems, *Mol. Biochem. Parasitol*., 2005, **144**, 167.

330. M. Hayashi, S. Taniguchi, Y. Ishizuka, H. S. Kim, Y. Wataya, A. Yamamoto and Y. Moriyama, *J. Biol. Chem*., 2001, **276**, 15249.
331. A. L. Boskey and E. Villarreal-Ramirez, *Matrix Biol*., 2016, **52-54**, 43.
332. X. R. Song, Z. Liu, L. Wang and L. Song, *Front. Mar. Sci*., 2019, **6**, e00041.
333. G. L. Rosano and E. A. Ceccarelli, *Front. Microbiol*., 2014, **5**, e00172.
334. K. A. de Villiers, C. H. Kaschula, T. J. Egan and H. M. Marques, *J. Biol. Inorg. Chem*., 2007, **12**, 101.
335. K. Flick, S. Ahuja, A. Chene, M. T. Bejarano and Q. J. Chen, *Malar. J*., 2004, **3**, 50.
336. G. Lindwall, M. Chau, S. R. Gardner and L. A. Kohlstaedt, *Protein Eng*., 2000, **13**, 67.
337. M. Vedadi, J. Lew, J. Artz, M. Amani, Y. Zhao, A. Dong, G. A. Wasney, M. Gao, T. Hills, S. Brokx, W. Qiu, S. Sharma, A. Diassiti, Z. Alam, M. Melone, A. Mulichak, A. Wernimont, J. Bray, P. Loppnau, O. Plotnikova, K. Newberry, E. Sundararajan, S. Houston, J. Walker, W. Tempel, A. Bochkarev, I. Kozieradzki, A. Edwards, C. Arrowsmith, D. Roos, K. Kain and R. Hui, *Mol. Biochem. Parasitol*., 2007, **151**, 100.
338. G. Qing, L. Ma, A. Khorchid, G. V. T. Swapna, T. K. Mal, M. M. Takayama, B. Xia, S. Phadtare, H. Ke, T. Acton, G. T. Montelione, M. Ikura and M. Inouye, *Nat. Biotechnol*., 2004, **22**, 877.
339. I. U. Heinemann, M. Jahn and D. Jahn, *Arch. Biochem. Biophys*., 2008, **474**, 238.
340. H. Y. Lu, L. L. Qiu, X. J. Yang, X. M. Zhang, Z. Zhang and S. L. Wang, *J. Biochem*., 2013, **153**, 555.
341. B. Miroux and J. E. Walker, *J. Mol. Biol*., 1996, **260**, 289.
342. K. D. Tartof and C. A. Hobbs, *Bethesda Res. Lab. Focus*, 1987, **9**, 12.
343. T. H. Grossman, E. S. Kawasaki, S. R. Punreddy and M. S. Osburne, *Gene*, 1998, **209**, 95.
344. K. Nishihara, M. Kanemori, M. Kitagawa, H. Yanagi and T. Yura, *Appl. Environ. Microbiol*., 1998, **64**, 1694.
345. A. J. Link, K. Robison and G. M. Church, *Electrophoresis*, 1997, **18**, 1259.
346. F. Baneyx and M. Mujacic, *Nat. Biotechnol*., 2004, **22**, 1399.
347. I. Palmer and P. T. Wingfield, *Curr. Protoc. Protein Sci*., 2004, **70**, DOI:10.1002/0471140864.ps0603s38.
348. N. Oganesyan, S. H. Kim and R. Kim, *J. Struct. Funct. Genomics*, 2005, **6**, 177.
349. D. Rathore, S. C. L. Hrstka, J. B. Sacci, P. De la Vega, R. J. Linhardt, S. Kumar and T. F. McCutchan, *J. Biol. Chem*., 2003, **278**, 40905.
350. Thermo Fisher Scientific, *InVision™ His-Tag In-Gel Stain User Guide*, California, 2012.
351. N. J. Greenfield, *Nat. Protoc*., 2006, **1**, 2876.
352. C. A. Royer, *Chem. Rev*., 2006, **106**, 1769.
353. L. Y. Yampolsky and A. Stoltzfus, *Genetics*, 2005, **170**, 1459.
354. S. Mann, R. B. Frankel and R. P. Blakemore, *Nature*, 1984, **310**, 405.
355. T. White, S. Bursten, D. Federighi, R. A. Lewis and E. Nudelman, *Anal. Biochem*., 1998, **258**, 109.
356. E. G. Bligh and W. J. Dyer, *Can. J. Biochem. Physiol*., 1959, **37**, 911.
357. R. B. Chan, T. G. Oliveira, E. P. Cortes, L. S. Honig, K. E. Duff, S. A. Small, M. R. Wenk, G. Shui and G. Di Paolo, *J. Biol. Chem*., 2012, **287**, 2678.
358. K. K. Ncokazi and T. J. Egan, *Anal. Biochem*., 2005, **338**, 306.
359. B. Gligorijevic, T. Bennett, R. McAllister, J. S. Urbach and P. D. Roepe, *Biochemistry*, 2006, **45**, 12411.
360. P. N. Tran, S. H. J. Brown, M. Rug, M. C. Ridgway, T. W. Mitchell and A. G. Maier, *Malar. J*., 2016, **15**, 73.

361. R. F. Waller, P. J. Keeling, R. G. K. Donald, B. Striepen, E. Handman, N. Lang-Unnasch, A. F. Cowman, G. S. Besra, D. S. Roos and G. I. McFadden, *Proc. Natl. Acad. Sci. U. S. A.*, 1998, **95**, 12352.
362. J. C. Touchstone, *J. Chromatogr. B Biomed. Appl.*, 1995, **671**, 169.
363. B. Fuchs, R. Suss, K. Teuber, M. Eibisch and J. Schiller, *J. Chromatogr. A*, 2011, **1218**, 2754.
364. K. Matheis, B. Fuchs, K. Lemmnitzer, R. Süb, H. Griesinger, S. Minarik, M. Oberle, M, Schulz, M and J. Schiller, *J. Glycomics Lipidomics*, 2015, **5**, e125.
365. E. D. Guerra, D. S. Bohle and M. Cerruti, *Langmuir*, 2016, **32**, 4479.
366. Agilent Technologies, *Concepts Guide The Big Picture*, California, 2012.
367. S. A. Gerber, J. Rush, O. Stemman, M. W. Kirschner and S. P. Gygi, *Proc. Natl. Acad. Sci. U. S. A.*, 2003, **100**, 6940.
368. R. Chan, P. D. Uchil, J. Jin, G. Shui, D. E. Ott, W. Mothes and M. R. Wenk, *J. Virol.*, 2008, **82**, 11228.
369. G. Shui, X. L. Guan, P. Gopalakrishnan, Y. Xue, J. S. Y. Goh, H. Yang and M. R. Wenk, *PLoS One*, 2010, **5**, e11956.
370. S. Suetsugu, S. Kurisu and T. Takenawa, *Physiol. Rev.*, 2014, **94**, 1219.
371. K. Athenstaedt and G. Daum, *Cell. Mol. Life Sci.*, 2006, **63**, 1355.
372. K. Leidl, G. Liebisch, D. Richter and G. Schmitz, *Biochim. Biophys. Acta*, 2008, **1781**, 655.
373. B. S. Nayak, B. Y. Beharry, S. Armoogam, M. Nancoo, K. Ramadhin, K. Ramesar, C. Ramnarine, A. Singh, A Singh, K. U. Nwachi, S. Teelucksing, R. Mathura and L. Roberts, *Vasc. Health Risk Manag.*, 2008, **4**, 893.
374. N. Mohandas and P. G. Gallagher, *Blood*, 2008, **112**, 3939.
375. M. Labaied, B. Jayabalasingham, N. Bano, S. J. Cha, J. Sandoval, G. Guan and I. Coppens, *Cell. Microbiol.*, 2011, **13**, 569.
376. V. L. Cebolla, E. Mateos, R. Garriga, C. Jarne, L. Membrado, F. P. Cossio, E. M. Gálvez, M. Matt and A. Delgado-Camón, *ChemPhysChem.*, 2012, **13**, 291.
377. F. P. Cossio, A. Arrieta, V. L. Cebolla, L. Membrado, M. P. Domingo, P. Henrion and J. Vela, *Anal. Chem.*, 2000, **72**, 1759.
378. E. M. Galvez, M. Matt, V. L. Cebolla, F. Fernandes, L. Membrado, F. P. Cossio, R. Garriga, J. S. Vela and M. H. Guermouche, *Anal. Chem.*, 2006, **78**, 3699.
379. P. Greenspan, E. P. Mayer and S. D. Fowler, *J. Cell Biol.*, 1985, **100**, 965.
380. S. A. Latt and G. Stetten, *J. Histochem. Cytochem.*, 1976, **24**, 24.
381. T. J. Sargeant, B. Lloyd-Lewis, H. K. Resemann, A. Ramos-Montoya, J. Skepper and C. J. Watson, *Nat. Cell Biol.*, 2014, **16**, 1057.
382. S. Fukumoto and T. Fujimoto, *Histochem. Cell Biol.*, 2002, **118**, 423.
383. R. G. Pourcho, M. H. Bernstein and S. F. Gould, *Stain Technol.*, 1978, **53**, 29.
384. S. Mukherjee, X. Zha, I. Tabas and F. R. Maxfield, *Biophys. J.*, 1998, **75**, 1915.
385. M. J. Bellemare, D. S. Bohle, C. N. Brosseau, E. Georges, M. Godbout, J. Kelly, M. L. Leimanis, R. Leonelli, M. Olivier and M. Smilkstein, *J. Phys. Chem. B*, 2009, **113**, 8391.
386. P.S. Maddox, B. Moree, J. C. Canman and E.D. Salmon, *Methods Enzymol.*, 2003, **360**, 597
387. A. Nakano, *Cell Struct. Funct.*, 2002, **27**, 349.
388. T. Wilson, *Cold Spring Harb. Protoc.*, 2010, **2010**, 1208.
389. D. A. Fidock, T. Nomura, A. K. Talley, R. A. Cooper, S. M. Dzekunov, M. T. Ferdig, L. M. B. Ursos, A. B. S. Sidhu, B. Naude, K. W. Deitsch, X. Su, J. C. Wootton, P. D. Roepe and T. E. Wellems, *Mol. Cell.*, 2000, **6**, 861.
390. K. J. Waldron and N. J. Robinson, *Nat. Rev. Microbiol.*, 2009, **7**, 25.
391. D. S. Johnson, A. Mortazavi, R. M. Myers and B. Wold, *Science*, 2007, **316**, 1497.

392. Q. He, J. Johnston and J. Zeitlinger, *Nat. Biotechnol.*, 2015, **33**, 395.
393. E. Betzig, G. H. Patterson, R. Sougrat, O. W. Lindwasser, S. Olenych, J. S. Bonifacino, M. W. Davidson, J. Lippincott-Schwartz and H. F. Hess, *Science*, 2006, **313**, 1642.
394. S. T. Hess, T. P. K. Girirajan and M. D. Mason, *Biophys. J.*, 2006, **91**, 4258.

Appendix

Table A1: Neutral lipids identified by lipidomics mass spectrometry occluded by haemozoin

Lipid Class	Lipid Species	Concentration (nmol/mg)[a]		
Cholesterol	Free CHL	28.9	±	8.9
Cholesterol esters	CE 16:0	0.04	±	0.007
	CE 16:1	0.03	±	0.006
	CE 18:0	0.004	±	0.0007
	CE 18:1	0.12	±	0.02
	CE 18:2	0.4	±	0.06
	CE 20:2	0.0003	±	0.0002
	CE 20:3	0.005	±	0.0006
	CE 20:4	0.034	±	0.0023
	CE 22:6	0.002	±	0.0003
Acyl Carnitine	AC C12:0	0.00042	±	0.0004
	AC C14:0	0.00021	±	0.00016
	AC C16:0	0.00037	±	0.00024
	AC C18:0	0.0008	±	0.0005
	AC C18:1	0.022	±	0.0031
	AC C8:0	0.002	±	0.0005
Monoacylglycerols	MG 16:0	0.052	±	0.0055
	MG 16:1	0.03	±	0.003
	MG 18:0	0.017	±	0.013
	MG 18:1	0.05	±	0.005
	MG 18:2	0.04	±	0.003
	MG 20:0	0.003	±	0.002
Diacylglycerols	DG 28:0/14:0	0.0024	±	0.00016
	DG 30:0/14:0	0.001	±	0.00001
	DG 32:0/16:0	0.0097	±	0.0016
	DG 32:1/16:0	0.001	±	0.0002
	DG 32:2/16:1	0.0009	±	0.00007
	DG 34:0/16:0	0.0098	±	0.0013
	DG 34:1/16:0	0.01	±	0.002
	DG 34:2/16:0	0.01	±	0.001
	DG 34:2/16:1	0.0024	±	0.00024
	DG 36:0/18:0	0.02	±	0.005
	DG 36:1/18:0	0.005	±	0.0009
	DG 36:2/18:0	0.003	±	0.0004
	DG 36:2/18:1	0.016	±	0.0017
	DG 36:3/18:1	0.012	±	0.00085
	DG 38:2/18:0	0.0002	±	0.00002
	DG 38:3/18:0	0.001	±	0.00007

	DG 38:4/18:0	0.0005	±	0.00008
	DG 38:4/18:1	0.0006	±	0.00004
	DG 40:4/18:0	0.0001	±	0.00001
	DG 40:5/18:0	0.0002	±	0.00003
	DG 40:5/18:1	0.00004	±	0.00003
	DG 40:6/18:0	0.00005	±	0.00002
	DG 40:6/18:1	0.0002	±	0.00003
Triacylglycerols	TG 48:0/16:0	0.01	±	0.003
	TG 48:1/16:0	0.0024	±	0.00048
	TG 50:0/16:0	0.0018	±	0.00032
	TG 50:2/16:1	0.001	±	0.0004
	TG 50:3/16:1	0.002	±	0.0005
	TG 52:1/18:0	0.002	±	0.0006
	TG 52:2/18:0	0.0007	±	0.0002
	TG 52:3/18:1	0.003	±	0.001
	TG 52:4/18:1	0.0005	±	0.0002
	TG 52:5/18:1	0.00005	±	0.000009
	TG 52:5/20:4	0.00018	±	0.000026
	TG 54:0/18:0	0.00008	±	0.00004
	TG 54:1/18:0	0.0003	±	0.00005
	TG 54:2/18:0	0.0005	±	0.0002
	TG 54:3/18:0	0.00034	±	0.00013
	TG 54:4/18:1	0.0015	±	0.00055
	TG 54:4/20:4	0.00018	±	0.000032
	TG 54:5/18:1	0.00053	±	0.00017
	TG 54:5/20:4	0.00055	±	0.00016
	TG 54:6/18:1	0.0001	±	0.00003
	TG 54:6/20:4	0.0003	±	0.00005
	TG 54:7/20:4	0.00007	±	0.00002
	TG 56:4/18:1	0.0001	±	0.00002
	TG 56:4/20:4	0.00003	±	0.000007
	TG 56:5/18:1	0.0002	±	0.00004
	TG 56:5/20:4	0.00009	±	0.00002
	TG 56:6/20:4	0.0003	±	0.00006
	TG 56:7/20:4	0.0002	±	0.00005
	TG 56:8/20:4	0.00014	±	0.000014
	TG 56:9/20:4	0.00004	±	0.000008
	TG 58:8/22:6	0.00002	±	0.000011
	TG 58:9/22:6	0.00003	±	0.000008

[a] Expressed per mg total parasite protein

Table A2: Phospholipids identified by lipidomics mass spectrometry to be occluded by haemozoin

Lipid Class	Lipid Species	Concentration (nmol/mg)[a]
Phosphatidic acid	PA 30:0	0.00017 ± 0.00002
	PA 32:0	0.000066 ± 0.00002
	PA 32:1	0.00003 ± 0.000007
	PA 34:0	0.00004 ± 0.00001
	PA 34:1	0.00031 ± 0.00004
	PA 34:2	0.0002 ± 0.00002
	PA 36:0	0.00002 ± 0.00001
	PA 36:1	0.0004 ± 0.00003
	PA 36:2	0.000095 ± 0.000011
	PA 36:3	0.00008 ± 0.00001
	PA 36:4	0.00008 ± 0.00001
	PA 38:0	0.00005 ± 0.00001
	PA 38:1	0.00005 ± 0.00001
	PA 38:3	0.00009 ± 0.00002
	PA 38:4	0.00015 ± 0.00003
	PA 38:5	0.00004 ± 0.00001
	PA 38:6	0.00007 ± 0.00001
	PA 40:4	0.0001 ± 0.00003
	PA 40:5	0.00006 ± 0.00002
	PA 40:6	0.00013 ± 0.00002
	PA 40:7	0.00004 ± 0.00001
	PA 42:5	0.00013 ± 0.00002
	PA 42:6	0.00033 ± 0.00009
	PA 42:7	0.00013 ± 0.00002
Phosphatidylcholine	PC 30:0	0.047 ± 0.004
	PC 32:0	0.12 ± 0.018
	PC 32:1	0.027 ± 0.0058
	PC 34:0	0.044 ± 0.0073
	PC 34:1	0.21 ± 0.041
	PC 34:2	0.11 ± 0.018
	PC 36:0	0.0067 ± 0.0012
	PC 36:1	0.049 ± 0.0091
	PC 36:2	0.051 ± 0.0089
	PC 36:3	0.026 ± 0.0044
	PC 36:4	0.04 ± 0.007
	PC 38:0	0.0012 ± 0.00023
	PC 38:1	0.0015 ± 0.00031
	PC 38:2	0.0019 ± 0.00033
	PC 38:3	0.0065 ± 0.0001
	PC 38:4	0.021 ± 0.0041
	PC 38:5	0.01 ± 0.001
	PC 38:6	0.01 ± 0.002

	PC 40:4	0.001	±	0.0003
	PC 40:5	0.002	±	0.0003
	PC 40:6	0.004	±	0.0008
	PC 40:7	0.0013	±	0.00033
	PC 42:5	0.0002	±	0.00005
	PC 42:6	0.0001	±	0.00004
	PC 42:7	0.00019	±	0.000054
Ether phosphatidylcholine	PCe 30:0	0.02	±	0.002
	PCe 32:0	0.007	±	0.0006
	PCe 32:1	0.0018	±	0.00013
	PCe 34:0	0.0045	±	0.00078
	PCe 34:1	0.0096	±	0.0016
	PCe 34:2	0.0046	±	0.00045
	PCe 36:0	0.0024	±	0.00038
	PCe 36:1	0.009	±	0.002
	PCe 36:2	0.006	±	0.001
	PCe 36:3	0.003	±	0.0004
	PCe 36:4	0.004	±	0.0008
	PCe 38:0	0.001	±	0.0001
	PCe 38:1	0.0016	±	0.00018
	PCe 38:2	0.0013	±	0.0003
	PCe 38:3	0.0012	±	0.00024
	PCe 38:4	0.003	±	0.0007
	PCe 38:5	0.003	±	0.001
	PCe 38:6	0.0016	±	0.0003
	PCe 40:4	0.0006	±	0.0001
	PCe 40:5	0.0007	±	0.0002
	PCe 40:6	0.0007	±	0.0002
	PCe 40:7	0.001	±	0.0002
	PCe 42:5	0.0002	±	0.00003
	PCe 42:6	0.0003	±	0.00005
	PCe 42:7	0.00014	±	0.000045
Phosphatidylethanolamine	PE 30:0	0.02	±	0.006
	PE 32:1	0.01	±	0.008
	PE 34:0	0.013	±	0.008
	PE 34:1	0.038	±	0.014
	PE 34:2	0.02	±	0.009
	PE 36:0	0.04	±	0.01
	PE 36:1	0.04	±	0.02
	PE 36:2	0.007	±	0.004
	PE 36:3	0.008	±	0.003
	PE 36:4	0.02	±	0.01
	PE 38:0	0.05	±	0.01
	PE 38:1	0.04	±	0.01
	PE 38:3	0.009	±	0.003
	PE 38:4	0.08	±	0.03
	PE 38:5	0.014	±	0.0096

	PE 38:6	0.013	±	0.0086
	PE 40:4	0.0051	±	0.005
	PE 40:5	0.0035	±	0.0026
	PE 40:6	0.041	±	0.025
	PE 40:7	0.01	±	0.005
	PE 42:5	0.006	±	0.004
Plasmalogen phosphatidylethanolamine	PEp 34:0	0.005	±	0.003
	PEp 34:1	0.015	±	0.0088
	PEp 34:2	0.002	±	0.001
	PEp 36:0	0.007	±	0.004
	PEp 36:1	0.014	±	0.0061
	PEp 36:2	0.026	±	0.0087
	PEp 36:3	0.0044	±	0.0023
	PEp 36:4	0.015	±	0.0035
	PEp 38:0	0.01	±	0.004
	PEp 38:4	0.018	±	0.007
	PEp 38:5	0.023	±	0.012
	PEp 38:6	0.04	±	0.01
	PEp 40:4	0.016	±	0.0062
	PEp 40:5	0.013	±	0.005
	PEp 40:6	0.06	±	0.02
	PEp 40:7	0.04	±	0.01
Phosphatidylserine	PS 34:0	0.0007	±	0.0003
	PS 34:1	0.002	±	0.0006
	PS 34:2	0.0004	±	0.0002
	PS 36:0	0.002	±	0.0005
	PS 36:1	0.02	±	0.003
	PS 36:2	0.005	±	0.001
	PS 36:3	0.0003	±	0.0002
	PS 36:4	0.0002	±	0.0001
	PS 38:2	0.00053	±	0.00022
	PS 38:3	0.0015	±	0.00051
	PS 38:4	0.006	±	0.0009
	PS 38:5	0.00065	±	0.00017
	PS 38:6	0.0006	±	0.0002
	PS 40:4	0.007	±	0.001
	PS 40:5	0.014	±	0.0026
	PS 40:6	0.067	±	0.015
	PS 40:7	0.0017	±	0.00054
Phosphatidylinositol	PI 30:0	0.001	±	0.0003
	PI 32:0	0.0003	±	0.0002
	PI 32:1	0.0002	±	0.0001
	PI 34:0	0.0006	±	0.0002
	PI 34:1	0.0024	±	0.00047
	PI 34:2	0.0008	±	0.0001
	PI 36:0	0.00079	±	0.00031

	PI 36:1	0.006	±	0.001
	PI 36:2	0.004	±	0.0009
	PI 36:3	0.0012	±	0.00023
	PI 36:4	0.0024	±	0.00085
	PI 38:2	0.00048	±	0.00025
	PI 38:3	0.0021	±	0.00069
	PI 38:4	0.02	±	0.003
	PI 38:5	0.003	±	0.0007
	PI 38:6	0.0004	±	0.0001
	PI 40:4	0.00024	±	0.00011
	PI 40:5	0.00047	±	0.00014
	PI 40:6	0.0004	±	0.00005
Phosphatidylglycerol	PG 32:1	0.00021	±	0.00011
	PG 34:0	0.0003	±	0.00007
	PG 34:1	0.0012	±	0.00041
	PG 34:2	0.00077	±	0.00025
	PG 36:0	0.00012	±	0.00005
	PG 36:1	0.0008	±	0.0003
	PG 36:2	0.0017	±	0.00044
	PG 36:3	0.00022	±	0.00006
	PG 36:4	0.0002	±	0.00007
	PG 38:4	0.00032	±	0.00012
Bis(monoacylglycero)phosphate	BMP 30:0	0.0002	±	0.00004
	BMP 32:0	0.0001	±	0.00004
	BMP 34:0	0.00012	±	0.000014
	BMP 34:1	0.00016	±	0.00004
	BMP 34:2	0.0001	±	0.00002
	BMP 36:0	0.00006	±	0.00003
	BMP 36:1	0.0001	±	0.00003
	BMP 36:2	0.00014	±	0.00002
	BMP 38:4	0.00008	±	0.00003
Acyl Phosphatidylglycerol	AcylPG 16:0-34:0	0.00004	±	0.00002
	AcylPG 16:0-34:1	0.0003	±	0.00007
	AcylPG 16:0-34:2	0.0003	±	0.00005
	AcylPG 16:0-36:1	0.00027	±	0.000064
	AcylPG 16:0-36:2	0.00017	±	0.000074
	AcylPG 16:0-36:3	0.00007	±	0.00002
	AcylPG 16:0-38:1	0.000097	±	0.000041
	AcylPG 16:0-38:2	0.000048	±	0.000022
	AcylPG 16:0-38:3	0.00007	±	0.00002
	AcylPG 16:0-38:5	0.000012	±	0.000008
	AcylPG 16:0-40:6	0.000007	±	0.000007
Lysophosphatidylcholine	LPC 16:0	0.013	±	0.00093
	LPC 16:1	0.00032	±	0.000027
	LPC 18:0	0.0046	±	0.00055
	LPC 18:1	0.0021	±	0.00032
	LPC 20:0	0.00016	±	0.000021

	LPC 20:1	0.00009	±	0.00003
	LPC 20:2	0.00002	±	0.00001
	LPC 20:3	0.00015	±	0.00002
	LPC 20:4	0.00053	±	0.00011
Ether lysophosphatidylcholine	LPCe 16:0	0.00067	±	0.00019
	LPCe 16:1	0.0003	±	0.0001
	LPCe 18:0	0.001	±	0.0002
	LPCe 18:1	0.0004	±	0.0001
	LPCe 20:0	0.0002	±	0.00003
	LPCe 20:1	0.00014	±	0.000020
	LPCe 20:2	0.00013	±	0.000012
Lysophosphatidylethanolamine	LPE 16:0	0.00098	±	0.00027
	LPE 18:0	0.00072	±	0.00014
	LPE 18:1	0.00039	±	0.00021
	LPE 20:4	0.0005	±	0.0002
Plasmogen Lysophosphatidylethanolamine	LPEp 16:0	0.003	±	0.001
	LPEp 18:0	0.006	±	0.002
Lysophosphatidylinositol	LPI 16:0	0.0005	±	0.0001
	LPI 18:0	0.002	±	0.0002
	LPI 18:1	0.0014	±	0.00031
	LPI 20:2	0.00014	±	0.000083
	LPI 20:3	0.00011	±	0.000079
	LPI 20:4	0.0006	±	0.0002
Lysophosphatidylserine	LPS 16:0	0.0009	±	0.0003
	LPS 18:0	0.015	±	0.0027
	LPS 18:1	0.0022	±	0.00064
	LPS 20:4	0.0009	±	0.0002
N-Acyl Phosphatidylethanolamine	NAPE 16:0/18:0/20:4	0.000015	±	0.000013
	NAPE 18:0/18:1/20:4	0.00002	±	0.000007
	NAPE p16:0/18:0/20:4	0.0002	±	0.00004
	NAPE p18:0/18:1/20:4	0.00009	±	0.00004
	NAPE p18:0/20:4/20:4	0.00002	±	0.00001
	NAPE p18:1/18:1/20:4	0.00007	±	0.00003
	NAPE p18:1/20:4/20:4	0.00002	±	0.00001
N-Acyl Phosphatidylserine	NAPS 16:0-36:1	0.000007	±	0.000006
	NAPS 16:0-38:4	0.000006	±	0.000006
N-Acyl Serine	NSer 16:0	0.003	±	0.0006
	NSer 18:0	0.002	±	0.0004
	NSer 18:1	0.001	±	0.0005

[a] Expressed per mg total parasite protein

Table A3: Sphingolipids identified by lipidomics mass spectrometry to be occluded by haemozoin

Lipid Class	Lipid Species	Concentration (nmol/mg)[a]		
Dihydroceramides	dhCer d18:0/16:0	0.003	±	0.0004
	dhCer d18:0/16:1	0.00064	±	0.00012
	dhCer d18:0/18:0	0.005	±	0.001
	dhCer d18:0/18:1	0.0004	±	0.00009
	dhCer d18:0/20:0	0.0002	±	0.00004
	dhCer d18:0/22:0	0.0004	±	0.0001
	dhCer d18:0/22:1	0.00004	±	0.00002
	dhCer d18:0/24:0	0.0004	±	0.0001
	dhCer d18:0/24:1	0.0006	±	0.00007
	dhCer d18:0/26:0	0.00023	±	0.000081
	dhCer d18:0/26:1	0.000087	±	0.000036
Ceramides	Cer d18:1/16:0	0.07	±	0.01
	Cer d18:1/16:1	0.02	±	0.002
	Cer d18:1/18:0	0.009	±	0.001
	Cer d18:1/18:1	0.001	±	0.0003
	Cer d18:1/20:0	0.002	±	0.0004
	Cer d18:1/20:1	0.0003	±	0.00005
	Cer d18:1/22:0	0.0095	±	0.0019
	Cer d18:1/22:1	0.0009	±	0.0002
	Cer d18:1/24:0	0.02	±	0.003
	Cer d18:1/24:1	0.012	±	0.0016
	Cer d18:1/26:0	0.002	±	0.0003
	Cer d18:1/26:1	0.0006	±	0.0002
Sphingomyelins	SM d18:1/16:0	0.1	±	0.008
	SM d18:1/16:1	0.004	±	0.0004
	SM d18:1/18:0	0.02	±	0.002
	SM d18:1/18:1	0.002	±	0.0002
	SM d18:1/20:0	0.009	±	0.001
	SM d18:1/20:1	0.001	±	0.0001
	SM d18:1/22:0	0.038	±	0.0053
	SM d18:1/22:1	0.005	±	0.0005
	SM d18:1/24:0	0.065	±	0.0095
	SM d18:1/24:1	0.027	±	0.0035
	SM d18:1/26:0	0.0027	±	0.00043
	SM d18:1/26:1	0.001	±	0.0002
Dihydrosphingomyelins	dhSM d18:0/16:0	0.000032	±	0.0000092
	dhSM d18:0/22:0	0.0007	±	0.0001
Monohexosylceramide	MhCer d18:0/16:0	0.0004	±	0.0002
	MhCer d18:0/16:1	0.00009	±	0.00007
	MhCer d18:0/18:0	0.0002	±	0.0001
	MhCer d18:0/22:0	0.00008	±	0.00006
	MhCer d18:0/22:1	0.00004	±	0.00003

	MhCer d18:0/24:0	0.00012	±	0.000081
	MhCer d18:0/24:1	0.00059	±	0.00029
	MhCer d18:1/16:0	0.00065	±	0.00022
	MhCer d18:1/16:1	0.0002	±	0.0001
	MhCer d18:1/18:0	0.0008	±	0.0001
	MhCer d18:1/18:1	0.00053	±	0.00023
	MhCer d18:1/20:0	0.0001	±	0.00005
	MhCer d18:1/20:1	0.00009	±	0.00004
	MhCer d18:1/22:0	0.001	±	0.0003
	MhCer d18:1/22:1	0.0014	±	0.00075
	MhCer d18:1/24:0	0.0015	±	0.00022
	MhCer d18:1/24:1	0.0016	±	0.00042
	MhCer d18:1/26:0	0.0003	±	0.0001
	MhCer d18:1/26:1	0.00042	±	0.00012
Sulfatides	Sulf d18:0/16:0	0.0043	±	0.00055
	Sulf d18:1/16:0	0.0004	±	0.0002
	Sulf d18:1/16:1	0.00017	±	0.000031
	Sulf d18:1/18:0	0.00066	±	0.00026
	Sulf d18:1/18:1	0.00022	±	0.000095
	Sulf d18:1/20:0	0.0006	±	0.0002
	Sulf d18:1/20:1	0.0003	±	0.0001
	Sulf d18:1/22:0	0.0008	±	0.0001
	Sulf d18:1/22:1	0.0006	±	0.0002
	Sulf d18:1/24:0	0.001	±	0.0002
	Sulf d18:1/24:1	0.00081	±	0.000088
Lactosylceramides	LacCer d18:1/16:0	0.00098	±	0.00031
	LacCer d18:1/18:0	0.00018	±	0.00013
	LacCer d18:1/18:1	0.000053	±	0.000026
	LacCer d18:1/22:0	0.00013	±	0.000069
	LacCer d18:1/24:0	0.00042	±	0.00027
	LacCer d18:1/24:1	0.000084	±	0.000042
Monosialodihexosylgangliosides	GM3 d18:1/16:0	0.00014	±	0.000082
	GM3 d18:1/18:0	0.00041	±	0.00019
	GM3 d18:1/20:0	0.00021	±	0.000091
Globotriaosylceramides	GB3 d18:1/16:0	0.0008	±	0.0005
	GB3 d18:1/22:0	0.0006	±	0.0001
	GB3 d18:1/24:0	0.003	±	0.001
	GB3 d18:1/24:1	0.0003	±	0.0002
	GB3 d18:1/26:0	0.00027	±	0.00014
	GB3 d18:1/26:1	0.000071	±	0.000058

[a] Expressed per mg total parasite protein